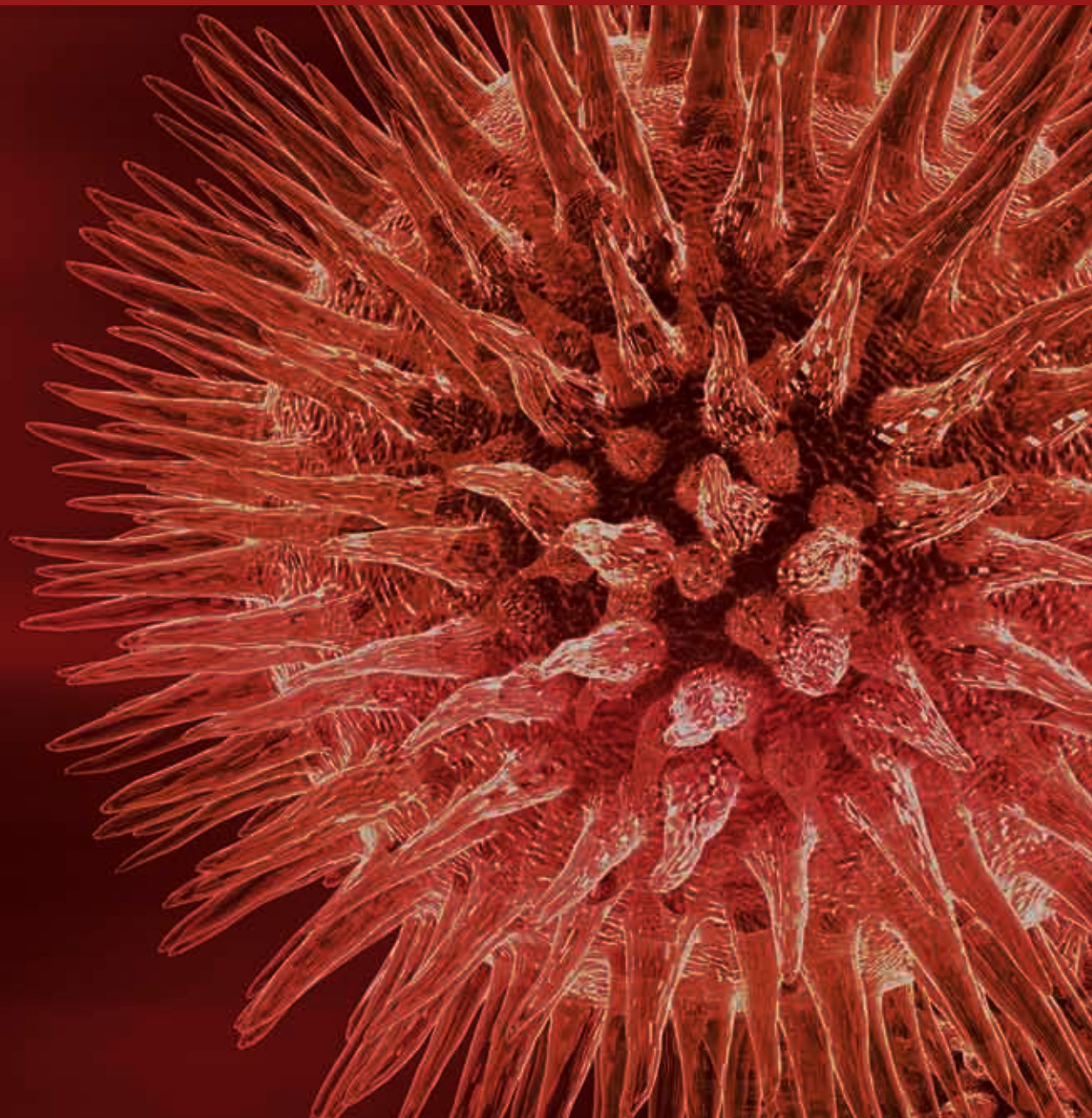


# **Development, Disease, and Regeneration of Tissues in the Dental-Craniofacial Complex**

Guest Editors: Brian L. Foster, Yong-Hee P. Chun, Erica L. Scheller,  
Zhao Lin, Chad M. Novince, and Avina Paranjpe





---

# **Development, Disease, and Regeneration of Tissues in the Dental-Craniofacial Complex**



## **Development, Disease, and Regeneration of Tissues in the Dental-Craniofacial Complex**

Guest Editors: Brian L. Foster, Yong-Hee P. Chun,  
Erica L. Scheller, Zhao Lin, Chad M. Novince,  
and Avina Paranjpe



---

Copyright © 2013 Hindawi Publishing Corporation. All rights reserved.

This is a special issue published in “BioMed Research International.” All articles are open access articles distributed under the Creative Commons Attribution License, which permits unrestricted use, distribution, and reproduction in any medium, provided the original work is properly cited.

# Contents

**Development, Disease, and Regeneration of Tissues in the Dental-Craniofacial Complex**, Brian L. Foster, Yong-Hee P. Chun, Erica L. Scheller, Zhao Lin, Chad M. Novince, and Avina Paranjpe  
Volume 2013, Article ID 836871, 3 pages

**The Adaptive Nature of the Bone-Periodontal Ligament-Cementum Complex in a Ligature-Induced Periodontitis Rat Model**, Ji-Hyun Lee, Jeremy D. Lin, Justine I. Fong, Mark I. Ryder, and Sunita P. Ho  
Volume 2013, Article ID 876316, 17 pages

**An *In Vitro* Culture System for Long-Term Expansion of Epithelial and Mesenchymal Salivary Gland Cells: Role of TGF- $\beta$  1 in Salivary Gland Epithelial and Mesenchymal Differentiation**, Kajohnkiart Janebodin, Worakanya Buranaphatthana, Nicholas Ieronimakakis, Aislinn L. Hays, and Morayma Reyes  
Volume 2013, Article ID 815895, 20 pages

**Expression and Function of NUMB in Odontogenesis**, Haitao Li, Amsaveni Ramachandran, Qi Gao, Sriram Ravindran, Yiqiang Song, Carla Evans, and Anne George  
Volume 2013, Article ID 182965, 11 pages

**Mineral and Matrix Changes in Brtl/+ Teeth Provide Insights into Mineralization Mechanisms**, Adele L. Boskey, Kostas Verdelis, Lyudmila Spevak, Lyudmila Lukashova, Elia Beniash, Xu Yang, Wayne A. Cabral, and Joan C. Marini  
Volume 2013, Article ID 295812, 9 pages

**New Therapeutics in Promoting and Modulating Mandibular Growth in Cases with Mandibular Hypoplasia**, Tarek El-Bialy and Adel Alhadlaq  
Volume 2013, Article ID 789679, 10 pages

**An Immunohistochemistry Study of Sox9, Runx2, and Osterix Expression in the Mandibular Cartilages of Newborn Mouse**, Hong Zhang, Xiaopeng Zhao, Zhiguang Zhang, Weiwei Chen, and Xinli Zhang  
Volume 2013, Article ID 265380, 11 pages

**Craniosynostosis-Associated Fgfr2<sup>C342Y</sup> Mutant Bone Marrow Stromal Cells Exhibit Cell Autonomous Abnormalities in Osteoblast Differentiation and Bone Formation**, J. Liu, T.-G. Kwon, H. K. Nam, and N. E. Hatch  
Volume 2013, Article ID 292506, 11 pages

**Platelet-Rich Fibrin Promotes Periodontal Regeneration and Enhances Alveolar Bone Augmentation**, Qi Li, Shuang Pan, Smit J. Dangaria, Gokul Gopinathan, Antonia Kolokythas, Shunli Chu, Yajun Geng, Yanmin Zhou, and Xianghong Luan  
Volume 2013, Article ID 638043, 13 pages

**Heparanase Localization during Palatogenesis in Mice**, Azumi Hirata, Kentaro Katayama, Takehito Tsuji, Nagato Natsume, Toshio Sugahara, Yuichi Koga, Kazufumi Takano, Yoshinori Otsuki, and Hiroaki Nakamura  
Volume 2013, Article ID 760236, 9 pages





---

**A *DSPP* Mutation Causing Dentinogenesis Imperfecta and Characterization of the Mutational Effect,**  
Sook-Kyung Lee, Kyung-Eun Lee, Su Jeong Song, Hong-Keun Hyun, Sang-Hoon Lee, and Jung-Wook Kim  
Volume 2013, Article ID 948181, 7 pages

**Bodyweight Assessment of Enamelin Null Mice,** Albert H.-L. Chan, Rangsiyakorn Lertlam,  
James P. Simmer, Chia-Ning Wang, and Jan C. C. Hu  
Volume 2013, Article ID 246861, 8 pages

## Editorial

# Development, Disease, and Regeneration of Tissues in the Dental-Craniofacial Complex

**Brian L. Foster,<sup>1</sup> Yong-Hee P. Chun,<sup>2</sup> Erica L. Scheller,<sup>3</sup> Zhao Lin,<sup>4</sup>  
Chad M. Novince,<sup>5</sup> and Avina Paranjpe<sup>6</sup>**

<sup>1</sup> National Institute of Arthritis and Musculoskeletal and Skin Diseases (NIAMS), National Institutes of Health (NIH),  
9000 Rockville Pike Building 50, Room 4120, Bethesda, MD 20892, USA

<sup>2</sup> Department of Periodontics, University of Texas Health Science Center at San Antonio, TX 78229, USA

<sup>3</sup> Department of Molecular and Integrative Physiology, University of Michigan Medical School, Ann Arbor, MI 48105, USA

<sup>4</sup> Department of Periodontics, Virginia Commonwealth University School of Dentistry, Richmond, VA 23298, USA

<sup>5</sup> Department of Periodontics, University of Washington School of Dentistry, Seattle, WA 98195, USA

<sup>6</sup> Department of Endodontics, University of Washington School of Dentistry, Seattle, WA 98195, USA

Correspondence should be addressed to Brian L. Foster; [brian.foster@nih.gov](mailto:brian.foster@nih.gov)

Received 25 July 2013; Accepted 25 July 2013

Copyright © 2013 Brian L. Foster et al. This is an open access article distributed under the Creative Commons Attribution License, which permits unrestricted use, distribution, and reproduction in any medium, provided the original work is properly cited.

## 1. Introduction

This special issue of BioMed Research International focuses on the theme of development, disease, and regeneration of tissues in the dental-craniofacial complex, highlighting dynamic research that makes this an exciting area of biomedical research. Dental and craniofacial diseases have significant implications for the oral and systemic health of the general public. The dental-craniofacial tissues, more than any other tissue and organ of the body, are key for communication and mastication. We are delighted to present in this special issue of biomed research international a glimpse into diseases of dental and craniofacial tissues, biology in development, and therapeutic innovations. The theme was chosen in order to include fundamental basic science research highlighting normal developmental processes and cases where these go awry (including disease models), as well as translational and clinical papers investigating therapeutic strategies for repair and regeneration of tissues. The aim of this introduction is to highlight central concepts of the 11 individual papers under each theme and further illuminate topics to be found in the papers and throughout the special issue.

## 2. Disease

Diseases of the dental-craniofacial complex include a broad spectrum of illnesses, ranging from rare hereditary conditions to some of the most prevalent pathologies in the world,

including periodontal disease and premature tooth loss. Osteogenesis imperfecta (OI) is a rare inherited skeletal disorder associated with defective collagen structure, production, or processing. Dental defects arising as a result of OI represent one form of dentinogenesis imperfecta (DGI), which include reduced and defective dentin mineralization, alterations in tooth crown and root formation, and predisposition to tooth fractures and abscesses. In their report, A. Boskey et al. employed the *Brtl/+ Gly349Cys* knock-in mouse as a model for type IV OI, adopting an array of imaging techniques, including the Fourier transformed infrared microscopic imaging (FTIRI), scanning electron microscopy (SEM), and microcomputed tomography (micro-CT) to elucidate the etiology of dentin defects in this mouse. The authors report reduced mineralized dentin volume in molars of the knock-in mice, without changes in enamel. The expected alterations in collagen structure were observed at two months of age but self-corrected by six months. FTIRI identified increased acid phosphate content at both ages in knock-in mice, implying dentin matrix mineralization defects. These results indicate an impaired matrix mineralization and a slower correction of the phenotype with age, implying that both the collagen matrix and the noncollagenous proteins that regulate the function of that matrix may be altered in the *Brtl/+* teeth and shedding light on pathological mechanisms involved in tooth defects in patients with DGI.

Nonsyndromic DGI is caused by mutations in the dentin sialophosphoprotein (*DSPP*) gene. *DSPP* encodes for a large precursor protein that is cleaved into dentin sialoprotein (DSP) and dentin phosphoprotein (DPP), two prominent extracellular matrix components involved with dentin mineralization. In their paper, “A *DSPP* mutation causing dentinogenesis imperfecta and characterization of the mutational effect,” S. K. Lee et al. identified a mutation in exon 2 of *DSPP* in association with type III DGI in a Korean family. The DGI phenotype was quite severe, featuring tooth discoloration, severe attrition, and periapical inflammation. Through mutational analysis and *in vitro* assays, the authors report that the *DSPP* mutation resulted in retention of the mutant protein in the endoplasmic reticulum, leading to defective secretion of DSP. The same mutation was also found recently in a Chinese family and, interestingly, alters the same propeptide cleavage site mutated in the classic Brandywine isolate of type III DGI, adding to genotype-phenotype understanding of DGI and other diseases affecting dentin formation and mineralization.

Craniosynostosis is a condition in which premature fusion of cranial bones leads to elevated intracranial pressure and dysmorphic cranial and facial shapes. Repeated surgical intervention is typically required to manage the associated morbidity and negative effects on quality of life. The Crouzon syndrome, associated with gain-of-function mutations in fibroblast growth factor receptor 2 (FGFR2), features craniosynostosis. The mechanism of its development remains incompletely understood. J. Liu et al. studied the *Fgfr2*<sup>C342Y</sup> mouse model of the Crouzon syndrome, documenting that primary osteoblasts from the Crouzon mice feature elevated expression of early osteoblast markers, but reduced alkaline phosphatase and late osteoblast markers, and inhibition of mineralization in 2D and 3D cultures. They also report, for the first time, defective long bone formation in *Fgfr2*<sup>C342Y</sup> animals. Their findings suggest that development of the axial and appendicular skeleton in *Fgfr2*<sup>C342Y</sup> mice is impaired due to cell autonomous defects in the osteoblast.

Periodontal disease, affecting the tooth root cementum, periodontal ligament, and surrounding alveolar bone, affects almost 50% of US adults and, worldwide, is the most prevalent cause of premature tooth loss. Despite numerous animal models focusing on periodontal disease progression, few studies have assessed the role of functional mechanics of the bone-PDL-tooth joint in disease progression. J. Lee et al. take this approach by employing a lipopolysaccharide soaked ligature induced rat model of periodontal disease. The authors mapped two trends in response to disease induction. First, inflammation-induced degeneration of more coronal root tissues and, second, mechanobiological changes in the apical periodontal regions, potentially resulting from coronal degeneration over time. Interestingly, the authors noted that coronal induction of inflammation by ligature placement affected the overall distribution of proinflammatory cytokine TNF- $\alpha$  in the entire periodontal complex. Breakdown and compromise of coronal attachment shifted physiological function into an impaired function mode that in turn led to accelerated tissue adaptation to meet functional demands, including increased secondary cementum formation. Overall, this study adds to the understanding of periodontal

disease progression and prompts future studies to consider biomechanical changes in addition to biochemical and morphological changes in periodontal disease and other cases of joint inflammation.

### 3. Development

Craniofacial development encompasses numerous pre- and postnatal processes, including growth of the cranium by both endochondral and intramembranous ossification, development of soft tissues including salivary glands, tongue, and the musculature, and odontogenesis, wherein two separate sets of teeth form in humans (the primary and secondary dentition), with each tooth home to three distinct mineralized tissues, the enamel, dentin, and cementum. The morphogenesis and growth of dental and craniofacial tissues is influenced by neural crest cells, cell-cell communications, and environmental factors.

Proper development of the mandibular cartilage is important for growth and mineralization of the mandible. However, while endochondral ossification of the axial and appendicular skeletal elements is well studied, the mandibular cartilages, which derive from ectomesenchyme of the first pharyngeal arch, are often overlooked or assumed to operate under a similar differentiation program as cartilage with different origins. In their paper, “An immunohistochemistry study of *Sox9*, *Runx2*, and *Osterix* expression in the mandibular cartilages of newborn mouse,” H. Zhang et al. investigated the developmental expression pattern of three key transcription factors, *Sox9*, *Runx2*, and *Osterix*, in cartilages of the mouse mandible. Interestingly, the authors report an overlapping expression pattern for *Sox9* and *Runx2* in mandible that is distinct from limb bud cartilage. Furthermore, despite similar localization of *Osterix* in mandibular secondary cartilages compared to limb bud, an intense expression of this factor in the degrading portion of Meckel’s cartilage of the mandible suggests a role in the ongoing processes there, possibly even phenotypic conversion of these chondrocytes. Overall, these data provide valuable information on an understudied aspect of mandibular development, providing insights for disease mechanisms in conditions such as agnathia and micrognathia, for example.

The reorientation and fusing of the palatal shelves are critical steps in formation of the secondary palate, where developmental defects can lead to cleft palate or cleft lip and palate. It has been hypothesized that changes in extracellular matrix (ECM) are involved in raising of the palatal shelves to the horizontal position and, further, that epithelial-mesenchymal interactions may be involved in the fusion of the palatal shelves. A. Hirata et al., in their paper, investigated the developmental expression of heparanase and its substrate, heparin sulfate, in the ECM during palate formation in mice. These authors documented heparanase expression in the medial epithelial seam in palatal shelves in the process of fusing, in parallel with expression of additional ECM remodeling enzymes, matrix metalloproteinases 2, 3, and 9, where expression of heparin sulfate, perlecan, laminin, and collagen type IV was depleted. The distribution of this panel of ECM enzymes is consistent with the hypothesis that they



play a role in palatal ECM remodeling and proper fusion of the hard palate.

Salivary gland function is essential not only for eating but also for speaking and prevention of dental decay. Reduced salivary gland function can result from diseases such as Sjögren's Syndrome and as a result of therapeutic radiation for treatment of head and neck cancers. Great strides have been made in understanding salivary gland function, and a phase 1 clinical trial currently underway at the National Institute of Dental and Craniofacial Research (NIDCR) is evaluating the potential for gene therapy using water channel Aquaporin 1 (AQP1) to improve salivary flow in patients with radiation-induced damage to parotid gland function (ClinicalTrials.gov NCT00372320). While salivary gland epithelial cell differentiation and branching have been the subject of intense study, the mesenchymal cell component is less well understood. K. Janebodin et al. employed a transgenic reporter mouse to study submandibular salivary gland mesenchyme *in vivo* and *in vitro*, developing an approach to study epithelial-mesenchymal interactions *in vitro* in order to better understand how signals such as TGF- $\beta$ 1 affect cell differentiation and formation of the functional acinus.

Teeth also form by crosstalk between the specialized odontogenic epithelium and ectomesenchyme arising from migrating cranial neural crest cells. The ameloblasts, highly specialized secretory cells derived from the epithelium, synthesize the enamel of the tooth crown, a unique epithelial mineralized tissue that is the hardest tissue in the human body. H. Li et al. studied the role of multifunctional membrane protein NUMB in a variety of dental cells, including ameloblasts, odontoblasts, and dental pulp cells, and found that interaction of this factor with the notch signaling pathway may have regulatory effects on ameloblast differentiation "Expression and function of NUMB in odontogenesis". Greater understanding of ameloblast differentiation is critical for understanding hereditary enamel defects, as well as efforts towards regenerating enamel or bioengineering teeth from dental stem cells, as the enamel organ is completely lost upon eruption of teeth, leaving no known progenitor cells behind.

Enamelin is a component of the enamel extracellular matrix, and mutations in the associated *ENAM* gene cause autosomal dominant amelogenesis imperfecta, marked by thin or pitted, easily abraded enamel and, in some cases, enamel aplasia. Lower body weight in *Enam* null mice prompted A. H.-L. Chan et al. to study the potential for enamel defects to influence body weight, operating with the hypothesis that dental pain arising from defective tooth structure causes reduced nutritional intake. The authors discovered that the significantly decreased average litter body weight of *Enam* null mice was improved by implementing a soft chow diet over the first six weeks of life. Because enamel is ameloblast specific, this effect on body weight is likely occurring via the interaction between the defective enamel phenotype and reduced ability to feed on a hard diet. The fact that food hardness becomes an important variable in body weight gain in mice with defective dentition can provide some mechanistic insight into the relationship between compromised oral health and poor growth in children, where dental caries and dental pain and sensitivity may contribute to poor nutrition.

## 4. Regeneration

Despite a wide range of approaches, periodontal therapies are currently unpredictable, few are truly regenerative, and many lack a biologic foundation. Research has shown that periodontal disease can be successfully treated, with biological periodontal tissue regeneration (i.e., return to structure and function of cementum, PDL, and bone) in some cases. Q. Li et al. focus on platelet-rich fibrin (PRF) as a potential scaffold for periodontal regeneration. The PRF technique was developed from platelet-rich plasma (PRP) which has been used to promote healing and regenerate bone and periodontal tissues. For PRP, platelets are concentrated and activated with thrombin and calcium chloride to promote instant release of growth factors and cytokines. In contrast, PRF is not activated by thrombin or anticoagulants and releases growth factors gradually. *In vitro*, PRF increased markers of proliferation and differentiation in periodontal progenitor cells, and isolated use of the major PRF component, fibrin, replicated these effects. Further, *in vivo* studies in mice supported that PRF promoted integration and soft tissue healing, and pilot studies placing PRF in peri-implant locations in two human patients were associated with new alveolar bone formation.

Finally, in their review article, T. A. El-Bialy and Alhadlaq create a primer on therapeutic approaches for underdeveloped mandibles, covering bite-jumping (functional) appliances, low intensity pulsed ultrasound (LIPUS), hormone treatment, photobiomodulation, and gene therapy. While these techniques hold promise for improving health outcomes for children with mandibular growth deficiency, all have inherent limitations and challenges, as detailed by the authors.

## 5. Concluding Remarks

This special issue of Biomed Research International showcases a unique collection of 11 papers that serve as touchstones for several areas of dental-craniofacial research for like-minded researchers, clinicians, and students, as well as scientists in other disciplines. These papers touch many of the exciting aspects of these fields in recent years, and we hope they will stimulate thought and further research to better understand these aspects of human health. Researchers and clinicians have never been better positioned to understand mechanisms of development, disease, and regeneration of dental and craniofacial tissues and, in turn, to apply that knowledge to make clinically meaningful advances.

Brian L. Foster  
Yong-Hee P. Chun  
Erica L. Scheller  
Zhao Lin  
Chad M. Novince  
Avina Paranjpe

## Research Article

# The Adaptive Nature of the Bone-Periodontal Ligament-Cementum Complex in a Ligature-Induced Periodontitis Rat Model

Ji-Hyun Lee,<sup>1</sup> Jeremy D. Lin,<sup>1</sup> Justine I. Fong,<sup>1</sup> Mark I. Ryder,<sup>2</sup> and Sunita P. Ho<sup>1</sup>

<sup>1</sup> Division of Biomaterials and Bioengineering, Department of Preventive and Restorative Dental Sciences, University of California, San Francisco, CA 94143, USA

<sup>2</sup> Division of Periodontology, Department of Orofacial Sciences, University of California, San Francisco, CA, USA

Correspondence should be addressed to Sunita P. Ho; [sunita.ho@ucsf.edu](mailto:sunita.ho@ucsf.edu)

Received 4 January 2013; Revised 18 March 2013; Accepted 24 March 2013

Academic Editor: Brian L. Foster

Copyright © 2013 Ji-Hyun Lee et al. This is an open access article distributed under the Creative Commons Attribution License, which permits unrestricted use, distribution, and reproduction in any medium, provided the original work is properly cited.

The novel aspect of this study involves illustrating significant adaptation of a functionally loaded bone-PDL-cementum complex in a ligature-induced periodontitis rat model. Following 4, 8, and 15 days of ligation, proinflammatory cytokines (TNF- $\alpha$  and RANKL), a mineral resorption indicator (TRAP), and a cell migration and adhesion molecule for tissue regeneration (fibronectin) within the complex were localized and correlated with changes in PDL-space (functional space). At 4 days of ligation, the functional space of the distal complex was widened compared to controls and was positively correlated with an increased expression of TNF- $\alpha$ . At 8 and 15 days, the number of RANKL(+) cells decreased near the mesial alveolar bone crest (ABC) but increased at the distal ABC. TRAP(+) cells on both sides of the complex significantly increased at 8 days. A gradual change in fibronectin expression from the distal PDL-secondary cementum interfaces through precementum layers was observed when compared to increased and abrupt changes at the mesial PDL-cementum and PDL-bone interfaces in ligated and control groups. Based on our results, we hypothesize that compromised strain fields can be created in a diseased periodontium, which in response to prolonged function can significantly alter the original bone and apical cementum formations.

## 1. Introduction

Mechanical loads as a result of chewing or biting promote homeostasis of the periodontal ligament (PDL) and that of the bone-PDL-cementum complex following development of the bone-PDL-tooth fibrous joint [1, 2]. Homeostasis of the joint is maintained by the PDL, which contains a heterogeneous population of cells, such as fibroblasts, osteoblasts, cementoblasts, and undifferentiated mesenchymal cells, and its entheses (attachment sites) with bone and cementum. These cells are sensitive to mechanical loads, which manifest into strains, and as a result can promote mineral formation or resorption. The cell-matrix and cell-cell interactions regulate continuous PDL turnover, modeling and remodeling of bone, and subsequent adaptation of primary and secondary cementum, including PDL-bone and PDL-cementum interfaces throughout their physiological

function [2–5]. Accommodation of functional loads within the physiological range continues as long as the bone-PDL-cementum complex is protected from the oral environment by gingival epithelium and underlying connective tissues. However, the complex is a target for bacterial infection due to commensal microorganisms in the oral environment and the unique anatomical feature of this environment [6]. As a result, periodontal tissues are susceptible to bacterial invasion.

The relationship between host-microbial interactions and progression to periodontitis is thought to depend on a combination of the ecological shift in subgingival biofilm composition, genetic factors, and other extraneous influences [7]. Despite many extraneous factors, the “critical pathway” model for periodontal pathogenesis developed by Offenbacher [8] does not account for mechanical loads, that is, the effect of functional mechanics on disease progression in the load bearing joint of humans. Biomechanics and other

functional perspectives on diseased joints are important areas of study since the altered homeostasis due to bacterial invasion can lead to pathological adaptation of unaffected tissues. Hence, the combinatorial effect of disease and functional (mechanical) loads on disease progression and joint adaptation is an important area of investigation. However, the challenge that lies in performing such studies is the limited access to specimens from humans. Hence, animal models in general and rat models in particular continue to be used extensively as an experimental system to elucidate the effect of diverse factors on periodontal pathogenesis and progression [9, 10]. Despite the extensive literature regarding the characteristics of periodontal progression in different animal models, few studies have described the effects of the disease from a biomechanical perspective.

Numerous human and animal studies have confirmed the infectious etiology of gingival inflammation [11–13], apical migration of the gingival epithelial attachment, and the eventual loss of underlying bone and connective tissue support [14, 15], that leads to clinical periodontitis. In this study, we employed the lipopolysaccharide-soaked rat ligature model to initiate the clinical features of periodontitis, namely inflammation and loss of PDL attachment and alveolar bone [16]. This model is an analog that stimulates the natural occurrence of periodontitis in humans—food impaction over time followed by acute and chronic inflammatory host responses [17–19]. Once disease is initiated, the complex is kept under continued function and the changes in clinical features can be correlated with the distribution of biochemical markers. In this study, the presence and distribution of the following biochemical markers in sections taken from hemimaxillae harvested at 4, 8, and 15 days of ligation and corresponding controls were assessed: receptor activator of nuclear factor  $\kappa$ B ligand (RANKL: a membrane-bound protein commonly found on PDL cells, osteoblasts, and T cells, that induce the expression of RANK on the surface of osteoclasts) [20, 21]; tartrate-resistant acid phosphatase (TRAP: an enzyme highly expressed by osteoclasts) [22]; tumor necrosis factor- $\alpha$  (TNF- $\alpha$ : a marker for systemic inflammation) [23], and fibronectin (FN: a glycoprotein adhesion molecule for fibroblasts that promotes extracellular matrix production) [24]. Moreover, changes in biochemical expressions and localization were correlated to morphological changes of the complex. Based on previous studies by others, morphological alterations of bone and cementum due to inflammation were associated with increased expressions of proinflammatory mediators [25–28], including a variety of cytokines, such as TNF- $\alpha$ , that are involved in inflammatory bone resorption [29]. RANKL, which is known to orchestrate osteoclastogenesis synergistically with TNF- $\alpha$  [30], was mapped throughout the bone-PDL-cementum complex and was expected to increase in inflamed periodontal tissue. In addition, active osteoclasts and correlative changes in biochemical distribution and alveolar bone resorption were identified. Finally, adaptive changes in secondary cementum marked by FN expression [31] were discussed within the context of joint function. Our overall hypothesis was that coronal degradation due to periodontitis can cause a significant change in the biomechanics of the complex and that the resulting adaptive

effects may not be the same between bone and secondary cementum. The objective was to identify the adaptation of this load-bearing joint, that is, the bone-PDL-tooth complex, with the onset of periodontitis by mapping and correlating morphological changes of the tooth and the alveolar socket to key biomolecular expressions within the complex.

## 2. Materials and Methods

To minimize the effects of environmentally induced periodontitis [32–34], 6-week-old male Sprague-Dawley rats were housed in a germ-free facility (Parnassus Services Building) and fed a hard pelleted diet for the duration of the study. All animals included in this study were housed in pathogen-free conditions in compliance with the guidelines of the Institutional Animal Care and Use Committee (IACUC) of UCSF and the National Institute of Health (NIH).

**2.1. Induction of Periodontitis Using an In Vivo Rat Ligature Model.** 4–0 silk suture threads soaked in 1 mg of lipopolysaccharide (LPS) from *Escherichia coli* serotype 055:B5 (Sigma-Aldrich, USA) per 1 mL of 1x Tris buffer were used to induce periodontitis ( $N = 5$  per time point). Threads were placed between the first and second molars and the second and third molars of both maxillae (Figure 1(a)). Molars were religated every 2–3 days to ensure retention. Control rats ( $N = 5$  per time point) were flossed every 2–3 days with 4–0 silk ligatures without LPS. Rats were euthanized after 4, 8, and 15 days of ligation. Maxillae were harvested and hemisected. Right hemimaxillae were stored in 70% ethanol for micro-XCT analysis. Left hemimaxillae were fixed in 4% paraformaldehyde (PFA) at room temperature overnight for histology.

**2.2. Histological Analysis of Cytokine Expressions Using Immunohistology, Identification of Bone Resorption through TRAP(+) Osteoclasts, and Observation of Changes in Collagen Birefringence.** Following fixation, intact hemimaxillae ( $N = 5$ ) were decalcified in 0.5 M ethylenediaminetetraacetic acid (EDTA) solution for 3 weeks. The EDTA solution was changed every 3 days. Specimens were then dehydrated through 80%, 95%, and 100% Flex Alcohol (Richard-Allan Scientific, Kalamazoo, MI USA) before embedding in paraffin (Tissue Prep-II, Fisher Scientific, Fair Lawn, NJ USA). Embedded specimens were sagittally sectioned on a rotary microtome (Reichert-Jung Biocut, Vienna, Austria) using a disposable steel blade (TBF Inc., Shur/Sharp, Fisher Scientific, Fair Lawn, NJ USA). Paraffin serial sections were mounted on Superfrost Plus microscope slides (Fisher Scientific, Fair Lawn, NJ). Sections were deparaffinized with xylene and rehydrated through a descending ethanol series of 100%, 95%, and 80% ethanol before further use.

**2.2.1. Immunostaining for RANKL, FN, and TNF- $\alpha$ .** The immunofluorescence staining protocol used for RANKL and FN was based on a previously described protocol [35]. In brief, deparaffinized sections were digested with trypsin (Sigma-Aldrich, St. Louis, MO, USA) at 37°C. Following



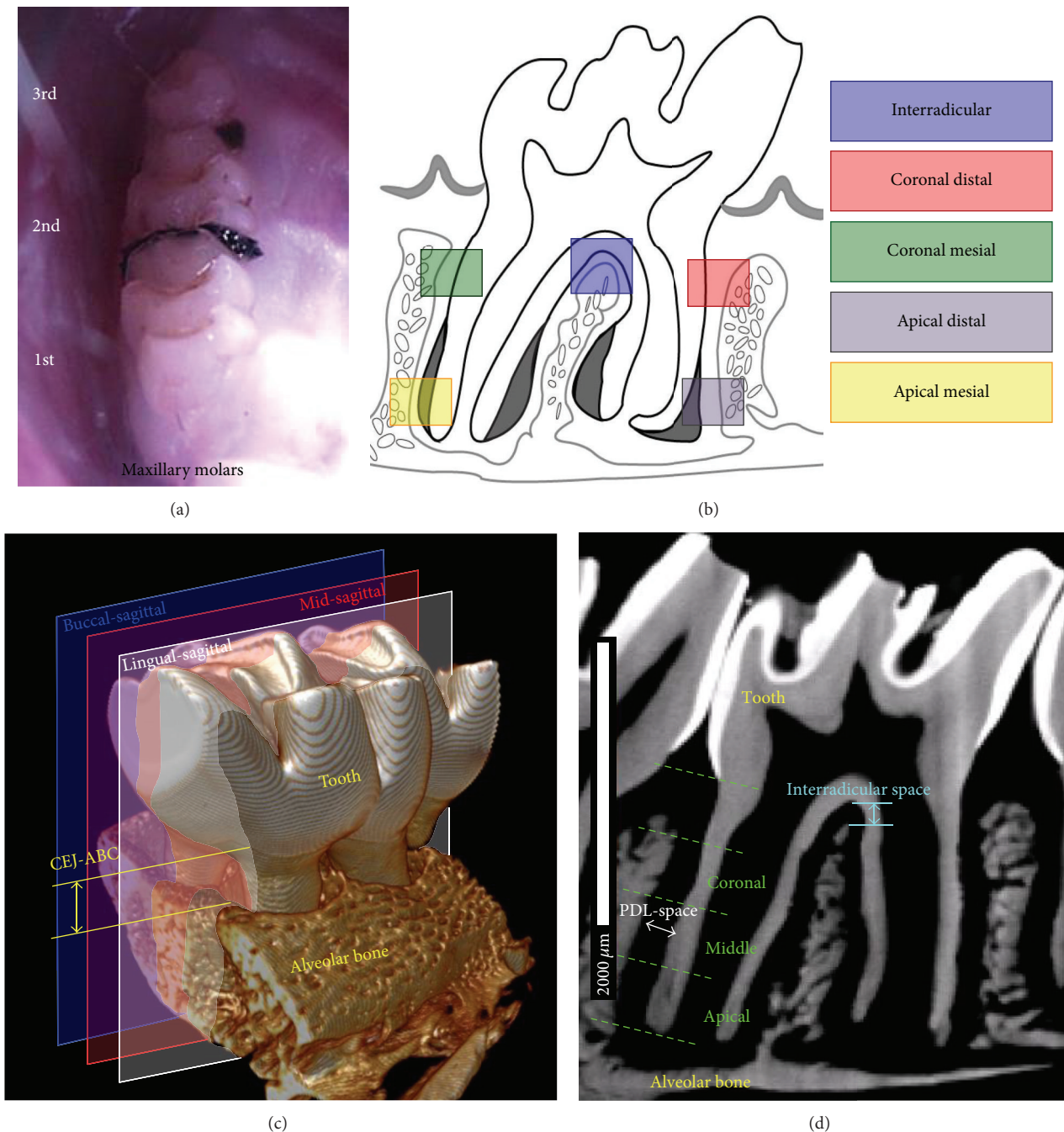


FIGURE 1: *In vivo* rat ligature model for the induction of acute periodontitis. (a) Photograph illustrates lipopolysaccharide (LPS) soaked 4–0 braided silk threads in the diastemata flanking left/right second maxillary molars. Controls were flossed in the same interproximal regions. (b) Schematic illustrates the targeted regions of the fibrous joint within the study. (c) 3D tomogram illustrates the lingual-sagittal, mid-sagittal, and buccal-sagittal 2D virtual sections through a second maxillary molar used for morphometrics. Anatomical landmarks used to measure alveolar bone crest recession (CEJ-ABC) are indicated. (d) 2D virtual section illustrates anatomical landmarks to measure interradicular distance and PDL width. Division of the bone-PDL-cementum complex into coronal, middle, and apical sections for PDL-space measurements is also illustrated.

washing, the specimens were incubated in blocking buffer (3% goat serum, 0.1% BSA in 1x PBS) and then in primary antibodies of polyclonal rabbit anti-RANKL (Santa Cruz Biotechnology Inc., sc-9073, Santa Cruz, CA, USA) and monoclonal mouse anti-FN (Santa Cruz Biotechnology Inc.,

sc-8422, Santa Cruz, CA, USA) diluted to 1:50 in blocking buffer. Slides were stored at 4°C followed by washing with 0.1% Tween-20 in PBS (PBST) and were incubated with secondary antibodies. AlexaFluor 594 goat anti-rabbit (Invitrogen, A-11012, Carlsbad, CA, USA) and AlexaFluor

488 goat anti-mouse (Invitrogen, A-11029, Carlsbad, CA, USA) were used to label polyclonal rabbit anti-RANKL and monoclonal mouse anti-FN at 1:300 (diluted in blocking buffer), respectively. Sections were washed with PBST and then stained with 1:10,000 trihydrochloride trihydrate (Invitrogen, Carlsbad, CA, USA) for ten minutes in the absence of light. Slides were rinsed twice with PBS and mounted using Fluoro-Gel (Electron Microscopy Sciences, Hatfield, PA, USA). Stained sections were visualized using Eclipse E800 fluorescent microscope (Nikon Inc., Melville, NY). TRITC filter (540–565 nm) was used to excite AlexaFluor 594 (abs. 590 nm, emit. 617 nm), FITC filter (465–495 nm) to excite AlexaFluor488 (abs. 495 nm, emit. 519 nm), and DAPI filter (340–380 nm) to excite trihydrochloride trihydrate (abs. 358 nm, emit. 461 nm). Images were stitched using Microsoft Research Image Composite Editor (Microsoft Corporation, Redmond, WA, USA).

For quantitative analysis for RANKL, the number of RANKL(+) cells in two 125  $\mu\text{m}$  square regions around the surface of alveolar bone crest was counted using Image J (v1.44p, National Institute of Health, USA). Group means ( $\pm$ standard deviation) were calculated. A two-way analysis of variance (ANOVA) was used to analyze the effect of time and experimental conditions. A follow-up post-hoc test was used to analyze the differences between groups.  $P < 0.05$  was taken to indicate significance. For comparative evaluation of FN, a 300  $\mu\text{m}$  line plot spanning dentin, secondary cementum, PDL, and alveolar bone, were generated for immunofluorescence micrographs of each group, and gradients of FN intensities were mapped using Image J.

3,3'-Diaminobenzidine (DAB) staining for detection of TNF- $\alpha$  was performed on serial sections. Endogenous peroxidases were deactivated with 80% methanol and 0.6%  $\text{H}_2\text{O}_2$ . Following antigen retrieval, sections were incubated with normal serum for 30 min to prevent nonspecific binding. For cytokine detection, the primary antibody (goat polyclonal anti-rat TNF- $\alpha$ , sc-1350 Santa Cruz Biotechnology, Inc., Santa Cruz, CA, USA) was applied on the sections at a dilution of 1:100 in PBS and incubated overnight at room temperature. The sections were incubated for 15 min at room temperature with the secondary antibody (biotinylated rabbit anti-goat IgG antibody, PK-6105, Vector Labs, Burlingame, CA, USA). Antigen-antibody complexes were visualized with DAB tetra-chloride solution (Sigma, D3939, St. Louis, MO, USA), washed in distilled water, counterstained with hematoxylin Gill (3X) (Fisher Scientific, Kalamazoo, MI, USA), and rinsed in running water. Finally, the sections were dehydrated in ascending concentrations of alcohol, cleared with xylene, and mounted. Negative controls were obtained by substitution of the primary antibodies with normal goat serum. Lung tissues harvested from the same animals were used as positive controls. The sections were evaluated by a single examiner, who was blinded to the treatment assignment using a light microscope (BX 51, Olympus America Inc., San Diego, CA, USA).

**2.2.2. Resorption by Mapping TRAP(+) Osteoclastic Cells.** Tartrate-resistant acid phosphatase (TRAP) staining for osteoclasts was performed by treating rehydrated specimens

with 0.2 M acetate buffer, a solution of 0.2 M sodium acetate, and 50 mM L-(+)-tartaric acid (Sigma-Aldrich, St. Louis, MO, USA). After 20 minutes of incubation at room temperature, naphthol AS-MX phosphate and fast red TR salt were added, followed by incubation at 37°C for 1 hour with close monitoring under the microscope after the first half hour to monitor the development of a bright red staining for osteoclastic activity. The stained sections were washed in deionized water, counterstained with hematoxylin, and mounted with Immu-Mount (ThermoScientific, Fremont, CA, USA) for subsequent examination under light microscopy. TRAP(+) stained regions were categorized based on location: the segment from alveolar crest (defined as the curved surface connecting the mesial and distal faces of the alveolar bone proper) to the starting point of secondary cementum as the coronal segment, and from secondary cementum to the apex as the apical segment. Criteria for identification of osteoclasts were TRAP(+) staining with greater than three nuclei [36]. The number of osteoclasts within each region was manually counted along the PDL-bone perimeter using Image-Pro Plus v6.0 data acquisition software (Media Cybernetics, Inc., Bethesda, MD, USA) and ratios of osteoclast count to perimeter per mesial and distal location were calculated [37]. These ratios were tested for statistical differences between control and ligature groups and across time points using two-way ANOVA followed by post-hoc tests to analyze the difference between the groups. Differences with  $P < 0.05$  were considered significant.

**2.2.3. Collagen Birefringence Using Picosirius Red (PSR) Stain.** Deparaffinized sections were stained with Sirius red F3B (C.I. 35782) and picric acid (American MasterTech Scientific Co., Lodi, CA, USA). Stained sections were analyzed with a light microscope and Image-Pro Plus. Polarized light was used to enhance the birefringence of collagen to illustrate changes in collagen fiber orientation and birefringence intensity throughout the complex [38, 39].

**2.3. Changes in Morphometrics of the Bone-PDL-Cementum Complex Using Micro-X-Ray Computed Tomography ( $\mu$ -XCT).** Macroscale structural analysis of intact right hemimaxillae ( $N = 5$  each group) was performed using micro-X-ray tomography ( $\mu$ -XCT, Micro XCT-200, Xradia, Inc., Pleasanton, CA, USA) at 2x magnification. X-ray imaging was performed on specimens using a tungsten anode with a setting of 75 KVp at 6W at binning 2 and quartz silica ( $\text{SiO}_2$ ) filter designed specifically for biological specimens. Specimens were scanned while immersed in 70% ethanol with the second molar centered in the field of view. 2000 projections were collected at an exposure time of 9–14 s for each projection.

Tomograms were reconstructed (XMReconstructor v8.1.6599, Xradia Inc., Pleasanton, CA, USA) and 2D virtual sections were generated (Xradia 3D viewer v1.1.6, Xradia Inc., Pleasanton, USA) to complete the following measurements using Image J. To analyze the progression of periodontitis through the time points, three sagittal sections containing apical foramen were made through each specimen: in

the mesiodistal direction through (1) both buccal roots, (2) both lingual roots, and (3) the interradicular region (Figure 1(c)). Alveolar bone crest (ABC) resorption was determined by measuring the distance from the cemento-enamel junction (CEJ) to the adjacent ABC of the second maxillary molar along mesial and distal roots (Figure 1(c)). The width of the PDL-space surrounding the second maxillary molar was determined using the aforementioned buccal and lingual sagittal sections ( $N = 3$  each group). Mesial and distal roots were divided into fourths from the CEJ to the root apex (Figure 1(d)). From the three apical fourths, five PDL-space measurements from the alveolar bone to the root cementum per quarter section were measured using Image J. Interradicular PDL spaces (or interradicular distances) measured using the midsagittal section as the distance from the crest of the interradicular bone to the molar root furcation (Figure 1(d)). All statistical analyses for significant differences in morphometrics across and within time points were performed using two-way ANOVA combined with post-hoc tests. Differences with  $P < 0.05$  were considered significant.

### 3. Results

*The Naturally Occurring Tension and Compression Fields in a Rat Bone-PDL-Tooth Complex* [35]. It should be noted that in a rat the distal side is more prone to mineral resorption while the mesial side is prone to mineral formation. From a biomechanical perspective, this is due to the tensile strains in the mesial side compared to reactionary compressive strains on the distal side. As a result, mineral is formed on the mesial side of the alveolar socket, while mineral is resorbed on the distal side of the same alveolar socket, thus maintaining a uniform functional space within the bone-PDL-tooth fibrous joint.

#### 3.1. Changes in the Expressions of Biochemical Markers within the LPS Soaked Ligature-Induced Periodontitis Model

**3.1.1. RANKL Expression in the Complex.** Intense expression of RANKL in endosteal spaces of alveolar bone and vasculature in PDL was detected (Figure 2(a)) in the ligated group. In addition, osteoclasts in resorption pits at both PDL-bone and PDL-cementum attachment sites strongly expressed RANKL (Figure 2(b)).

To correlate RANKL expression with osteoclastic activity, RANKL(+) cell number was counted in subepithelial connective tissue (CT) near the alveolar crest (Figures 2(c)–2(e)). RANKL(+) cell count interestingly exhibited advancing trends to TRAP(+) staining. On the mesial side (Figure 2(d)), the number of RANKL(+) cells in the ligated group was greater than that in the control group. However, the number of RANKL(+) cells was reduced with time in both groups, showing a significant decrease in ligated group from 4 days to 15 days ( $P < 0.05$ ). On the distal side (Figure 2(e)), there was a significant elevation of RANKL(+) cells in the ligated group compared to the control group ( $P < 0.05$ ) at 4 days, but a decrease was observed at 8 days. A higher number of RANKL(+) cell count was identified on the distal side

compared to mesial side of the ligated group and distal and mesial sides of the control group (Figures 2(d) and 2(e)).

**3.1.2. Osteoclastic Activity in the Complex.** Morphological changes were also evaluated in mesiodistal stained sections, and increased alveolar bone resorption with time was observed (Figure 3(a)). Consistent with  $\mu$ -XCT morphometric analysis, the CEJ-ABC distance was higher in ligated groups (Figures 3(a) and 5(a)(i)). Multinucleated TRAP(+) cells were observed in endosteal and bone marrow spaces, irrespective of experimental conditions or time points (Figure 3(b)(i–ix)). Active osteoclasts at the PDL-bone interface were also found on the alveolar crest in the 8-day ligated group (Figure 3(b)(ii)). Quantification of TRAP(+) cells showed preferential distal localization regardless of experimental condition or time point (Figures 3(b)(x) and 3(b)(xi)).

Data for the 4-day ligated group was discarded due to inadequate samples. TRAP(+) cells showed preferential distal localization regardless of experimental condition or time point (Figures 3(b)(x) and 3(b)(xi)) and peaked at 8 days except in apical segments on the distal side. On the mesial side, osteoclastic activity at 8 days was significantly greater than that observed at 4 days in coronal segments and that of the 15-day ligated group in apical segments (Figure 3(b)(x)). Within control groups, no significant increase or decrease was seen in both coronal and apical segments. However, the mesial osteoclastic activity of ligated groups significantly increased at 8 days in apical segments compared to respective control groups before decreasing at 15 days (Figure 3(b)(x)). On the distal side, osteoclastic activity both at 8 days and 15 days was significantly greater than that of the 4-day control group in coronal segments when the 4-day control group was used as the reference (data not shown). At both 8 and 15 days, ligated groups showed an increase in osteoclastic activity in coronal segments compared to corresponding control groups, while osteoclastic activity in ligated groups decreased in apical segments (Figure 3(b)(xi)). Between 8 and 15 days, the distal osteoclastic activity of ligated groups decreased in both coronal and apical segments (Figure 3(b)(xi)).

**3.1.3. Immunohistochemical Localization of TNF- $\alpha$ .** TNF- $\alpha$  was identified in the gingival epithelium, subepithelial CT, endosteal spaces, predentin, and secondary cementum (Figure 4(a)). Particularly, TNF- $\alpha$  expression in ligated groups was more intense than that of control groups at both mesial and distal PDL-cementum interfaces, the interradicular complex, and in endosteal spaces (Figure 4(b)). At a higher magnification, osteoclast-like cells were detected at PDL-bone interfaces in ligated groups (Figure 4(b), arrowheads).

#### 3.2. LPS Soaked Ligature-Induced Periodontitis Rat

*Model Stimulated Significant Changes in Alveolar Bone Resorption, PDL-Space Width, Collagen Birefringence, and Fibronectin Expression*

**3.2.1. Alveolar Bone Resorption.** Morphometric analysis using  $\mu$ -XCT revealed that at all time points, the distance from



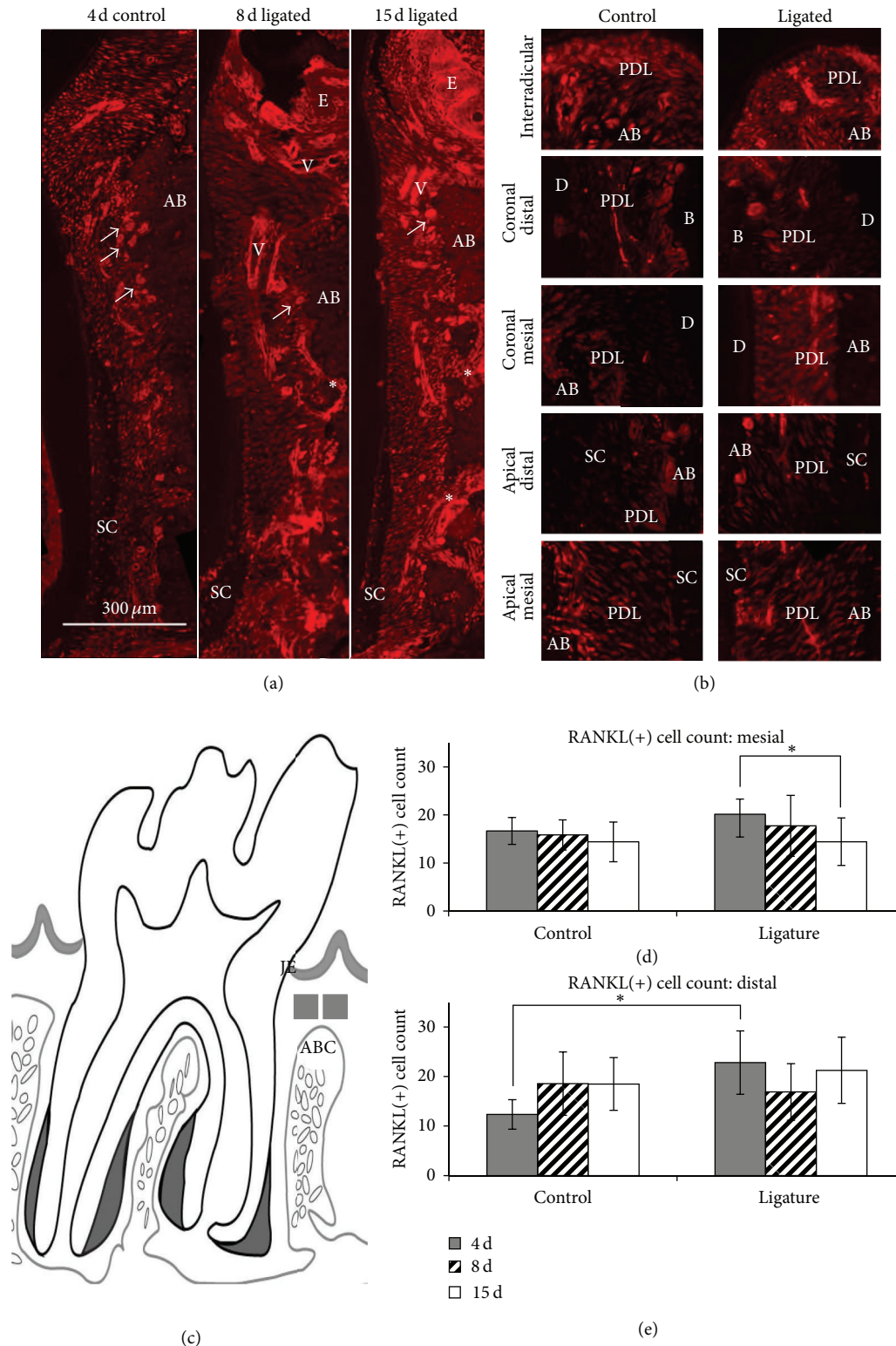


FIGURE 2: Identification of RANKL using immunofluorescence. (a) Representative micrographs illustrate immunofluorescence of antibodies against RANKL at 4-day control and 8- and 15-day ligated groups. Note RANKL expression around the vasculature (V) and endosteal spaces (asterisks). Multinucleated osteoclast-like cells were also observed at the PDL-bone interface (white arrows). (b) Higher magnification micrographs show RANKL immunofluorescence in local regions of the complex at 15 days of ligation. (c) Schematic of rat periodontal tissue (mesiodistal section) with gray boxes ( $125\ \mu\text{m} \times 125\ \mu\text{m}$ ) that indicate target areas used to count RANKL(+) cells. (d, e) Bar graphs illustrate RANKL(+) cell count within specified target areas between control and ligated groups on mesial (d) and distal (e) sides. \*Statistically significant difference at 95% confidence interval was observed. Junctional epithelium (JE), epithelium (E), periodontal ligament (PDL), alveolar bone (AB), alveolar bone crest (ABC), dentin (D), and secondary cementum (SC).

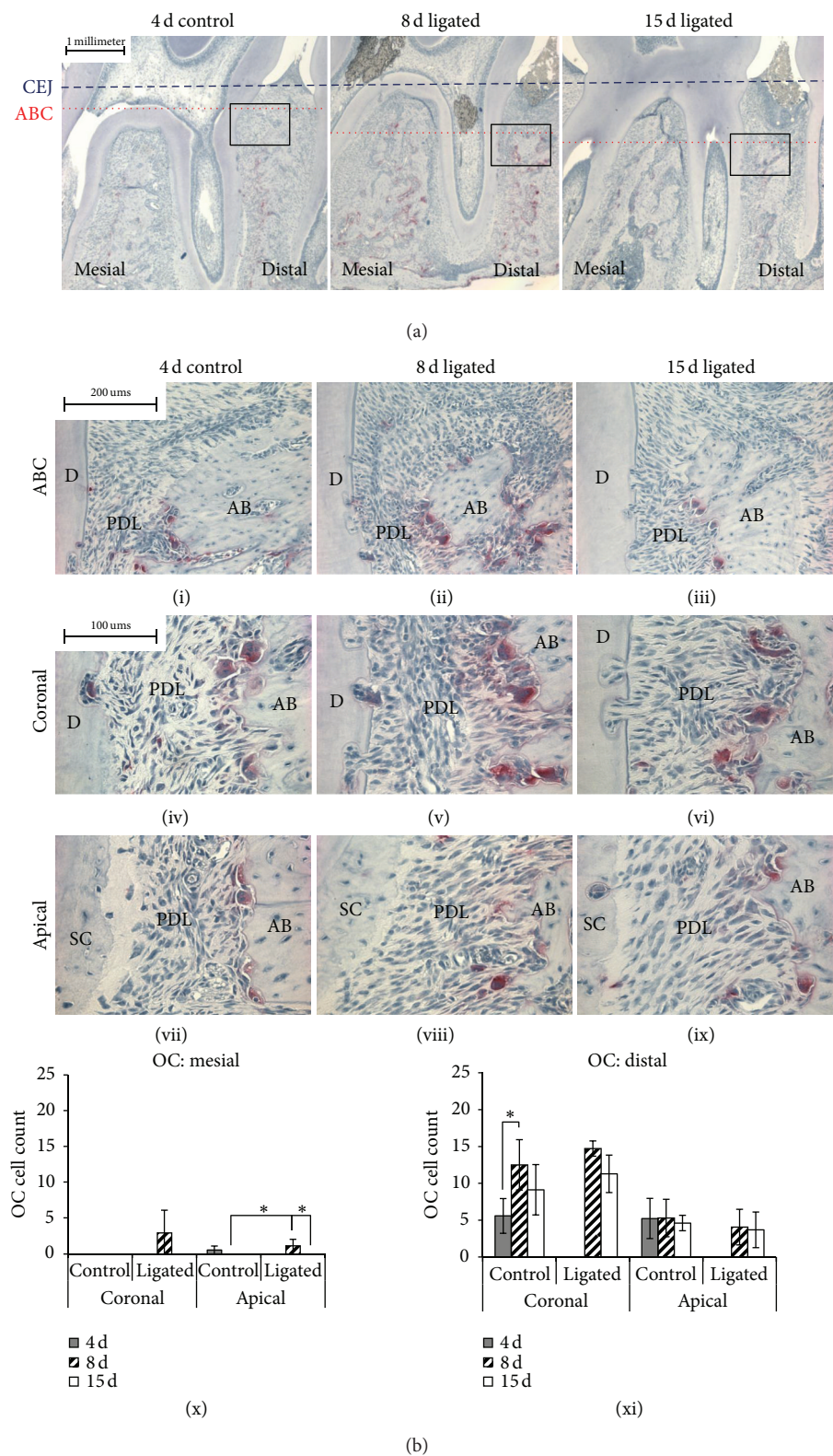


FIGURE 3: Alveolar bone resorption through TRAP(+) osteoclast identification. (a) Mesiodistal histological sections illustrate TRAP(+) cells on distal surfaces. The relative height of the alveolar bone crest (ABC) in relation to the cemento enamel junction (CEJ) is shown to decrease with duration of ligation. (b) Magnified images of 3A show alveolar bone crest (ABC), coronal, and apical regions of distal surfaces across time points and between control and ligated complexes (i–ix). The number of multinucleated osteoclasts (OC) located along the bone perimeter was counted in coronal and apical root segments on mesial (x) and distal (xi) sides. \* Statistically significant difference at 95% confidence interval was observed. Alveolar bone (AB), periodontal ligament (PDL), dentin (D), and secondary cementum (SC).



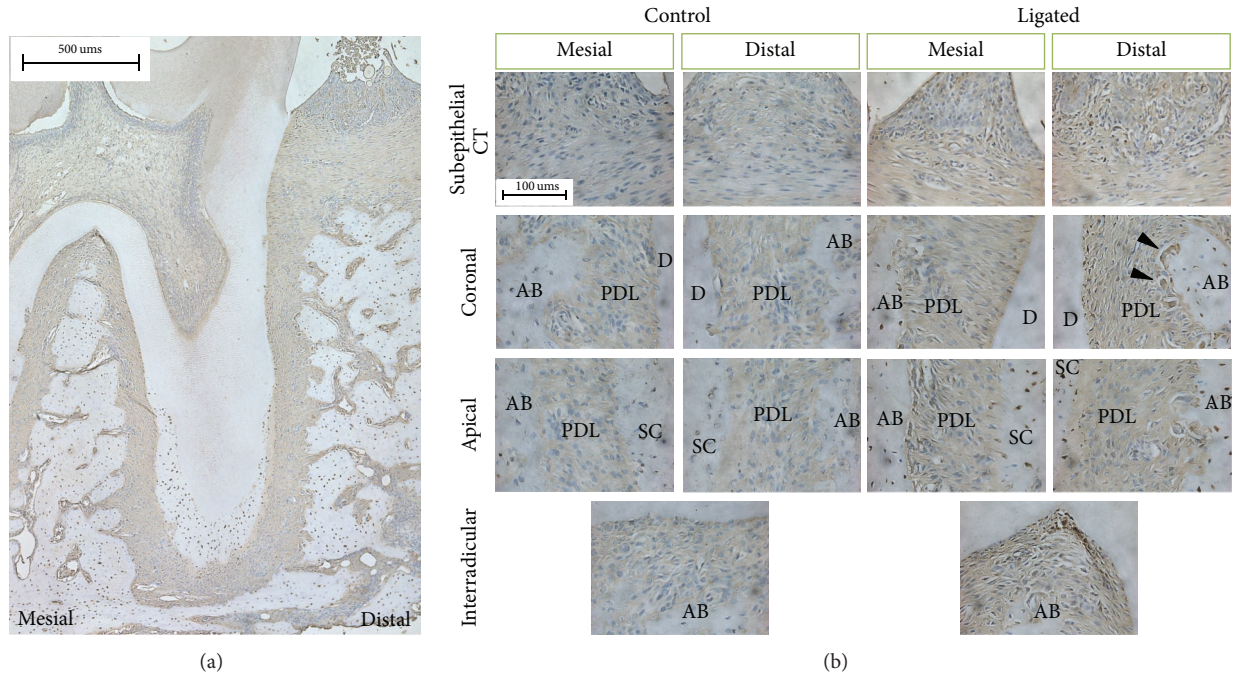


FIGURE 4: Immunohistochemical staining for identification of TNF- $\alpha$ . (a) Representative light micrograph of the complex at 15 days of ligation illustrates localization of TNF- $\alpha$ . (b) Representative images illustrate immunohistochemical localization of TNF- $\alpha$  at subepithelial connective tissue, coronal and apical PDL spaces, and interradicular PDL regions, according to experimental conditions. For example, note TNF- $\alpha$  expression at the distal coronal PDL-bone interface (black arrow heads). Connective tissue (CT), alveolar bone (AB), periodontal ligament (PDL), dentin (D), and secondary cementum (SC).

CEJ to ABC (CEJ-ABC) was greater in ligated groups when compared to control groups in both mesial and distal regions (Figure 5(a)(i)). While at 4 days both mesial and distal regions of ligated groups exhibited significant increases in CEJ-ABC compared to controls, only the distal regions exhibited significant increases in corresponding comparisons. In mesial regions of both control and ligated complexes, CEJ-ABC exhibited a decreasing trend between 4 days to 8 days and an increase from 8 to 15 days; however, only the ligated mesial region exhibited a significant increase between 8 and 15 days ( $P < 0.05$ ). In distal regions, the CEJ-ABC exhibited increasing trends in both control and ligated complexes with time, increasing significantly at 8 and 15 days when compared to 4 days ( $P < 0.05$ ). The interradicular distance within the control complex decreased with time (Figure 5(a)(ii)). In contrast, the interradicular distance within the ligated complex decreased significantly between 4 and 8 days of ligation ( $P < 0.05$ ) and then increased slightly after 15 days of ligation. Comparisons of the averages in ligated and control interradicular PDL-spaces at each time point showed that the ligated complex had a significantly greater interradicular PDL-space at 4 days ( $P < 0.05$ ). This significant increase was not maintained at 8 days but was reestablished at 15 days.

**3.2.2. PDL-Space.** PDL-space measurements showed differences in trends across time between control (Figure 5(a)(iii)) and ligated complexes (Figure 5(a)(iv)) in both coronal and apical regions. In all ligated regions, a decreasing followed by an increasing trend in PDL-space was found over time with a

significant decrease in the distal apical region ( $P < 0.05$ ). In contrast, control complexes did not exhibit this trend with the exception of the distal coronal region. Instead, between 8 and 15 days the PDL-space of both mesial and distal sides showed a decreasing trend with time in the control complex, with a significant decrease between 4 and 15 days at the mesial apical region ( $P < 0.05$ ). When comparing the PDL-space between control and ligated complexes, it was interesting to note that all observed significant differences in the mesial regions occurred at the earlier time points of 4 and 8 days ( $P < 0.05$ ). The significant differences in distal regions occurred mostly at later time points of 8 and 15 days ( $P < 0.05$ ).

To separate the effect of treatment from that of development, the average control PDL-space was subtracted from the average treated PDL-space for each region (Figure 5(b)). The mesial apical and all distal PDL-spaces of the ligated complex increased at 4 days, while mesial coronal and mesial middle PDL-spaces decreased compared to controls. The mesial coronal, mesial middle, and distal apical regions, exhibited significant differences in PDL-space between ligated and control groups. Regardless of anatomical location at 8 days, the difference between ligated and control mesial PDL-spaces increased negatively and the difference between ligated and control of distal PDL-spaces increased positively with time relative to corresponding control regions ( $P < 0.05$ ). As such, there was a significant difference in PDL-space between ligated and control groups in all regions. At 15 days, the distal PDL-spaces of ligated coronal regions remained greater than the corresponding control region but decreased in

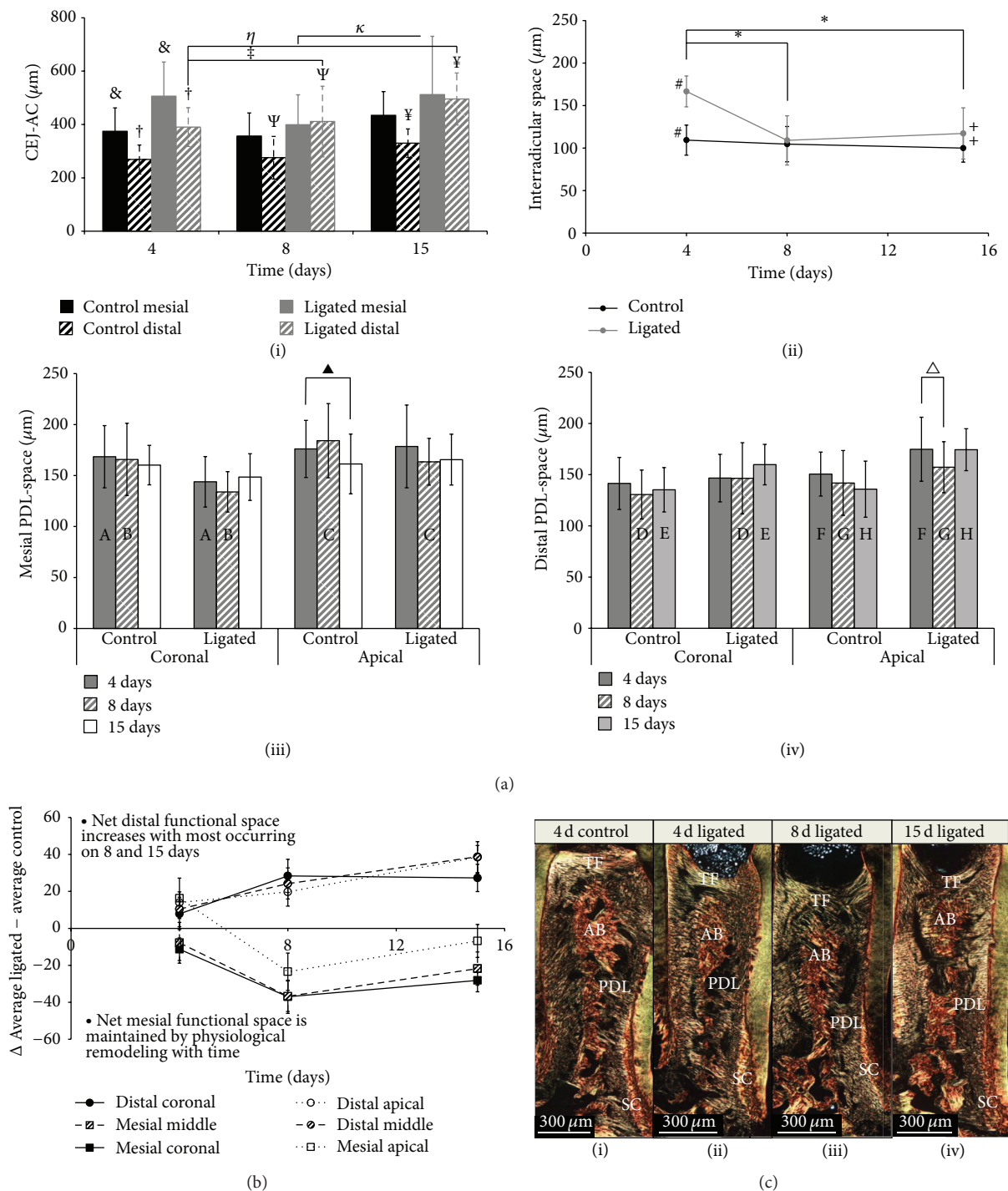


FIGURE 5: Morphometric comparisons of control and ligated bone-PDL-cementum complexes, including changes in collagen birefringence. (a) Comparisons of measurements in mesial and distal regions of the CEJ-ABC (i), the interradicular region (ii), and the PDL-space (iii, iv) between control and ligated complexes at 4, 8, and 15 days. Individual graphs were used to compare PDL-space measurements between coronal and apical anatomical locations within mesial (iii) and distal (iv) complexes. (b) The differences between average ligated and average control PDL-space measurements are plotted for each aforementioned anatomical location across time. (c) Histological sections show the distal complex stained with PSR and visualized under polarized light microscopy. Alveolar bone (AB), periodontal ligament (PDL), secondary cementum (SC), and transseptal fibers (TF). Symbols within plots indicate statistically significant differences at 95% confidence interval.  $\&$ ,  $\dagger$ ,  $\Psi$ ,  $\Upsilon$  Significant difference between control and ligated groups.  $\eta$ ,  $\kappa$  Significant difference over time.  $\#$ ,  $*$  Significant difference between control and ligated groups.  $*$  Significant difference over time.  $A, B, C, D, E, F, G, H$  Significant difference between control and ligated groups.  $\blacktriangle$ ,  $\triangle$  Significant difference over time.

difference, while the distal PDL-spaces of ligated middle and apical regions increased in difference with corresponding control regions. Similarly, the mesial ligated regions still remained smaller than the PDL-spaces of controls; however, they decreased in difference with the corresponding control regions. Interestingly, only the distal regions exhibited significant differences between ligated and control PDL-space measurements at 15 days.

**3.2.3. Collagen Birefringence.** PSR birefringence changes were observed on the distal side depending on the duration of the insult (Figure 5(c), see Figure S1 and supplemental movies in Supplementary Material available online at <http://dx.doi.org/10.1155/2013/876316>). In coronal regions, the ligated complex showed compromised transseptal fiber integrity with decreased birefringence, unlike the observed high birefringence with straight collagen fibers in the control complex. In apical regions, the width of increased birefringence in the distal PDL-secondary cementum of the ligated complex widened across 4, 8, and 15 days (Figure 5(c)). It should be noted that birefringence is dependent on the angle between the PSR-stained specimen and the polarized light. For a complete representation of the above observation, supplemental movies are included.

**3.2.4. FN Expression at the PDL-Bone and PDL-Cementum Interfaces.** On the mesial side, FN expressions were illustrated as sharp peaks at both PDL-bone and PDL-cementum interfaces, regardless of the experimental condition and time point. However, the width of high FN intensity was wider in the ligated group compared to controls (Figures 6(a1), 6(a3), 6(b1), 6(b3), 6(c1), and 6(c3)). On the distal side, the display of FN over a larger width of cementum from the PDL-cementum attachment site was observed. On the other hand, only a sudden drop of intensity with no peak at the PDL-bone attachment site was shown (Figures 6(a2), 6(a4), 6(b2), 6(b4), 6(c2), 6(c4), and Figure S2).

## 4. Discussion

The results of this study are from a commonly used experimental rat model for periodontitis [40–44]. The impetus for choosing the ligature model is that it promotes scenarios similar to food impaction between teeth in humans. The ligatures between the 1st and 2nd molars and the 2nd and 3rd molars (Figure 1(a)) are speculated to promote equal and opposite forces, negating or minimizing effects due to the ligature itself. Additionally, LPS was used as a catalyst to accelerate coronal tissue degeneration by inducing hallmarks of periodontitis, such as alveolar crest resorption and PDL degeneration, thus promoting the loss of coronal tooth attachment. It should be noted that morphometrics, that is, PDL-space can increase or decrease. As a result, the functional space is either widened or narrowed, which in turn can alter overall biomechanics of the organ.

Based on observations from this study, it can be inferred that changes in biochemical expression and/or coronal-apical gradients resulting from inflammation could explain

tissue degradation and a subsequent adaptive response driven by mechanobiology. However, future studies are needed to investigate potential bone formation and resorption effects during disease. This can be done by temporal mapping of mineral formation- and resorption-related events to elucidate PDL-cementum and PDL-bone interfaces under tension and/or compression using dynamic histomorphometry through a fluorochrome technique. Furthermore, our investigation is limited to the early stage of periodontitis, so a model for chronic periodontitis should be developed through observations made at longer time points by using the proposed endotoxin-ligature model. The longer ligation times would elucidate time-related mechanobiological effects on overall joint morphology and soft-hard tissue microstructure, including impairment of joint function—a topic currently under investigation.

The results of this study are discussed on the basis that both disease and function (continued mastication of hard pellets by the rats) have a concomitant effect on biochemical and subsequent morphological changes in the organ. The combined effect can result in positive or negative feedback, thus shifting organ function to impairment. Even though comprehensive studies have postulated a cause-and-effect relationship between bacteria and/or inflammatory cytokines and tissue destruction [44–51], they are spatially limited and describe only alveolar bone destruction. As a result, studies are needed to illustrate effects on the entire bone-PDL-cementum complex, in which the role of no one tissue dominates specifically when in function.

Hence, the two concomitant effects that will be discussed will include: (1) inflammation-induced coronal degeneration as a result of LPS soaked threads, and (2) potential mechanobiological effects specifically in the apical regions of the tooth attachment apparatus due to coronal degeneration over time. To identify a host inflammatory response, we mapped expressions of RANKL, osteoclastic resorption, and TNF- $\alpha$ . Resulting adaptation was detailed through a change in morphology due to increased alveolar bone resorption and net changes in the PDL-space, coronal losses, apical increases in collagen birefringence within the complex, and a gain in FN expression specifically at the apical regions, that is, within secondary cementum and bone. These observed patterns are summarized in Figures S2 and S3.

**4.1. Inflammation-Related Biomolecular Expressions within the Complex.** Ligature-induced inflammation is a host response to eliminate the harmful stimuli due to foreign body and bacterial colonization. The response triggers recruitment of immune cells from the blood into various vascularized connective tissues predominantly exposed to LPS and ligature impaction [27]. The recruited inflammatory cells in turn promote a biochemical cascade, causing proteinase-induced fibrinolysis, osteoclastogenesis, and activation of latent osteoclasts [16]. Formation and activity of osteoclasts *in vivo* are dependent on the expression of RANKL by osteoblastic or bone marrow stromal cells [52, 53]. As a result, we observed RANKL expression in endosteal spaces and vasculature of PDL. In this study, the coronal part of alveolar bone is most affected by LPS due to its proximity



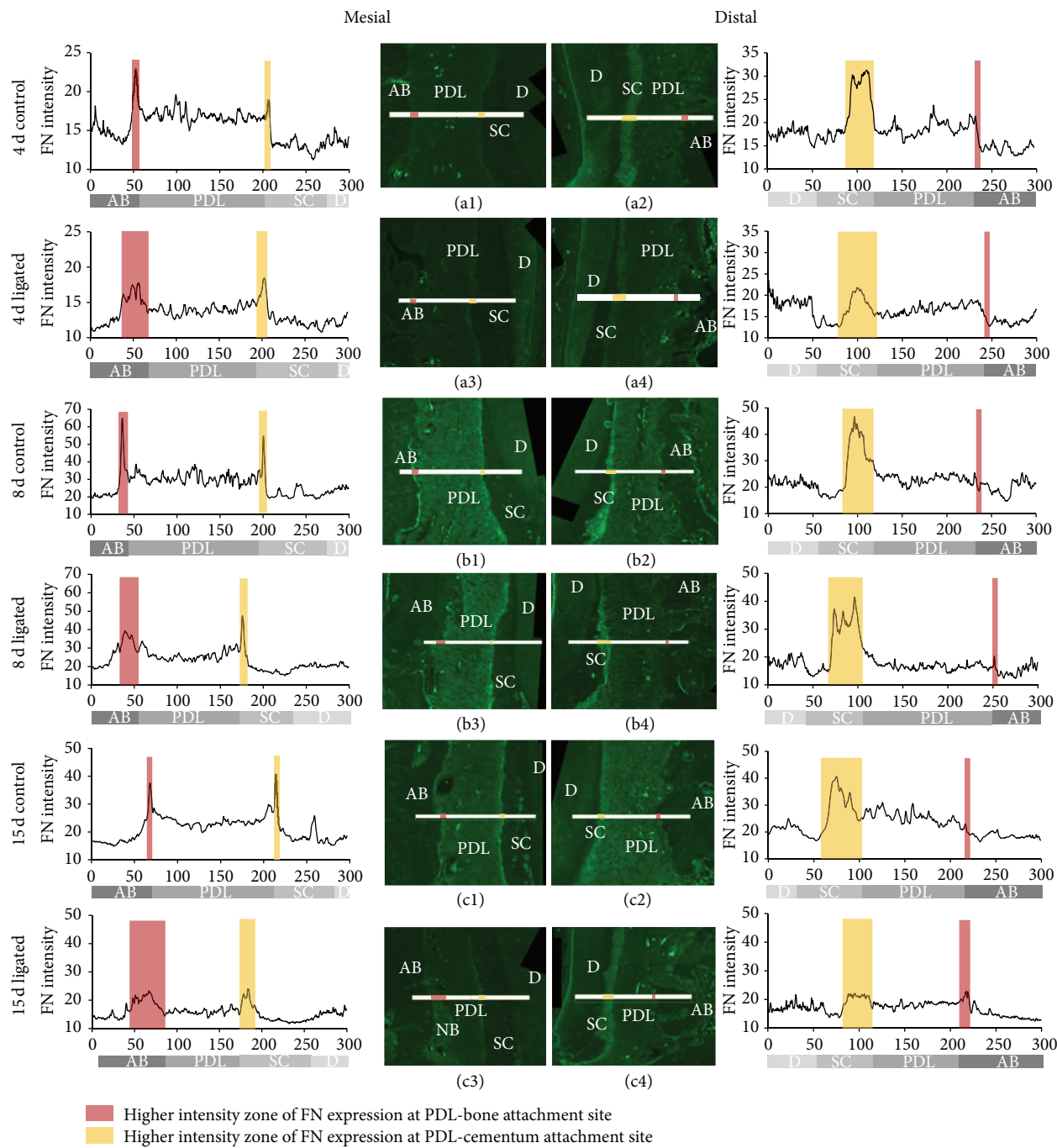


FIGURE 6: Line profiles and micrographs of immunolabeled fibronectin (FN). Representative micrographs illustrate FN immunofluorescence in apical regions of control and ligated complexes at 4, 8, and 15 days. The intensity of FN expression was measured along the anatomical locations indicated by the 300  $\mu\text{m}$  long bar. For the mesial complex, the x-axis of the 300  $\mu\text{m}$  long profile corresponds to alveolar bone (AB), periodontal ligament (PDL), secondary cementum (SC), and dentin (D). Note that the direction for the distal complex is reversed. (a1) 4-day control mesial complex, (a2) 4-day control distal complex, (a3) 4-day ligated mesial complex, (a4) 4-day ligated distal complex, (b1) 8-day control mesial complex, (b2) 8-day control distal complex, (b3) 8-day ligated mesial complex, (b4) 8-day ligated distal complex, (c1) 15-day control mesial complex, (c2) 15-day control distal complex, (c3) 15-day ligated mesial complex, and (c4) 15-day ligated distal complex. Dentin (D), secondary cementum (SC), periodontal ligament (PDL), alveolar bone (AB), new bone (NB).

to the ligature, and as such the expression of RANKL(+) cells near the alveolar crest was quantified (Figures 2(d) and 2(e)). Interestingly, the observed RANKL(+) trend opposed the trend of TRAP(+) osteoclastic activity (Figures 3(b)(x) and 3(b)(xi)). In other words, the number of RANKL(+) cells increased at 4 days before decreasing and then rebounding at 15 days in the distal sides of ligated groups. It is well known that osteoclastogenesis involves a complex series of sequential steps, including RANKL-RANK signaling [54]. This could explain the observed trend of delayed osteoclastic activity, that is, TRAP(+) cells.

Along with RANKL, TNF- $\alpha$  also plays a role in inflammatory bone resorption since TNF- $\alpha$  synergizes with RANKL to potentiate osteoclastogenesis [52, 55, 56]. The known mechanism by which TNF- $\alpha$  modulates bone destruction is related to RANKL stimulation of osteoclast differentiation through autocrine signaling [57]. The majority of *in vivo* studies show that TNF- $\alpha$  is mainly produced by activated macrophages and acts as an agonist or antagonist to advance or restrain alveolar bone resorption, respectively [47, 58–60]. From our observation, TNF- $\alpha$  was distributed throughout the periodontium (Figure 4(a)). This can be attributed to immune cells, the source of TNF- $\alpha$  that is recruited along the blood stream in highly vascularized PDL. The overall TNF- $\alpha$  expression was elevated in ligated groups, especially at PDL-primary cementum interfaces, the interradicular complex, and endosteal spaces. This implies that coronally placed ligatures introduced inflammation to the entire bone-PDL-cementum complex and was not just limited to the coronal area. Anatomically, TNF- $\alpha$  positive osteoclasts were predominant at the PDL-bone interface on the distal side in ligated groups. This observation was positively correlated with increased immunofluorescence of RANKL in conjunction with previous studies that have shown that TNF- $\alpha$  shares the mechanism by which RANKL exerts its osteoclastogenic effect [26, 57]. Additionally, TNF- $\alpha$  was localized to the junctional epithelium. It is plausible that TNF- $\alpha$  released extracellularly drifted into the epithelial layer, since the intercellular space in the junctional epithelium is comparatively wider and contains proportionately fewer desmosomes than in the oral epithelium [61], allowing cytokines to permeate epithelium.

**4.2. Changes in Morphometrics of the Complex, Common Hallmarks of Periodontitis.** Ligated groups showed increased ABC and interradicular resorption compared to controls at 4 days. This observation is most likely caused by the early-stage host inflammatory events due to LPS as the primary stimulus. The argument can be further corroborated by the observation of a decrease in CEJ-ABC distance in mesial regions and a decrease in interradicular PDL-space at 8 days. However, the decrease in bone resorption despite heightened inflammation could have been caused by age-dependent bone modeling processes [42, 62] between 4 and 8 days as bone has a rapid rate of turnover. By 15 days, the resorptive effects of inflammation are speculated to overcome growth-related processes in ligated complexes, resulting in resumed increases of both mesial and distal CEJ-ABC, as well as interradicular PDL-space. It should be noted that within this observed effect

is the effect of osteoclasts in controls due to natural distal resorption in rats [31, 62, 63]. However, the ligated complex included active osteoclasts on the alveolar crest in addition to the distal PDL-bone interface. Furthermore, the osteoclastic activity peaked at 8 days of ligation. This phenomenon can be explained in terms of the characteristics of inflammation induced with ligature placement, an acute and short-termed inflammation that resulted in the initial shift of equilibrium from bacterial endotoxin, that is, LPS, to host response. However, the osteoclastic activity was not maintained after 8 days, suggesting that the effect of inflammation induced by ligation was not sustained because (1) the location of ligature was relatively coronal, and (2) the host response that could have subsided as the local concentration of LPS was diffused [64]. This result is consistent with previous studies [65–69] and can be identified as remission of bone modeling following acute phase of inflammation.

**4.3. Resulting Early Mechanobiological Effects of a Diseased Fibrous Joint.** Based on observed morphological differences (Figures 5(a) and 5(b)), we predict that the coronal degeneration could have shifted from physiological to nonphysiological, that is, pathological function. This shift from physiological to aberrant loads on the complex is hypothesized to be a significant deviation from optimum function. This is because increased joint mobility due to PDL degeneration and coronal alveolar bone support can cause increased tooth movement with the alveolar socket. Such argument can be further reinforced by the fact that the ligature had to be reintroduced every two to three days in the rats. Based on our previous work, regions that are predicted to experience increased strain during the initial disease stages include coronal attachment sites, apical compression-dominant regions, and predominantly the interradicular regions [70] (the PDL-space at the interradicular region is narrower compared to PDL-space around the tooth (Figure 5(a))). As such, it is conceivable that, within ligated groups, healthy PDL in interradicular regions, and apical to diseased regions could experience amplified strains during mastication compared to their control counterparts. Additionally, strains could be altered at the PDL-bone and PDL-cementum interfaces [71] in ligated groups. These altered three-dimensional strain profiles are of special interest because deviations from normal physiological strain can lead to pathological function (aberrant loads/function), and compromised mechanotransduction over time [5, 72, 73] including the soft-hard tissue interfaces where multiple cell types reside.

Ligated groups exhibited different patterns of morphological adaptation over time compared to control groups as indicated by changes in PDL-space. Complementary increase in RANKL expression and osteoclast activity, an increase in interradicular PDL-space (15 days, Figure 5(a)(ii)) could indicate excessive strains in the interradicular complex at a later time, resulting in resorption and shifting the adaptive effects of our model to those observed in a hyperocclusion model [74, 75]. As such, it is possible that in our study the interradicular bone commonly known as the fulcrum for tooth rotation [70] shifted, thus altering the strain field within the entire bone-PDL-cementum complex.

The shift toward aberrant function can promote a net change in the localization and intensity of RANKL. RANKL is a mechanosensitive molecule that decreases in expression with tension in osteoblasts [76]. When comparing alveolar crests within ligated complexes, RANKL expression was seen to increase between 8 and 15 days on the distal side but decreased over time on the mesial side (Figures 2(d) and 2(e)). Although RANKL expression increases at each time point between ligated and controls both mesially and distally due to a host inflammatory response, the suggested age dominated mesial-tension due to growth may have counteracted this increase during prolonged mechanical loading. As such, while a RANKL expression increase was seen in 4-day ligated complexes compared to controls, a similar number of RANKL(+) cells were seen between ligated and control complexes at 15 days. In contrast, the progressive increase of RANKL(+) cell count from 8 days to 15 days on the distal side was most likely caused by the compounded effect of compression-induced expression due to distal drift and host inflammatory response [77, 78]. Although we correlate RANKL expression increase to osteoclast activation, it is important to note that a RANKL/osteoprotegerin (OPG) ratio should be used as the standard index for formative and resorptive bone [16]. Together, this data suggests that an early host inflammatory response drives increased biochemical expressions coronally. However, later changes in expressions of respective biomolecules due to opposing mechanobiological effects on mesial and distal sides are induced by aberrant function of the ligated joint. Aberrant function-related effects were seen in secondary cementum. In this study, the complementary data of collagen birefringence and FN expression seen at the distal secondary cementum is proposed as a compensatory adaptation due to a net increase in distal bone resorption and maintenance of age-related normal physiological activity at the mesial complex (Figure 5(c)). However, birefringence indicated by PSR is only a complementary marker to the more confirmatory FN expression. This is because collagen birefringence identified through PSR staining is also a function of section thickness and is highly dependent on fiber orientation relative to the polarizers (movies were included to highlight the specificity of our results—Figure S1 and supplemental movies) and level of tissue demineralization and collagen integrity.

Secondary cementum is hypothesized to adapt to occlusion during the posteruption phase of tooth development and has been shown to respond to load [35, 79]. As such, it is conceivable that secondary cementum adaptation would follow coronal bone resorption as a mechanism to compensate for disruption due to inflammation. In this study, we used two identifiers to detail the adaptation of secondary cementum. These included collagen birefringence and FN expression [24, 80, 81]. The triggering of the local biochemical effects caused an increase in apical collagenous matrix organization with time (Figure 5(c)). As a result, an altered birefringence was observed at the mesial, but higher at the distal PDL-secondary cementum interface in ligated groups (Figure S1 supplemental movies). This implies that inflammation-induced mechanobiology remotely stimulated organic matrix within the apical cementum (Figures 5(c),

6, S1, and S2). Although an increased level of birefringence equivalent to that of controls was observed at 4 days, with increased time, both the width and intensity of birefringence at the distal secondary cementum surface increased. It is plausible that the complex has adapted to changes resulting from ligature-induced coronal inflammation in the tension-dominant mesial region and the compression-dominant distal region. However, adaptation manifested itself in apical regions as new bone formation, which was predominant on the mesial side, and new cementum formation on the distal side (Figures 5(c) and 6) within respective groups.

The aforementioned secondary cementum adaptation detailed through collagen birefringence can be further strengthened by FN expressions. Nonphysiological tensions at the mesial complex of ligated rats due to coronal degeneration of transseptal and periodontal fibers could have altered the FN mRNA expression and protein content apically (Figure 6) [82, 83]. The localization pattern of a wide FN expression band apically could be from an increased organization around periphery of osteo- or cementoblast cells and increased density as the collagenous matrix is generated [84].

FN is an important chemotactic protein for the storage of growth factors, along with its prolific interactions with cell surface molecules to facilitate cellular adhesion, migration and regulate cellular differentiation and proliferation [24]. Although FN is not a direct marker for hard-tissue formation using immunohistochemistry, it provides evidence that this multipurpose protein can amplify the response of osteoblast progenitors to alter the regenerative or reparative potential of organic matrices during mechanobiological adaptation [83]. The same may hold true for cementoblast progenitors on the tooth side, resulting in mesial deposition of secondary cementum. While compressive loads have been shown to cause a decrease in FN expression within PDL cells [82, 83], when compared to controls, the distal regions in ligated molars interestingly illustrated increased FN expression at PDL-cementum attachment sites and through the distal precementum layers of the complex (Figure 6).

We summarize the results by presenting a biomechanical model representative of the measured downstream localization and expression level changes of mechanosensitive proteins and net spatiotemporal changes in the PDL-space (Figure S3). On the distal coronal side, temporal trends of PDL-space were directly correlated with those of osteoclastic activity. As such, the net increase in PDL-space on the distal coronal side in ligated groups could be explained by an increased osteoclastic activity due to increased compressive strains within the PDL. Increased compression could arise from increased whole body distal rotation of the tooth (Figure S3A.3) coupled with coronal inflammation. In both control and ligated groups, osteoclastic activity increased significantly at 8 days and remained significantly higher at 15 days when compared to 4-day controls. While there was greater osteoclastic activity in ligated groups at 8 days compared to the controls, the lack of significant difference between control and ligated groups at both time points could be explained by (1) development-related changes at early-time points, which may have masked the effect of inflammation and mechanobiological response, and/or (2) a need for



a larger sample size. However, it is interesting to note that there was a decreased but sustained osteoclastic activity at 15 days, which could have affected the observed PDL-space.

In the apical segment of the distal complex, the trend observed in PDL-space did not correspond to the osteoclastic activity change. Specifically, when correlating trends of osteoclastic activity and PDL-space over time, the increased osteoclastic activity did not match the decreased PDL-space in 8-day ligated joints. Furthermore, the measured increase in width of FN expression adjacent to the distal secondary cementum, which indicates new cementum apposition, calls for speculation that the PDL-space in this region experienced increased tensile strains during increased distal rotation and vertical displacement (Figure S3A.3). Therefore, the PDL-space is expected to become narrower than that of control groups over time (Figure S3A.4). However, the opposite morphological change was observed. The increase in PDL-space of ligated joints at 15 days when compared to controls and 8-day ligated joints suggests that there was a delay in observable morphological effects (resorption of bone) after the increase of osteoclast activity [69]. Namely, it can be speculated that 8 days of ligation was closer to the beginning of an increase in osteoclastic activity that carried into 15 days of ligation, resulting in an increased PDL-space. As such, the new cementum apposition labeled by FN could have been missed in micro-XCT measurements, since the FN-labeled band indicates a predominance of organic matrix. Therefore, PDL-space could be narrowed with prolonged observation as the cementum layer is given time to mineralize. Further studies identifying cementum growth using fluorochrome technique or cementum-specific markers are necessary and could be used to verify this phenomenon. Similarly, the trends in osteoclastic activity on the mesial side reflected opposite morphological changes in PDL-space at corresponding time points.

From a morphological standpoint, the significantly reduced PDL-space in more apical, unaffected regions of ligated fibrous joints can be attributed to increased tensile strains in this area due to coronal degradation [70]. Although it is well established that experimentally induced periodontitis stimulates inflammation-induced osteoclastic activity, such activity is limited to the coronal regions [85]. Therefore, the osteoclastic activity observed in more apical regions of ligated complexes could be the manifestation of the resorption/formation coupling of physiological bone turnover [86]. However, the amplified strains could have accelerated adaptation of the complex with an increased rate of bone turnover. From a strain localization perspective, these normally compression-dominant regions are predicted to be shifted to tension-dominant regions. This is due to an apically migrating fulcrum of tooth rotation that stems from the increased mobility of the tooth as a result of coronal attachment loss and resorption of interradicular bone (Figure S3A.3). Our model is also supported by the increased band width of FN expression observed at the PDL bone attachment site at the apical region on the mesial side (Figures 6(a3), 6(b3), 6(c3), and S3A.4).

From these results, we speculate that disease-related changes promote adaptation of bone and apical cementum,

which was predominantly observed on the mesial-coronal and distal-apical sides of the tooth. It is important to note that the mechanical strains within the complex of a single root are assumed to be similar to strains in the entire complex of a tooth despite the ligature. Hence, the mesiodistal effects discussed in the bone-PDL-tooth complex should be similar to those observed in the corresponding complexes of the mesial and distal roots of the same tooth.

## 5. Conclusions

In this present study, we clarified the alteration due to disease by distinguishing disease-induced effects from physiologically determined phenomena with unpaired control groups. In conclusion, our results showed that coronal induction of an inflammatory perturbation affected the overall distribution of biochemical molecules in the entire complex. Furthermore, concomitant function imposed on the compromised complex could have accelerated tissue adaptation to meet functional demands (Figures S2 and S3). To be specific, a net decrease in functional space was identified in the mesial complex, whereas a net increase in functional space was identified in the distal complex. In addition, an adaptive response in secondary cementum, that is, predominant cementum formation, was more apparent distally. The altered expression at later time points suggests that prolonged function can manifest into excessive loads on the diseased fibrous joint, shifting physiological function into an impaired function when compared to controls. It is imperative that future studies should measure the biomechanical response of joints that have undergone short- and long-term changes to inflamed and degraded fibrous joints. When measured, the biomechanical results will validate the proposed model that early morphological changes due to disease can impair function, eventually causing the observed secondary adaptations of the fibrous joint.

## Authors' Contribution

Ji-Hyun Lee and Jeremy D. Lin contributed equally.

## Acknowledgments

The authors thank the Biomaterials and Bioengineering MicroCT Imaging Facility, UCSF for the use of Micro XCT. Support was provided by NIH/NIDCR R00DE018212, NIH/NIDCR R01DE022032, NIH/NIDCR T32 DE07306-14, NIH/NCRR S10RR026645, and Departments of Preventive and Restorative Dental Sciences and Orofacial Sciences, UCSF. The authors acknowledge that they do not have conflict of interests and were fully involved in the study and preparation of the paper.

## References

- [1] M. Shimono, T. Ishikawa, H. Ishikawa et al., "Regulatory mechanisms of periodontal regeneration," *Microscopy Research and Technique*, vol. 60, no. 5, pp. 491–502, 2003.

- [2] C. A. G. McCulloch, P. Lekic, and M. D. McKee, "Role of physical forces in regulating the form and function of the periodontal ligament," *Periodontology 2000*, vol. 24, no. 1, pp. 56–72, 2000.
- [3] W. Beertsen, C. A. G. McCulloch, and J. Sodek, "The periodontal ligament: a unique, multifunctional connective tissue," *Periodontology 2000*, vol. 14, no. 1, pp. 20–40, 1997.
- [4] P. Lekic and C. A. McCulloch, "Periodontal ligament cell population: the central role of fibroblasts in creating a unique tissue," *The Anatomical Record*, vol. 245, no. 2, pp. 327–341, 1996.
- [5] J. M. Hurng, M. P. Kurylo, G. W. Marshall, S. M. Webb, M. I. Ryder, and S. P. Ho, "Discontinuities in the human bone-PDL-cementum complex," *Biomaterials*, vol. 32, no. 29, pp. 7106–7117, 2011.
- [6] S. S. Socransky and A. D. Haffajee, "The nature of periodontal diseases," *Annals of periodontology*, vol. 2, no. 1, pp. 3–10, 1997.
- [7] K. S. Kornman, "Mapping the pathogenesis of periodontitis: a new look," *Journal of Periodontology*, vol. 79, no. 8, supplement, pp. 1560–1568, 2008.
- [8] S. Offenbacher, "Periodontal diseases: pathogenesis," *Annals of periodontology*, vol. 1, no. 1, pp. 821–878, 1996.
- [9] H. V. Jordan, "Rodent model systems in periodontal disease research," *Journal of Dental Research*, vol. 50, no. 2, pp. 236–242, 1971.
- [10] D. T. Graves, D. Fine, Y. T. A. Teng, T. E. Van Dyke, and G. Hajishengallis, "The use of rodent models to investigate host-bacteria interactions related to periodontal diseases," *Journal of Clinical Periodontology*, vol. 35, no. 2, pp. 89–105, 2008.
- [11] H. Loe, E. Theilade, and S. B. Jensen, "Experimental gingivitis in man," *The Journal of Periodontology*, vol. 36, pp. 177–187, 1965.
- [12] P. Axelsson and J. Lindhe, "Effect of controlled oral hygiene procedures on caries and periodontal disease in adults," *Journal of Clinical Periodontology*, vol. 5, no. 2, pp. 133–151, 1978.
- [13] P. Axelsson and J. Lindhe, "Effect of controlled oral hygiene procedures on caries and periodontal disease in adults. Results after 6 years," *Journal of Clinical Periodontology*, vol. 8, no. 3, pp. 239–248, 1981.
- [14] R. C. Page and H. E. Schroeder, "Pathogenesis of inflammatory periodontal disease: a summary of current work," *Laboratory Investigation*, vol. 34, no. 3, pp. 235–249, 1976.
- [15] J. Lindhe, S. E. Hamp, and H. Loe, "Plaque induced periodontal disease in beagle dogs. A 4 year clinical, roentgenographical and histometrical study," *Journal of Periodontal Research*, vol. 10, no. 5, pp. 243–255, 1975.
- [16] D. L. Cochran, "Inflammation and bone loss in periodontal disease," *Journal of Periodontology*, vol. 79, no. 8, supplement, pp. 1569–1576, 2008.
- [17] H. S. Oz and D. A. Puleo, "Animal models for periodontal disease," *Journal of Biomedicine and Biotechnology*, vol. 2011, Article ID 754857, 8 pages, 2011.
- [18] R. Liu, H. S. Bal, T. Desta et al., "Diabetes enhances periodontal bone loss through enhanced resorption and diminished bone formation," *Journal of Dental Research*, vol. 85, no. 6, pp. 510–514, 2006.
- [19] C. A. Genco, T. Van Dyke, and S. Amar, "Animal models for Porphyromonas gingivalis-mediated periodontal disease," *Trends in Microbiology*, vol. 6, no. 11, pp. 444–449, 1998.
- [20] T. Ogasawara, Y. Yoshimine, T. Kiyoshima et al., "In situ expression of RANKL, RANK, osteoprotegerin and cytokines in osteoclasts of rat periodontal tissue," *Journal of Periodontal Research*, vol. 39, no. 1, pp. 42–49, 2004.
- [21] M. A. Taubman, P. Valverde, X. Han, and T. Kawai, "Immune response: they key to bone resorption in periodontal disease," *Journal of Periodontology*, vol. 76, no. 11, supplement, pp. 2033–2041, 2005.
- [22] C. Minkin, "Bone acid phosphatase: tartrate-resistant acid phosphatase as a marker of osteoclast function," *Calcified Tissue International*, vol. 34, no. 3, pp. 285–290, 1982.
- [23] E. F. Rossomando, J. E. Kennedy, and J. Hadjimichael, "Tumour necrosis factor alpha in gingival crevicular fluid as a possible indicator of periodontal disease in humans," *Archives of Oral Biology*, vol. 35, no. 6, pp. 431–434, 1990.
- [24] W. J. Grzesik and A. S. Narayanan, "Cementum and periodontal wound healing and regeneration," *Critical Reviews in Oral Biology and Medicine*, vol. 13, no. 6, pp. 474–484, 2002.
- [25] J. E. Rogers, F. Li, D. D. Coatney et al., "Actinobacillus actinomycetemcomitans Lipopolysaccharide-mediated experimental bone loss model for aggressive periodontitis," *Journal of Periodontology*, vol. 78, no. 3, pp. 550–558, 2007.
- [26] S. Kwan Tat, M. Padrines, S. Theoleyre, D. Heymann, and Y. Fortun, "IL-6, RANKL, TNF-alpha/IL-1: interrelations in bone resorption pathophysiology," *Cytokine and Growth Factor Reviews*, vol. 15, no. 1, pp. 49–60, 2004.
- [27] D. Graves, "Cytokines that promote periodontal tissue destruction," *Journal of Periodontology*, vol. 79, no. 8, supplement, pp. 1585–1591, 2008.
- [28] S. Ma, J. Guo, X. You, W. Xia, and F. Yan, "Expressions of interleukin-1 $\beta$  and interleukin-6 within aortas and uteri of rats with various severities of ligature-induced periodontitis," *Inflammation*, vol. 34, no. 4, pp. 260–268, 2011.
- [29] K. Kobayashi, N. Takahashi, E. Jimi et al., "Tumor necrosis factor  $\alpha$  stimulates osteoclast differentiation by a mechanism independent of the ODF/RANKL-RANK interaction," *Journal of Experimental Medicine*, vol. 191, no. 2, pp. 275–285, 2000.
- [30] K. Fuller, C. Murphy, B. Kirstein, S. W. Fox, and T. J. Chambers, "TNF $\alpha$  potentially activates osteoclasts, through a direct action independent of and strongly synergistic with RANKL," *Endocrinology*, vol. 143, no. 3, pp. 1108–1118, 2002.
- [31] G. Anastasi, G. Cordasco, G. Matarese et al., "An immunohistochemical, histological, and electron-microscopic study of the human periodontal ligament during orthodontic treatment," *International Journal of Molecular Medicine*, vol. 21, no. 5, pp. 545–554, 2008.
- [32] M. J. Björnsson, S. Velschow, K. Stoltze, A. Havemose-Poulsen, S. Schou, and P. Holmstrup, "The influence of diet consistence, drinking water and bedding on periodontal disease in Sprague-Dawley rats," *Journal of Periodontal Research*, vol. 38, no. 6, pp. 543–550, 2003.
- [33] L. Heijl, J. Wennstrom, J. Lindhe, and S. S. Socransky, "Periodontal disease in gnotobiotic rats," *Journal of Periodontal Research*, vol. 15, no. 4, pp. 405–419, 1980.
- [34] H. Sicher and J. P. Weinmann, "Bone growth and physiologic tooth movement," *The American Journal of Orthodontics and Oral Surgery*, vol. 30, no. 3, pp. C109–C132, 1944.
- [35] R. P. Herber, J. Fong, S. A. Lucas, and S. P. Ho, "Imaging an adapted dentoalveolar complex," *Anatomy Research International*, vol. 2012, Article ID 782571, 13 pages, 2012.
- [36] K. J. Ibbotson, G. D. Roodman, L. M. McManus, and G. R. Mundy, "Identification and characterization of osteoclast-like cells and their progenitors in cultures of feline marrow mononuclear cells," *Journal of Cell Biology*, vol. 99, no. 2, pp. 471–480, 1984.



- [37] A. Sawyer, P. Lott, J. Titrud, and J. M. McDonald, "Quantification of tartrate resistant acid phosphatase distribution in mouse tibiae using image analysis," *Biotechnic and Histochemistry*, vol. 78, no. 5, pp. 271–278, 2003.
- [38] L. C. U. Junqueira, G. Bignolas, and R. R. Brentani, "Picrosirius staining plus polarization microscopy, a specific method for collagen detection in tissue sections," *Histochemical Journal*, vol. 11, no. 4, pp. 447–455, 1979.
- [39] S. P. Ho, B. Yu, W. Yun, G. W. Marshall, M. I. Ryder, and S. J. Marshall, "Structure, chemical composition and mechanical properties of human and rat cementum and its interface with root dentin," *Acta Biomaterialia*, vol. 5, no. 2, pp. 707–718, 2009.
- [40] M. P. Galvão, C. K. Rösing, and M. B. Ferreira, "Effects of ligature-induced periodontitis in pregnant Wistar rats," *Brazilian Oral Research*, vol. 17, no. 1, pp. 51–55, 2003.
- [41] A. Györfi, A. Fazekas, Z. Suba, F. Ender, and L. Rosivall, "Neurogenic component in ligature-induced periodontitis in the rat," *Journal of Clinical Periodontology*, vol. 21, no. 9, pp. 601–605, 1994.
- [42] A. Kuhr, A. Popa-Wagner, H. Schmoll, C. Schwahn, and T. Kocher, "Observations on experimental marginal periodontitis in rats," *Journal of Periodontal Research*, vol. 39, no. 2, pp. 101–106, 2004.
- [43] K. Sallay, F. Sanavi, I. Ring, P. Pham, U. H. Behling, and A. Nowotny, "Alveolar bone destruction in the immunosuppressed rat," *Journal of Periodontal Research*, vol. 17, no. 3, pp. 263–274, 1982.
- [44] S. Kimura, A. Nagai, T. Onitsuka et al., "Induction of experimental periodontitis in mice with Porphyromonas gingivalis-adhered ligatures," *Journal of Periodontology*, vol. 71, no. 7, pp. 1167–1173, 2000.
- [45] R. Achong, I. Nishimura, H. Ramachandran, T. H. Howell, J. P. Fiorellini, and N. Y. Karimbux, "Membrane type (MT) 1-matrix metalloproteinase (MMP) and MMP-2 expression in ligature-induced periodontitis in the rat," *Journal of Periodontology*, vol. 74, no. 4, pp. 494–500, 2003.
- [46] J. P. Bezerra, L. R. F. Da Silva, V. A. D. A. Lemos, P. M. Duarte, and M. F. Bastos, "Administration of high doses of caffeine increases alveolar bone loss in ligature-induced periodontitis in rats," *Journal of Periodontology*, vol. 79, no. 12, pp. 2356–2360, 2008.
- [47] X. Cai, C. Li, G. Du, and Z. Cao, "Protective effects of baicalin on ligature-induced periodontitis in rats," *Journal of Periodontal Research*, vol. 43, no. 1, pp. 14–21, 2008.
- [48] G. D. R. Nogueira-Filho, B. T. Rosa, J. B. César-Neto, R. S. Tunes, and U. D. R. Tunes, "Low- and high-yield cigarette smoke inhalation potentiates bone loss during ligature-induced periodontitis," *Journal of Periodontology*, vol. 78, no. 4, pp. 730–735, 2007.
- [49] K. Okuda, T. Kato, Y. Naito et al., "Protective efficacy of active and passive immunizations against experimental infection with Bacteroides gingivalis in ligated hamsters," *Journal of Dental Research*, vol. 67, no. 5, pp. 807–811, 1988.
- [50] Y. Samejima, S. Ebisu, and H. Okada, "Effect of infection with Eikenella corrodens on the progression of ligature-induced periodontitis in rats," *Journal of Periodontal Research*, vol. 25, no. 5, pp. 308–315, 1990.
- [51] F. Sanavi, M. A. Listgarten, F. Boyd, K. Sallay, and A. Nowotny, "The colonization and establishment of invading bacteria in periodontium of ligature-treated immunosuppressed rats," *Journal of Periodontology*, vol. 56, no. 5, pp. 273–280, 1985.
- [52] T. Suda, N. Takahashi, N. Udagawa, E. Jimi, M. T. Gillespie, and T. J. Martin, "Modulation of osteoclast differentiation and function by the new members of the tumor necrosis factor receptor and ligand families," *Endocrine Reviews*, vol. 20, no. 3, pp. 345–357, 1999.
- [53] T. J. Chambers, "Regulation of the differentiation and function of osteoclasts," *The Journal of Pathology*, vol. 192, no. 1, pp. 4–13, 2000.
- [54] T. Wada, T. Nakashima, N. Hiroshi, and J. M. Penninger, "RANKL-RANK signaling in osteoclastogenesis and bone disease," *Trends in Molecular Medicine*, vol. 12, no. 1, pp. 17–25, 2006.
- [55] J. Lam, S. Takeshita, J. E. Barker, O. Kanagawa, F. P. Ross, and S. L. Teitelbaum, "TNF- $\alpha$  induces osteoclastogenesis by direct stimulation of macrophages exposed to permissive levels of RANK ligand," *Journal of Clinical Investigation*, vol. 106, no. 12, pp. 1481–1488, 2000.
- [56] C. T. Ritchlin, S. A. Haas-Smith, P. Li, D. G. Hicks, and E. M. Schwarz, "Mechanisms of TNF- $\alpha$  and RANKL-mediated osteoclastogenesis and bone resorption in psoriatic arthritis," *Journal of Clinical Investigation*, vol. 111, no. 6, pp. 821–831, 2003.
- [57] H. Lin, S. W. Wang, R. Y. Wang, and P. S. Wang, "Tumor necrosis factor- $\alpha$  mediates RANK ligand stimulation of osteoclast differentiation by an autocrine mechanism," *Journal of Cellular Biochemistry*, vol. 83, no. 1, pp. 70–83, 2001.
- [58] R. Assuma, T. Oates, D. Cochran, S. Amar, and D. T. Graves, "IL-1 and TNF antagonists inhibit the inflammatory response and bone loss in experimental periodontitis," *Journal of Immunology*, vol. 160, no. 1, pp. 403–409, 1998.
- [59] D. T. Graves, A. J. Delima, R. Assuma, S. Amar, T. Oates, and D. Cochran, "Interleukin-1 and tumor necrosis factor antagonists inhibit the progression of inflammatory cell infiltration toward alveolar bone in experimental periodontitis," *Journal of Periodontology*, vol. 69, no. 12, pp. 1419–1425, 1998.
- [60] A. J. Delima, T. Oates, R. Assuma et al., "Soluble antagonists to interleukin-1 (IL-1) and Tumor Necrosis Factor (TNF) inhibits loss of tissue attachment in experimental periodontitis," *Journal of Clinical Periodontology*, vol. 28, no. 3, pp. 233–240, 2001.
- [61] S. Hashimoto, T. Yamamura, and M. Shimono, "Morphometric analysis of the intercellular space and desmosomes of rat junctional epithelium," *Journal of periodontal research*, vol. 21, no. 5, pp. 510–520, 1986.
- [62] N. L. Leong, J. M. Hurng, S. I. Djomehri, S. A. Gansky, M. I. Ryder, and S. P. Ho, "Age-related adaptation of bone-PDL-tooth complex: Rattus-Norvegicus as a model system," *PloS One*, vol. 7, no. 4, Article ID e35980, 2012.
- [63] C. M. Belting, I. Schour, J. P. Weinmann, and M. J. Shepro, "Age changes in the periodontal tissues of the rat molar," *Journal of Dental Research*, vol. 32, no. 3, pp. 332–353, 1953.
- [64] J. C. McLeod and E. Balish, "Endotoxin in germfree, gnotobiotic, or conventional-flora Sprague-Dawley rats," *Canadian Journal of Microbiology*, vol. 24, no. 12, pp. 1602–1606, 1978.
- [65] R. A. Adams, H. A. Zander, and A. M. Polson, "Cell populations in the transseptal fiber region before, during and after experimental periodontitis in squirrel monkeys," *Journal of Periodontology*, vol. 50, no. 1, pp. 7–12, 1979.
- [66] S. Nyman, H. E. Schroeder, and J. Lindhe, "Suppression of inflammation and bone resorption by indomethacin during experimental periodontitis in dogs," *Journal of Periodontology*, vol. 50, no. 9, pp. 450–461, 1979.

- [67] L. Heijl, B. R. Rifkin, and H. A. Zander, "Conversion of chronic gingivitis to periodontitis in squirrel monkeys," *Journal of Periodontology*, vol. 47, no. 12, pp. 710–716, 1976.
- [68] H. E. Schroeder and J. Lindhe, "Conversion of stable established gingivitis in the dog into destructive periodontitis," *Archives of Oral Biology*, vol. 20, no. 12, pp. 775–782, 1975.
- [69] C. H. Li and S. Amar, "Morphometric, histomorphometric, and microcomputed tomographic analysis of periodontal inflammatory lesions in a murine model," *Journal of Periodontology*, vol. 78, no. 6, pp. 1120–1128, 2007.
- [70] J. D. Lin, H. Ozcoban, J. Greene et al., "Biomechanics of a bone-periodontal ligament-tooth fibrous joint," *Journal of Biomechanics*, vol. 46, no. 3, pp. 443–449, 2012.
- [71] L. Qian, M. Todo, Y. Morita, Y. Matsushita, and K. Koyano, "Deformation analysis of the periodontium considering the viscoelasticity of the periodontal ligament," *Dental Materials*, vol. 25, no. 10, pp. 1285–1292, 2009.
- [72] S. P. Ho, M. P. Kurylo, T. K. Fong et al., "The biomechanical characteristics of the bone-periodontal ligament-cementum complex," *Biomaterials*, vol. 31, no. 25, pp. 6635–6646, 2010.
- [73] J. D. Lin, S. Aloni, V. Altoe, S. M. Webb, M. I. Ryder, and S. P. Ho, "Elastic discontinuity due to ectopic calcification in a human fibrous joint," *Acta Biomaterialia*, vol. 9, no. 1, pp. 4787–4795, 2012.
- [74] K. Nozaki, M. Kaku, Y. Yamashita, M. Yamauchi, and H. Miura, "Effect of cyclic mechanical loading on osteoclast recruitment in periodontal tissue," *Journal of Periodontal Research*, vol. 45, no. 1, pp. 8–15, 2010.
- [75] C. G. Walker, Y. Ito, S. Dangaria, X. Luan, and T. G. H. Diekwisch, "RANKL, osteopontin, and osteoclast homeostasis in a hyperocclusion mouse model," *European Journal of Oral Sciences*, vol. 116, no. 4, pp. 312–318, 2008.
- [76] Z. Zhong, X. L. Zeng, J. H. Ni, and X. F. Huang, "Comparison of the biological response of osteoblasts after tension and compression," *European Journal of Orthodontics*, vol. 35, no. 1, pp. 59–65, 2011.
- [77] K. Nakao, T. Goto, K. K. Gunjigake, T. Konoo, S. Kobayashi, and K. Yamaguchi, "Intermittent force induces high RANKL expression in human periodontal ligament cells," *Journal of Dental Research*, vol. 86, no. 7, pp. 623–628, 2007.
- [78] Y. Li, W. Zheng, J. S. Liu et al., "Expression of osteoclastogenesis inducers in a tissue model of periodontal ligament under compression," *Journal of Dental Research*, vol. 90, no. 1, pp. 115–120, 2011.
- [79] B. L. Foster, "Methods for studying tooth root cementum by light microscopy," *International Journal of Oral Science*, vol. 4, no. 3, pp. 119–128, 2012.
- [80] M. A. Matias, H. Li, W. G. Young, and P. M. Bartold, "Immunohistochemical localisation of extracellular matrix proteins in the periodontium during cementogenesis in the rat molar," *Archives of Oral Biology*, vol. 48, no. 10, pp. 709–716, 2003.
- [81] R. L. MacNeil and M. J. Somerman, "Molecular factors regulating development and regeneration of cementum," *Journal of Periodontal Research*, vol. 28, no. 6, pp. 550–559, 1993.
- [82] Y. He, E. J. Macarak, J. M. Korostoff, and P. S. Howard, "Compression and tension: differential effects on matrix accumulation by periodontal ligaments fibroblasts in vitro," *Connective Tissue Research*, vol. 45, no. 1, pp. 28–39, 2004.
- [83] P. S. Howard, U. Kucich, R. Taliwal, and J. M. Korostoff, "Mechanical forces alter extracellular matrix synthesis by human periodontal ligament fibroblasts," *Journal of Periodontal Research*, vol. 33, no. 8, pp. 500–508, 1998.
- [84] R. L. Steward, C. M. Cheng, J. D. Ye, R. M. Bellin, and P. R. Leduc, "Mechanical stretch and shear flow induced reorganization and recruitment of fibronectin in fibroblasts," *Scientific Reports*, vol. 1, p. 147, 2011.
- [85] T. Shibutani, Y. Murahashi, E. Tsukada, Y. Iwayama, and J. N. M. Heersche, "Experimentally induced periodontitis in beagle dogs causes rapid increases in osteoclastic resorption of alveolar bone," *Journal of Periodontology*, vol. 68, no. 4, pp. 385–391, 1997.
- [86] A. M. Parfitt, "The cellular basis of bone remodeling: the quantum concept reexamined in light of recent advances in the cell biology of bone," *Calcified Tissue International*, vol. 36, no. 1, pp. S37–S45, 1984.

## Research Article

# An *In Vitro* Culture System for Long-Term Expansion of Epithelial and Mesenchymal Salivary Gland Cells: Role of TGF- $\beta$ 1 in Salivary Gland Epithelial and Mesenchymal Differentiation

Kajohnkiart Janebodin,<sup>1,2</sup> Worakanya Buranaphatthana,<sup>1,3</sup> Nicholas Ieronimakis,<sup>4</sup> Aislinn L. Hays,<sup>4</sup> and Morayma Reyes<sup>1,4,5</sup>

<sup>1</sup> Department of Oral Health Sciences, School of Dentistry, University of Washington, Seattle, WA 98195, USA

<sup>2</sup> Department of Anatomy, Faculty of Dentistry, Mahidol University, Bangkok 10400, Thailand

<sup>3</sup> Department of Oral Biology and Diagnostic Sciences, Faculty of Dentistry, Chiang Mai University, Chiang Mai 50200, Thailand

<sup>4</sup> Department of Pathology, School of Medicine, University of Washington, Seattle, WA 98195, USA

<sup>5</sup> Department of Laboratory Medicine, School of Medicine, University of Washington, Seattle, WA 98195, USA

Correspondence should be addressed to Morayma Reyes; [morayma@uw.edu](mailto:morayma@uw.edu)

Received 7 February 2013; Revised 16 April 2013; Accepted 21 April 2013

Academic Editor: Brian L. Foster

Copyright © 2013 Kajohnkiart Janebodin et al. This is an open access article distributed under the Creative Commons Attribution License, which permits unrestricted use, distribution, and reproduction in any medium, provided the original work is properly cited.

Despite a pivotal role in salivary gland development, homeostasis, and disease, the role of salivary gland mesenchyme is not well understood. In this study, we used the *Colla1-GFP* mouse model to characterize the salivary gland mesenchyme *in vitro* and *in vivo*. The *Colla1-GFP* transgene was exclusively expressed in the salivary gland mesenchyme. *Ex vivo* culture of mixed salivary gland cells in DMEM plus serum medium allowed long-term expansion of salivary gland epithelial and mesenchymal cells. The role of TGF- $\beta$ 1 in salivary gland development and disease is complex. Therefore, we used this *in vitro* culture system to study the effects of TGF- $\beta$ 1 on salivary gland cell differentiation. TGF- $\beta$ 1 induced the expression of collagen, and inhibited the formation of acini-like structures in close proximity to mesenchymal cells, which adapted a fibroblastic phenotype. In contrast, TGF- $\beta$ 1 inhibition increased acini genes and fibroblast growth factors (*Fgf-7* and *Fgf-10*), decreased collagen and induced formation of larger, mature acini-like structures. Thus, inhibition of TGF- $\beta$  signaling may be beneficial for salivary gland differentiation; however, due to differential effects of TGF- $\beta$ 1 in salivary gland epithelial versus mesenchymal cells, selective inhibition is desirable. In conclusion, this mixed salivary gland cell culture system can be used to study epithelial-mesenchymal interactions and the effects of differentiating inducers and inhibitors.

## 1. Introduction

The mesenchymal component of salivary glands plays a pivotal role during development of the salivary gland tissue for induction of epithelial differentiation and branching [1–9]. However, the role of the mesenchymal cells in homeostasis of the adult salivary gland and during repair following injury is understudied. Many salivary gland diseases, if not all, involve and affect the mesenchymal component of the salivary glands, particularly diseases that result in fibrosis of

the salivary gland tissue such as radiation-induced damage, Graft-versus-host disease (GVHD), Sjogren's syndrome, and aging [10–14]. In addition, certain salivary gland tumors originate from or involve the mesenchyme [15, 16]. Nonetheless, little attention has been paid in characterizing the salivary gland mesenchymal cells and in developing *in vitro* systems to model the epithelial-mesenchymal interaction during adult homeostasis and disease/injury of the salivary gland tissue.

We analyzed a transgenic mouse expressing GFP driven by the procollagen promoter (*Colla1-GFP*) to identify and

characterize the mesenchymal cells in the salivary gland tissue. Histological analysis of the salivary glands revealed that only mesenchymal cells of the salivary gland tissue expressed the *GFP* transgene. We tested different culture conditions to *ex vivo* expand mixed cultures of salivary gland mesenchymal and epithelial cells. We determined that medium containing DMEM +10% serum allowed *in vitro* long-term expansion of a mixed culture containing both mesenchymal and epithelial cells. Upon *in vitro* induction on matrigel, this mixed culture differentiated into acini-like structures surrounded by GFP-positive mesenchymal cells.

TGF- $\beta$ 1 signaling is important for development and maintenance of salivary gland tissue but its differential effects on salivary gland epithelium versus mesenchyme have yet not been dissected apart [17–24]. Therefore, we tested the effects of TGF- $\beta$ 1 induction and its inhibition in our culture system. TGF- $\beta$ 1 induction resulted in elongation of GFP-positive mesenchymal cells, increased collagen production and inhibition of acini-like structure formation. In contrast, inhibition of TGF- $\beta$ 1 resulted in decreased collagen production, increased expression of the mesenchymal fibroblast growth factors, *Fgf-7* and *Fgf-10*, increased expression of mature acini markers, and formation of larger and more mature acini-like structures.

This new *in vitro* culture system can be used to expand salivary gland mesenchymal and epithelial cells for tissue regeneration and also to *in vitro* study the role of mesenchymal cells in salivary gland differentiation and alterations of the mesenchymal-epithelial interactions in disease.

## 2. Materials and Methods

**2.1. Isolation of Submandibular Salivary Gland Cells.** *Colla1-GFP* mice were a kind donation from Dr. Jeremy Duffield [25, 26]. Submandibular salivary gland (SMG) tissues were dissected (one gland per mouse) from 3-month-old *Colla1-GFP* mice ( $n = 3$  different preparations) in accordance with approved Institutional Animal Care and Use Committee (IACUC) guidelines, University of Washington. The SMG was separated from the cervical fascia and connective tissue, then gently isolated and kept in phosphate buffer saline (PBS) (Corning Cellgro). The tissues were washed with PBS, mechanically minced with a pair of curved scissors, and enzymatically dissociated with a 1.2 units/mL dispase II, 2 mg/mL collagenase type IV (Worthington) supplemented with 2 mM  $\text{CaCl}_2$  in PBS for 45 min at 37°C. The digested tissues were pipetted up and down several times every 15 min to break up clumps and release mononuclear cells. Subsequently, an equal volume of Dulbecco's modification of eagle's medium (DMEM) with 4.5 g/L glucose, L-glutamine, and sodium pyruvate (Cellgro) was added to the digest prior to filtering through 70 mm nylon cell strainers (BD Falcon) and then centrifuging at 300 g for 10 min at room temperature. The mononuclear cells were then resuspended in two types of growth media described below, and single cell suspensions were initially plated at 50,000 cells/cm<sup>2</sup> on plastic tissue culture dishes (BD Biosciences).

**2.2. Culture of Submandibular Salivary Gland Cells.** Cells (50,000 cells/cm<sup>2</sup>) were cultured at 37°C under 5% CO<sub>2</sub> in two kinds of culture media to determine their difference in cell growth, DMEM medium plus 10% heat-inactivated fetal calf serum (HyClone), 100 units/mL penicillin with 100 mg/mL streptomycin (HyClone), and N2 medium containing DMEM, penicillin, streptomycin, 20 ng/mL EGF (Sigma), 20 ng/mL bFGF (Shenandoah biotechnology), 1/100 N2 supplement (Gibco, Invitrogen), 10  $\mu$ g/mL insulin-transferrin-selenium (ITS) (Cellgro), and 1  $\mu$ M dexamethasone (Sigma). Fresh medium was added or changed every three days. Once adherent cells were more than 70% confluent, they were detached with 0.25% trypsin-EDTA (Cellgro) and replated at a 1 : 4 dilution under the same culture condition with fresh media. For cells cultured in N2 medium, since they formed spheres, before trypsinization, spheres were collected and then mixed with trypsinized cells before replating in the same condition.

**2.3. In Vitro Differentiation of Submandibular Salivary Gland Cells on Matrigel.** Mixed SMG cells (line 1; passage 9;  $5 \times 10^4$  cells per well) were seeded in either noncoated cells or matrigel-coated plastic surfaces as undifferentiated or differentiated cells, respectively, with 300  $\mu$ L of additional DMEM media plus serum. Growth factor-reduced matrigel (20 mg/mL; BD Biosciences) was thawed on ice and diluted in PBS at a final concentration of 2 mg/mL. To form three-dimensional matrix in culture dishes, 150  $\mu$ L of matrigel was added to 48-well tissue culture plate (0.75 cm<sup>2</sup> per well), incubated at 37°C for 1 hour, and the matrigel excess was removed before cell seeding. Culture media were changed every three days. For differentiation, mixed SMG cells cultured on matrigel were divided into three treatment groups: (1) matrigel alone (control group), (2) transforming growth factor-beta1 (TGF- $\beta$ 1; cell signaling; 10 ng/mL), and (3) TGF- $\beta$ 1 plus TGF- $\beta$  receptor 1 inhibitor (SB525334; Selleck Chemicals; 1  $\mu$ M) (TGF- $\beta$ 1 + SB525334). At day 3 and 5 of differentiation, both undifferentiated and differentiated cells were fixed with 4% formaldehyde in PBS for 30 min and washed with three times of PBS to preserve GFP expression. The stained cells were determined for acini-like structure formation and further stained for specific salivary gland epithelial and mesenchymal markers.

**2.4. RT-PCR and Q-RT-PCR Analyses.** Undifferentiated and differentiated mixed SMG cells were extracted for total RNA by using the total RNA kit (Omega Bio-tek) according to the manufacturer's protocol. Quantity and purity of RNA was determined by 260/280 nm absorbance. First-strand cDNA was synthesized from 1  $\mu$ g of RNA using the high capacity cDNA synthesis kit from Applied Biosystems per manufacturer's protocols using a randomized primer. RT-PCR and Q-RT-PCR mouse-specific primers were included in Table 1. For RT-PCR, cDNA of undifferentiated cells cultured in different passages (20 ng) was diluted in a final volume of 20  $\mu$ L per reaction using the Immomix PCR Mastermix from Bioline. PCR was performed using the following thermal cycling conditions; 95°C 7 min for initial activation followed



TABLE 1: Mouse-specific primer sequences.

Gene	Forward primer (5' → 3')	Reverse primer (5' → 3')	GenBank accession number
<i>Gapdh</i> (R)	CTCGTCCCGTAGACAAAATGG	CGTCTCTGGAAGATGGTG	NM_008084
<i>Gapdh</i> (Q)	GGGAAGCCCATCACCATCT	GCCTCACCCCATTTGATGTT	NM_008084
<i>Amylase-1(Amy-1)</i> (B)	GGTGCAACAATGTTGGTGTC	ACTGCTTTGTCCAGCTTGAG	NM_007446
<i>Aqp-5</i> (B)	CGACCGTGTGGCTGTGGTCA	GTGCCGGTCAGTGTGCCGTC	NM_009701
<i>Collagen type I</i> (B)	ACGGCTGCACGAGTCACAC	GGCAGGCGGGAGGTCTT	NM_007742
<i>Fgf-7</i> (R)	ACTGTTCCAGCCCCGAGCGA	TTCCCCCTCCGCTGTGTGTCCA	NM_008008
<i>Fgf-7</i> (Q)	GTCCGGAGCAAACGGCTACGA	TGTGTCGCTCGGGGCTGGAA	NM_008008
<i>Fgf-10</i> (R)	CGCAGAGGGGCGCAGATGTC	GCCTGTCCTCGCTCCGTCCT	NM_008002
<i>Fgf-10</i> (Q)	TGGTGTACAGGAGGCCACCAA	CGCACATGCCTTCCCGCACT	NM_008002
<i>Pdgfr-α</i> (R)	TTTGTGCCTCTCGGGATGA	TGACGGGCAGCACATTCA	NM_011058
<i>Occludin</i> (Q)	AGACCCAAGAGCAGCCAAAG	GGAAGCGATGAAGCAGAAGG	NM008756
<i>Tgf-β1</i> (Q)	CTACTATGCTAAAGAGGTCACC	TTTCTCATAGATGGCGTTGTTGC	NM_011577
<i>Tgf-β1</i> (Q)	GGAAATTGCTCGACGCTGTT	TTCTCATTTCTTCAACCGATGGA	NM_009370
<i>ZO-1</i> (Q)	CGAGGCATCATCCCAAATAAGAAC	TCCAGAAGTCTGCCCGATCAC	NM_009386

Note: (R): primer sequences used for RT-PCR; (Q): primer sequences used for Q-RT-PCR; (B): primer sequences used for both RT-PCR and Q-RT-PCR.

TABLE 2: Antibody used for immunohistochemical staining.

Marker	Antibody	Species	Dilution	Company
AMY-1	Polyclonal	Rabbit	1:50	Thermo Scientific
AQP-5	Polyclonal	Rabbit	1:50	Calbiochem
CD44-PE	Monoclonal	Rat	1:400	eBioscience
Collagen type I	Polyclonal	Rabbit	1:400	Abcam
E-cad-biotin	Monoclonal	Rat	1:400	eBioscience
LAMP-1	Monoclonal	Rat	1:100	Developmental Hybridoma Bank
S100	Polyclonal	Rabbit	1:400	Dako
SMA-Cy3	Monoclonal	Mouse	1:400	Sigma
TGF-β1	Polyclonal	Rabbit	1:100	Abcam
TGF-βR1	Polyclonal	Rabbit	1:100	Millipore
TGF-βR2	Polyclonal	Rabbit	1:50	Millipore
vWF	Polyclonal	Rabbit	1:100	Dako

by 95°C/30 s; 57°C/30 s; 72°C/45 s, for 35 cycles, with a final 5-min extension at 72°C. Glyceraldehyde-3-phosphate dehydrogenase (*Gapdh*) was utilized as control housekeeping gene. RNA extracted from mouse submandibular salivary gland (SMG) was used as positive controls while negative controls lacked cDNA. For Q-RT-PCR, cDNA of undifferentiated cells cultured in different growth media and differentiated cells (10 ng) was prepared using the Maxima SYBR Green/ROX qPCR master mix (Thermo Scientific). Reactions were processed by the ABI 7900HT PCR system with the following parameters: 50°C/2 min and 95°C/10 min, followed by 40 cycles of 95°C/15 s and 60°C/1 min. Results were analyzed using SDS 2.3 software, and relative expression was calculated using the comparative Ct method. Each sample was run in triplicate reactions for each gene.

**2.5. Histology and Staining of Submandibular Salivary Gland Tissues.** Submandibular salivary glands (SMGs) were isolated from 3-month-old *Colla1-GFP* mice ( $n = 3$ ) and removed surrounding connective tissues. To preserve GFP,

*Colla1-GFP* derived SMG was fixed with 4% formaldehyde/PBS for 2 h at RT and washed. The first wash was 30 min followed by 20-min and 10-min washes, respectively. After washing, the fixed SMG was immersed through a gradient of sucrose solutions (10% for 20 min, 20% for 20 min, and 30% for overnight) at 4°C to preserve tissue morphology before embedding in OCT media (VWR) and frozen with liquid nitrogen cooled isobutane. The frozen SMG tissues were cut into 10 μm thickness to get a good morphology of tissue section. Fixed sections were rehydrated and permeabilized with 1% BSA in 0.1% Triton X-100 (Sigma)/PBS for 10 min. Then, sections were blocked with 10% normal goat serum for 1 h at RT and incubated overnight at 4°C with primary antibodies listed in Table 2, following three wash steps. Stained sections were subsequently incubated with goat-derived Alexa 594-conjugated secondary antibody (Invitrogen) at 1:1000 dilutions for 1 h at RT, following three times of washing. The tissues were stained with 4', 6-diamine-2-phenylindol (DAPI) (Life Technologies) at 1:1000 to visualize the nuclei.



**2.6. Staining of Submandibular Salivary Gland Cells.** For immunocytochemistry, undifferentiated and differentiated cells were fixed with 4% formaldehyde in PBS for 30 min and washed three times of PBS. Fixed cells were permeabilized with 1% BSA in 0.1% Triton-X 100/PBS for 10 min and blocked nonspecific binding sites with 10% goat normal serum (Vector Burlingame, CA) for 1 h. All primary antibodies listed in Table 2 were used and incubated overnight at 4°C. Stained cells were incubated with goat-derived Alexa 594-conjugated secondary antibodies (Invitrogen) which were diluted at 1:1000 and incubated for 1 h. Cells were stained with DAPI at 1:1000 to visualize the nuclei. All antibodies were diluted in 1% BSA in 0.1% Triton-X 100/PBS. IgG isotype from the species made for the primary antibody (0.1 µg/mL) (Vector Burlingame, CA) was used as negative control for all staining. All immunofluorescence images described in this manuscript was detected using either a Zeiss Axiovert 200 fluorescent microscope (Thornwood, NY) or a Nikon A1R Confocal microscope. Photomicrographs were taken with an onboard monochrome AxioCam MRm camera and colored using Adobe Photoshop (San Jose, CA). Background was reduced using brightness and contrast adjustments, and color balance was performed to enhance colors. All the modifications were applied to the whole image using Adobe Photoshop.

**2.7. Statistical Analysis.** Data of Q-RT-PCR analyses were represented as  $\pm$  the standard error of the mean (SEM) of results from three separated experiments. The data were analyzed by Student's *t*-test where \*\*\**P* value  $\leq$  0.001, \*\**P* value  $\leq$  0.005, or \**P* value  $\leq$  0.05 represented significant differences between different culture media or treatments.

### 3. Results

**3.1. The *Colla1*-GFP Transgenic Mouse Selectively Identifies Mesenchymal Cells in the Salivary Glands.** In this study, we analyzed GFP expression in the submandibular salivary glands of *Colla1*-GFP transgenic mice. The *Colla1*-GFP mice express enhanced green fluorescent protein gene under the control of the procollagen, type 1, alpha 1 (*Colla1*) promoter. We hypothesized that salivary gland mesenchymal cells, but not epithelial cells, express *Collagen type I (Colla1)* and drive the expression of GFP, resulting in labeled mesenchymal cells by green fluorescence. The histological analysis demonstrated that salivary gland mesenchymal stroma was GFP-positive whereas salivary gland parenchyma or epithelium was GFP-negative (Figure 1). To confirm the specificity of the *Colla1*-GFP mouse model and distinguish differences between salivary gland epithelium and mesenchyme, we stained for markers specific of salivary gland epithelium, CD44, E-cadherin (E-cad), amylase (AMY-1), aquaporin-5, and LAMP-1. CD44 is a cell surface glycoprotein found on basal epithelial cells including salivary gland epithelium [27, 28]. CD44 staining was positive in basal and lateral membranes of salivary gland acini (AC) but not in ductal epithelium (DE) and mesenchyme (Figures 1(a) and 1(b)). E-cadherin (epithelial-calcium-dependent adhesion or E-cad) is a transmembrane protein which is crucial for cell-cell

interaction in organ development including salivary gland formation, and expressed by salivary gland epithelium [29]. E-cadherin staining was positive for both salivary gland epithelial cells of acini and ducts (D) in particular at acinar cell-ductal cell contacts but not mesenchyme (Figures 1(c) and 1(d)). Salivary amylase catalyses the breakdown of starch into sugars and is found in the granular convoluted tubular cells and to a lesser extent in the acinar cells of submandibular gland (Figures 1(e) and 1(f)) [30]. Aquaporin 5 is important for fluid transport and saliva secretion and is found in luminal, lateral, and basal membrane of acinar cells (Figures 1(g) and 1(h)) [31]. LAMP-1 is a lysosome-associated protein found in the ductal and acinar cells in salivary gland (Figures 1(i) and 1(j)) [32]. Smooth muscle actin (SMA) staining for myoepithelial cells [29] exhibited no colocalization between SMA and GFP found in mesenchymal cells, illustrating a differential staining pattern between mesenchymal and myoepithelial cells in normal salivary glands (Figures 2(a) and 2(b)). Additionally, staining for collagen type I mostly colocalized with GFP-positive mesenchymal cells, confirming the specificity of the *Colla1*-GFP mouse model. As expected, we also observed positive collagen type I staining in salivary gland extracellular matrices labeling the basement membrane which was not positive for GFP as it was not cytoplasmic but extracellular collagen (Figures 2(c) and 2(d)).

**3.2. Mixed Salivary Gland Cells Cultured in Different Media Exhibited Differential Growth of Salivary Gland Epithelial and Mesenchymal Cells.** To select a culture condition system capable of promoting proliferation of mixed cell populations containing salivary gland epithelium and mesenchyme, we used two different kinds of media to culture mixed salivary gland cells, N2 medium and DMEM plus 10% serum. N2 medium contains DMEM supplemented with EGF, bFGF, N2, and ITS and has been used as growth and differentiation media for salivary gland stem cells [33]. DMEM plus 10% serum has previously been used as medium to promote salivary gland epithelial and mesenchymal cell growth [34, 35]. After 2 weeks in culture (cell passage 1), in N2 medium we observed sphere formation combined with monolayer of polyhedral- and spindle-shaped cells (Figure 3(a), arrowheads). The monolayer cells were mainly negative for GFP (Figure 3(b)). Most of the spheres formed were negative for GFP but some of them were also GFP-positive (Figure 3(c), arrowheads). This indicates that N2 medium induces both salivary gland epithelium and mesenchyme to form spheres, and a majority of cells proliferating in N2 medium were epithelial cells. However, mixed salivary gland cells in this N2 medium failed to proliferate beyond 2 weeks of culture and were not able to survive. In contrast, mixed cells cultured in DMEM plus serum did not form spheres but grew as polyhedral-shaped or round cells on top of spindle-shaped monolayer cells (Figure 3(d)). The major cell population was spindle-shaped cells expressing GFP (Figures 3(e) and 3(f)). This cell mixture was able to proliferate and grow beyond passage 10 (2 month in culture). Interestingly, after several cell passages, both spindle-shaped and polyhedral-shaped cells

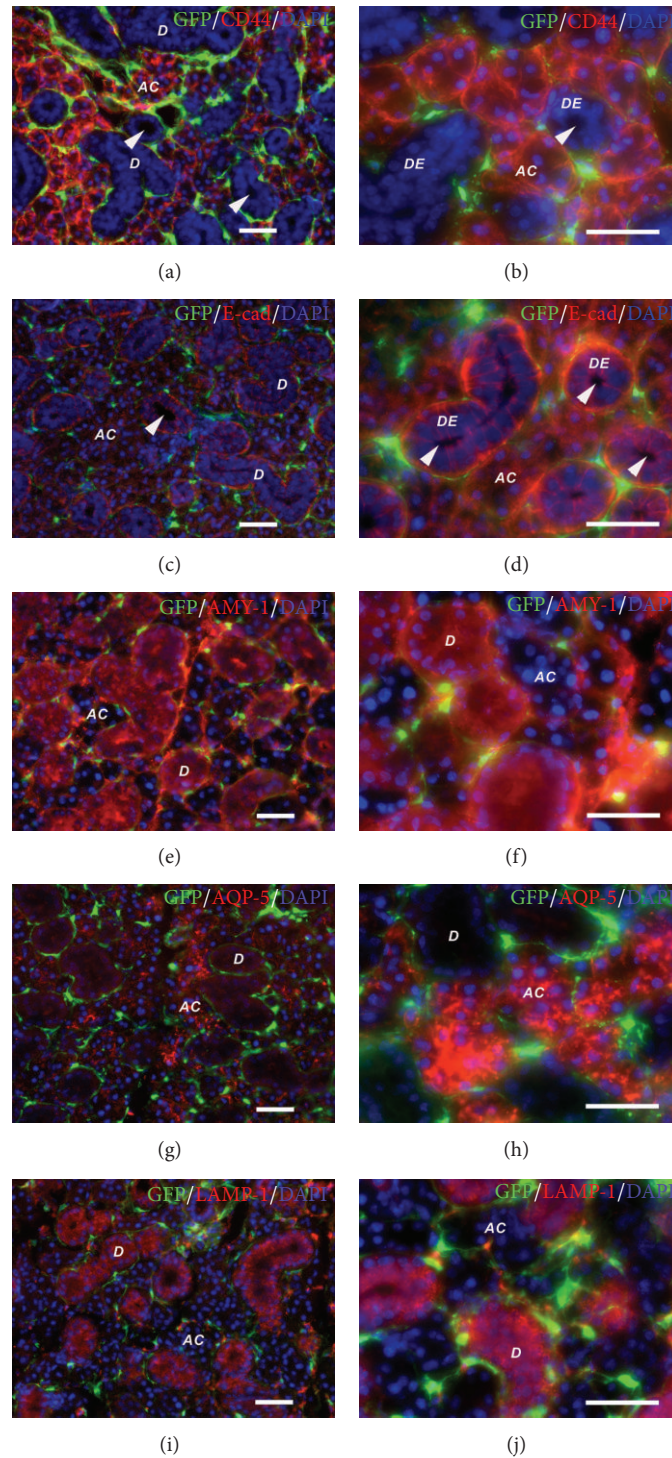


FIGURE 1: Histology of *Colla1*-GFP derived submandibular salivary gland demonstrates salivary gland epithelial markers. The sections showed that a majority of cells, namely, parenchymal cells in salivary gland tissues were GFP-negative cells, representing salivary gland epithelium (acini and ducts). GFP-positive cells (in green) were anatomically localized in the position of salivary gland mesenchyme and identified as supporting or stromal cells surrounding salivary gland acini or ducts. Salivary gland ducts (D) were anatomically identified as structures with lumens (indicated by arrowheads). (a)–(j), CD44, E-cadherin (E-cad), amylase-1 (AMY-1), aquaporin-5 (AQP-5), and lysosomal-associated membrane protein-1 (LAMP-1) (in red) stained specifically salivary gland epithelium but not mesenchyme. Salivary gland acini (AC) but not salivary gland ductal epithelium (DE) was positive for CD44 (a and b) whereas both salivary gland acini and ductal epithelium were positive for E-cad (c and d). AMY-1 staining was positive in salivary gland acini and particularly strongly positive in ductal epithelium (e and f). Apical and lateral membranes of salivary gland acini were strongly positive for AQP-5 (g and h). LAMP-1 staining was strongly positive in salivary gland ductal epithelium (i and j). Scale bars = 100  $\mu$ m.

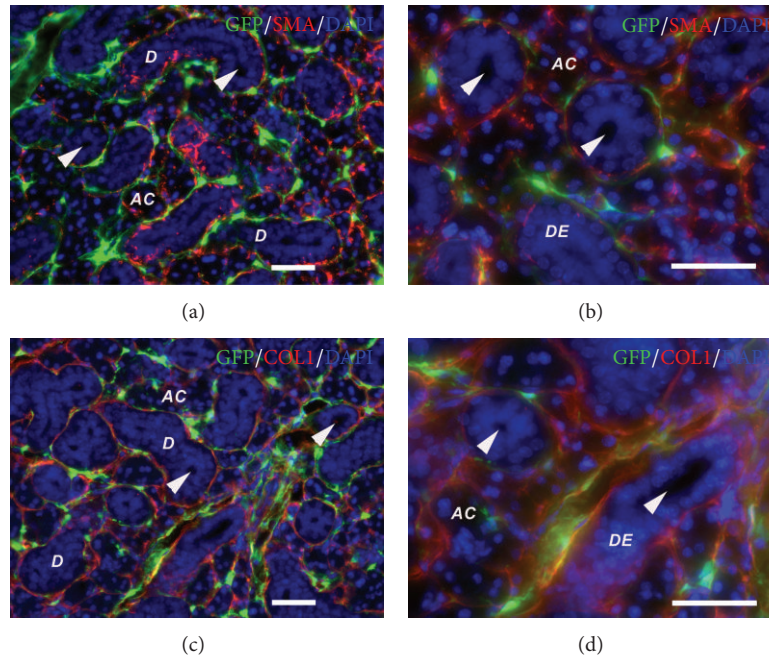


FIGURE 2: Histology of *Col1a1*-GFP derived submandibular salivary gland demonstrates salivary gland mesenchymal markers. (a) and (b), smooth muscle actin (SMA) (in red) staining for myoepithelial cells surrounding acini and ductal structures demonstrated that SMA-positive cells were located closely to, but did not colocalized with, GFP-positive cells. (c) and (d), collagen type I (in red) stained the extracellular matrix in salivary glands, and also colocalized with GFP-positive cells, confirming that GFP expression was driven by the procollagen type I promoter. AC = salivary gland acini, D = salivary gland duct, DE = ductal epithelium. Arrowheads indicate salivary gland ducts (D) with lumens. Scale bars = 100  $\mu$ m.

formed clusters of monolayer cells. The former showed cells that were GFP-positive while the latter were GFP-negative. Thus, the DMEM plus serum medium effectively enhanced the proliferation of both salivary gland epithelial and mesenchymal cells even in late passages. To confirm the presence of epithelial and mesenchymal cells in our cultures, Q-RT-PCR was performed to compare the level of salivary gland epithelial and mesenchymal gene expression between cells cultured in N2 versus DMEM media (Figures 3(g)–3(m)). As expected, mixed cells cultured in N2 medium significantly upregulated all salivary gland epithelial genes, *Amylase-1*, *Aqp-5*, *ZO-1*, *Occludin* ( $P \leq 0.005$ ), and downregulated all salivary gland mesenchymal genes, *Fgf-7* ( $P \leq 0.005$ ), *Fgf-10* ( $P \leq 0.05$ ), and *Collagen type I* ( $P \leq 0.05$ ). In contrast, DMEM plus serum seems to support salivary gland mesenchymal cell growth as evidence by increased gene expression levels of mesenchymal genes. Based on the culture morphological analysis and gene expression analysis the N2 medium enhanced more growth of salivary gland epithelium than mesenchyme but was only able to sustain these cells for a short period whereas the DMEM plus serum effectively promoted the proliferation of both salivary gland epithelium and mesenchyme in long-term culture. Therefore, we selected to use DMEM plus serum as the expanding culture medium for all the further experiments described herein.

### 3.3. DMEM Plus Serum Medium Enhanced In Vitro Long Term Proliferation and Maintenance of Salivary Gland Mesenchymal and Epithelial Cells. Mixed salivary gland cells

cultured in DMEM plus serum medium proliferated for at least 10 passages (approximately 2 months in culture) without alterations in morphology and proliferation rate. In each passage, the presence of GFP-positive cells and GFP-negative cells was monitored. Two cell types were consistently observed in each passage: a majority of spindle-shaped cells expressing GFP and GFP-negative polyhedral-shaped cells, representing salivary gland mesenchymal and epithelial cells, respectively (Figures 4(a)–4(e)). In early passage we detected several cell types in addition to GFP+ mesenchymal cells and epithelial cells. von Willebrand Factor (vWF) is expressed by microvascular endothelial cells of multiple tissues, including the salivary gland [36]. We detected vWF+ endothelial cells in early and late cultures (Figures 4(a) and 4(b)). As shown in Figures 2(a) and 2(b), SMA is expressed by myoepithelial cells in the salivary gland tissue. We detected SMA+ cells in early and late cultures that were GFP negative (Figures 4(c) and 4(d)). Interestingly, we observed that some GFP+ cells are also SMA+ in late culture suggesting that some GFP+ mesenchymal cells can upregulate SMA expression (Figure 4(d)). S100 is another marker expressed by myoepithelial cells [37]. We detected S100+ cells in early and late cultures (Figures 4(e) and 4(f)). Interestingly, some GFP+ cells costained positive for S100 (Figure 4(f)). Epithelial cells expressed CD44 in early and late cultures (Figures 4(g) and 4(h)). However, we also observed that some GFP+ cells coexpressed CD44 in late cultures (Figure 4(h)). Epithelial cells expressed amylase (AMY-1) in early and late cultures (Figures 4(i) and 4(j)). Epithelial cells in late cultures also expressed E-cad,



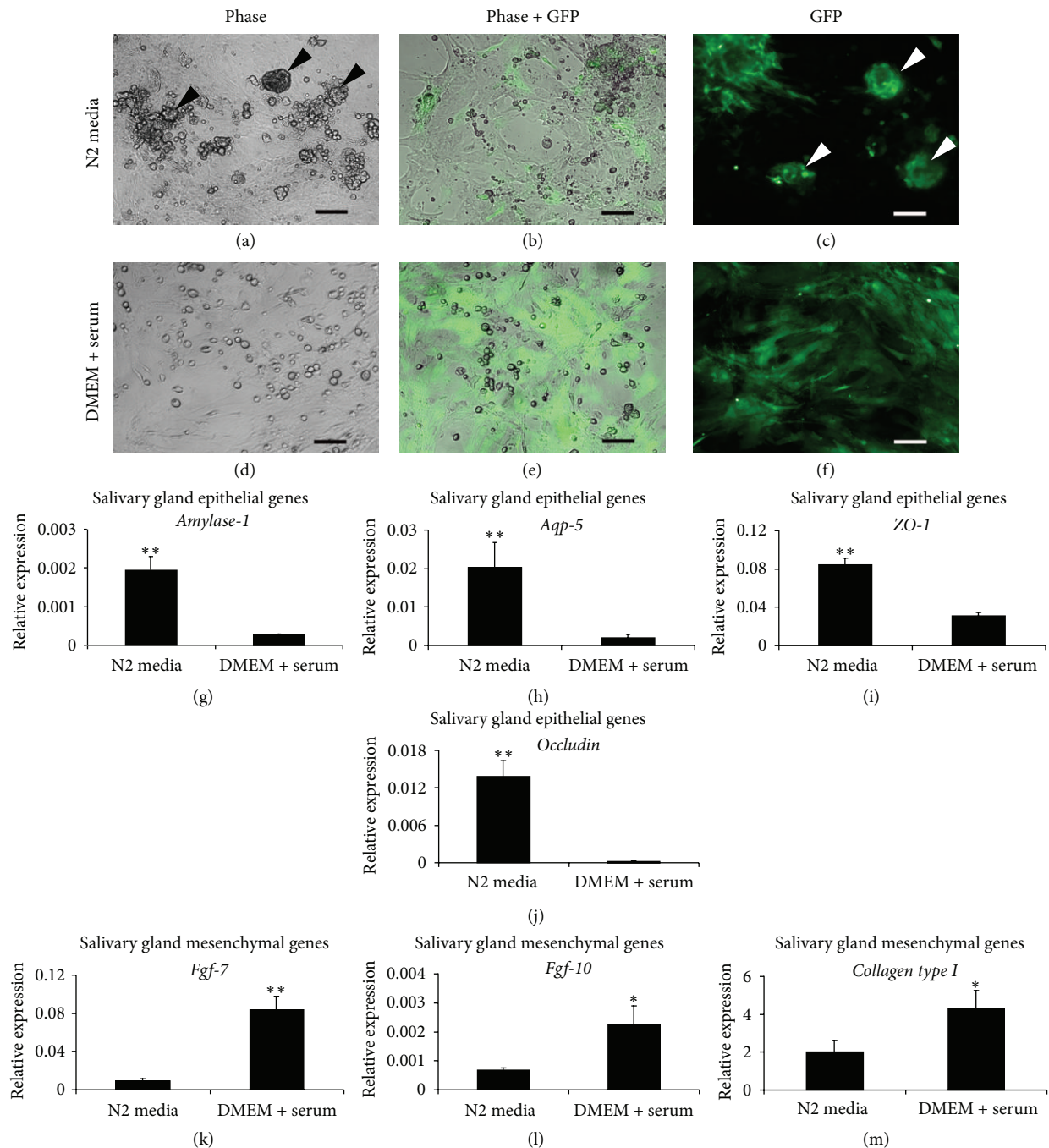


FIGURE 3: *In vitro* culture of *Col1a1*-GFP derived submandibular salivary gland cells. Mixed salivary gland epithelial and mesenchymal cells (passage 1, for 2 weeks) exhibited different growth pattern and morphology when cultured in N2 media versus DMEM plus serum medium. (a)–(c) Mixed salivary gland cells were cultured in N2 media. A majority of cells grown in N2 media were polyhedral-shaped and GFP-negative, representing salivary gland epithelial cells (a and b). Some GFP+ mesenchymal cells were also found in this culture condition (b and c). N2 media enhanced sphere formation containing both salivary gland epithelial and mesenchymal cells (indicated by arrowheads) (a and c). (d)–(f) DMEM plus 10% serum promoted the growth of salivary gland mesenchymal cells which were shown as spindle-shaped and GFP-positive cells. Small round and GFP-negative cells were also observed on top of the mesenchymal or stromal monolayer, indicating the existence of salivary gland epithelial cells (d and e). (g)–(m) Quantitative specific gene expression was analyzed to confirm the presence of salivary gland epithelium and mesenchyme in both N2 and DMEM media plus serum. The expression of salivary gland epithelial genes, *Amylase-1* (g), *Aquaporin-5* (*Aqp-5*) (h), *Zonula occludens-1* (*ZO-1*) (i), and *Occludin* (j), were significantly upregulated in N2 media-cultured cells. The expression of salivary gland mesenchymal genes, *Fgf-7* (k), *Fgf-10* (l), and *Collagen type I* (m), significantly increased in cells cultured in DMEM plus serum medium. Relative expression was normalized to the expression of *Gapdh* which was used as the reference gene. Values were represented as mean  $\pm$  SEM from three independent experiments ( $n = 3$ ). Student's *t*-test was analyzed to compare between cells cultured in N2 and DMEM media plus serum, \*\* $P \leq 0.005$  and \* $P \leq 0.05$ . Scale bars = 100  $\mu$ m.



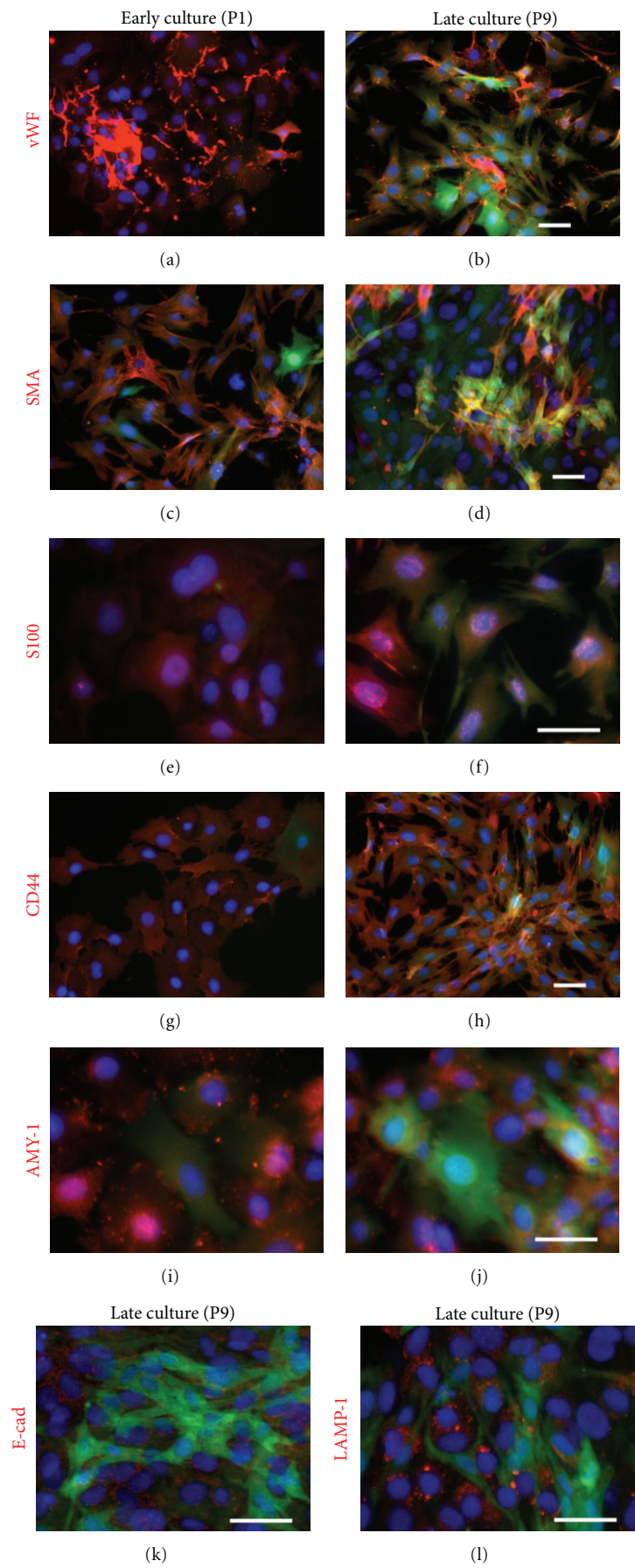


FIGURE 4: Continued.

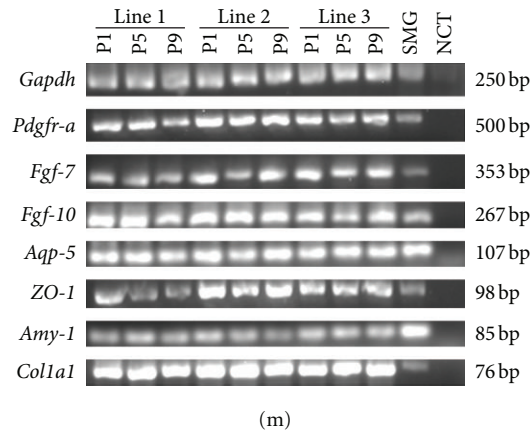


FIGURE 4: Characterization of *Colla1*-GFP derived submandibular salivary gland cells cultured in DMEM plus serum media. (a)–(l) Specific staining showed the presence of salivary gland epithelial and mesenchymal cells in DMEM media plus serum in early (passage 1; 1 week in culture) and late cultures (passage 9; 8 weeks in culture). GFP-positive spindle-shaped cells represented mesenchymal cell population. Cells in early culture were stained positively for von Willebrand Factor (vWF) (a), smooth muscle actin (SMA) (c) and S100 (e), CD44 (g), and amylase-1 (AMY-1) (i) (in red), which are markers for endothelial cells, myoepithelial cells, and salivary gland epithelial cells, respectively. In the late culture, an increased number of GFP-positive cells was observed. vWF (b), SMA (d), S100 (e), and CD44 (h) staining were seen. SMA, S100, and CD44 expression seem to be increased in the late passaged mesenchymal cells, which was illustrated by the costaining of SMA, S100, and CD44 with GFP. SMA staining demonstrated four cell populations in mixed salivary gland cultured cells, GFP+/SMA+, GFP+/SMA–, GFP–/SMA+, and GFP–/SMA– cells but a majority of cells were GFP+/SMA– cells, indicating some mesenchymal cells upregulated SMA expression in the late culture (d), compared to that in the early culture (c). AMY-1 (j), E-cadherin (E-cad) (k), and LAMP-1 (l) were specifically positive for salivary gland epithelium in red, but not mesenchymal cells. (f) RT-PCR analysis displayed a gene profile corresponding of a mixed salivary gland cell culture throughout long-term culture in DMEM plus serum medium from early through late passages. The gene expression of salivary gland epithelium, *Aqp-5* (Aquaporin-5), *ZO-1* (Zona occludens-1), and *Amy-1* (Amylase-1), as well as salivary gland mesenchyme, *Pdgfr-a*, *Fgf-7*, *Fgf-10*, *Colla1* (Collagen type I), were detected in both early and late passages, indicating the existence of salivary gland epithelial and mesenchymal in these cultures. This gene expression profile was detected in three different lines of salivary gland cells which were derived from three different *Colla1*-GFP mice. Early culture = passage 1 (P1), and late culture = passage 9 (P9). P1, 5, and 9 = passages 1, 5, and 9, respectively. Submandibular salivary gland (SMG) was used as positive control whereas no template was used as negative control (NCT). Scale bars = 100  $\mu$ m.

and lysosomal associated membrane protein (LAMP-1) [38] (Figures 4(k) and 4(l)). In addition, we examined the gene expression of salivary gland epithelium, *Aqp-5*, *ZO-1*, *Amy-1*, and mesenchyme, *Pdgfr-a*, *Fgf-7*, *Fgf-10*, *Colla1*, in cells from different passages (passages 1, 5, and 9) to confirm whether the cultured cells in the late passage still contained two cell populations. The gene profile by RT-PCR demonstrated the existence of both salivary gland epithelial and mesenchymal cells in the late passage of our culture (Figure 4(m)).

**3.4. Expression of TGF- $\beta$ 1 Ligand and Receptor in Salivary Gland Tissues and Cultured Cells.** We then examined the expression of TGF- $\beta$ 1 ligand (TGF- $\beta$ 1) and its receptors, TGF- $\beta$ 1 receptor 1 (TGF- $\beta$ R1) and receptor 2 (TGF- $\beta$ R2), in both salivary gland tissues and cultured cells. Murine submandibular salivary gland tissues showed the expression of TGF- $\beta$ 1, TGF- $\beta$ R1, and TGF- $\beta$ R2 in salivary gland epithelium, particularly in ductal epithelium (Figures 5(a)–5(f)). However, we observed very low expression of TGF- $\beta$ 1 and TGF- $\beta$ R1 in the salivary gland mesenchyme. In contrast, some mesenchymal cells (GFP)+ in the salivary gland stained positive for TGF- $\beta$ R2 (Figures 5(e) and 5(f)). As negative control, staining of salivary gland tissues with rabbit IgG control exhibited completely negative staining result used to confirm the specificity of TGF- $\beta$ 1, TGF- $\beta$ R1,

and TGF- $\beta$ R2 antibodies (Figures 5(g) and 5(h)). We then studied the protein expression of TGF- $\beta$ 1 and its receptors in early and late cultures. Salivary gland epithelial cells stained strongly positive for TGF- $\beta$ 1 and TGF- $\beta$ R1 in early cultures. Interestingly, in early cultures mesenchymal cells, which were GFP-positive, showed weak positive staining for TGF- $\beta$ 1 and its receptors (Figures 5(i), 5(k), and 5(m)). In contrast, in late cultures GFP+ mesenchymal cells stained strongly positive for TGF- $\beta$ 1 and its receptors (Figures 5(j), 5(l), and 5(n)). In particular, cultured salivary gland mesenchymal cells showed stronger TGF- $\beta$ R1 expression than that in epithelial cells (Figure 5(l)). The TGF- $\beta$ R1 antibody we used recognizes the cytoplasmic domain which can be cleaved and can translocate to the nucleus [39]. This explains why we observed mainly nuclear staining. Q-RT-PCR analysis of mixed salivary gland cells from passage 2 demonstrated that the N2 medium which contained a majority of epithelial cells showed increased levels of *Tgf-b1* and *Tgf-br1*, compared to DMEM plus serum ( $P \leq 0.05$ ) (Figures 5(o) and 5(p)).

The regulation TGF- $\beta$  signaling pathway at the receptor level is well understood. Briefly, TGF- $\beta$  ligands (TGF- $\beta$ 1, 2, 3) bind TGF- $\beta$ R2 which recruits TGF- $\beta$ R1 to form a heterotetramer (two type I and two type II receptors) [40]. The formation of this heterotetramer is needed for TGF- $\beta$  signaling. TGF- $\beta$ R2 phosphorylates TGF- $\beta$ R1, activating

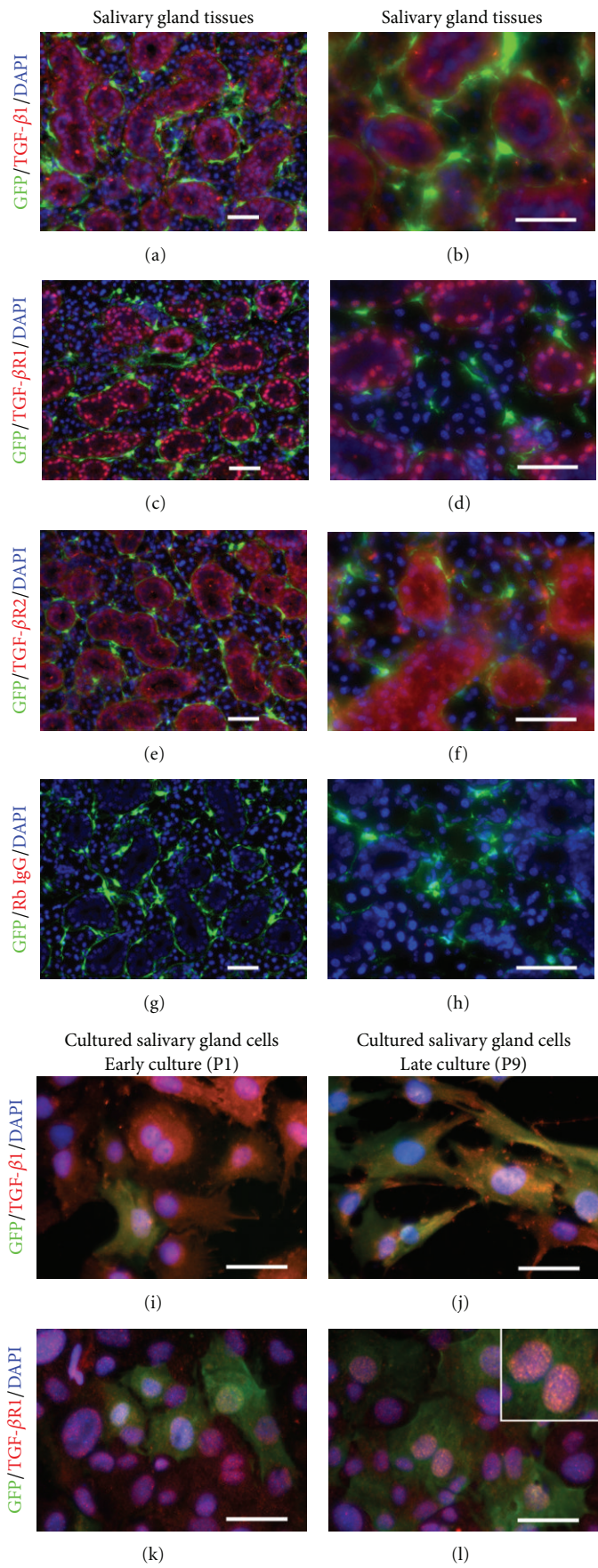


FIGURE 5: Continued.



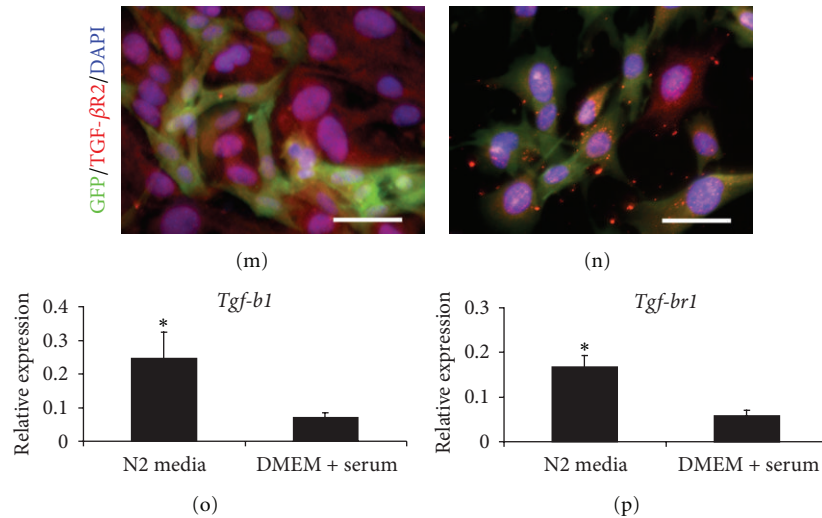


FIGURE 5: The expression of TGF- $\beta$ 1 ligand and receptors in *Coll1a1*-GFP derived submandibular salivary gland tissues and cultured cells. (a)–(h) Immunofluorescence of *Coll1a1*-GFP derived submandibular salivary gland tissues taken by Zeiss fluorescence microscope. Salivary gland epithelium, in particular ductal epithelium, strongly expressed TGF- $\beta$ 1 (in cytoplasm) (a and b), TGF- $\beta$  receptor 1 (TGF- $\beta$ R1) (in nuclei and cytoplasm) (c and d), and TGF- $\beta$  receptor 2 (TGF- $\beta$ R2) (in nuclei and cytoplasm) (in red) (e and f). GFP-positive salivary gland mesenchyme (in green) did not seem to highly express either TGF- $\beta$ 1 or TGF- $\beta$ R1, in normal salivary gland tissues. (e) and (f) Rabbit IgG control was used as negative control to confirm the specificity of TGF- $\beta$ 1, TGF- $\beta$ R1, and TGF- $\beta$ R2 antibodies. (i)–(n) Cultured salivary gland cells in DMEM plus serum medium from early (passage 1) and late (passage 9) cultures showed the different expression of TGF- $\beta$ 1, TGF- $\beta$ R1, and TGF- $\beta$ R2. In the early culture, TGF- $\beta$ 1 and TGF- $\beta$ R2 were strongly expressed in the cytoplasm of epithelial cells (i and m, resp.) whereas the strong TGF- $\beta$ R1 expression was found in cultured salivary gland epithelial cells in cytoplasmic and nuclear areas (k), but not in mesenchymal cells. In the late culture, the expression of TGF- $\beta$ 1, TGF- $\beta$ R1, and TGF- $\beta$ R2 was seen in both salivary gland epithelial and mesenchymal cells (j, l, and n). The salivary gland mesenchymal cells increased the expression of TGF- $\beta$ 1 (j), TGF- $\beta$ R1 (l, inset), and TGF- $\beta$ R2 (n) after late culture. The staining pattern of TGF- $\beta$ 1 and TGF- $\beta$ R1 in late cell passage was similar to early cell passage (j and l) whereas that of TGF- $\beta$ R2 was shown in both membrane and nuclei (n). (o) and (p) Mixed salivary gland cells cultured in N2 media which contained a majority of salivary gland epithelium showed higher levels of both *Tgf-b1* and *Tgf-br1* expression, compared to that in DMEM media plus serum. Relative expression was normalized to the expression of *Gapdh* which was used as the reference gene. Values were represented as mean  $\pm$  SEM from three independent experiments ( $n = 3$ ). Student's  $t$ -test was analyzed to compare between cells cultured in N2 and DMEM media plus serum,  $*P \leq 0.05$ . Scale bars = 100  $\mu$ m.

TGF- $\beta$ R1 kinase which mediates the Smad pathway. We observed membranous and nuclear staining of TGF- $\beta$ R1 and TGF- $\beta$ R2 on GFP+ mesenchymal cells, indicating that the TGF- $\beta$  signaling is active in cultures, especially in late cultures. To confirm the staining pattern for TGF- $\beta$  and its receptors, we performed fluorescence image analysis by confocal microscopy. Similar to the results presented in Figure 5, in the salivary gland tissue, TGF- $\beta$ 1 and TGF- $\beta$ R1 is expressed mainly by epithelial cells (Figures 6(a) and 6(b)), whereas TGF- $\beta$ R2 is expressed by epithelial cells but also strongly expressed by GFP+ mesenchymal cells (Figure 6(c), inset). In contrast, in late cultures TGF- $\beta$ 1 and its receptors are expressed by both epithelial cells and GFP+ mesenchymal cells (Figures 6(d)–6(f)), indicating an up-regulation of TGF- $\beta$ 1 and its receptors in cultured GFP+ cells, perhaps mediated by a positive feedback driven by the TGF- $\beta$ 1 produced by the epithelial cells early in culture (Figure 5(i)).

**3.5. TGF- $\beta$ R1 Inhibitor Promoted the In Vitro Formation of Acinar-Like Structures.** Mixed salivary gland cells (from passage 9) induced on matrigel differentiated into acini-like structures demonstrating that cells maintained in long-term cultures still have differentiation capacity [6, 7]. TGF- $\beta$ 1 signaling is important for salivary gland formation during

development [18, 21, 23]. To determine the effect of TGF- $\beta$ 1 signaling on *in vitro* differentiation of salivary gland cells, we compared the differentiation capacity of matrigel-induced cells exposed to TGF- $\beta$ 1 (TGF- $\beta$ 1) or TGF- $\beta$ 1 plus TGF- $\beta$ R1 inhibitor (TGF- $\beta$ 1 + SB525334). SB525334 is a potent inhibitor of TGF- $\beta$ R1 kinase activity [41, 42]. The *in vitro* differentiation was conducted at two time points between day 3 and 5 and analyzed by specific antibody staining to salivary gland epithelium (at day 5) and the gene expression of salivary gland epithelial and mesenchymal genes (at day 3 and 5). The specific staining of epithelium, CD44 (Figures 7(a)–7(c)), E-cad (Figures 7(d), 7(e) inset, 7(f)), LAMP-1 (Figures 7(g), 7(h) inset, 7(i)), amylase (Figures 7(j)–7(l)), and aquaporin 5 (Figures 7(m)–7(o)) showed that salivary gland epithelial cells plated on matrigel in all three groups were able to differentiate based on the formation of acinar-like structures. As expected, all acinar-like structures found were GFP-negative, suggesting that only salivary gland epithelial cells differentiated into acini-like structures on matrigel (Figures 7(a)–7(c)). In addition, in all the differentiation cultures on matrigel we observed areas of mesenchymal clusters and areas free of mesenchymal cells (shown as figures with empty black backgrounds in Figures 7(a)–7(c), 7(k), and 7(n) and all insets). In control (matrigel only) and



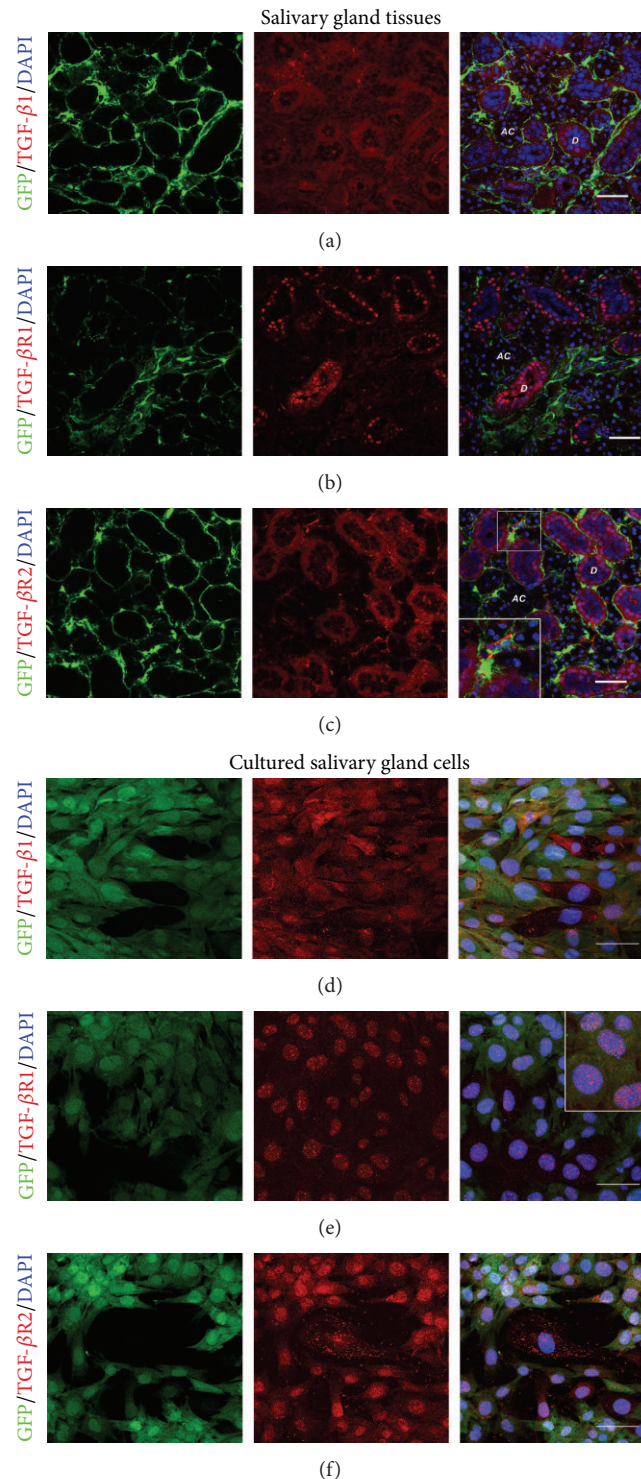


FIGURE 6: Confocal microscopy allows clear visualization of the differential protein expression of TGF-β1 ligand and receptors in *Col1a1-GFP* derived submandibular salivary gland tissues and cultured cells. (a)–(c) Salivary gland epithelium, in particular ductal epithelium, strongly expressed TGF-β1 (in cytoplasm) (a), TGF-β receptor 1 (TGF-βR1) (in nuclei and membrane) (b), and TGF-β receptor 2 (TGF-βR2) (in nuclei and membrane) (in red) (c). GFP-positive salivary gland mesenchyme (in green) did not seem to highly express either TGF-β1 or TGF-βR1 in normal salivary gland tissues. However, some GFP+ mesenchymal cells were strongly positive for membranous TGF-βR2 staining in normal salivary gland tissues (c and inset). (d)–(f) Both cultured salivary gland epithelial and mesenchymal cells in late cultures (passage 9) showed the expression of TGF-β1, TGF-βR1, TGF-βR2. The salivary gland mesenchymal cells increased the expression of TGF-β1 (d), TGF-βR1 (e, inset), and TGF-βR2 (f) after late culture. The staining pattern of TGF-β1 was seen in cytoplasm (d) whereas those of TGF-βR1 and TGF-βR2 were shown in both membrane and nuclei (e, inset, and f). AC = salivary gland acini, D = salivary gland duct. Scale bars = 50 μm.

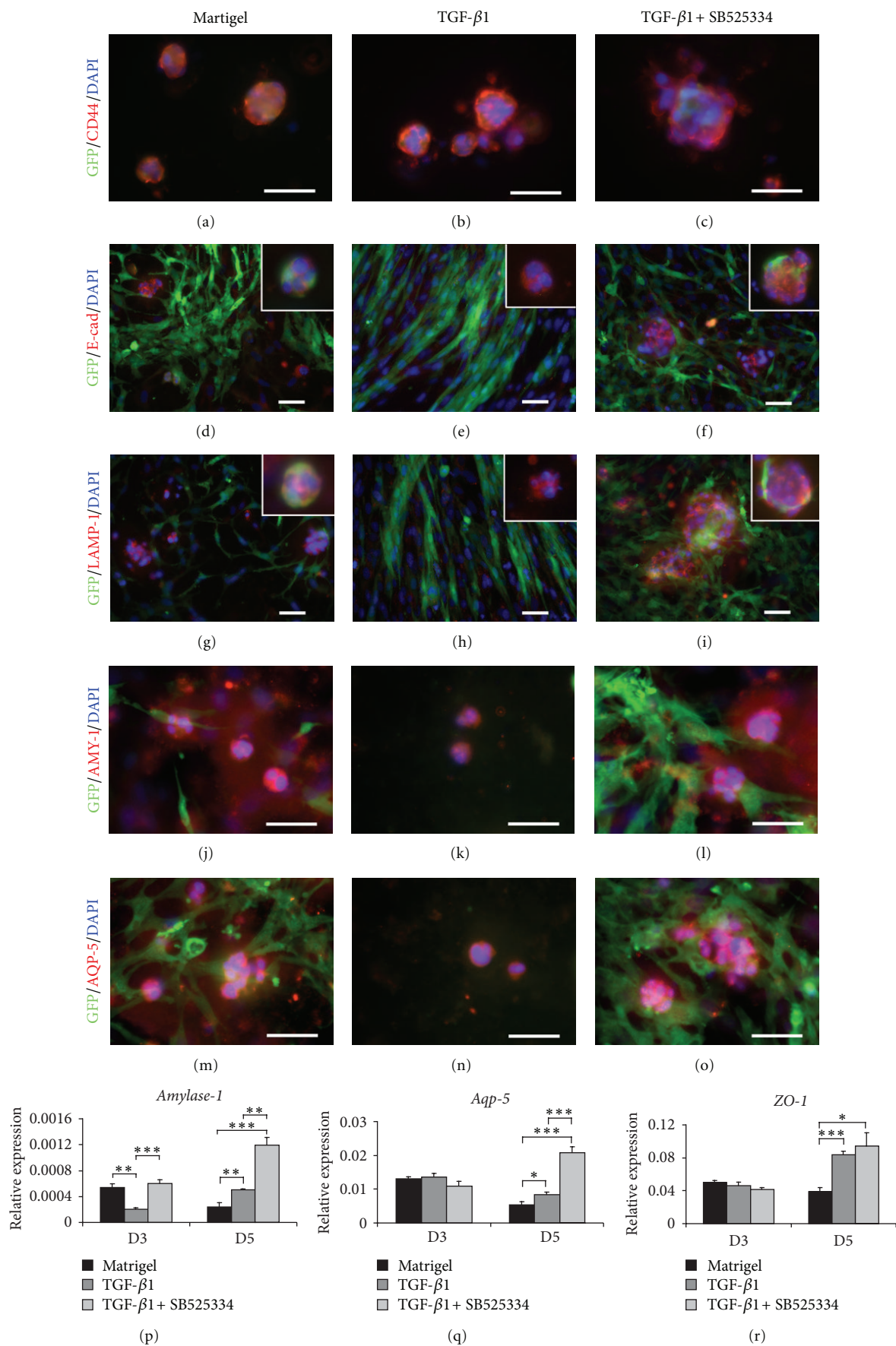


FIGURE 7: Continued.

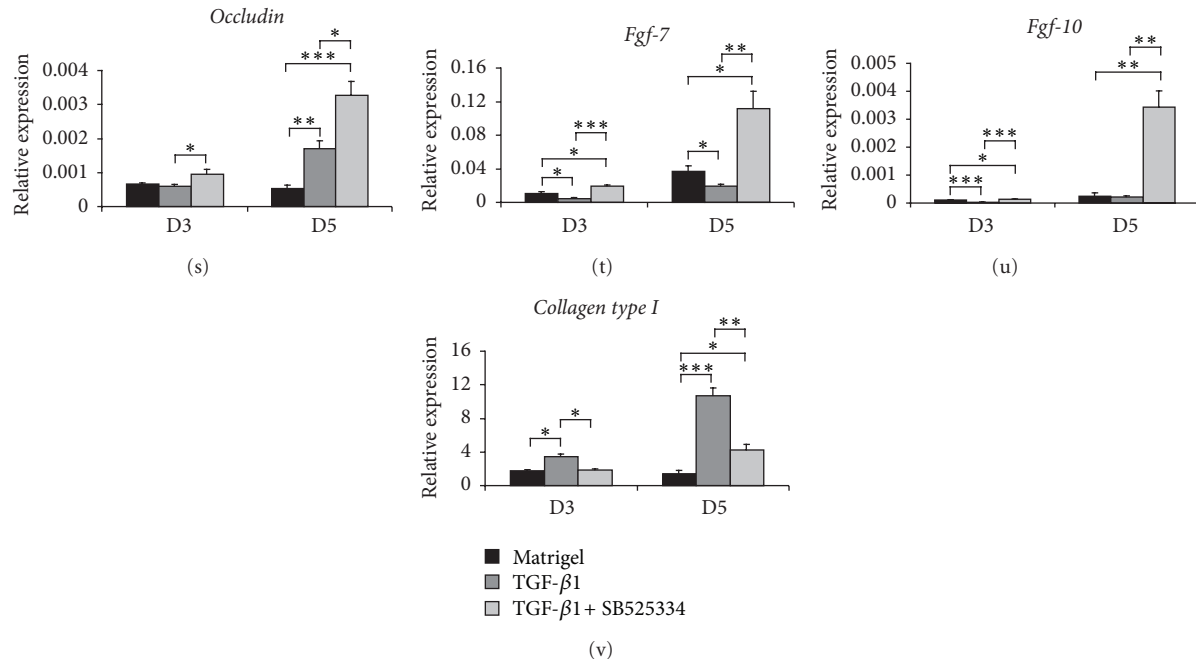


FIGURE 7: *In vitro* differentiation of *Colla1*-GFP derived submandibular salivary gland cells on matrigel treated with TGF- $\beta$ 1 or TGF- $\beta$ 1 plus TGF- $\beta$ R1 inhibitor, SB525334 (TGF- $\beta$ 1 + SB525334). Mixed cells were plated on matrigel with DMEM plus serum medium alone (left column) or supplemented with TGF- $\beta$ 1 (middle column) or TGF- $\beta$ 1 with SB525334 inhibitor (right column). Specific staining for salivary gland epithelial cells demonstrated the presence of differentiated salivary gland cells at day 5. (a)–(c) CD44 staining (in red) showed the formation of acinar-like structures (round structures with polarized nuclei) in all three groups. Large acini-like structures with branching were found in the TGF- $\beta$ 1 + SB525334 (c). (d)–(o) Salivary gland epithelium and acinar formation were identified by E-cadherin (E-cad), LAMP-1, AMY-1, and AQP-5 staining (in red). Salivary gland acini-like structures (in red) closely located to mesenchymal cells (in green) were found in the matrigel (d, g, j, and m) and TGF- $\beta$ 1 + SB525334 (f, i, l, and o) groups whereas no acinar formation was observed in close proximity of mesenchymal cells in the TGF- $\beta$ 1 group (e and h). Acinar-like structures were also found in areas free of mesenchymal cells in all three groups. Cells in the TGF- $\beta$ 1 + SB525334 (c, f, i insets, l, and o) formed larger acini-like structures than those in the matrigel alone (a, d, g insets, j, and m) and TGF- $\beta$ 1 (b, e, h insets, k, and n). Salivary gland mesenchymal cells were polarized and elongated in the TGF- $\beta$ 1 (e and h) whereas mesenchymal cells in the matrigel (d, g, and m) and TGF- $\beta$ 1 + SB525334 (f, i, l, and o) demonstrated cobblestone appearance. Some GFP-positive cells were found to integrate or locate peripherally to acini-like structures in the matrigel (a, d, and g insets) and TGF- $\beta$ 1 + SB525334 (c, f, and i insets), but not in the TGF- $\beta$ 1 (b, e, and h insets). (j)–(p) The expression of salivary gland epithelial genes, *Amylase-1*, *Aquaporin-5* (*Aqp-5*), *Zonula occludens* (*ZO-1*), *Occludin*, and salivary gland mesenchymal genes, *Fgf-7*, *Fgf-10*, and *Collagen type I*, was determined after 3- and 5-day treatments. At day 3 (D3), cells treated with TGF- $\beta$ 1 + SB525334 significantly upregulated some of salivary gland epithelial genes, *Amylase-1* and *Occludin*, and all salivary gland mesenchymal genes except *Collagen type I*, compared to cells on matrigel alone and/or cells treated with TGF- $\beta$ 1. The TGF- $\beta$ 1-treated cells significantly expressed lower level of *Amylase-1* expression (p), but higher level of *Collagen type I* (v), compared to untreated cells, and TGF- $\beta$ 1 + SB525334-treated cells. At day 5 (D5), cells treated with TGF- $\beta$ 1 + SB525334 expressed the highest levels of both salivary gland epithelial and mesenchymal genes and were significantly different compared to untreated and TGF- $\beta$ 1 treated cells. The *ZO-1* expression was comparable but insignificantly different between TGF- $\beta$ 1 and TGF- $\beta$ 1 + SB525334 treated cells (r). The expression of *Fgf-7* and *Fgf-10* was remarkably increased in the TGF- $\beta$ 1 + SB525334 group (t and u). The highest level of *Collagen type I* was observed and shown a significantly statistical difference in TGF- $\beta$ 1 treated cells at both day 3 and 5 compared to other groups (v). Relative expression was normalized to the expression of *Gapdh* which was used as the reference gene. Values were represented as mean  $\pm$  SEM from three independent experiments ( $n = 3$ ). Student's *t*-test was analyzed to compare between Matrigel (untreated; black bar), TGF- $\beta$ 1 treated (dark gray bar), and TGF- $\beta$ 1 + SB525334 treated cells (light gray bar), \*\*\*  $P \leq 0.001$ , \*\*  $P \leq 0.005$ , or \*  $P \leq 0.05$ . Scale bars = 100  $\mu$ m.

TGF- $\beta$ 1 + SB525334 cultures, abundant acinar-like structures were found in both mesenchymal rich and mesenchymal free areas whereas in TGF- $\beta$ 1 exposed cultures acinar-like structures were observed only in the mesenchymal free areas. Most of the acinar-like structures in control (matrigel only) and TGF- $\beta$ 1 + SB525334 cultures were in close proximity to mesenchymal cells (Figures 7(d), 7(g), 7(j), and 7(m) and Figures 7(f), 7(i), 7(l), and 7(o)). Moreover, the size of acinar-like structures found in the TGF- $\beta$ 1 + SB525334

group (Figures 7(c), 7(f), 7(i), 7(l), and 7(o) and insets) was remarkably larger than that in TGF- $\beta$ 1 group (Figures 7(b), 7(e), 7(k), and 7(n), and insets). Interestingly, in the control (matrigel only) (Figures 7(d), 7(j), 7(m), and 7(g), and insets) and TGF- $\beta$ 1 + SB525334 groups (Figures 7(f), 7(i), 7(l), and 7(o) and insets), we found GFP-positive cells located peripherally and closely associated with most acinar-like structures, mimicking salivary gland acini *in vivo*, but this association was not found in the TGF- $\beta$ 1 group (Figures 7(e)



and 7(h) insets). The mesenchymal cells in control (matrigel only) and TGF- $\beta$ 1 + SB525334 groups showed a cobblestone-appearance (Figures 7(d), 7(g), 7(m) and 7(f), 7(i), 7(l), 7(o)) whereas that in TGF- $\beta$ 1 showed elongation and polarization (Figures 7(e) and 7(h)). However, no difference in number of acini-like structures among three groups was found.

Q-RT-PCR analysis showed that at day 3 (Figures 7(p)–7(v)), cells in both the control (matrigel only) and TGF- $\beta$ 1 + SB525334 groups showed higher levels of salivary gland epithelial and mesenchymal genes, but lower levels of *Collagen type I*, compared to cells in TGF- $\beta$ 1. Cells in control group (matrigel only) showed significantly higher levels of *Amylase-1* ( $P \leq 0.05$ ), *Fgf-7* ( $P \leq 0.005$ ), and *Fgf-10* ( $P \leq 0.001$ ) but lower levels of *Collagen type I* ( $P \leq 0.05$ ), compared to cells in the TGF- $\beta$ 1 group. Likewise, cells in the TGF- $\beta$ 1 + SB525334 group showed significantly higher levels of *Amylase-1* ( $P \leq 0.001$ ), *Occludin* ( $P \leq 0.05$ ), *Fgf-7*, and *Fgf-10* ( $P \leq 0.001$ ) but lower *Collagen type I* ( $P \leq 0.05$ ), compared to cells in the TGF- $\beta$ 1 group. At day 3, no difference was found in salivary gland epithelial genes expressed by cells in the control (matrigel only) compared to that in the TGF- $\beta$ 1 + SB525334 group. In contrast, significantly higher levels of *Fgf-7* and *Fgf-10* ( $P \leq 0.005$ ) were expressed by cells in the TGF- $\beta$ 1 + SB525334 group compared to the control group (matrigel only).

The comparison of the acinar genes from day 3 to day 5 in the control group (matrigel only) indicates a decreasing trend which suggests that additional supplementation of differentiation factors may be needed to induce progression of differentiation on matrigel. Interestingly, at day 5, cell induced with TGF- $\beta$ 1 showed significantly higher levels of all of salivary gland epithelial genes, *Amylase-1* (5 folds,  $P \leq 0.005$ ), *Aqp-5* ( $P \leq 0.05$ ), *ZO-1* and *Occludin* (4 folds,  $P \leq 0.005$ ), and *Collagen type I* (10 folds,  $P \leq 0.001$ ), compared to the matrigel group, whereas *Fgf-7* levels were decreased ( $P \leq 0.05$ ), compared to the matrigel group. This suggested that TGF- $\beta$ 1 may be beneficial for epithelial cell differentiation but inhibited expression of mesenchymal FGFs. Conversely, cells in the TGF- $\beta$ 1 + SB525334 group significantly upregulated most of the salivary gland epithelial genes, *Amylase-1* (3 folds) and *Aqp-5* ( $P \leq 0.005$ ), *Occludin* ( $P \leq 0.05$ ), and mesenchymal genes, *Fgf-7* (10 folds) and *Fgf-10* (15 folds) ( $P \leq 0.05$ ), but downregulated *Collagen type I* (3 folds,  $P \leq 0.05$ ), when compared with cells in the TGF- $\beta$ 1 group. Interestingly, at day 5 cells treated with TGF- $\beta$ 1 + SB525334 upregulated all epithelial and mesenchymal genes including *Collagen type I* when compared with control group (matrigel only), indicating TGF- $\beta$ 1 signaling inhibition acts differentially on epithelial and mesenchymal cells.

**3.6. TGF- $\beta$ 1 Induced Expression TGF- $\beta$ 1 Ligand and Its Receptor.** TGF- $\beta$ 1 and TGF- $\beta$ R1 stainings highlighted acinar formation in all three groups (Figures 8(a), 8(c), 8(d)–8(f), 8(g), 8(i), 8(j)–8(l)). In matrigel and TGF- $\beta$ 1 + SB525334, acini-like structures were formed in both areas rich in mesenchymal cells (Figures 8(a), 8(g) and 8(c), 8(i)) and also mesenchymal free area (Figures 8(d), 8(j) and 8(f), 8(l)) whereas acini-like structures in TGF- $\beta$ 1 group were not found

in the areas rich in mesenchymal cells (Figures 8(b) and 8(h)). Larger acini-like structures with ductal-like structures were found in TGF- $\beta$ 1 + SB525334 (Figures 8(f), 8(l) arrowheads) compared to those in the TGF- $\beta$ 1 (Figures 8(e) and 8(k)) and control (matrigel only) groups (Figures 8(d) and 8(j)).

The expression of *Tgf-b1* and *Tgf-br1* was also analyzed after *in vitro* differentiation and compared between the three different groups (Figures 8(m) and 8(n)). TGF- $\beta$ 1 induced up-regulation of both *Tgf-b1* and *Tgf-br1* expression whereas inhibition of TGF- $\beta$ 1 signaling in the TGF- $\beta$ 1 + SB525334 resulted in significant downregulation of both *Tgf-b1* and *Tgf-br1* at day 3 and whereas at day 5, *Tgf-b1* was still downregulated both not its receptor, *Tgf-br1*.

## 4. Discussion

Although the epithelium of the parotid glands is ectoderm-derived whereas the epithelium of the submandibular and sublingual glands is endoderm-derived, the salivary gland mesenchyme is neural crest-derived [43]. The interactions of epithelium and mesenchyme are essential for the branching morphogenesis of the salivary gland. Molecular cues such as secretion of fibroblast growth factors (FGF-10, FGF-7) by the ectomesenchyme and expression of FGF receptors (FGFR1, FGF-R2) by the epithelium are important for the development salivary gland [5, 43–48]. Also other morphogens such as Shh and Wnt are also important for the saliva gland development [49–51]. Although the role of the mesenchyme during salivary gland development is well studied, the role of mesenchyme in adult salivary gland tissue homeostasis and its potential involvement in salivary diseases is understudied.

Therefore, we sought to better characterize the phenotype of salivary gland mesenchyme and to develop a culture system to *in vitro* study the interactions of adult salivary gland epithelial cells and mesenchymal cells. We used the transgenic *Colla1-GFP* reporter mice to identify mesenchymal cells in the salivary gland [26]. Upon histological analysis of the *Colla1-GFP* mice we can exclusively identify mesenchymal cells as GFP-positive cells in salivary glands.

*Ex vivo* cultures of the mixed salivary gland cells in N2 versus DMEM plus serum media revealed the presence of both epithelial and mesenchymal (GFP-positive) cells in culture. Cells in N2 medium stopped proliferating early in culture whereas the cells in DMEM plus serum medium continued proliferating for more than 10 passages. The levels of TGF- $\beta$ 1 expression in early cultures are higher in N2 medium which may explain why cells cultured in this medium stopped proliferating early in culture. RT-PCR and immunohistochemical analysis of the DMEM plus serum cultures at several passages revealed the presence of both epithelial and mesenchymal cells even in late cultures. Upon differentiation on matrigel the mixed culture cells were able to differentiate into mature acini-like structures.

Therefore, this culture condition allows the long-term expansion of both epithelial and mesenchymal cells which in turn can be induced to differentiate *in vitro*. This culture system offers many advantages over existing culture conditions: (1) long-term expansion of mesenchymal cells, (2) long-term



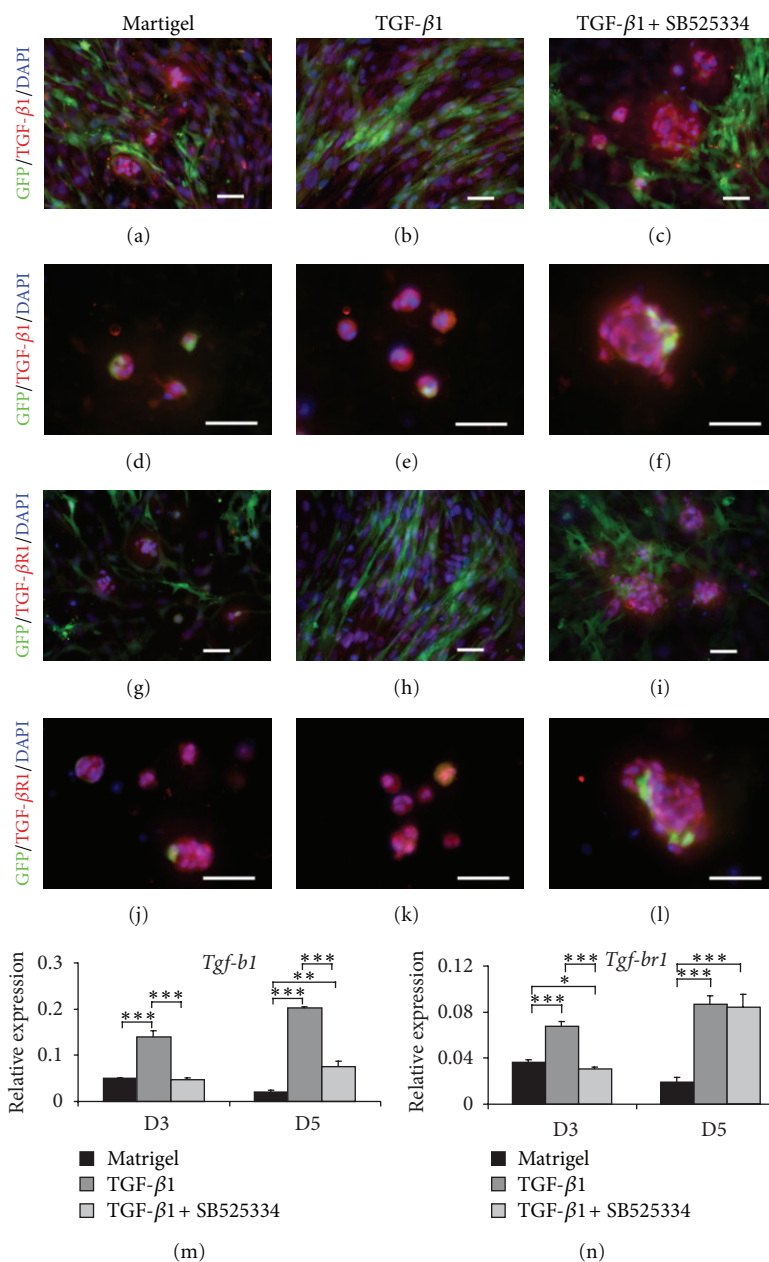


FIGURE 8: The expression of TGF- $\beta$ 1 ligand and receptor in *Col1a1*-GFP derived submandibular salivary gland cells after *in vitro* differentiation on matrigel treated with TGF- $\beta$ 1 or TGF- $\beta$ 1 and plus TGF- $\beta$ 1R inhibitor, SB525334 (TGF- $\beta$ 1 + SB525334). (a)–(f) and (g)–(l) TGF- $\beta$ 1 and TGF- $\beta$ 1R staining (in red) showed the formation of acinar-like structures, respectively. Acinar formation was observed adjacent to mesenchymal cells in the matrigel only (a and g) and TGF- $\beta$ 1 + SB525334 (c and i) groups, but not in the TGF- $\beta$ 1 (b and h) group. In the areas free of mesenchymal cells, acinar-like structures were also found in all three groups. TGF- $\beta$ 1 + SB525334 treated cells formed larger acinar-like structures (c, f, i, and l) compared to untreated (a, d, g, and j) and TGF- $\beta$ 1 treated cells (e and k). Acini-like structures in the matrigel (d and j) and TGF- $\beta$ 1 + SB525334 (f and l), but not in the TGF- $\beta$ 1 (e and k) showed GFP-positive mesenchymal cells located peripherally or adjacent to acini-like structures. Elongated and polarized salivary gland mesenchymal cells were found in the TGF- $\beta$ 1 treated group (b and h), but not in the untreated (a and g) and TGF- $\beta$ 1 + SB525334 groups (c and i). (m) and (n) The expression of TGF- $\beta$ 1 ligand (*Tgf-β1*) and receptor (*Tgf-βr1*) were also examined. The cells treated with TGF- $\beta$ 1 significantly increased the level of *Tgf-β1* and *Tgf-βr1* expression compared to untreated and TGF- $\beta$ 1 + SB525334 treated cells both day 3 (D3) and similar pattern was observed at day 5 (D5). In the control, untreated cells on matrigel, the expression levels of both *Tgf-β1* and receptor *Tgf-βr1* decreased at D5 compared to D3 but this pattern is not seen in the TGF- $\beta$ 1 and TGF- $\beta$ 1 + SB525334 groups. Relative expression was normalized to the expression of *Gapdh* which was used as the reference gene. Values were represented as mean  $\pm$  SEM from three independent experiments ( $n = 3$ ). Student's *t*-test was analyzed to compare between matrigel (untreated; black bar), TGF- $\beta$ 1 treated (dark gray bar), and TGF- $\beta$ 1 + SB525334 treated cells (light gray bar), \*\*\*  $P \leq 0.001$ , \*\*  $P \leq 0.005$ , or \*  $P \leq 0.05$ . Scale bars = 100 μm.

expansion of epithelial cells, and (3) *in vitro* differentiation of mixed cultured cells to study epithelial-mesenchymal interactions and effects of inducers and inhibitors.

The effects of TGF- $\beta$ 1 on the salivary glands are complex and somewhat paradoxical. TGF- $\beta$  null mice developed multifocal infiltrates in heart, lungs and salivary glands [18, 52]. These multifocal lesions and resulting damage to salivary glands were gender-specific and not only caused by defects in T-cell suppression but also by defects in TGF- $\beta$  signaling in salivary gland epithelial cells, as in another study it was shown that conditional deletion of TGF- $\beta$ R1 on salivary gland epithelial cells using the mammary tumor virus *Cre* mouse led to salivary gland inflammatory lesions and abnormal pattern of aquaporin-5 distribution, resulting in saliva secretion defects only in females but not in males mice [53]. On the other hand, conditional over-expression of TGF- $\beta$ 1 in secretory cells (mammary and salivary gland epithelial cells) resulted in hyposalivation due to salivary gland fibrosis and atrophy [21]. We hypothesized these paradoxical effects may be explained by differential roles of TGF- $\beta$  signaling in different salivary gland cell types, namely epithelial cells versus mesenchymal cells. Therefore, we tested the utility of our mixed cell culture system to study the effects TGF- $\beta$ 1 *in vitro*.

Supplementation of TGF- $\beta$ 1 to mixed cell cultures induced expression of higher levels of acini markers; however, we also observed reduction of mesenchymal derived fibroblast growth factors (*Fgf-7* and *Fgf-10*) and dramatic increased in the procollagen type 1 levels. FGF-7 (aka, Keratinocyte Growth Factor, KGF) in particular has been proven beneficial for salivary gland epithelial differentiation. *In vitro* salivary gland explants in the absence of mesenchyme can undergo differentiation with EGF and FGF-7. EGF induced lobule formation whereas FGF-7 induced stalk elongation morphogenesis [54]. FGF-7 has been shown beneficial for salivary gland restoration [55, 56]. Transgenic mice expressing *Fgf-7* under the keratin (K14) promoter exhibited excessive salivation [57].

Histological examination of the differentiation cultures revealed lack of acini-like structures formation and undifferentiated appearance of epithelial cells adjacent to mesenchymal cells which in turn adapted a fibroblasts morphology (elongated and polarized) in the TGF- $\beta$ 1 induced group. In contrast, inhibition of TGF- $\beta$ R1 signaling with SB525334 results in the highest levels of acini markers, highest levels of *Fgfs*, and lowest levels of *collagen type I*, which corresponds with the most mature and largest acini-like structures, especially in the areas rich in mesenchymal cells which adapted a cobblestone morphology. Thus we conclude that inhibition of TGF- $\beta$ 1 signaling in these *in vitro* differentiation cultures is beneficial, particularly in mesenchymal cells.

Alterations in the TGF- $\beta$  signaling have been associated with several salivary gland disorders. Sjogren's syndrome is an autoimmune disorder characterized primarily by T-cell but also B-cell infiltration in the salivary glands. Immunohistochemical staining showed TGF- $\beta$ 1 was strongly expressed in ductal epithelial cells of normal and inflamed salivary glands but downregulated in Sjogren's salivary glands [22]. In another study, normal and Sjogren's salivary glands expressed

TGF- $\beta$  in ductal and acinar epithelial cells, but TGF- $\beta$  production was reduced in Sjogren's salivary gland cultures [58]. Another study showed all three isoforms of TGF- $\beta$  expressed in lymphocytes, endothelial cells and ductal cells of Sjogren's versus benign lymphoepithelial lesions. Interestingly, the expression of TGF- $\beta$  isoforms in ductal cells of Sjogren's was increased as compared to benign lesions [59]. These reports suggest that alterations of TGF- $\beta$ 1 pathway may be involved in pathogenesis of Sjogren's disease

Alterations of the TGF- $\beta$  pathway and abnormal expression of TGF- $\beta$  ligands and receptors have been reported in several salivary gland tumors. In pleomorphic adenomas (PA), the most common type of salivary gland tumors, TGF- $\beta$ 2 was expressed in the inner ductal cells and TGF- $\beta$ 3 was expressed in the myoepithelial cells of PA tumors [60]. Mucoepidermoid carcinoma (MEC) is another salivary gland tumor that exhibits differentiation in multiple lineages. TGF- $\beta$ 1 was expressed in the salivary gland ducts, stroma and endothelial cells of the MEC tumors. Interestingly, TGF- $\beta$ R2 expression inversely correlated with tumor grade: all low grade tumors showed expression of TGF- $\beta$ R2 whereas none of the high-grade tumors, with greatest metastatic potential, showed TGF- $\beta$ R2 expression. TGF- $\beta$ R2 was expressed in surface epithelium, endothelial cells, nonneoplastic salivary gland ducts and stromal fibroblasts of the low-grade MEC [61]. Loss of TGF- $\beta$ R2 expression correlated with loss of tumor differentiation. In another study, it was shown that the Ms cell line derived from MEC, which highly expressed TGF- $\beta$ 1, exhibited decreased invasion and migration capacity when TGF- $\beta$ 1 was silenced by siRNA [24]. Likewise, another study showed that TGF- $\beta$ 1 was highly expressed in a metastatic salivary adenoid cystic carcinoma cell line and exposure to TGF- $\beta$ 1 *in vitro* activated the classical TGF- $\beta$  pathway, suggesting that TGF- $\beta$ 1 may promote migration and invasion of this tumor [19]. This suggests that the expression of TGF- $\beta$ 1 on certain tumor salivary gland epithelial cells induces migration, invasion and metastasis, and that TGF- $\beta$ 1 inhibition in these tumors may be beneficial.

In summary, given the complexity of TGF- $\beta$  signaling in salivary gland development, homeostasis and diseases, better tools are needed to understand the differential effects and role of TGF- $\beta$  signaling in different salivary gland cells (epithelial versus mesenchymal cells). The emergence of tissue specific conditional knockouts such as *Cre-lox* recombination [62], specific for salivary gland mesenchyme versus epithelium are necessary to dissect apart the differential roles of TGF- $\beta$  signaling.

## Conflict of Interests

The authors indicate no potential conflict of interests.

## Acknowledgments

This study was supported by funding from Departments of Pathology and Laboratory Medicine, University of Washington, the 2012 John H. Tietze Stem Cell Scientist Award to

M. Reyes, and the Anandamahidol Foundation Scholarship of Thailand to K. Janebodin and W. Buranaphatthana.

## References

- [1] L. S. Cutler and W. Gremski, "Epithelial-mesenchymal interactions in the development of salivary glands," *Critical Reviews in Oral Biology and Medicine*, vol. 2, no. 1, pp. 1-12, 1991.
- [2] K. Kratochwil, "Organ specificity in mesenchymal induction demonstrated in the embryonic development of the mammary gland of the mouse," *Developmental Biology*, vol. 20, no. 1, pp. 46-71, 1969.
- [3] K. A. Lawson, "The role of mesenchyme in the morphogenesis and functional differentiation of rat salivary epithelium," *Journal of Embryology and Experimental Morphology*, vol. 27, no. 3, pp. 497-513, 1972.
- [4] K. A. Lawson, "Mesenchyme specificity in rodent salivary gland development: the response of salivary epithelium to lung mesenchyme *in vitro*," *Journal of Embryology and Experimental Morphology*, vol. 32, no. 2, pp. 469-493, 1974.
- [5] V. N. Patel, I. T. Rebustini, and M. P. Hoffman, "Salivary gland branching morphogenesis," *Differentiation*, vol. 74, no. 7, pp. 349-364, 2006.
- [6] Y. Takahashi and H. Nogawa, "Branching morphogenesis of mouse salivary epithelium in basement membrane-like substratum separated from mesenchyme by the membrane filter," *Development*, vol. 111, no. 2, pp. 327-335, 1991.
- [7] A. S. Tucker, "Salivary gland development," *Seminars in Cell and Developmental Biology*, vol. 18, no. 2, pp. 237-244, 2007.
- [8] K. Okumura, M. Shinohara, and F. Endo, "Capability of tissue stem cells to organize into salivary rudiments," *Stem Cells International*, vol. 2012, Article ID 502136, 2012.
- [9] N. Patel, P. T. Sharpe, and I. Miletich, "Coordination of epithelial branching and salivary gland lumen formation by Wnt and FGF signals," *Developmental Biology*, vol. 358, no. 1, pp. 156-167, 2011.
- [10] M. M. Imanguli, J. C. Atkinson, S. A. Mitchell et al., "Salivary gland involvement in chronic graft-versus-host disease: prevalence, clinical significance, and recommendations for evaluation," *Biology of Blood and Marrow Transplantation*, vol. 16, no. 10, pp. 1362-1369, 2010.
- [11] C. de la Cal, J. Fernández-Solari, C. E. Mohn et al., "Radiation produces irreversible chronic dysfunction in the submandibular glands of the rat," *Open Dentistry Journal*, vol. 6, no. 1, pp. 8-13, 2012.
- [12] C. A. Sullivan, R. I. Haddad, R. B. Tishler, A. Mahadevan, and J. F. Krane, "Chemoradiation-induced cell loss in human submandibular glands," *Laryngoscope*, vol. 115, no. 6, pp. 958-964, 2005.
- [13] R. E. Friedrich, S. Bartel-Friedrich, K. Röser, and C. Lautenschläger, "The expression pattern of collagen I in irradiated mandibular salivary glands of rats," *Anticancer Research*, vol. 23, no. 2, pp. 927-930, 2003.
- [14] A. Busuttil, "Irradiation induced changes in human salivary glands," *Clinical Otolaryngology and Allied Sciences*, vol. 2, no. 3, pp. 199-206, 1977.
- [15] M. Y. Kwon and M. Gu, "True malignant mixed tumor (carcinosarcoma) of parotid gland with unusual mesenchymal component: a case report and review of the literature," *Archives of Pathology and Laboratory Medicine*, vol. 125, no. 6, pp. 812-815, 2001.
- [16] T. Aigner, D. Neureiter, U. Volker, J. Belke, and T. Kirchner, "Epithelial-mesenchymal transdifferentiation and extracellular matrix gene expression in pleomorphic adenomas of the parotid salivary gland," *The Journal of Pathology*, vol. 186, pp. 178-185, 1998.
- [17] M. Azuma, T. Tamatani, K. Fukui, T. Yuki, K. Motegi, and M. Sato, "Different signalling pathways involved in transforming growth factor- $\beta$ 1-induced morphological change and type IV collagen synthesis in simian virus-40-immortalized normal human salivary gland duct and myoepithelial cell clones," *Archives of Oral Biology*, vol. 41, no. 5, pp. 413-424, 1996.
- [18] G. P. Boivin, B. A. O'Toole, I. E. Orsmy et al., "Onset and progression of pathological lesions in transforming growth factor- $\beta$ 1-deficient mice," *American Journal of Pathology*, vol. 146, no. 1, pp. 276-288, 1995.
- [19] L. Dong, Y. X. Wang, S. L. Li et al., "TGF- $\beta$ 1 promotes migration and invasion of salivary adenoid cystic carcinoma," *Journal of Dental Research*, vol. 90, no. 6, pp. 804-809, 2011.
- [20] S. G. Hakim, J. Ribbat, A. Berndt et al., "Expression of Wnt-1, TGF- $\beta$  and related cell-cell adhesion components following radiotherapy in salivary glands of patients with manifested radiogenic xerostomia," *Radiotherapy and Oncology*, vol. 101, no. 1, pp. 93-99, 2011.
- [21] B. E. Hall, C. Zheng, W. D. Swaim et al., "Conditional overexpression of TGF- $\beta$ 1 disrupts mouse salivary gland development and function," *Laboratory Investigation*, vol. 90, no. 4, pp. 543-555, 2010.
- [22] Y. Kizu, H. Sakurai, S. Katagiri et al., "Immunohistological analysis of tumour growth factor  $\beta$ 1 expression in normal and inflamed salivary glands," *Journal of Clinical Pathology*, vol. 49, no. 9, pp. 728-732, 1996.
- [23] S. V. Lourenço, S. H. Uyekita, D. M. C. Lima, and F. A. Soares, "Developing human minor salivary glands: morphological parallel relation between the expression of TGF-beta isoforms and cytoskeletal markers of glandular maturation," *Virchows Archiv*, vol. 452, no. 4, pp. 427-434, 2008.
- [24] J. Wang, J. Chen, K. Zhang, Y. Zhao, J. E. Nör, and J. Wu, "TGF- $\beta$ 1 regulates the invasive and metastatic potential of mucoepidermoid carcinoma cells," *Journal of Oral Pathology and Medicine*, vol. 40, no. 10, pp. 762-768, 2011.
- [25] T. Kisseleva, M. Cong, Y. Paik et al., "Myofibroblasts revert to an inactive phenotype during regression of liver fibrosis," *Proceedings of the National Academy of Sciences of the United States of America*, vol. 109, pp. 9448-9453.
- [26] S.-L. Lin, T. Kisseleva, D. A. Brenner, and J. S. Duffield, "Pericytes and perivascular fibroblasts are the primary source of collagen-producing cells in obstructive fibrosis of the kidney," *American Journal of Pathology*, vol. 173, no. 6, pp. 1617-1627, 2008.
- [27] I. Fonseca, J. F. Moura Nunes, and J. Soares, "Expression of CD44 isoforms in normal salivary gland tissue: an immunohistochemical and ultrastructural study," *Histochemistry and Cell Biology*, vol. 114, no. 6, pp. 483-488, 2000.
- [28] S. J. Kennel, T. K. Lankford, L. J. Foote, S. G. Shinpock, and C. Stringer, "CD44 expression on murine tissues," *Journal of Cell Science*, vol. 104, no. 2, pp. 373-382, 1993.
- [29] I. Amano, Y. Imaizumi, C. Kaji, H. Kojima, and Y. Sawa, "Expression of podoplanin and classical cadherins in salivary gland epithelial cells of klotho-deficient mice," *Acta Histochemica et Cytochemica*, vol. 44, no. 6, pp. 267-276, 2011.
- [30] A. P. Vreugdenhil, A. V. Nieuw Amerongen, G. L. de Lange, and P. A. Roukema, "Localization of amylase and mucins in the



- major salivary glands of the mouse," *Histochemical Journal*, vol. 14, no. 5, pp. 767–780, 1982.
- [31] H. S. Larsen, M. H. Aure, S. B. Peters, M. Larsen, E. B. Messelt, and H. Kanli Galtung, "Localization of AQP5 during development of the mouse submandibular salivary gland," *Journal of Molecular Histology*, vol. 42, no. 1, pp. 71–81, 2011.
- [32] C. K. McPhee, M. A. Logan, M. R. Freeman, and E. H. Baehrecke, "Activation of autophagy during cell death requires the engulfment receptor Draper," *Nature*, vol. 465, no. 7301, pp. 1093–1096, 2010.
- [33] I. M. A. Lombaert, J. F. Brunsting, P. K. Weirenga et al., "Rescue of Salivary gland function after stem cell transplantation in irradiated glands," *PLoS ONE*, vol. 3, no. 4, article e2063, 2008.
- [34] K. Janebodin and M. Reyes, "Neural crest-derived dental pulp stem cells function as ectomesenchyme to support salivary gland tissue formation," *Dentistry*, vol. S13, article 001, 2012.
- [35] O. M. Maria, A. Zeitouni, O. Gologan, and S. D. Tran, "Matrigel improves functional properties of primary human salivary gland cells," *Tissue Engineering A*, vol. 17, no. 9-10, pp. 1229–1238, 2011.
- [36] M. Toida, J. Takeuchi, K. Hara et al., "Histochemical studies of intercellular components of salivary gland tumors with special reference to glycosaminoglycan, laminin and vascular elements," *Virchows Archiv A Pathological Anatomy and Histopathology*, vol. 403, no. 1, pp. 15–26, 1984.
- [37] K. Hara, M. Ito, J. Takeuchi, S. Iijima, T. Endo, and H. Hidaka, "Distribution of S-100b protein in normal salivary glands and salivary gland tumors," *Virchows Archiv A Pathological Anatomy and Histology*, vol. 401, no. 2, pp. 232–249, 1983.
- [38] M. Heffernan, S. Yousefi, and J. W. Dennis, "Molecular characterization of P2B/LAMP-1, a major protein target of a metastasis-associated oligosaccharide structure," *Cancer Research*, vol. 49, no. 21, pp. 6077–6084, 1989.
- [39] Y. Mu, R. Sundar, N. Thakur et al., "TRAF6 ubiquitinates TGF $\beta$  type I receptor to promote its cleavage and nuclear translocation in cancer," *Nature Communications*, vol. 2, article 330, 2011.
- [40] H. Ikushima and K. Miyazono, "Biology of transforming growth factor- $\beta$  signaling," *Current Pharmaceutical Biotechnology*, vol. 12, no. 12, pp. 2099–2107, 2011.
- [41] E. T. Grygielko, W. M. Martin, C. Tweed et al., "Inhibition of gene markers of fibrosis with a novel inhibitor of transforming growth factor- $\beta$  type I receptor kinase in puromycin-induced nephritis," *Journal of Pharmacology and Experimental Therapeutics*, vol. 313, no. 3, pp. 943–951, 2005.
- [42] H. Higashiyama, D. Yoshimoto, T. Kaise et al., "Inhibition of activin receptor-like kinase 5 attenuates Bleomycin-induced pulmonary fibrosis," *Experimental and Molecular Pathology*, vol. 83, no. 1, pp. 39–46, 2007.
- [43] S. Yamamoto, E. Fukumoto, K. Yoshizaki et al., "Platelet-derived growth factor receptor regulates salivary gland morphogenesis via fibroblast growth factor expression," *Journal of Biological Chemistry*, vol. 283, no. 34, pp. 23139–23149, 2008.
- [44] T. Jaskoll, G. Abichaker, D. Witcher et al., "FGF10/FGFR2b signaling plays essential roles during in vivo embryonic submandibular salivary gland morphogenesis," *BMC Developmental Biology*, vol. 5, article 11, 2005.
- [45] A. K. Madan and B. Kramer, "Immunolocalization of fibroblast growth factor-2 (FGF-2) during embryonic development of the rat submandibular gland," *SADJ*, vol. 60, no. 2, pp. 58–61, 2005.
- [46] T. Jaskoll, D. Witcher, L. Toreno, P. Bringas, A. M. Moon, and M. Melnick, "FGF8 dose-dependent regulation of embryonic submandibular salivary gland morphogenesis," *Developmental Biology*, vol. 268, no. 2, pp. 457–469, 2004.
- [47] M. P. Hoffman, B. L. Kidder, Z. L. Steinberg et al., "Gene expression profiles of mouse submandibular gland development: FGFR1 regulates branching morphogenesis *in vitro* through BMP- and FGF- dependent mechanisms," *Development*, vol. 129, no. 24, pp. 5767–5778, 2002.
- [48] T. Jaskoll, Y. M. Zhou, Y. Chai et al., "Embryonic submandibular gland morphogenesis: stage-specific protein localization of FGFs, BMPs, Pax6 and Pax9 in normal mice and abnormal smg phenotypes in FgfR2-IIIc(+/ $\Delta$ ), BMP7(-/-) and Pax6(-/-) mice," *Cells Tissues Organs*, vol. 170, no. 2-3, pp. 83–98, 2001.
- [49] T. Jaskoll, T. Leo, D. Witcher et al., "Sonic hedgehog signaling plays an essential role during embryonic salivary gland epithelial branching morphogenesis," *Developmental Dynamics*, vol. 229, no. 4, pp. 722–732, 2004.
- [50] B. Hai, Z. Yang, S. E. Millar et al., "Wnt/ $\beta$ -catenin signaling regulates postnatal development and regeneration of the salivary gland," *Stem Cells and Development*, vol. 19, no. 11, pp. 1793–1801, 2010.
- [51] H. Dang, A. L. Lin, B. Zhang, H.-M. Zhang, M. S. Katz, and C.-K. Yeh, "Role for Notch signaling in salivary acinar cell growth and differentiation," *Developmental Dynamics*, vol. 238, no. 3, pp. 724–731, 2009.
- [52] M. Christ, N. L. McCartney-Francis, A. B. Kulkarni et al., "Immune dysregulation in TGF- $\beta$ 1-deficient mice," *Journal of Immunology*, vol. 153, no. 5, pp. 1936–1946, 1994.
- [53] S. R. Nandula, S. Amarnath, A. Molinolo et al., "Female mice are more susceptible to developing inflammatory disorders due to impaired transforming growth factor  $\beta$  signaling in salivary glands," *Arthritis and Rheumatism*, vol. 56, no. 6, pp. 1798–1805, 2007.
- [54] K. Morita and H. Nogawa, "EGF-dependent lobule formation and FGF7-dependent stalk elongation in branching morphogenesis of mouse salivary epithelium *in vitro*," *Developmental Dynamics*, vol. 215, pp. 148–154, 1999.
- [55] I. M. A. Lombaert, J. F. Brunsting, P. K. Wierenga, H. H. Kampinga, G. de Haan, and R. P. Coppes, "Keratinocyte growth factor prevents radiation damage to salivary glands by expansion of the stem/progenitor pool," *Stem Cells*, vol. 26, no. 10, pp. 2595–2601, 2008.
- [56] C. Zheng, A. P. Cotrim, A. Rowzee et al., "Prevention of radiation-induced salivary hypofunction following hKGF gene delivery to murine submandibular glands," *Clinical Cancer Research*, vol. 17, no. 9, pp. 2842–2851, 2011.
- [57] L. Guo, Q.-C. Yu, and E. Fuchs, "Targeting expression of keratinocyte growth factor to keratinocytes elicits striking changes in epithelial differentiation in transgenic mice," *The EMBO Journal*, vol. 12, no. 3, pp. 973–986, 1993.
- [58] N. Ogawa, H. Dang, K. Lazaridis, H. S. McGuff, T. B. Aufdemorte, and N. Talal, "Analysis of transforming growth factor  $\beta$  and other cytokines in autoimmune exocrinopathy (Sjogren's syndrome)," *Journal of Interferon and Cytokine Research*, vol. 15, no. 9, pp. 759–767, 1995.
- [59] G. I. Mason, J. Hamburger, S. Bowman, and J. B. Matthews, "Salivary gland expression of transforming growth factor  $\beta$  isoforms in Sjogren's syndrome and benign lymphoepithelial lesions," *Journal of Clinical Pathology—Molecular Pathology*, vol. 56, no. 1, pp. 52–59, 2003.
- [60] K. Kusafuka, A. Yamaguchi, T. Kayano, and T. Takemura, "Immunohistochemical localization of members of the transforming growth factor (TGF)- $\beta$  superfamily in normal human



salivary glands and pleomorphic adenomas,” *Journal of Oral Pathology and Medicine*, vol. 30, no. 7, pp. 413–420, 2001.

- [61] D. G. Dillard, S. Muller, C. Cohen, D. Bloch, J. M. del Gaudio, and A. A. Gal, “High tumor grade in salivary gland mucoepidermoid carcinomas and loss of expression of transforming growth factor  $\beta$  receptor type II,” *Archives of Otolaryngology—Head and Neck Surgery*, vol. 127, no. 6, pp. 683–686, 2001.
- [62] P. C. Orban, D. Chui, and J. D. Marth, “Tissue- and site-specific DNA recombination in transgenic mice,” *Proceedings of the National Academy of Sciences of the United States of America*, vol. 89, no. 15, pp. 6861–6865, 1992.

## Research Article

# Expression and Function of NUMB in Odontogenesis

Haitao Li,<sup>1</sup> Amsaveni Ramachandran,<sup>2</sup> Qi Gao,<sup>2</sup> Sriram Ravindran,<sup>2</sup> Yiqiang Song,<sup>2</sup> Carla Evans,<sup>3</sup> and Anne George<sup>2</sup>

<sup>1</sup> Department of Orthodontics, College of Dental Medicine, Nova Southeastern University, 3200 S. University Drive, Fort Lauderdale, FL 33328, USA

<sup>2</sup> Brodie Tooth Development Genetics & Regenerative Medicine Research Laboratory, Department of Oral Biology (M/C 690), College of Dentistry, University of Illinois at Chicago, Chicago IL 60612, USA

<sup>3</sup> Department of Orthodontics, College of Dentistry, University of Illinois at Chicago, 801 S. Paulina Street, Chicago IL 60612, USA

Correspondence should be addressed to Anne George; [anneg@uic.edu](mailto:anneg@uic.edu)

Received 6 January 2013; Revised 2 May 2013; Accepted 13 May 2013

Academic Editor: Avina Paranjpe

Copyright © 2013 Haitao Li et al. This is an open access article distributed under the Creative Commons Attribution License, which permits unrestricted use, distribution, and reproduction in any medium, provided the original work is properly cited.

NUMB is a multifunctional protein implicated to function in self-renewal and differentiation of progenitors in several tissues. To characterize the transcripts and to analyze the expression pattern of NUMB in odontogenesis, we isolated 2 full-length clones for NUMB from mouse dental pulp mRNA. One novel sequence contained 200 bp insertion in the phosphotyrosine binding domain (PTB). Confocal microscopy analysis showed strong NUMB expression in human dental pulp stem cells (hDPSC) and preameloblasts. Western blot analysis indicated that NUMB isoforms were differentially expressed in various dental tissues. Immunohistochemical analysis showed that in postnatal mouse tooth germs, NUMB was differentially expressed in the preameloblasts, odontoblasts, cervical loop region, and in the dental pulp stem cells during development. Interestingly, overexpression of NUMB in HAT-7, a preameloblast cell line, had dramatic antagonizing effects on the protein expression level of activated Notch 1. Further analysis of the Notch signaling pathway showed that NUMB significantly downregulates sonic hedgehog (Shh) expression in preameloblasts. Therefore, we propose that NUMB maintains ameloblast progenitor phenotype at the cervical loop by downregulating the activated Notch1 protein and thereby inhibiting the mRNA expression of Shh.

## 1. Introduction

NUMB protein was initially identified in *Drosophila*. Its name comes from the fact that the gene mutation causes flies to lose their sensory neurons and become “numb.” NUMB is demonstrated to play roles in lineage commitment by both gain- and loss-of-functions approaches. Its function has been attributed to asymmetric distribution in daughter cells as well as interaction with Notch signaling components. After its identification, NUMB has been extensively studied in the development of sensory organs, and subsequently in cancer research [1]. We recently identified NUMB as one of the genes that are differentially expressed in rat immortalized odontoblast cells (T4-4) [2].

The *Drosophila* NUMB is a membrane-associated protein in the sensory organ precursor cells, and its mutation is lethal resulting from the abnormality of the peripheral

nervous systems [3]. Spana et al. identified that the unequal distribution of NUMB in the descendants controls the cell fate of the neurons projecting towards two directions: daughter cells remain as stem cells from maintaining high level NUMB expression, and daughter cells differentiate into neurons with the loss of NUMB expression [4]. NUMB knockout mice die around embryonic day 11.5. They exhibit severe defects in cranial neural tube closure and precocious neuron production, indicating that NUMB promotes progenitor cell fates [5]. Mammalian NUMB is not only expressed in the embryonic tissues but also in most adult tissues, suggesting more complex functions other than neurogenesis [6]. To date, four mammalian NUMB isoforms were identified from alternatively spliced transcripts in neuronal lineage cells [7]. The two members of PRRL isoforms (have long proline rich region) were expressed in early mouse embryonic ages (E7–E10) and were undetectable at E13 when the cells are

in rapid expansion stage. The two members of the PRRS isoforms (have short proline rich region) were detected in all developmental stages and adult brains [7, 8]. This differential expression pattern is associated with the function of NUMB in maintaining progenitor cells in the early phase of cortical neurogenesis [9] versus its function in self-renewal and differentiation in late stages of neuron development [10]. Recently, three novel isoforms of NUMB were identified in the human extravillous trophoblast [11].

In rodent incisors, the cervical loop situated at the posterior end of the epithelium consists of progenitor cells which are capable of continuously amplifying and differentiating into ameloblasts and support the lifelong growth of the enamel on the labial side [12]. These progenitor cells in the labial cervical loop give rise to the transit-amplifying cells which will further differentiate into preameloblasts and eventually into well-differentiated enamel forming ameloblasts [13]. Notch and sonic hedgehog (Shh) signaling pathway have been shown to be important in regulating this transformation [14].

Seidel et al. demonstrated that Shh produced by the transit amplifying/preameloblasts signals to the stem cells in the cervical loop for continuous ameloblast regeneration. After injecting a hedgehog pathway inhibitor in the mouse mandible, new enamel formation on the labial surface of the mouse incisors was completely blocked. However, the stem cell survival was not endangered due to the fact that normal ameloblasts as well as the enamel were able to form after the removal of the hedgehog signal inhibitor [15]. These results clearly revealed the existence of a positive feedback signal loop between the differentiating cells and the stem cells. Shh produced by the differentiating ameloblasts signals to the stem cells located in the labial cervical loop to continuously provide progenies in order to support the differentiation demand. In addition, Shh is also important in regulating the preameloblasts to elongate, polarize, and deposit enamel matrix [16].

Notch 1, a transmembrane protein, has been shown to be important in specifying dental cell-type identity [14]. Notch signaling regulates the maintenance, fate decision, and proliferation of progenitor cells in multiple tissues such as bone marrow and various neuronal tissues [17]. Notch 1 expressing cells in the cervical loop respond to FGF signaling secreted by the adjacent mesenchyme during mitogenesis and cell fate decision [18]. Inhibition of Notch signaling leads to impaired growth of the mouse incisor cervical loop with reduced proliferation and increased apoptosis. In addition, the inhibition also reduced the population of the ameloblast precursors [19].

NUMB inhibits Notch signaling through interaction with the Notch intracellular domain and promotes its ubiquitination and degradation [20]. NUMB was also shown to control the intracellular trafficking of the Notch to suppress its function [21]. Studies also indicated that the expression of NUMB correlates with the suppression of hedgehog signaling [22]. NUMB is also involved in the TP53-activated pathway [23], endocytosis [24], and the determination of cell polarity [25]. These studies suggest that there is a finely tuned

regulatory network centered by NUMB in determination of cell fates [26].

Even though the expression of NUMB has been reported in several tissues, there are no reports thus far during tooth development. In this study, we identified several NUMB isoforms that are differently expressed in dental tissues. They were expressed in the cervical loop, immature ameloblasts, odontoblasts, and in specific dental pulp cells. Overexpression of NUMB in preameloblast cells inhibited both the activated Notch 1 protein and Shh expression. Therefore, we propose that NUMB regulates ameloblasts differentiation by modulating the expression levels of Notch 1 protein and Shh expressions.

## 2. Materials and Methods

**2.1. RT-PCR.** Dental pulp tissues were isolated from postnatal day 5 mouse tooth germs. Single cell suspension was derived by digesting the dental pulp tissues at 37°C for 30 min under constant agitation in a digestion cocktail containing (0.05% trypsin and 0.1% collagenase P). Dental pulp cells were cultured in  $\alpha$ MEM with addition of 10% fetal bovine serum and 50 U/mL of penicillin and streptomycin for 7 days. RNA was extracted from the cultures using TRIzol reagent (Invitrogen, CA, USA) according to the manufacturer's instructions. cDNA library was generated using SuperScript First-Strand Synthesis System (Invitrogen, CA, USA). Primers were designed to amplify the longest NUMB open reading frame using sequence derived from Ensembl Genome Browser database with the additions of the endonuclease sites on the forward and reverse primers. The primer sequences are Forward: 5'-SalI+ATGAACAACTACGGC-3' and Reverse: 5'-SacI+TAAAGTTCTATTTCAAAT-3'. PCR products were amplified using high-fidelity Taq with 65°C annealing temperature and 2 minutes extension time.

**2.2. Immunohistochemistry (IHC).** E13.5, E16.5, E18.5 mouse embryos, postnatal day 3, day 5, and day 7 mouse heads were fixed in 10% neutral buffered formalin for 3 days at 4°C and processed for paraffin section. Serial sections were used for immunohistochemical analysis for NUMB (abcam ab14140) and activated Notch 1 (abcam ab8925) using the Vectastain ABC Kit (Vector Labs, CA, USA) following the manufacturer's instructions. Sections were imaged using Zeiss microscope.

**2.3. Immunocytochemistry (ICC).** Human dental pulp stem cells (DPSCs), T4-4 preodontoblasts, and HAT-7 cells were plated on sterilized cover slips placed in 6-well culture dishes. Cells were fixed in 10% neutral buffered formalin at 4°C for 2 hours. Cells were permeabilized with 0.5% Triton in PBS for 30 minutes, then blocked in 5% BSA for 1 hour at room temperature, and incubated with primary antibody NUMB (abcam ab14140) and activated Notch 1 (abcam ab8925) overnight at 4°C. TRITC-conjugated goat anti-rabbit secondary antibody and FITC-conjugated goat anti-rabbit secondary antibody were utilized for the visualization of the proteins of interest. Cells were counterstained



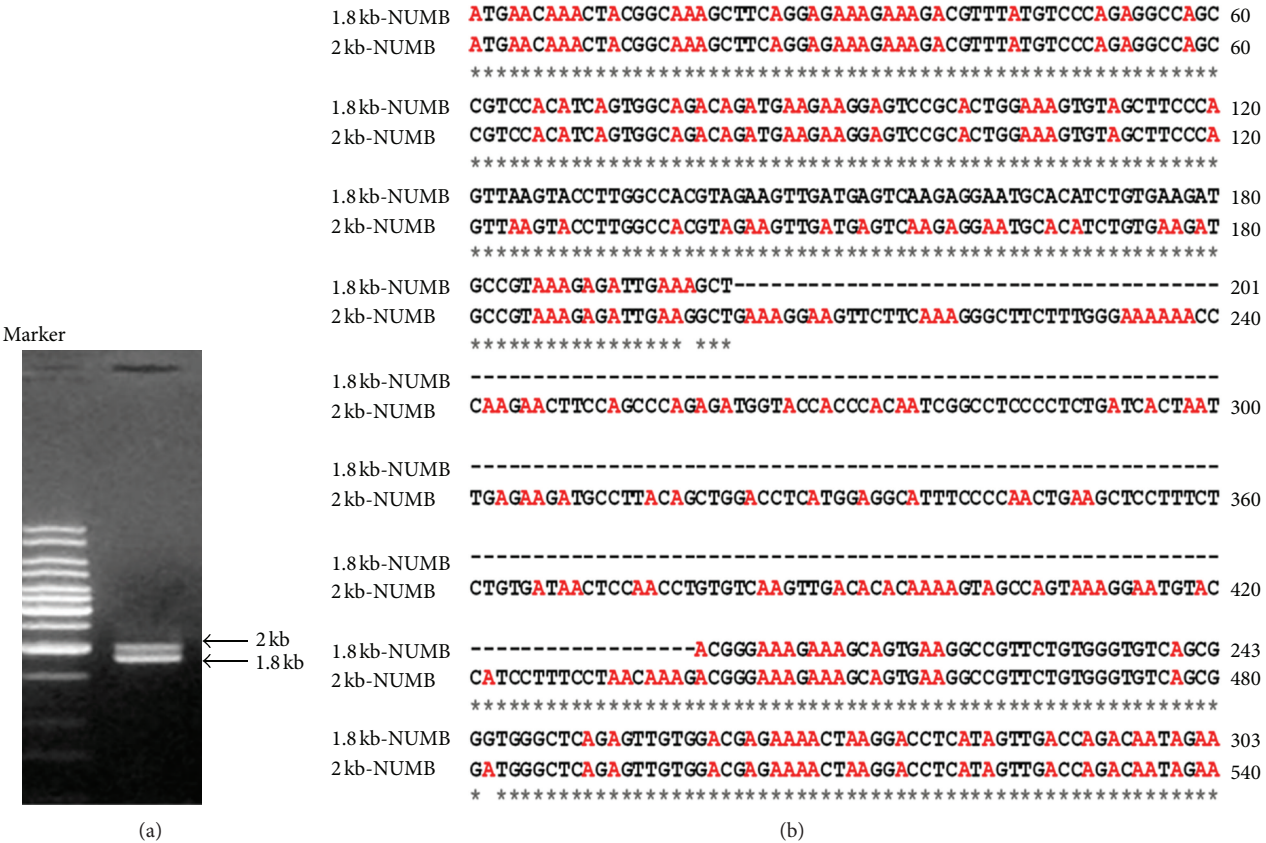


FIGURE 1: (a) RT-PCR analysis of NUMB isoforms in day 7 dental pulp cells. RT-PCR analysis of mRNA extracted from day 7 dental pulp culture shows two PCR bands corresponding to 2 kb and 1.8 kb obtained using primers designed to amplify the longest NUMB reading frame. (b) The alignment of the sequence obtained from 1.8 kb and the 2 kb PCR fragments. The 2 kb PCR fragment contains 236 bp insertion in the phosphotyrosine binding domain (PTB) 201 bp downstream of the initiation start site.

with nuclei-specific fluorescent stain, DAPI (Vectashield Mounting Medium, CA, USA), and imaged using confocal microscopy with corresponding fluorescent channel.

**2.4. Generation of Plasma Membrane Patches.** Plasma membrane patches from HAT-7 cells were prepared as described previously [27, 28]. The patches were fixed in 4% paraformaldehyde and immunostained with anti-NUMB antibody.

**2.5. Total Protein Lysate.** Total protein lysate was prepared using RIPA buffer (50 mM Tris, 150 mM NaCl, 0.1% SDS, 0.5% Na. Deoxycholate, and 1% NP40) in the presence of proteinase inhibitor cocktail (Sigma, MO, USA). For protein extraction from cell lines, the cells were cultured in 100 mm petri dish and washed with ice-cold PBS at the time of harvest. Cells were lysed with 700  $\mu$ L of RIPA buffer, scraped off from the culture dish, vortexed for 10 seconds, and incubated on ice for 10 minutes. The supernatant was collected after centrifugation at 14 k rpm at 4°C. For protein extraction from whole tooth buds, day 4 postnatal mouse tooth buds were dissected under the microscope. The tooth buds were frozen with liquid nitrogen, ground in a mortar and pestle with the addition of the RIPA buffer supplemented with proteinase inhibitor cocktail, and processed as above.

**2.6. Western Blot Analysis.** Total protein extracted from cell cultures and embryonic tooth germs was quantified using Bradford protein assay with an MBA 2000 spectrometer (Perkin Elmer, MA, USA). A total of 35–40  $\mu$ g of protein were loaded on the 10% SDS polyacrylamide gel for separation. Well-separated proteins were transferred onto a nitrocellulose membrane at 4°C. The nitrocellulose membrane was then blocked with 5% nonfat milk in PBS for 1 hour and then incubated with primary antibody in 3% BSA/PBS overnight (NUMB: abcam ab14140; 1/1500 dilution; activated Notch 1: abcam; ab8925 1/1600; tubulin 1/3000) under constant agitation at 4°C. The blot was incubated with the secondary antibody (goat antirabbit conjugated with HRP 1/3000) at room temperature for 1 hour. Chemiluminescent Western Blot Substrate (Thermo Scientific Pierce ECL, IL, USA) was utilized for developing, and the blot was exposed on CL-XPosure Film (Thermo Scientific, IL, USA).

**2.7. Culturing HAT-7 Cells.** HAT-7 cells [29] were maintained in DMEM/F-12 medium with addition of 10% FBS and 50 U/mL of penicillin and streptomycin. To overexpress NUMB, HAT-7 cells were plated in 6-well culture dish 24 hour in advance with 90% confluence in antibiotic-free medium. Plasmids including pSR-GFP/Neo (gifts from Wang et al. [30]); GFP-NUMB (NUMB isoform 4) (gifts from

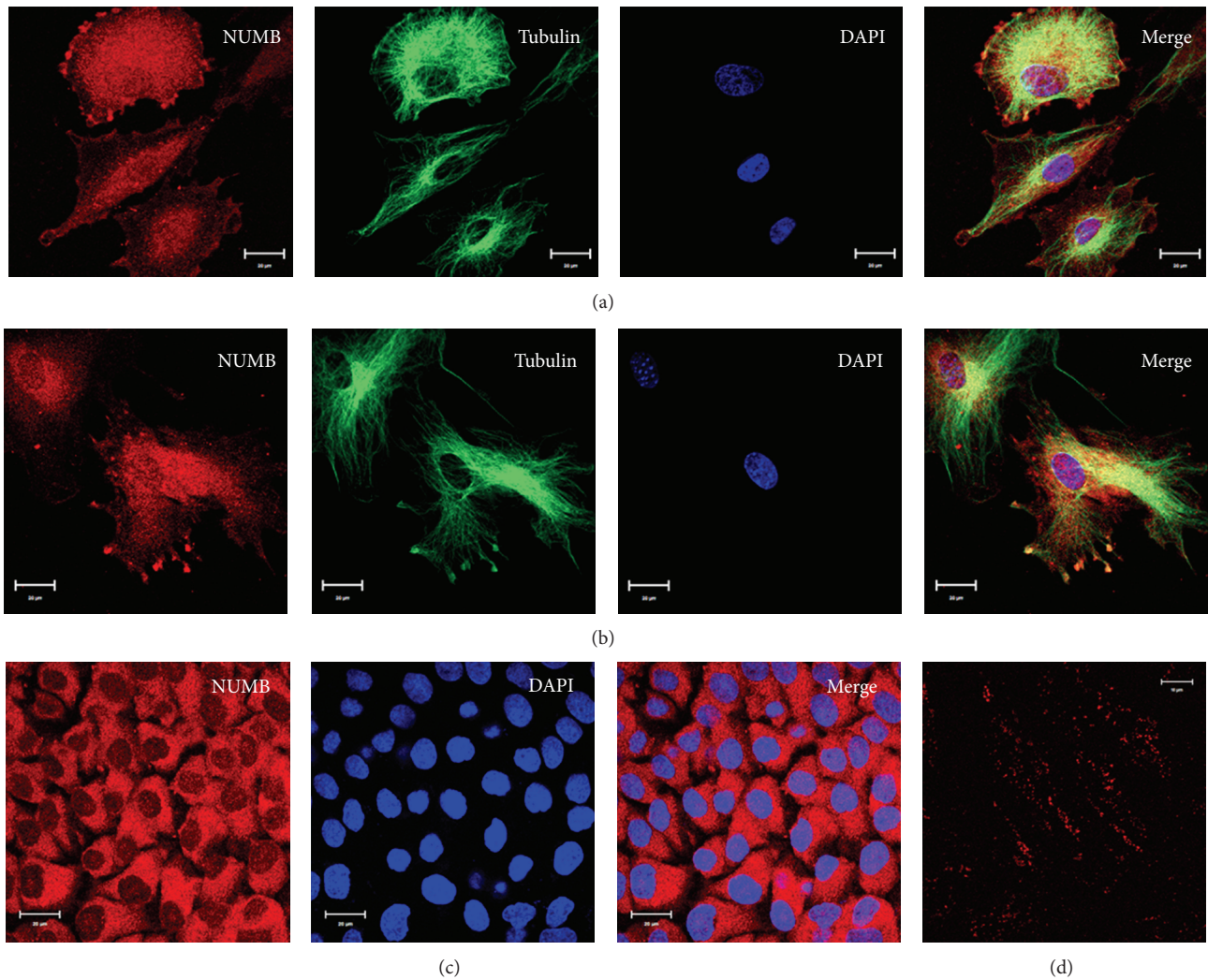


FIGURE 2: Localization of NUMB in various odontogenic cells: immunocytochemistry staining of NUMB expression in T4-4 odontoblast cells (a), human dental pulp stem cell (b), and preameloblast cells (c). Membrane patches isolated from preameloblast HAT-7 cells stained using NUMB antibody (d).

Nishimura and Kaibuchi [31]) were reconstituted in serum-free and antibiotics-free DMEM/F-12 medium for transfection by Lipofectamine 2000 (Invitrogen). Transfection medium was replaced with fresh culture medium in 24 hours. Cells were allowed to recover for 48 hours before being placed in selection medium. The selection medium contains 1 to 100 dilution of the G418 neomycin sulfate (Sigma) stock solution (100 mg/mL) in DMEM/F-12 medium. The G418 concentration was determined from the killing curve where 50% of the cells were killed in 48 hours. Cells were cultured in selection medium for 6 weeks before any experiments were carried out in order to completely remove the nontransfected or transiently transfected cells. Cells were maintained in the selection medium hereafter. For the PCR-based Notch 1 superarray signaling pathway analysis, transiently transfected cells for 48 hours were utilized.

#### 2.8. Functional Analysis of NUMB in Notch Signaling Using Pathway-Specific PCR-Based Superarray. HAT-7 cells were

transiently transfected with NUMB-GFP expression vector and control Neomycin-GFP expression vector. RNA was extracted using Qiagen RNA easy kit following the manufacturer's protocol. cDNA was generated using RT First-Strand cDNA Synthesis Kit (C-03 Qiagen, CA, USA) from 4 μg of RNA. Genomic DNA was eliminated by on column DNase digestion during RNA extraction and before reverse transcription. RT<sup>2</sup> Profiler PCR Array System was used for analyzing the mouse Notch 1 signaling pathway (PAMM-059C).

### 3. Results

**3.1. Expression of NUMB Transcripts in Dental Tissue.** To demonstrate the presence of NUMB transcripts in dental pulp cells, we performed RT-PCR using cDNA generated from day 7 primary dental pulp cultures. Primers were designed to amplify the longest NUMB open reading frame. Two specific PCR fragments were amplified (Figure 1(a)). Sequence



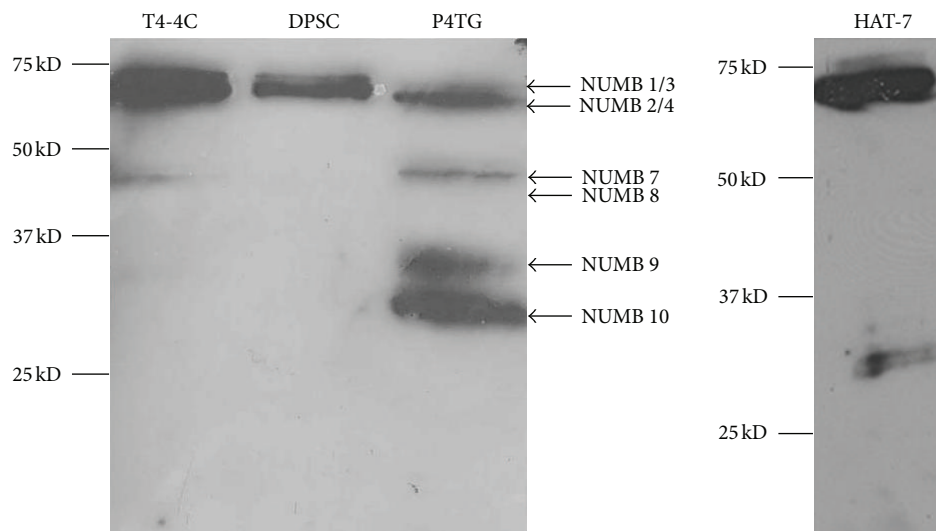


FIGURE 3: Western blot analysis of NUMB isoforms in odontogenic cells: total protein lysates were obtained from odontoblasts (T4-4 cells); dental pulp stem cells (DPCs); preameloblasts (HAT-7); tooth germs isolated from postnatal day 4 molars (P4TG). Notice that NUMB isoforms are differentially expressed in these tissues.

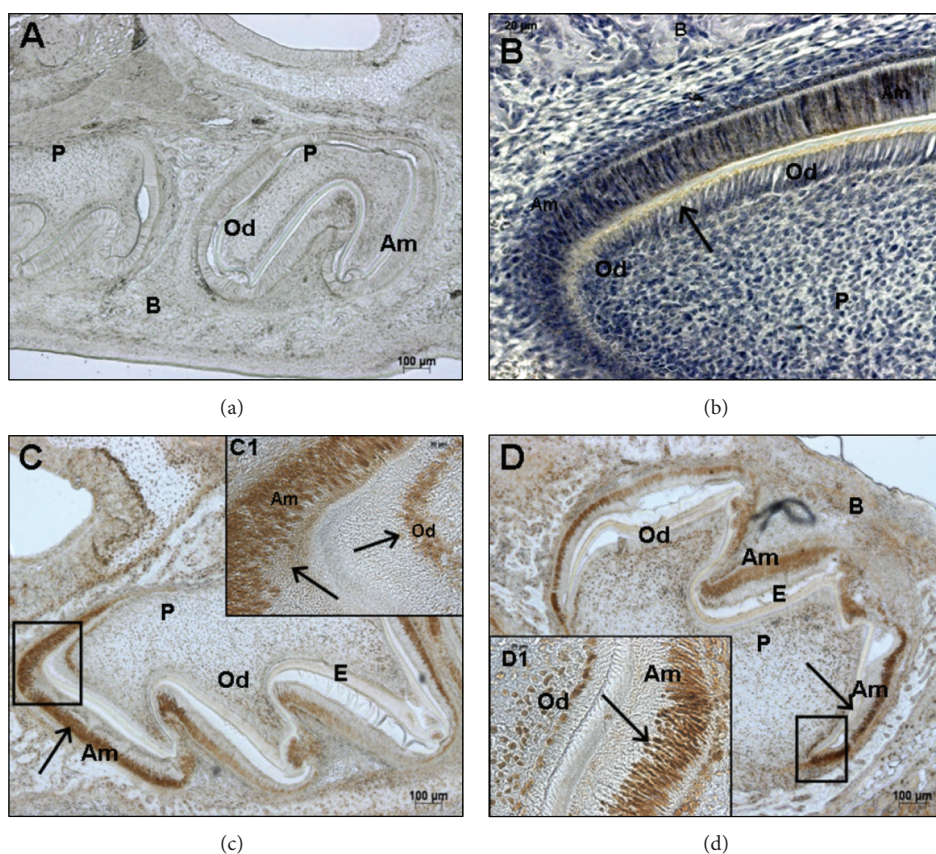


FIGURE 4: Localization of NUMB in odontogenic tissues at postnatal day 3: localization of NUMB in P3 incisors (B) and molars (C and D). NUMB can be detected in the ameloblasts (Am); odontoblasts (Od); ameloblast progenitors (cervical loop); in the dental pulp cells (P) in close vicinity to the odontoblasts. (D1) shows the immature ameloblasts, immature odontoblasts, and dental pulp cells from incisor and molar, respectively. (a) is the negative control. Scale bar represents 100  $\mu\text{m}$  for (a), (c), and (d) and 20  $\mu\text{m}$  for C1 and D1, respectively.



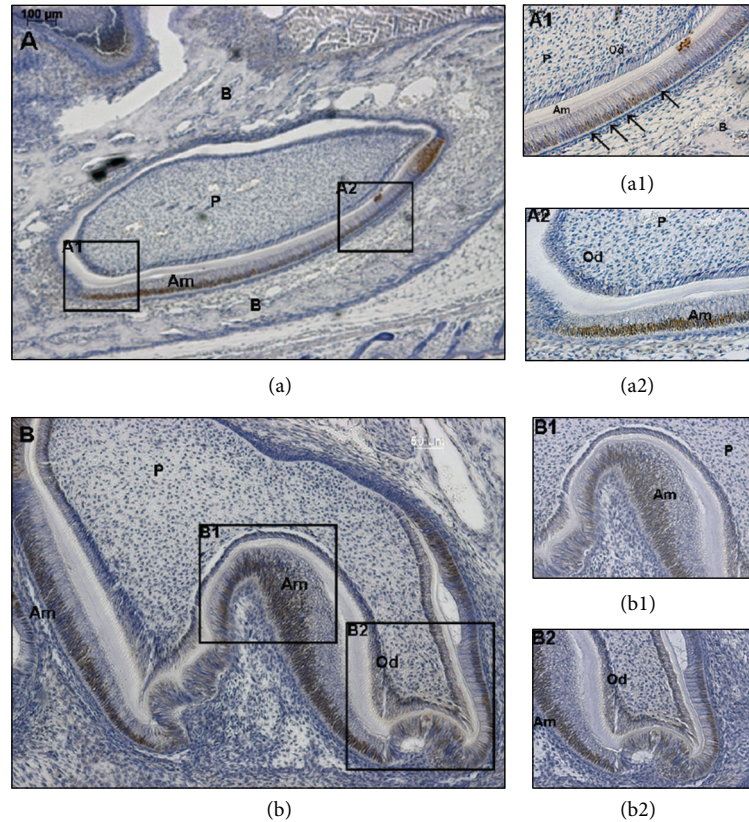


FIGURE 5: Localization of NUMB in odontogenic tissues at postnatal day 5: NUMB expression can be detected in the ameloblasts and odontoblasts. Notice that in (a1), NUMB is positively stained in some ameloblasts but negatively stained in the adjacent cells (indicated by arrows). Scale bar represents 100  $\mu\text{m}$  for (a); 50  $\mu\text{m}$  for (b); 20  $\mu\text{m}$  for (a1), (a2), and (b1), (b2), respectively.

analysis indicated that the 1.8 kb PCR fragment is consistent with the mRNA sequence of NUMB isoform 4. The 2 kb PCR fragment contains 236 bp insertion in the phosphotyrosine binding domain (PTB) 201 bp downstream of the initiation codon (Figure 1(b)). However, protein prediction analysis from the 2 kb DNA fragment did not lead to a longer protein product but a protein of 100 amino acids that contained an early termination codon.

**3.2. Expression of NUMB in Dental Cell Lines.** To investigate the subcellular localization of NUMB, immunocytochemical analysis was performed on human dental pulp stem cells (DPSCs), T4-4 preodontoblasts, and HAT-7 preameloblast cells (Figure 2). NUMB was clearly expressed in these 3 cell types. Specifically, NUMB was localized on the cell membrane, within the cytoplasm, and in the nucleus in only the DPSCs. In order to confirm the localization of NUMB on the cell membrane, plasma membrane patches from HAT-7 cells were used in immunostaining. The positively stained cell membrane patches by NUMB antibody confirmed the presence of NUMB on the cell membrane of HAT-7 cells (Figure 2(d)).

In order to identify the NUMB isoforms that are present in the dental tissue, Western blot analysis was performed using total protein lysates prepared from postnatal day 4 tooth germ and from the dental cell lines (Figure 3). All

the high molecular weight NUMB proteins ~72 KD and ~66 KDa were detected in all the dental tissues (proteins that have 1 KD difference were unable to be separated). To our surprise, multiple low molecular weight proteins located between 25 KD and 50 KD were also detected in the tooth germ as well as in HAT-7 cells. Since there are no published reports on the proteolytic cleavage of NUMB, we speculated that these could be due to NUMB isoforms expressed in dental tissues that have not yet been identified. While this work was in progress, two new isoforms, namely, NUMB 5 and NUMB 6 were published [32]. These proteins were described to be rare and were transiently expressed in cancer cells. The novel isoforms identified by Karaczyn et al. [32] appeared to have higher molecular weight than the proteins we identified. For the sake of simplicity, in Figure 3, we have described the 37–50 KD proteins as NUMB 7 and NUMB 8 and the 25–37 KD proteins as NUMB 9 and NUMB10. This needs to be further validated by mass spectrometry or protein sequencing analysis and determine if it is similar to the NUMB 7 and 8 isoform reported by Haider et al. in human placenta [11]. The ameloblast cell line, HAT-7 cells, expresses high levels of NUMB 1/2 and NUMB 3/4, as well as NUMB 9/10 but is deficient in the expression of NUMB 7/8. The dental pulp cells show very low levels of low molecular weight NUMB isoform expression. Among the high molecular weight NUMB isoforms, the NUMB 2/4

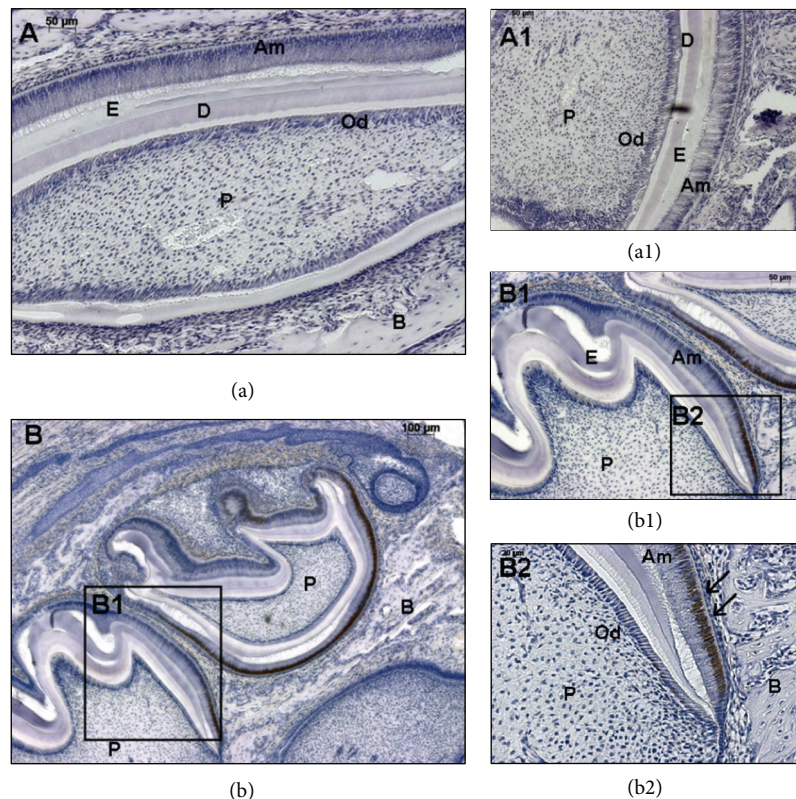


FIGURE 6: Localization of NUMB in odontogenic tissues at postnatal day 7: NUMB expression is more defined in the immature ameloblasts, and very low expression levels can be detected in the immature odontoblasts. Scale bar represents 50  $\mu\text{m}$  for (a), 100  $\mu\text{m}$  for (b), and 50 and 20  $\mu\text{m}$  for (a1), (b1), and (b2), respectively.

appeared to be the major isoforms in the dental tissue. These data suggest that there is differential expression of NUMB isoforms in dental tissues.

**3.3. Expression of NUMB in Developing Tooth Germs.** NUMB expression patterns were analyzed in the developing tooth germs from embryonic stage 13.5 to postnatal day 7 by immunohistochemistry. At E13.5, E16.5, and E18.5, there was no detectable NUMB expression in the developing tooth germs (data not shown). However, during postnatal tooth development, there was strong NUMB expression. Mouse incisors have enamel and dentin present on the labial surface, and only dentin on the lingual surface [33]. In P3 mouse incisor, NUMB protein was strongly expressed in the ameloblasts on the labial surface, in the cervical loop, in the odontoblasts at both labial and lingual surfaces, and in the dental pulp cells in close vicinity to the odontoblasts. In the P3 molar, NUMB expression can be detected in the ameloblasts, immature odontoblasts, and the dental pulp cells adjacent to the odontoblasts (Figure 4). In the P5 incisor, NUMB is localized in the ameloblasts and immature odontoblasts, and the expression is less intense compared to the P3 dental tissues. Also, there was no expression of NUMB in the dental pulp cells (Figure 5). In P7 dental tissues, the NUMB expression is more specifically limited to the stem cells of the stratum intermedium (Figure 6). Overall, in the postnatal dental tissues, NUMB is expressed in the ameloblast

progenitors in the cervical loop of the incisor, immature ameloblasts and odontoblasts, and in the dental pulp cells in the vicinity of the odontoblasts. Note that some ameloblasts in P5 and P7 express NUMB, but their neighboring cells do not, indicating that NUMB is asymmetrically distributed in the daughter cells.

**3.4. NUMB Downregulates Activated Notch 1.** The *in vivo* temporal and spatial expression pattern of NUMB in the developing tooth germ suggested that NUMB may play a role in regulating ameloblast differentiation. Our study shows that NUMB has a defined expression pattern in the ameloblast lineage cells, more specifically in the ameloblast progenitors and preameloblasts. Several publications have reported that Notch signaling is critical in ameloblast differentiation, and NUMB is involved in regulating Notch1 proteolysis. Therefore, we investigated the relationship of NUMB and Notch 1 in preameloblasts.

We first established that NUMB and Notch 1 colocalized in the same cell types. Activated Notch 1 was found to be strongly expressed in ameloblasts, odontoblasts, and dental pulp cells (see Supplementary Data 1 available online at <http://dx.doi.org/10.1155/2013/182965>). In order to study the functional relationship between NUMB and activated Notch 1, we generated NUMB overexpressing HAT-7 cells (Figure 7(a)). The activated Notch 1 expression pattern was evaluated by immunocytochemical analysis. Confocal



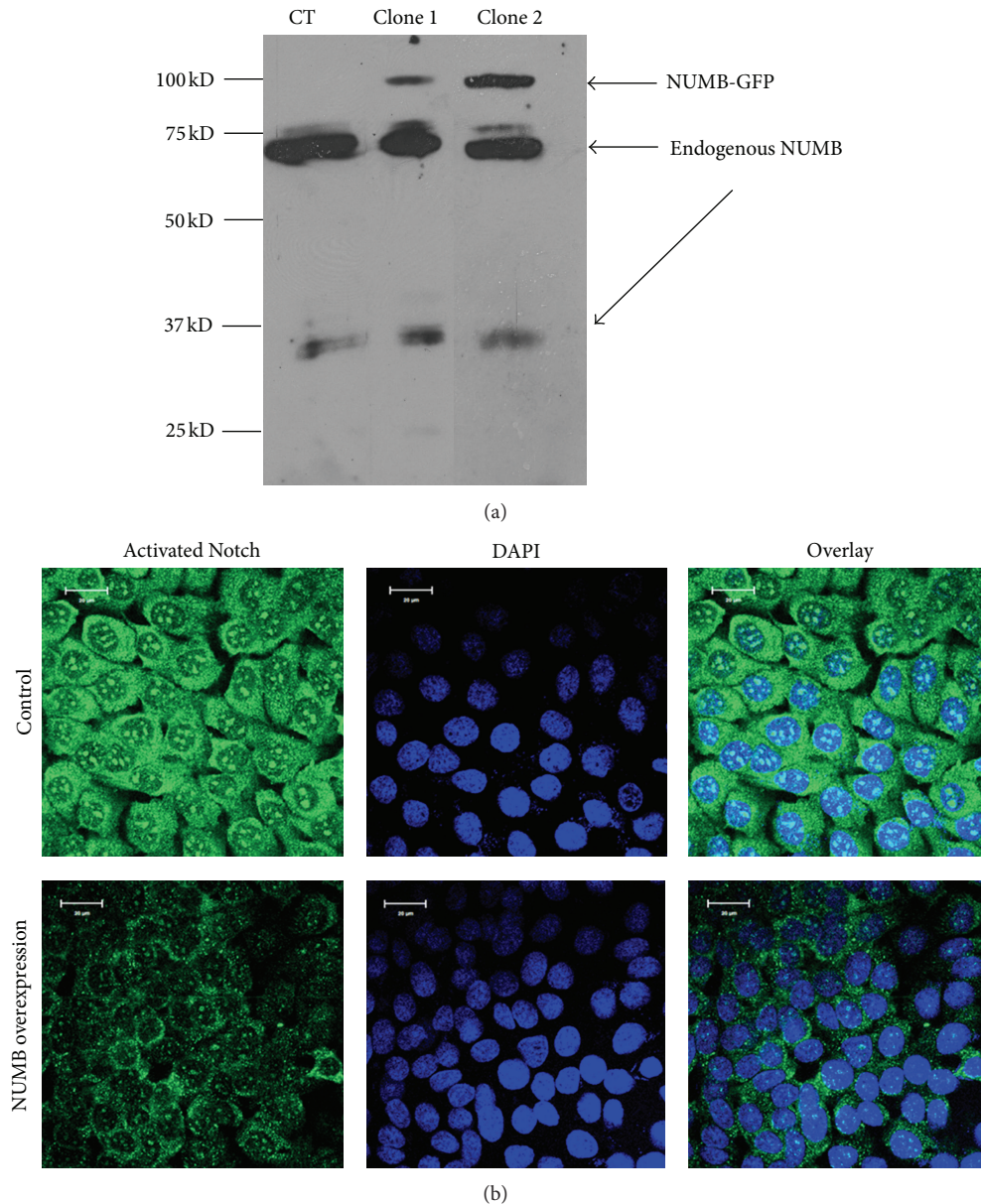


FIGURE 7: Overexpression of NUMB-GFP in HAT-7 cells: (a) Western blot analysis to detect overexpression of NUMB-GFP in HAT-7 cells. Total proteins were isolated from 2 clones, namely, clone 1 and 2. (b) Immunohistochemical analysis detected that Notch1 protein expression is dramatically reduced in the NUMB overexpressing cell line (stable cell line clone 2 was used). The green fluorescence represents activated Notch1 protein.

microscopy clearly indicated that the NUMB overexpressing HAT-7 cells had dramatically reduced expression of activated Notch 1 represented by the expression of green fluorescence (Figure 7(b)).

Next, we investigated the key players in the Notch 1 signaling pathway using a PCR-based array. The RT<sup>2</sup> Profiler PCR Array profiles the expression of 84 genes involved in Notch signaling. Results in Figure 9 show that NUMB mRNA is 7.5 times upregulated in the NUMB overexpressing cells compared to the control vector transfected cells. Majority of the genes in the Notch 1 signaling pathway were down-regulated. Noteworthy among them were Shh, Fos, Fzd2, and PParg with *P* values < 0.05 (Figure 8).

#### 4. Discussion

While we were isolating the NUMB isoforms expressed in dental pulp cells using primers designed to amplify the longest reading frame, we repeatedly obtained two PCR fragments. The 1.8 kb fragment is consistent with published NUMB isoform 4 cDNA sequence, while the 2 kb PCR fragment contained a 237 bp insertion in the PTB domain. The predicted protein sequence indicated an early termination codon which allows only 103 amino acids being translated. The NUMB antibody utilized in this study was raised against the NUMB C-terminal polypeptide (the synthetic peptide derived from residues 600 to the C-terminus of human NUMB). Therefore, isoforms that end upstream of this



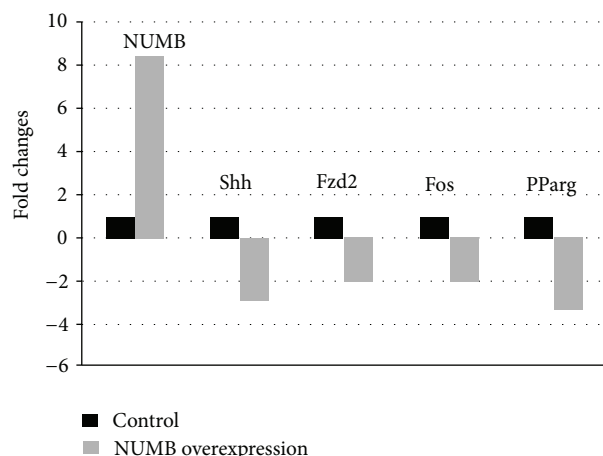


FIGURE 8: Notch signaling pathway PCR array. Genes from the Notch1 signaling pathway that were affected by NUMB overexpression.

polypeptide were not detected. The total protein lysate from the whole tooth germ contained all the detectable NUMB isoforms. The high molecular weight NUMB isoform which is the major published isoform is expressed in all dental tissues. 40 KDa isoform was detected in the odontoblasts, and the low molecular weight NUMB isoform (30 KDa) was predominantly expressed in the ameloblasts. While this paper was in preparation, 2 new NUMB isoforms, namely, NUMB 5 and 6 were reported and identified in the human cancer cells [32]. These two new isoforms are reported to be above 50 KD with 10 KD difference. They were characterized as being expressed rarely and transiently in these cancer cells. Recently, NUMB 7, 8, and 9 isoforms were identified by RT-PCR cloning in the human extravillous trophoblast [11]. In this study, four possible NUMB isoforms were detected in dental tissues. Further analysis is required to confirm the protein sequences. The differentially expressed NUMB isoforms in various dental tissues and possibly at different stages of tooth development suggest that NUMB might play specific functional role during tooth development.

Subcellular localization of NUMB in various odontogenic cell lines showed its localization in the cytoplasm, nucleus, and the cell membrane. Nuclear NUMB is particularly interesting, and its functional role in the nucleus has yet to be determined. Immunohistochemical analysis showed prominent NUMB expression during early tooth development. No NUMB expression was detected during embryonic development of the tooth. Strong NUMB expression was detected in the early postnatal development and was mainly localized in immature ameloblasts, preameloblasts, cervical loop, immature odontoblasts, and dental pulp cells.

As NUMB is regulated by Notch 1, we therefore examined the effect of overexpression of NUMB on Notch expression in preameloblasts. Results from this study showed that overexpression of NUMB dramatically reduced the expression of activated Notch 1 protein expression in HAT-7 cells. Further, we examined if the reduced expression of Notch1 had an effect on downstream signaling events. Results from this study showed that with NUMB overexpression (7.5-fold increase), several genes in the Notch signaling pathway

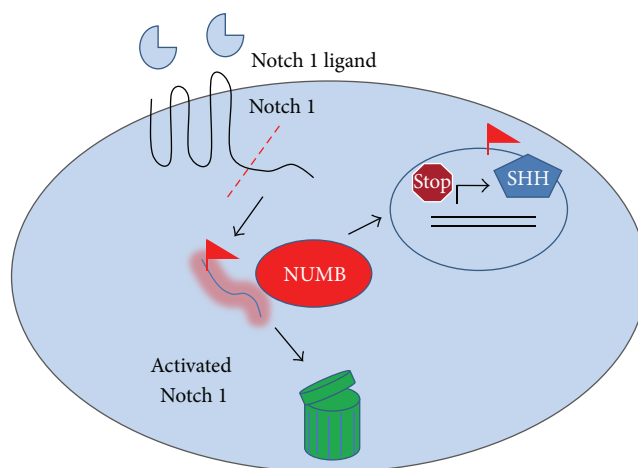


FIGURE 9: Hypothetical model. NUMB regulates stem cell properties at two levels. NUMB downregulates the expression of the activated Notch 1 protein level in the progenitor cells at the cervical loop and thereby inhibits the Shh expression in the adjacent preameloblasts. Thus, NUMB influences the expression of downstream genes such as Notch1 and Shh and thus performs critical role in ameloblast differentiation.

were downregulated. Most notable was the downregulation of sonic hedgehog.

The preameloblast HAT-7 cells used in this study were derived from the rat incisor cervical loop and its proximity [29]. This region contains stem cell population as well as immature preameloblasts. Based on our findings, we suggest that NUMB can have multiple effects on ameloblast differentiation by exerting its effect on both the stem cells and the preameloblasts. In the stem cells at the cervical loop, NUMB is highly expressed, and this downregulates Notch 1 which in turn inhibits Shh mRNA expression. Thus, the expression of NUMB is responsible for the maintenance of the progenitor cells in the cervical loop. During development, NUMB regulates the differentiation of preameloblasts into ameloblasts. In day 3, NUMB is expressed in the preameloblasts, but by day 7 there is less NUMB expression and thereby relieving its influence on suppressing the expression of Shh. This differential expression of NUMB and Shh in preameloblasts might be necessary for its differentiation and polarization. This observation corroborates well with published reports that demonstrate the critical role that NUMB plays in regulating cell polarization and differentiation [23–25].

Based on our findings, we propose a hypothetical model as shown in Figure 9. NUMB regulates the putative stem cell number and property by inhibiting Notch 1 signaling and thereby downregulating the expression of Shh. At the same time, NUMB can influence the differentiation of preameloblasts to ameloblasts. The signaling mechanism involved in this differentiation cascade will be pursued in the future.

## Conflict of Interests

The authors have no conflict of interests with any of the companies/manufactories whose products were utilized in this work.

## Acknowledgments

The authors would like to acknowledge the help from Dr. Shawn Li and Dr. Kozo Kaibuchi in providing them with the NUMB expression vectors and control vectors. This work is supported by NIH Grant DE 11657, Brodie Endowment Fund, research funding provided by Department of Orthodontics, University of Illinois at Chicago, and the American Association of Orthodontists Foundation (AAOF).

## References

- [1] S. Pece, S. Confalonieri, P. R. Romano, and P. P. Di Fiore, "NUMB-ing down cancer by more than just a NOTCH," *Biochimica et Biophysica Acta*, vol. 1815, no. 1, pp. 26–43, 2011.
- [2] J. Hao, K. Narayanan, T. Muni, A. Ramachandran, and A. George, "Dentin matrix protein 4, a novel secretory calcium-binding protein that modulates odontoblast differentiation," *The Journal of Biological Chemistry*, vol. 282, no. 21, pp. 15357–15365, 2007.
- [3] T. Uemura, S. Shepherd, L. Ackerman, L. Y. Jan, and Y. N. Jan, "Numb, a gene required in determination of cell fate during sensory organ formation in *Drosophila* embryos," *Cell*, vol. 58, no. 2, pp. 349–360, 1989.
- [4] E. P. Spana, C. Kopczynski, C. S. Goodman, and C. Q. Doe, "Asymmetric localization of numb autonomously determines sibling neuron identity in the *Drosophila* CNS," *Development*, vol. 121, no. 11, pp. 3489–3494, 1995.
- [5] W. Zhong, M. Jiang, M. D. Schonemann et al., "Mouse numb is an essential gene involved in cortical neurogenesis," *Proceedings of the National Academy of Sciences of the United States of America*, vol. 97, no. 12, pp. 6844–6849, 2000.
- [6] A. Gulino, L. Di Marcotullio, and I. Screpanti, "The multiple functions of Numb," *Experimental Cell Research*, vol. 316, no. 6, pp. 900–906, 2010.
- [7] S. E. Dho, M. B. French, S. A. Woods, and C. J. McGlade, "Characterization of four mammalian numb protein isoforms. Identification of cytoplasmic and membrane-associated variants of the phosphotyrosine binding domain," *The Journal of Biological Chemistry*, vol. 274, no. 46, pp. 33097–33104, 1999.
- [8] J. M. Verdi, A. Bashirullah, D. E. Goldhawk et al., "Distinct human NUMB isoforms regulate differentiation vs. proliferation in the neuronal lineage," *Proceedings of the National Academy of Sciences of the United States of America*, vol. 96, no. 18, pp. 10472–10476, 1999.
- [9] P. H. Petersen, K. Zou, S. Krauss, and W. Zhong, "Continuing role for mouse Numb and Numbl in maintaining progenitor cells during cortical neurogenesis," *Nature Neuroscience*, vol. 7, no. 8, pp. 803–811, 2004.
- [10] Y. Zhou, J. B. Atkins, S. B. Rompani et al., "The mammalian Golgi regulates numb signaling in asymmetric cell division by releasing ACBD3 during mitosis," *Cell*, vol. 129, no. 1, pp. 163–178, 2007.
- [11] M. Haider, Q. Qiu, M. Bani-Yaghoob, B. K. Tsang, and A. Gruslin, "Characterization and role of NUMB in the human extravillous trophoblast," *Placenta*, vol. 32, no. 6, pp. 441–449, 2011.
- [12] T. A. Mitsiadis, A. S. Tucker, C. De Bari, M. T. Cobourne, and D. P. Rice, "A regulatory relationship between Tbx1 and FGF signaling during tooth morphogenesis and ameloblast lineage determination," *Developmental Biology*, vol. 320, no. 1, pp. 39–48, 2008.
- [13] C. E. Smith and H. Warshawsky, "Cellular renewal in the enamel organ and the odontoblast layer of the rat incisor as followed by radioautography using 3H thymidine," *Anatomical Record*, vol. 183, no. 4, pp. 523–561, 1975.
- [14] T. A. Mitsiadis, E. Hirsinger, U. Lendahl, and C. Goridis, "Delta-Notch signaling in odontogenesis: correlation with cytodifferentiation and evidence for feedback regulation," *Developmental Biology*, vol. 204, no. 2, pp. 420–431, 1998.
- [15] K. Seidel, C. P. Ahn, D. Lyons et al., "Hedgehog signaling regulates the generation of ameloblast progenitors in the continuously growing mouse incisor," *Development*, vol. 137, no. 22, pp. 3753–3761, 2010.
- [16] H. R. Dassule, P. Lewis, M. Bei, R. Maas, and A. P. McMahon, "Sonic hedgehog regulates growth and morphogenesis of the tooth," *Development*, vol. 127, no. 22, pp. 4775–4785, 2000.
- [17] J. J. Breunig, J. Silbereis, F. M. Vaccarino, N. Šestan, and P. Rakic, "Notch regulates cell fate and dendrite morphology of newborn neurons in the postnatal dentate gyrus," *Proceedings of the National Academy of Sciences of the United States of America*, vol. 104, no. 51, pp. 20558–20563, 2007.
- [18] H. Harada, P. Kettunen, H. Jung, T. Mustonen, Y. A. Wang, and I. Thesleff, "Localization of putative stem cells in dental epithelium and their association with Notch and FGF signaling," *Journal of Cell Biology*, vol. 147, no. 1, pp. 105–120, 1999.
- [19] S. Felszeghy, M. Suomalainen, and I. Thesleff, "Notch signalling is required for the survival of epithelial stem cells in the continuously growing mouse incisor," *Differentiation*, vol. 80, no. 4–5, pp. 241–248, 2010.
- [20] M. A. McGill and C. J. McGlade, "Mammalian Numb proteins promote Notch1 receptor ubiquitination and degradation of the Notch1 intracellular domain," *The Journal of Biological Chemistry*, vol. 278, no. 25, pp. 23196–23203, 2003.
- [21] M. A. McGill, S. E. Dho, G. Weinmaster, and C. J. McGlade, "Numb regulates post-endocytic trafficking and degradation of notch1," *The Journal of Biological Chemistry*, vol. 284, no. 39, pp. 26427–26438, 2009.
- [22] L. Di Marcotullio, E. Ferretti, A. Greco et al., "Numb is a suppressor of Hedgehog signalling and targets Gli1 for Itch-dependent ubiquitination," *Nature Cell Biology*, vol. 8, no. 12, pp. 1415–1423, 2006.
- [23] T. Ito, H. Y. Kwon, B. Zimdahl et al., "Regulation of myeloid leukaemia by the cell-fate determinant Musashi," *Nature*, vol. 466, no. 7307, pp. 765–768, 2010.
- [24] D. Berdnik, T. Török, M. González-Gaitán, and J. A. Knoblich, "The endocytic protein  $\alpha$ -adaptin is required for numb-mediated asymmetric cell division in *Drosophila*," *Developmental Cell*, vol. 3, no. 2, pp. 221–231, 2002.
- [25] S. X. Atwood and K. E. Prehoda, "aPKC phosphorylates Miranda to polarize fate determinants during neuroblast asymmetric cell division," *Current Biology*, vol. 19, no. 9, pp. 723–729, 2009.
- [26] G. Chapman, L. Liu, C. Sahlgren, C. Dahlqvist, and U. Lendahl, "High levels of Notch signaling down-regulate Numb and Numlike," *Journal of Cell Biology*, vol. 175, no. 4, pp. 535–540, 2006.
- [27] R. Stan, W. Gregory Roberts, D. Predescu et al., "Immunolocalization and partial characterization of endothelial plasmalemmal vesicles (caveolae)," *Molecular Biology of the Cell*, vol. 8, no. 4, pp. 595–605, 1997.
- [28] S. Ravindran, Q. Gao, A. Ramachandran, S. Blond, S. A. Predescu, and A. George, "Stress chaperone GRP-78 functions

- in mineralized matrix formation,” *The Journal of Biological Chemistry*, vol. 286, no. 11, pp. 8729–8739, 2011.
- [29] S. Kawano, T. Morotomi, T. Toyono et al., “Establishment of dental epithelial cell line (HAT-7) and the cell differentiation dependent on Notch signaling pathway,” *Connective Tissue Research*, vol. 43, no. 2-3, pp. 409–412, 2002.
- [30] Z. Wang, S. Sandiford, C. Wu, and S. S. Li, “Numb regulates cell-cell adhesion and polarity in response to tyrosine kinase signalling,” *EMBO Journal*, vol. 28, no. 16, pp. 2360–2373, 2009.
- [31] T. Nishimura and K. Kaibuchi, “Numb controls integrin endocytosis for directional cell migration with aPKC and PAR-3,” *Developmental Cell*, vol. 13, no. 1, pp. 15–28, 2007.
- [32] A. Karaczyn, M. Bani-Yaghoub, R. Tremblay et al., “Two novel human NUMB isoforms provide a potential link between development and cancer,” *Neural Development*, vol. 5, no. 1, article 31, 2010.
- [33] T. A. Mitsiadis and D. Graf, “Cell fate determination during tooth development and regeneration,” *Birth Defects Research C*, vol. 87, no. 3, pp. 199–211, 2009.

## Research Article

# Mineral and Matrix Changes in *Brtl/+* Teeth Provide Insights into Mineralization Mechanisms

Adele L. Boskey,<sup>1</sup> Kostas Verdelis,<sup>2</sup> Lyudmila Spevak,<sup>1</sup> Lyudmila Lukashova,<sup>1</sup>  
Elia Beniash,<sup>3</sup> Xu Yang,<sup>3</sup> Wayne A. Cabral,<sup>4</sup> and Joan C. Marini<sup>4</sup>

<sup>1</sup> Musculoskeletal Integrity Program, Hospital for Special Surgery, 535 E 70th Street, New York, NY 10021, USA

<sup>2</sup> Department of Endodontics, School of Dental Medicine, University of Pittsburgh, 3501 Terrace Street, Pittsburgh, PA 15261, USA

<sup>3</sup> Department of Oral Biology, School of Dental Medicine, University of Pittsburgh, 3501 Terrace Street, Pittsburgh, PA 15261, USA

<sup>4</sup> Bone & Extracellular Matrix Branch, NIH/ NICHD, Bethesda, MD 20892, USA

Correspondence should be addressed to Adele L. Boskey; [boskeya@hss.edu](mailto:boskeya@hss.edu)

Received 11 January 2013; Revised 27 March 2013; Accepted 3 May 2013

Academic Editor: Yong-Hee P. Chun

Copyright © 2013 Adele L. Boskey et al. This is an open access article distributed under the Creative Commons Attribution License, which permits unrestricted use, distribution, and reproduction in any medium, provided the original work is properly cited.

The *Brtl/+* mouse is a knock-in model for osteogenesis imperfecta type IV in which a Gly349Cys substitution was introduced into one COL1A1 allele. To gain insight into the changes in dentin structure and mineral composition in these transgenic mice, the objective of this study was to use microcomputed tomography (micro-CT), scanning electron microscopy (SEM), and Fourier transform infrared imaging (FTIRI) to analyze these structures at 2 and 6 months of age. Results, consistent with the dental phenotype in humans with type IV OI, showed decreased molar volume and reduced mineralized tissue volume in the teeth without changes in enamel properties. Increased acid phosphate content was noted at 2 and 6 months by FTIRI, and a trend towards altered collagen structure was noted at 2 but not 6 months in the *Brtl/+* teeth. The increase in acid phosphate content suggests a delay in the mineralization process, most likely associated with the defect in the collagen structure. It appears that in the *Brtl/+* teeth slow maturation of the mineralized structures allows correction of altered mineral content and acid phosphate distribution.

## 1. Introduction

Osteogenesis imperfecta (OI) and dentinogenesis imperfecta (DGI) are rare genetic diseases associated, for the most part, with abnormalities in collagen structure, production, or processing, which result in fragile (brittle) mineralized tissues [1–4]. In addition to the four types of OI originally described by Sillence et al. [5], additional types have been identified in humans [6], and their underlying molecular origins for the most part have been determined. The reasons for the variation in mineralization and mechanical properties in OI and DGI are less certain. The *Brtl/+* mouse is a knock-in model for moderately severe OI in which a Gly349Cys substitution identified in a child with type IV OI was introduced into one COL1A1 allele, resulting in a phenotype representative of type IV OI [7]. Changes in the whole bone mechanical strength and collagen D-spacing in these *Brtl/+* mice have previously been reported [8, 9] along with variations in their osteoblast and osteoclast activities [10]. The animals were also noted,

based on light microscopy, to have a DGI phenotype at 2 months due to changes in the pulp cavities of their teeth [7]. The purpose of the present study was to gain further insight into the mineralization and collagen defects in *Brtl/+* mouse teeth using a combination of Fourier transform infrared microscopic imaging (FTIRI), scanning electron microscopy (SEM), and microcomputed tomography (micro-CT) and to use this information to elucidate the mechanism underlying these defects.

## 2. Materials and Methods

**2.1. Animals.** The *Brtl/+* mice were derived as described [7] and sacrificed for other purposes under an NIH-approved IACUC approval at two and six months. The mice were fed a standard (NIH 31) chow and were given sterilized fluoridated tap water, ad libitum. *Brtl/+* mice have a mixed background of Sv129/CD-1/C57BL/6S and are bred by crossing heterozygous



Brtl/+ with WT [7]. Based on preliminary analyses using GraphPad StatMate 2.0 (GraphPad Corp, San Diego, CA, USA) it was determined that to detect a significant difference with a power of 80% in mineral/matrix content by FTIRI, six teeth would be needed at 2 months of age. Jaws ( $n = 6$  per genotype), provided frozen, were fixed in ethanol for micro-CT analyses. Jaws were then embedded in polymethyl methacrylate (PMMA) for backscattered SEM and Fourier transform infrared imaging (FTIRI).

**2.2. Micro-CT.** Three-dimensional architecture and geometry of both the crowns and roots of first and second molars were determined by microcomputed tomography using a Scanco  $\mu$ CT35 (Scanco Medical, Basselsdorf, Switzerland) system with a  $12\ \mu\text{m}$  voxel size at 55 kVp as detailed elsewhere [11, 12]. Crown and root regions of interest were generated by defining the respective contours on sequential reconstructed volume slices [12, 13]. Because of clear and consistent respective interfaces, the segmentation of dentin from the background and enamel from dentin was based on 0.6 and 1.7 g/cc, respectively, global thresholds. The parameters evaluated were tissue volume (TV-representing the total crown or root volume including the pulp or root canal space), enamel + dentin volume (BV), the volumes of Enamel and Dentin separately (EV and DV), the mineral density for each fraction (TMD (E) and TMD (D)), and the tissue volume fraction (BV/TV). All parameters were evaluated on the molar 3D volumes using the crown and root regions of interest through the Scanco evaluation software operating in an open VMS environment. Mineral density for dentin was calculated on basis of the dentin/background segmentation value as a minimum threshold and the dentin/enamel one as a maximum threshold, while the enamel mineral density was calculated using only the dentin/enamel segmentation value as a minimum threshold with maximum threshold kept as the highest available in the scale. The Scanco system uses built-in beam energy-specific algorithms for the conversion of attenuation coefficient into  $\text{mg}/\text{cm}^3$  values.

**2.3. Backscattered Scanning Electron Microscopy (BS SEM).** First and second mandibular molars were embedded in PMMA resin and polished on a MiniMet polisher (Buehler, Lake Bluff, IL, USA) down to  $0.25\ \mu\text{m}$  using series of MetaDi diamond suspensions, as previously described [14]. Three WT and 3 Brtl/+ samples were studied in JEOL 6335F Field Emission SEM equipped with a backscattered electron detector. The microscopy was conducted at 10 KV and at a working distance of 14 mm.

**2.4. Fourier Transform Infrared Imaging.** Multiple sections (1-2 microns) of nondecified molars, embedded in PMMA, were examined by Fourier transform infrared spectroscopic imaging (Perkin Elmer model Spotlight 100 imaging system) as detailed elsewhere [15, 16]. In brief, dentin spectral images from the whole crown (sectioned along the sagittal plane) or root areas (the mesial or distal root, imaged separately) from first and second molars were examined at  $4\ \mu\text{m}$  spatial resolution. ISYS software (Spectral Dimensions, Olney, MD,

USA) was used to process the data, including a subtraction of water vapor and PMMA. Parameters calculated and exhibited as images were (i) mineral-to-matrix ratios (Min/Mat, a comparison of the relative ratios of the integrated intensities of the  $\nu_1$ ,  $\nu_3$  phosphate band,  $\sim 900\text{--}1200\ \text{cm}^{-1}$  to that of the protein amide I band (centered at  $1660\ \text{cm}^{-1}$ )), (ii) carbonate ( $855\text{--}890\ \text{cm}^{-1}$ ) to phosphate band area ratio ( $\text{CO}_3/\text{PO}_4$ , indicating carbonate substitution for phosphate in the mineral) (iii) crystallinity (XST, an estimate of crystallite size and perfection, based on the proportion of stoichiometric and non-stoichiometric apatite), (iv) collagen maturity (XLR, a peak height ratio of subbands in the collagen amide I peak), and (v) acid phosphate content  $\text{HPO}_4$ , ( $1128\ \text{cm}^{-1}/1096\ \text{cm}^{-1}$ ) an estimate of the amount of acid phosphate substitution in the mineral lattice. The validation of these parameters is described in detail elsewhere [15–17].

**2.5. Statistics.** The mean values and standard deviations for each tissue type and each parameter in each animal were calculated and the values were compared by ANOVA between Brtl/+ and WT crown and root areas, followed by a Bonferroni multiple comparison test. Due to the limited number of animals available for analysis no correction for animal sex was made. Where multiple comparisons of data were involved, a  $P < (0.05/n)$ , where  $n$  is the number of comparisons, was considered significant.

### 3. Results

The molars of the Brtl/+ animals differed from those of the WT when examined by micro-CT (Figures 1(a) and 1(b)) with small but significant ( $P < 0.01$ ) decrease in the first and second molar Brtl/+ crowns and root total volume and dentin volumes relative to WT at 2 months and 6 months (Table 1). This decrease of dentin thickness was most pronounced in the root. The mineralized tissue volume fraction (BV/TV) was decreased in the root of the Brtl/+ molars at both 2 and 6 months. There was a small, not consistent increase in the first and second molars, crowns and root mineral density in the Brtl/+ molars at 2 months. As previously noted [7], both first and second molars had widened pulp spaces and a disorganized bone structure around the molar roots.

No major morphological difference between Brtl/+ (Figure 2) and wild type (Figure 3) mandibular molars was observed by backscattered electron imaging, based on the analysis of 3 samples per group. The density and organization of dentinal tubules were similar in WT and Brtl/+ molars. The reduced dentin thickness and increased pulp chamber size in Brtl/+ molars observed in the micro-CT 3-dimensional volumes were not noticeable in the SEM images. Only one tooth had an abnormal mesial root with thin root dentin and a wide root canal. Interestingly, the presence of globular dentin was observed in the cervical portions of the roots of all Brtl/+ molars (Figure 2), while no globular dentin was detected in wild type molars (Figure 3). At higher magnifications, however, significant abnormalities in dentin mineralization in Brtl/+ were observed. Specifically, noticeable variations in

TABLE 1: Micro-CT parameters measured in Brtl/+ and wild type molars at 2 and 6 months.

	Two months				Six months			
	First molars		Second molars		First molars		Second molars	
	Brtl/+	WT	Brtl/+	WT	Brtl/+	WT	Brtl/+	WT
Crown								
BV (D + E) mm <sup>3</sup>	0.552 ± 0.0002 <sup>a</sup>	0.578 ± 0.0003	0.286 ± 0.0003 <sup>a</sup>	0.342 ± 6.71E - 05	0.516 ± 0.0015	0.552 ± 0.0004	0.293 ± 1.44E - 05 <sup>a</sup>	0.332 ± 0.0010
BV (D) mm <sup>3</sup>	0.404 ± 0.0001 <sup>a</sup>	0.435 ± 0.0005	0.200 ± 0.0001 <sup>a</sup>	0.247 ± 0.0001	0.368 ± 0.0007 <sup>a</sup>	0.411 ± 0.0002	0.195 ± 1.98E - 05 <sup>a</sup>	0.235 ± 0.0007
BV (E) mm <sup>3</sup>	0.148 ± 7.69E - 05	0.143 ± 7.58E - 05	0.086 ± 5.35E - 05 <sup>a</sup>	0.095 ± 2.99E - 05	0.148 ± 0.0002	0.141 ± 2.64E - 05	0.098 ± 3.76E - 05	0.098 ± 8.37E - 05
TMD (D) mg/cm <sup>3</sup>	1327 ± 336 <sup>a</sup>	1266 ± 304	1275 ± 1121	1264.9 ± 271	1337 ± 1080	1306 ± 267	1328 ± 1907	1299 ± 295
TMD (E) mg/cm <sup>3</sup>	2024 ± 627	2005 ± 329	1996 ± 382	1995.6 ± 347	2008 ± 1436	2007 ± 244	2002 ± 1346	2006 ± 96
Root								
TV mm <sup>3</sup>	0.482 ± 0.0005 <sup>a</sup>	0.544 ± 0.0004	0.243 ± 0.0001 <sup>a</sup>	0.309 ± 0.0002	0.557 ± 0.0014 <sup>a</sup>	0.610 ± 0.0005	0.294 ± 0.0008 <sup>a</sup>	0.355 ± 0.0004
BV mm <sup>3</sup>	0.362 ± 0.0007 <sup>a</sup>	0.460 ± 0.0004	0.111 ± 0.0014 <sup>a</sup>	0.253 ± 0.0002	0.430 ± 0.0034 <sup>a</sup>	0.530 ± 0.0004	0.211 ± 0.025 <sup>a</sup>	0.303 ± 0.0004
BV/TV%	0.752 ± 0.003 <sup>a</sup>	0.845 ± 0.0002	0.454 ± 0.021 <sup>a</sup>	0.820 ± 0.0001	0.773 ± 0.086 <sup>a</sup>	0.870 ± 8.03E - 05	0.712 ± 0.018 <sup>a</sup>	0.853 ± 0.0003
TMD mg/cm <sup>3</sup>	1146 ± 416	1162 ± 406	1056 ± 2187 <sup>a</sup>	1131 ± 704	1177 ± 2709	1227 ± 684	1141 ± 2945	1199.4 ± 644

<sup>a</sup> P < 0.0125 versus WT of same age and same tooth type, n = 6/genotype.

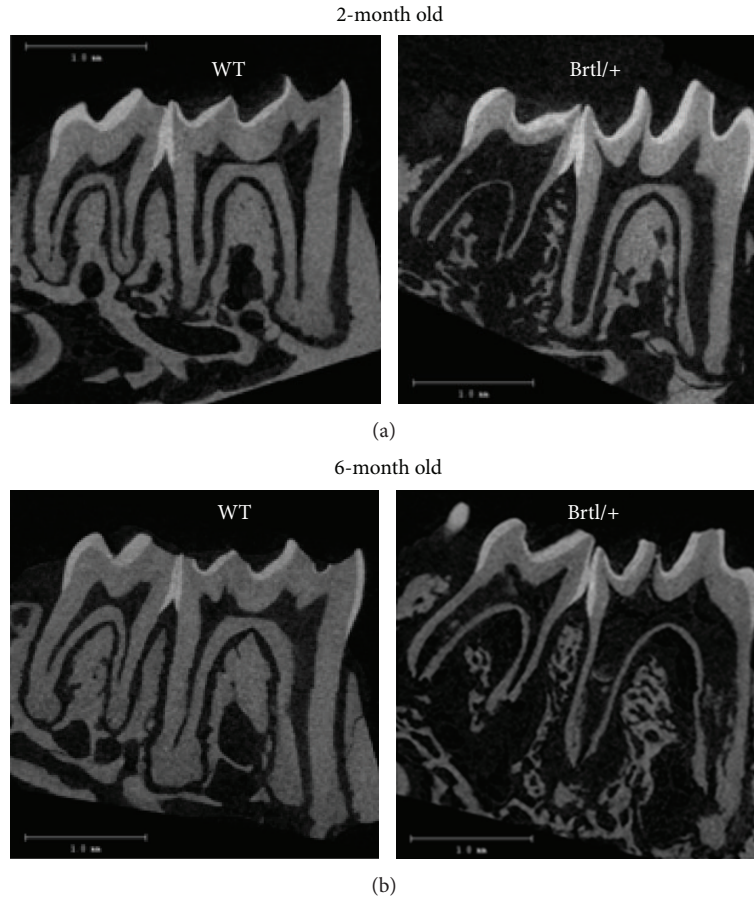


FIGURE 1: Sagittal views from micro-CT images of Brtl/+ and WT first and second molars at (a) 2 and (b) 6 months. Brtl/+ images show wide pulp spaces and decreased dentin thickness, more pronounced in the root, compared to age matched WT. Note the disorganized trabecular jaw bone around the Brtl/+ roots.

the dentin density were observed in the  $\sim 50\ \mu\text{m}$  thick proximal dentin layer adjacent to the pulp cavity (Figure 2(c)). Additional studies are needed to further investigate this phenomenon.

Fourier transform infrared imaging (FTIRI) of the molars showed the average mineral/matrix ratio not being significantly altered in the Brtl/+ molars at both 2 and 6 months (Table 2). In fact, the only significant differences in the mean values of the FTIRI images of the teeth were in the acid phosphate content, which was increased in the Brtl/+ roots and crowns at both ages. The distribution of mineral/matrix ratio, crystallinity, and acid phosphate content looked different in typical images of the molars and roots (Figure 4). These “chemical photographs” [18] show, as is typical for mouse molar sections, a broad distribution of mineral properties with visibly increased mineral/matrix ratio in the Brtl/+ molars, as shown in terms of standard deviation in Table 2. The sharp lines and small holes in the section (indicated by arrows) are an artifact due to folds and actual holes made during sectioning and were not included when the average values were calculated. The increased acid phosphate accumulation was apparent in the images (far right column, Figure 4). In the 2-month-old animals the mean crystallinity tended to be reduced in the Brtl/+ crowns and roots, and at

6 months there were some differences in  $\text{CO}_3/\text{PO}_4$  ratio, but the most significant differences were in the acid phosphate substitution.

#### 4. Discussion

Dentin and enamel mineralizations occur on different types of matrices. The enamel matrix mineralization is influenced by globular proteins such as amelogenin and enamelin [19, 20] which constitute a small fraction of the final mineralized matrix. Dentin mineralization, by contrast, is controlled by the fibrous protein collagen and its associated noncollagenous proteins [21] which persist throughout the lifetime of the tissue. Many of the noncollagenous proteins are intrinsically disordered and assume conformations to match their binding partners [22], such as collagen and hydroxyapatite mineral. In the Brtl/+ molars, the defect in the collagen structure [9] may affect the binding and the concentration of these noncollagenous proteins, their synthesis by collagen producing cells, and their ability to regulate mineralization, as occurs in both Brtl/+ stem cells and bone [23]. This is seen in the data at both 2 and 6 months, where the teeth are smaller and the mineral properties of the dentin, but not the enamel, are distinct from those of the wild type.



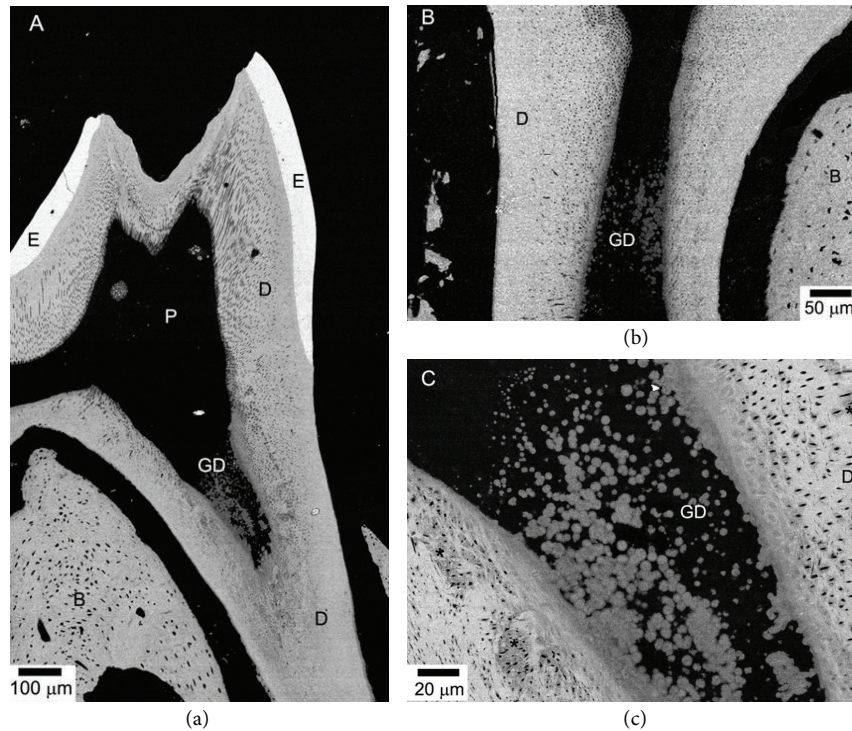


FIGURE 2: BS SEM micrographs of *Brtl/+* mandibular molars. (a) Low resolution micrograph showing overall morphology of the tooth. Note an area of globular dentin (GD) in the cervical root. (b) A micrograph of a molar from a different animal also featuring GD. (c) Closeup of the area containing GD from (a). Note the variations in the degree of mineralization. B: bone, D: dentin, E: enamel, and P: pulp. Asterisks mark undermineralized areas.



FIGURE 3: BS SEM micrograph of WT mandibular molars. Abbreviations are as in Figure 2.

There is only one report of changes in mouse molar micro-CT parameters with age, in which fibromodulin-deficient mice at 3 weeks and 10 weeks were compared to wild type mice, and a reversal of phenotypic differences was found [24]. It is not clear from only two time points in each of the

fibromodulin studies whether older animals begin to show degradation of their teeth or whether the KO animal's molars simply begin to approach the WT values as they age. This is one of the limitations of our *Brtl/+* study as we only studied animals at 2 and 6 months. It might have been interesting if we had included teeth from *Brtl/+* mice at a younger age. The increases in mineralization of teeth with age, along with the altered collagen structure, imply that the hypermineralization in this variant of classical OI is associated with an abnormal collagen matrix and provide one possible mechanism for the way these abnormal collagen matrices could affect initial mineralization. In the mice studied here, the 2-month-old *Brtl/+* mice have completed their tooth development and have been weaned for about a month. Thus they are chewing their food, and the phenotypic difference between their less mineralized teeth and those of the wild type animals may be more apparent than those which are noted at 6 months when age-related physiologic effects (grinding of the teeth, change in curvature due to alveolar osteoclasts, etc. [25]) may mask the *Brtl/+* phenotype.

Our data represent the first quantitative evaluations of the mineral properties of the teeth in *Brtl/+* mice. Earlier studies had reported the presence of widened and infected pulp cavities characteristic of dentinogenesis imperfecta in patients with osteogenesis imperfecta [7]. Although age-dependent changes were noted in both WT and *Brtl/+* molars, the absence of studies monitoring age-dependent change in healthy mice teeth during development made it



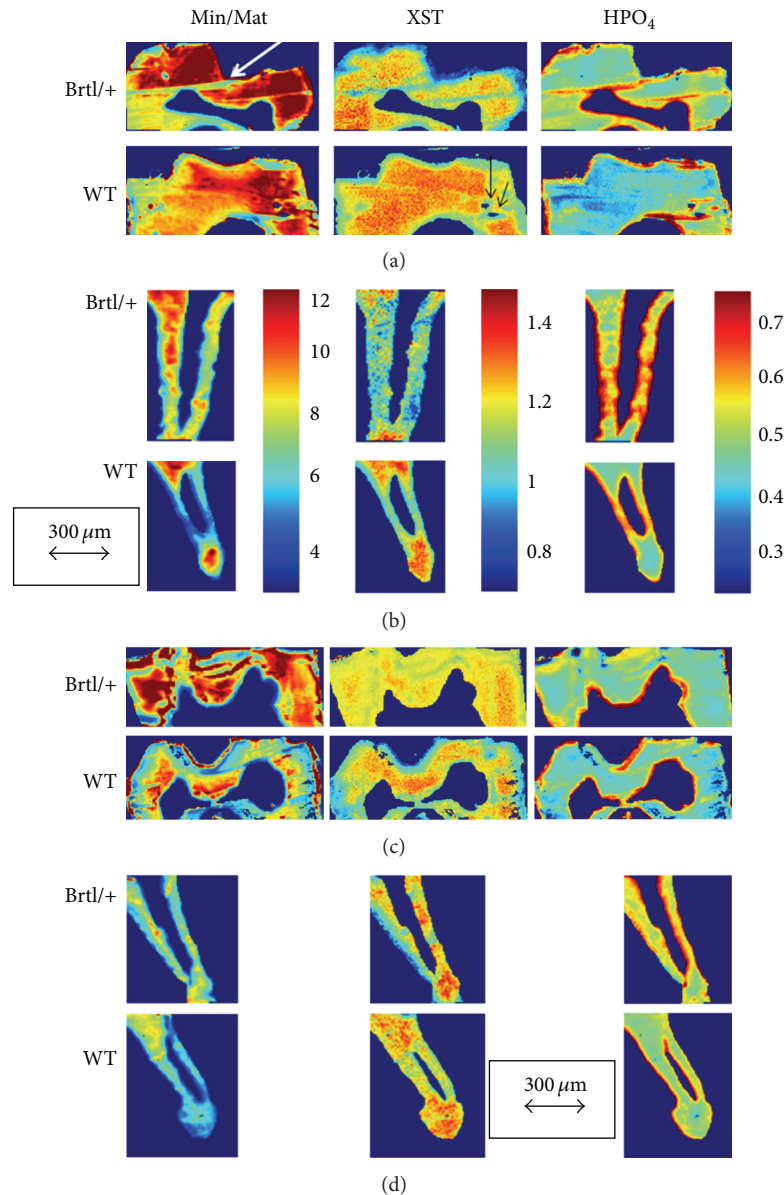


FIGURE 4: Typical FTIRI images for Brtl/+ and WT molars showing mineral/matrix ratio (Min/Mat), crystal size and perfection (XST), and acid phosphate content ( $\text{HPO}_4$ ) in (a) first molar crowns at 2 months; (b) second molar root at 2 months; (c) first molar crowns at 6 months; and (d) second molar root at 6 months. The arrows indicate the distance corresponding to  $300\ \mu\text{m}$ . The color bars shown for (b) are the same for all similar parameters in the figure. White arrow indicates folds in specimen while black arrows show holes in the replicate images. These areas were masked when calculating numeric data.

difficult to comment on the effect of the transgene in this study. However there is definitely a suggestion of impaired matrix formation which in turn leads to the persistence of a more acid phosphate containing mineral phase in the Brtl/+ molars at both ages. Acid phosphate is present to a greater extent in newly deposited mineral [16]. The observation that no significant change in mineral/matrix ratio was detected in the FTIRI analysis of the molars agreed with the finding of no change in dentin or enamel mineral density but may indicate that these tissues were already fully mineralized by 2 months as suggested by a comparison of the mineral/matrix ratios of comparable sites in wild type teeth at 2 and 6 months.

The presence of globular dentin in the cervical areas of the roots and density variations in the proximal dentin of Brtl/+ detected by SEM is suggestive of mild dysplasia associated with dentinogenesis imperfecta type I (DGI-I), a dental manifestation of osteogenesis imperfecta [26–28]. Although a globular mineralization pattern can be found in normal teeth, where interglobular areas eventually mineralize, extensive areas of globular dentin are often associated with biomineralization abnormalities such as vitamin D deficient X-linked hypophosphatemia, vitamin D deficiency [29–31], and DGI-I.

Brtl/+ mice demonstrate bone fragility, a moderately deformed skeleton, and a low ductility phenotype, accurately

TABLE 2: FTIRI analysis of Brtl/+ and WT molars (all values are dimensionless ratios).

	Min/Mat	CO <sub>3</sub> /PO <sub>4</sub>	XLR	XST	HPO <sub>4</sub>
2 months					
First molar crown					
WT	10.6 ± 1.0	0.0052 ± 0.0003	4.06 ± 0.20	1.184 ± 0.05	0.44 ± 0.04
BRTL/+	11.0 ± 2.0	0.0051 ± 0.0007	4.07 ± 0.37	1.13 ± 0.03	0.48 ± 0.03
P	NS	NS	NS	0.06	0.07
Second molar crown					
WT	10.3 ± 1.0	0.0050 ± 0.0004	4.1 ± 0.29	1.171 ± 0.06	0.450 ± 0.03
BRTL/+	10.6 ± 3.0	0.0050 ± 0.0004	4.2 ± 0.37	1.133 ± 0.04	0.469 ± 0.04
P	NS	NS	NS	NS	NS
First molar mesial root					
WT	7.99 ± 0.94	0.0053 ± 0.0004	3.97 ± 0.19	1.175 ± 0.041	0.46 ± 0.03
BRTL/+	7.28 ± 1.54	0.0047 ± 0.0007	4.21 ± 0.39	1.14 ± 0.025	0.53 ± 0.05
P	NS	NS	0.08	NS	0.009
Second molar distal root					
WT	6.78 ± 1.0	0.0048 ± 0.0004	4.38 ± 0.89	1.15 ± 0.076	0.51 ± .04
BRTL/+	6.54 ± 0.75	0.0048 ± 0.0006	4.97 ± 0.85	1.09 ± 0.087	0.61 ± 0.05
P	NS	NS	NS	0.10	0.001
6 months					
First molar crown					
WT	10.9 ± 2.2	0.0066 ± 0.0005	4.1 ± 0.3	1.1 ± 0.02	0.45 ± 0.02
Brtl/+	13.0 ± 2.6	0.0064 ± 0.0008	4.4 ± 0.7	1.1 ± 0.01	0.49 ± 0.01
P	NS	NS	NS	NS	0.015
Second molar crown					
WT	9.0 ± 0.2	0.0063 ± 0.0006	4.1 ± 0.2	1.1 ± 0.01	0.48 ± 0.04
Brtl/+	9.8 ± 1.5	0.0064 ± 0.0007	4.2 ± 1.1	1.06 ± 0.51	0.51 ± 0.05
P	NS	NS	NS	NS	NS
Second molar mesial root					
WT	7.1 ± 0.8	0.0062 ± 0.0003	4.2 ± 0.3	1.08 ± 0.03	0.53 ± 0.02
Brtl/+	6.7 ± 1.5	0.0053 ± 0.0004	4.4 ± 0.4	1.09 ± 0.02	0.61 ± 0.15
P	NS	0.0009	NS	NS	NS
Second molar distal root					
WT	7.9 ± 0.5	0.0065 ± 0.0004	4.5 ± 0.3	1.08 ± 0.03	0.49 ± 0.03
Brtl/+	7.1 ± 1.5	0.0065 ± 0.0006	4.6 ± 0.4	1.07 ± 0.03	0.59 ± 0.09
P	NS	NS	NS	NS	0.07

representing the biomechanical phenotype of OI as a disease [8]. Their bones also sustain more microdamage than the WT [32]. The respective failure of the odontoblasts to make the physiologic type I collagen trimer results in dental abnormalities and tooth discolorations in patients with all types of the classic OI types [33]. Since we did not observe any enamel wear, we think that the mouse diet had no effect on the 2-month or 6-month molar phenotype.

The overall mechanism of biologic hydroxyapatite formation is similar in dentin and bone [21, 34, 35]; however, the dental and bone phenotypes can be expected to differ, to some extent because bone is remodeled, and dentin, in general, is not. Future TEM or AFM studies using a fluid cell to provide a source of ions should examine age dependent changes in Brtl/+ teeth and bones to separate effects of mineral nucleation and mineral propagation [36]. Thus the increased

remodeling caused by increased RANKL expression in the Brtl/+ mice bones [10] may accentuate the bone phenotype compared to the dentin, but it may also affect alveolar bone remodeling and similarly affect the dentin. It is important to note that the RANKL/OPG ratio in the Brtl/+ mice is normal. Study of the dentin phenotype indicates an impaired matrix mineralization and a slower correction of the phenotype with age, implying that both the collagen matrix and the noncollagenous proteins that regulate the function of that matrix may be altered in the Brtl/+ teeth.

This study has several limitations. Firstly, the Brtl/+ mice were heterozygous rather than homozygous for the mutant allele, resulting in greater heterogeneity of matrix collagen including forms with no, one, or two mutant  $\alpha 1(I)$  alleles. This heterogeneity may contribute to greater variation in the data for mutant as opposed to wild type mice. Nonetheless,

significant differences were seen in some critical parameters that can help explain the phenotype. Secondly, animals were studied at 2 and 6 months; thus, initial developmental time points were missed. However, all the earlier studies on the *Brtl*/+ mice bones used 2- [8–10, 18] and sometimes both 2- and 6-month-old animals [8, 10], and the FTIRI and micro-CT data for the teeth were limited to jaws from these earlier studies. The use of frozen jaws precluded histologic evaluation beyond that already published [7]. The use of jaws from previous studies also prevented observation of the molars as they erupted during their early development.

## 5. Conclusions

In conclusion, this imaging study of *Brtl*/+ teeth demonstrated decreased molar volume and reduced mineralized tissue volume in the teeth with the mutant collagen. The *Brtl*/+ molar dentin was also thinner. As expected there were no changes in enamel properties demonstrating the different mechanisms involved in collagen-based dentin mineralization and collagen-free enamel mineralization. Increased acid phosphate content was noted at 2 months by FTIRI, and altered collagen structure was noted at 2 but not 6 months in the *Brtl*/+ teeth.

## Conflict of Interests

None of the authors have conflicts of interests.

## Acknowledgments

This work is supported by NIH Grants DE04141 and AR046121 (to Adele L. Boskey) and by the NICHD Intramural Funding to Joan C. Marini.

## References

- [1] J. C. Marini, A. Forlino, W. A. Cabral et al., "Consortium for osteogenesis imperfecta mutations in the helical domain of type I collagen: regions rich in lethal mutations align with collagen binding sites for integrins and proteoglycans," *Human Mutation*, vol. 28, no. 3, pp. 209–221, 2007.
- [2] F. Rauch, L. Lalic, P. Roughley, and F. H. Glorieux, "Genotype-phenotype correlations in nonlethal osteogenesis imperfecta caused by mutations in the helical domain of collagen type I," *European Journal of Human Genetics*, vol. 18, no. 6, pp. 642–647, 2010.
- [3] R. D. Blank and A. L. Boskey, "Genetic collagen diseases: influence of collagen mutations on structure and mechanical behavior," in *Collagen: Structure and Mechanics*, P. Fratzl, Ed., Chapter 16, pp. 447–474, Springer Science, Business Media, 2008.
- [4] M. J. Barron, S. T. McDonnell, I. MacKie, and M. J. Dixon, "Hereditary dentine disorders: dentinogenesis imperfecta and dentine dysplasia," *Orphanet Journal of Rare Diseases*, vol. 3, no. 1, article 31, 2008.
- [5] D. O. Sillence, A. Senn, and D. M. Danks, "Genetic heterogeneity in osteogenesis imperfecta," *Journal of Medical Genetics*, vol. 16, no. 2, pp. 101–116, 1979.
- [6] A. Forlino, W. A. Cabral, A. M. Barnes, and J. C. Marini, "New perspectives on osteogenesis imperfecta: invited review," *Nature Reviews Endocrinology*, vol. 7, pp. 540–557, 2011.
- [7] A. Forlino, F. D. Porter, L. Eric J, H. Westphal, and J. C. Marini, "Use of the Cre/lox recombination system to develop a non-lethal knock-in murine model for osteogenesis imperfecta with an  $\alpha 1(I)$  G349C substitution. Variability in phenotype in *Brtl*IV mice," *Journal of Biological Chemistry*, vol. 274, no. 53, pp. 37923–37931, 1999.
- [8] K. M. Kozloff, A. Carden, C. Bergwitz et al., "Brittle IV mouse model for osteogenesis imperfecta IV demonstrates postpubertal adaptations to improve whole bone strength," *Journal of Bone and Mineral Research*, vol. 19, no. 4, pp. 614–622, 2004.
- [9] J. M. Wallace, B. G. Orr, J. C. Marini, and M. M. B. Holl, "Nanoscale morphology of Type I collagen is altered in the *Brtl* mouse model of Osteogenesis Imperfecta," *Journal of Structural Biology*, vol. 173, no. 1, pp. 146–152, 2011.
- [10] T. E. Uveges, P. Collin-Osdoby, W. A. Cabral et al., "Cellular mechanism of decreased bone in *Brtl* mouse model of OI: imbalance of decreased osteoblast function and increased osteoclasts and their precursors," *Journal of Bone and Mineral Research*, vol. 23, no. 12, pp. 1983–1994, 2008.
- [11] A. L. Boskey, M. F. Young, T. Kiltz, and K. Verdelis, "Variation in mineral properties in normal and mutant bones and teeth," *Cells Tissues Organs*, vol. 181, no. 3–4, pp. 144–153, 2006.
- [12] L. G. Sloofman, K. Verdelis, L. Spevak et al., "Effect of HIP/ribosomal protein L29 deficiency on mineral properties of murine bones and teeth," *Bone*, vol. 47, no. 1, pp. 93–101, 2010.
- [13] K. Verdelis, L. Lukashova, E. Atti et al., "MicroCT morphometry analysis of mouse cancellous bone: intra- and inter-system reproducibility," *Bone*, vol. 49, no. 3, pp. 580–587, 2011.
- [14] M. Baldassarri, H. C. Margolis, and E. Beniash, "Compositional determinants of mechanical properties of enamel," *Journal of Dental Research*, vol. 87, no. 7, pp. 645–649, 2008.
- [15] S. Gourion-Arsiquaud, P. A. West, and A. L. Boskey, "Fourier transform-infrared microspectroscopy and microscopic imaging," *Methods in Molecular Biology*, vol. 455, pp. 293–303, 2008.
- [16] A. L. Boskey and R. Mendelsohn, "Infrared spectroscopic characterization of mineralized tissues," *Vibrational Spectroscopy*, vol. 38, no. 1–2, pp. 107–114, 2005.
- [17] L. Spevak, C. Flach, T. Hunter, R. Mendelsohn, and A. L. Boskey, "FTIRI parameters describing acid phosphate substitution in biologic hydroxyapatite," *Calcified Tissue International*, vol. 92, pp. 418–428, 2013.
- [18] S. G. Kazarian and K. L. A. Chan, "Chemical photography' of drug release," *Macromolecules*, vol. 36, pp. 9866–9872, 2003.
- [19] J. P. Simmer, A. S. Richardson, Y. Y. Hu, C. E. Smith, and J. Ching-Chun Hu, "A post-classical theory of enamel biomineralization...and why we need one," *International Journal of Oral Science*, vol. 4, pp. 129–134, 2012.
- [20] J. Moradian-Oldak, "Protein-mediated enamel mineralization," *Frontiers in Bioscience*, vol. 17, pp. 1996–2023, 2012.
- [21] M. Goldberg, A. B. Kulkarni, M. Young, and A. Boskey, "Dentin: structure, composition and mineralization," *Frontiers in Bioscience*, vol. 3, pp. 711–735, 2011.
- [22] A. L. Boskey, B. Christensen, H. Taleb, and E. S. Sørensen, "Post-translational modification of osteopontin: effects on in vitro hydroxyapatite formation and growth," *Biochemical and Biophysical Research Communications*, vol. 419, pp. 333–338, 2012.

- [23] R. Gioia, C. Panaroni, R. Besio et al., "Impaired osteoblastogenesis in a murine model of dominant osteogenesis imperfecta: a new target for osteogenesis imperfecta pharmacological therapy," *Stem Cells*, vol. 30, pp. 1465–1476, 2012.
- [24] M. Goldberg, A. Marchadier, C. Vidal et al., "Differential effects of fibromodulin deficiency on mouse mandibular bones and teeth: a micro-CT time course study," *Cells Tissues Organs*, vol. 194, no. 2–4, pp. 205–210, 2011.
- [25] N. L. Leong, J. M. Hurng, S. I. Djomehri, S. A. Gansky, M. I. Ryder, and S. P. Ho, "Age-related adaptation of bone-PDL-tooth complex: Rattus-Norvegicus as a model system," *PLoS One*, vol. 7, Article ID e35980, 2012.
- [26] J. W. Kim and J. P. Simmer, "Hereditary dentin defects," *Journal of Dental Research*, vol. 86, no. 5, pp. 392–399, 2007.
- [27] T. Murayama, R. Iwatsubo, S. Akiyama, A. Amano, and I. Morisaki, "Familial hypophosphatemic vitamin d-resistant rickets: dental findings and histologic study of teeth," *Oral Surgery, Oral Medicine, Oral Pathology, Oral Radiology, and Endodontics*, vol. 90, no. 3, pp. 310–316, 2000.
- [28] D. Pallos, P. S. Hart, J. R. Cortelli et al., "Novel COL1A1 mutation (G599C) associated with mild osteogenesis imperfecta and dentinogenesis imperfecta," *Archives of Oral Biology*, vol. 46, no. 5, pp. 459–470, 2001.
- [29] T. Boukpepsi, D. Septier, S. Bagga, M. Garabedian, M. Goldberg, and C. Chaussain-Miller, "Dentin alteration of deciduous teeth in human hypophosphatemic rickets," *Calcified Tissue International*, vol. 79, no. 5, pp. 294–300, 2006.
- [30] G. Hillmann and W. Geurtsen, "Pathohistology of undecalcified primary teeth in vitamin D-resistant rickets Review and report of two cases," *Oral Surgery, Oral Medicine, Oral Pathology, Oral Radiology, and Endodontics*, vol. 82, no. 2, pp. 218–224, 1996.
- [31] H. Fong, E. Y. Chu, K. A. Tompkins et al., "Aberrant cementum phenotype associated with the hypophosphatemic Hyp mouse," *Journal of Periodontology*, vol. 80, no. 8, pp. 1348–1354, 2009.
- [32] M. S. Davis, B. L. Kovacic, J. C. Marini, A. J. Shih, and K. M. Kozloff, "Increased susceptibility to microdamage in *Brlt*/ $+$  mouse model for osteogenesis imperfecta," *Bone*, vol. 50, pp. 784–791, 2012.
- [33] A. Majorana, E. Bardellini, P. C. Brunelli, M. Lacaita, A. P. Cazzolla, and G. Favia, "Dentinogenesis imperfecta in children with osteogenesis imperfecta: a clinical and ultrastructural study," *International Journal of Paediatric Dentistry*, vol. 20, no. 2, pp. 112–118, 2010.
- [34] A. Veis, C. Sfeir, and C. B. Wu, "Phosphorylation of the proteins of the extracellular matrix of mineralized tissues by casein kinase-like activity," *Critical Reviews in Oral Biology and Medicine*, vol. 8, no. 4, pp. 360–379, 1997.
- [35] A. Veis and J. R. Dorvee, "Biomineralization mechanisms: a new paradigm for crystal nucleation in organic matrices," *Calcified Tissue International*, 2012.
- [36] D. Li, M. H. Nielsen, J. R. Lee, C. Frandsen, J. F. Banfield, and J. J. De Yoreo, "Direction-specific interactions control crystal growth by oriented attachment," *Science*, vol. 336, pp. 1014–1018, 2012.



## Review Article

# New Therapeutics in Promoting and Modulating Mandibular Growth in Cases with Mandibular Hypoplasia

**Tarek El-Bialy<sup>1</sup> and Adel Alhadlaq<sup>2</sup>**

<sup>1</sup> 7-020D Katz Group Centre for Pharmacy and Health Research, University of Alberta, Edmonton, AB, Canada T6G 2E1

<sup>2</sup> College of Dentistry, King Saud University, P.O. Box 60169, Riyadh 11545, Saudi Arabia

Correspondence should be addressed to Tarek El-Bialy; [telbialy@ualberta.ca](mailto:telbialy@ualberta.ca)

Received 13 January 2013; Revised 10 April 2013; Accepted 18 April 2013

Academic Editor: Brian L. Foster

Copyright © 2013 T. El-Bialy and A. Alhadlaq. This is an open access article distributed under the Creative Commons Attribution License, which permits unrestricted use, distribution, and reproduction in any medium, provided the original work is properly cited.

Children with mandibular growth deficiency may develop airway obstruction. The standard treatment of severe airway obstruction involves invasive procedures such as tracheostomy. Mandibular distraction osteogenesis has been proposed in neonates with mandibular deficiency as a treatment option to avoid tracheostomy procedure later in life. Both tracheostomy and distraction osteogenesis procedures suffer from substantial shortcomings including scarring, unpredictability, and surgical complications. Forward jaw positioning appliances have been also used to enhance mandible growth. However, the effectiveness of these appliances is limited and lacks predictability. Current and future approaches to enhance mandibular growth, both experimental and clinical trials, and their effectiveness are presented and discussed.

## 1. Introduction

Underdeveloped mandibles can cause severe psychological and functional impact upon the growing child and may be associated with life-threatening complications such as obstructive sleep apnea (OSA) due to severe airway constriction [1, 2]. The prevalence of OSA in children is approximately 3% [3]. Patients with OSA usually have underdeveloped mandible (mandible) [4, 5]. The mortality rate due to OSA has been reported to reach 15% of the affected individuals [6, 7]. This increased mortality is mainly attributed to the retruded position of the mandible which compromises the airway [8].

When the airway is compromised because of severe mandible underdevelopment, jaw-positioning appliances [9], nasopharyngeal airway [10], orthodontic plates with velar extension [11], intubation [12], tongue-lip adhesion [13], continuous positive airway pressure (CPAP) [14], tracheostomy [15], mandibular advancement with orthognathic surgery/distraction osteogenesis [16, 17], or an anterior mandibular positioning device is used to manage the airway obstruction [18, 19].

It is to be noted that tracheotomy and mandibular distraction osteogenesis (DO) have major limitations; they are lifesaving and provide substantial lengthening of the mandible quickly. In spite of recent advancements, the tracheostomy procedure remains a treatment with serious and frequent side effects. These side effects include potential tissue traumatization, injury of the laryngeal or tracheal mucosa, and/or other complications (e.g., pneumothorax, hemorrhage, wound complication, tracheal stenosis, and laryngeal stenosis) [15]. To avoid tracheostomies, distraction osteogenesis of the mandible (surgical lengthening of the mandible) has recently been recommended as a viable option for pediatric patients with upper airway obstruction due to mandibular deficiency [16]. This technique has been described as an alternative to tracheostomy in neonates (6 to 26 days of age) to improve airway and breathing [17].

Conversely, improving the airway in OSA adult patients with the use of a removable mandibular advancement device (MAD) has recently been shown to have a success rate of only 54.8% [18]. Advancing the mandible with oral appliances depends solely on patient's compliance and has been reported

to be effective in short term only [19]. Nonetheless, the long-term efficacy of all above-mentioned treatment modalities is unknown.

## 2. Mandibular Growth

The condylar cartilage in the mandible is a secondary cartilage. It has been shown that mechanical stimuli are necessary for the normal growth of this type of cartilage [20–24]. Bite-jumping appliances (orthodontic/orthopedic functional appliances) have long been used for “growth modification” of the mandible in the field of orthodontics and craniofacial orthopedics. However, the effectiveness of these appliances has been criticized and is still considered an area of controversy [25]. Other currently available mechanical loading techniques, for example, electroforce 3200 mechanical testing machine, are not clinically applicable for severe mandibular underdevelopment due to the large size of the device (mechanical testing machine) or because patients can not fit within the proposed devices (electroforce or mechanical testing machines) [20].

## 3. Current Treatment Modalities and Challenges

**3.1. Bite-Jumping Appliances (Functional Appliances).** Growth modification of the mandible using functional appliances (FAs) has been used to enhance forward positioning of the mandible. They are commonly used clinically to enhance mandibular growth in patients with underdeveloped mandibles. Recent animal experiments have demonstrated significant increase in the endochondral ossification (bone formation within the growing cartilage) at the mandibular condyle in response to the mandibular protrusive forces [20, 26, 27]. This forward mandibular positioning has been hypothesized to solicit a sequence of cellular events that lead to increased vascularization, new bone formation, and enhanced condylar growth [28]. Also, a recent clinical trial on the effectiveness of twin block functional appliance on mandibular growth in 15 boys and 19 girls ranging in age from 9 years 3 months to 10 years 8 months at the start of treatment showed that its use increases the mandibular length 2.3 mm more than that of a control group [29]. Controversially, other clinical trials of FAs therapy have demonstrated either no substantial growth enhancement or increased mandibular growth only at the initial stage, with the growth phenotype of the mandible returning to its original pattern afterwards [30, 31]. Interestingly, FAs were reported to increase the number of replicating mesenchymal stem cells in growing rats at both the mandibular condyle and the glenoid fossa [32]. In a related study, a correlation was demonstrated between the application of FAs as a mechanical stimulator and the number of stem cells in mandibular condyles and the glenoid fossa [33]. These studies demonstrated that the number of mesenchymal cells in a given locus normally determines the potential for bone growth in that area and that the number of

mesenchymal cells in the glenoid fossa is directly correlated with the amount of bone produced during natural growth and mandibular advancement [32, 33]. It has been hypothesized that a lack of native stem cells in the mandibular condyle and glenoid fossa contributes to the underdevelopment of the mandible [32, 33]. Consequently, development of new techniques to foster stem cell recruitment to the growing condyles and the glenoid fossa becomes practical.

Although the exact mechanism of FAs involvement in promoting mandibular growth is not fully understood, previous reports have shown that FAs enhance mandibular growth through an increase in the production of Runx2 [27], which is a transcription factor that belongs to the Runt domain gene family. The Runx2 promotes osteoblast's differentiation and function by transcriptionally upregulating all the major osteoblast-specific genes, including osteocalcin, type-I collagen, bone sialoprotein, osteopontin, alkaline phosphatase, and collagenase-3 [34]. Also, FAs enhance Sox9 and type II collagen expression in rats [35], a result that has been confirmed by immunostaining techniques [20, 26–28].

**3.2. Low-Intensity Pulsed Ultrasound.** Low-intensity pulsed ultrasound (LIPUS) produces mechanical waves that propagate through biological tissues at a pulse frequency of 1.5 MHz with a pulse repetition frequency of 1 kHz. At an output power of 30 mW/cm<sup>2</sup>, LIPUS can stimulate tissue growth without heating [15, 16]. A daily treatment with LIPUS for 20 minutes has been established as a favorable treatment modality in the field of orthopedics [36–39]. This treatment protocol has been found to stimulate bone healing after fracture in a variety of human and animal models by promoting new vascularization and bone formation [35–37]. Also, this technique has been applied successfully to promote growth and healing after distraction (i.e., excessive separation of bony segments) of the tibia in a rabbit model and after distraction of the callus [36, 39]. Daily direct application of LIPUS for 4 weeks also stimulated mandibular bone growth in rats and rabbits [22, 23]. However, achieving similar results in monkeys required four months of treatment [40] and about a year in humans (when combined with FAs) [41] (Figure 1). Such long periods of daily application of LIPUS are challenging and highly demanding for a clinical implementation. Thus, the development of an approach to boost the stimulatory effect of LIPUS on bone growth is necessary.

Recent reports have shown that LIPUS has anabolic effect in chondrocytes with increased stimulation when LIPUS is applied for longer durations [42]. Furthermore, the current consensus in the literature is that the stimulatory effect of therapeutic ultrasound on bone formation is dose dependent (daily treatment time) [42–44]. Angiogenesis has also been shown to be increased with LIPUS treatment, thus improving the blood flow to the treatment area that is critical for bone growth [45, 46]. In addition, it has been shown that LIPUS promotes stem cell expansion and differentiation [47–49]. Indeed, the application of ultrasound in stem cell expansion and differentiation as well as in bone mineralization and regeneration has gained considerable attention in recent years [50, 51].

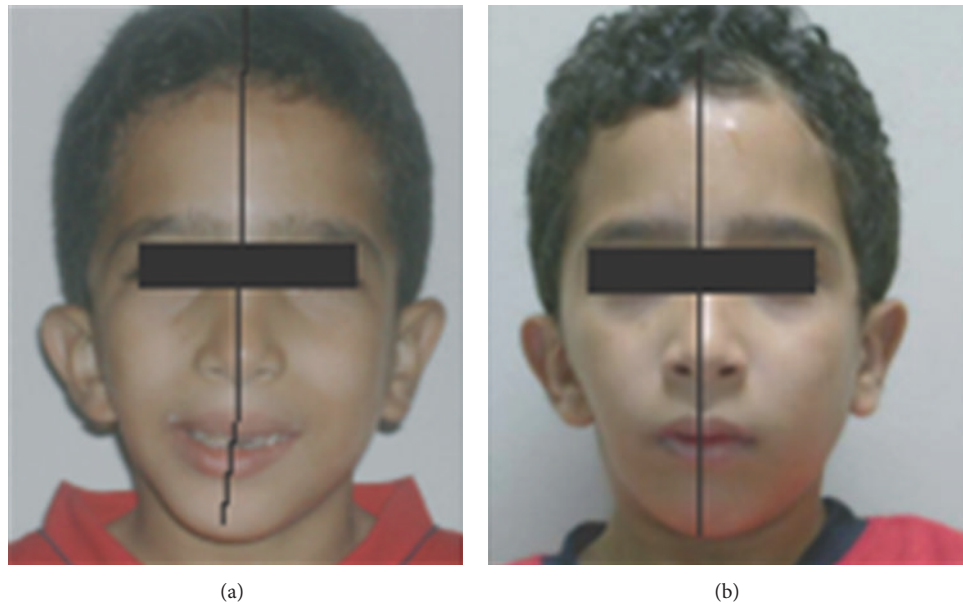


FIGURE 1: A hemifacial microsomia patient treated with 20 minutes LIPUS per day for a year with a hybrid functional appliance. (a) Before and (b) after treatment.

The mechanism of mandibular growth enhancement by LIPUS is not fully understood. The hypothesized mechanism of action of LIPUS to stimulate mandibular growth is through increase in vascular endothelial growth factor (VEGF) and Runx2 in bone healing since these have been shown to be correlated to increased mandibular growth [46]. LIPUS is known to increase the expression of VEGF and Runx2 in bone healing [45]. Also, LIPUS has been shown to increase the expression of osteocalcin, Runx2, and bone sialoprotein in stem cells [52]. In addition, the expression of Runx2, Msx2, Dlx5, osterix, bone sialoprotein, and bone morphogenetic protein-2 has been shown to be enhanced in MG-63 osteoblasts [53]. Sox9 is known to be a crucial molecule in stem cell proliferation, condensation, and chondrocyte differentiation [54–56]. Runx2 is involved in chondrocyte differentiation, whereas VEGF and collagen type X are involved in endochondral ossification [46, 54]. Integrins may act as mechanotransducers that can transform acoustic pulsed energy into intracellular biochemical signals that subsequently induce cell proliferation [57]. Although the mechanisms are still to be uncovered, current knowledge indicates that FAs and LIPUS have a potential synergistic effect in enhancing mandibular growth through mutual upregulation of Sox9, Runx2, and type-II collagen. This synergistic effect may be further increased by neovascularization produced by local application of bone marrow stem cells to mandibular condyles [58–64]. A critical need still exists for an optimized and effective technique to promote mandibular growth in a reasonable period of time (2-3 months in humans) for clinical application. Yet, it is to be tested the effect of LIPUS on increase of Sox9, Runx2, VEGF, and Type-II collagen in mandibular condyles treated by LIPUS. It is possible that once LIPUS parameters are optimize (Frequency, intensity, and treatment time), they may be used

clinically with minimum compliance of growing children with underdeveloped mandibles.

Growth hormone: growth hormone (GH) is an anterior pituitary hormone that induces general growth including bone [65–69]. It has been reported that systemic administration of GH enhances bone formation in animals [68]. Also, GH plays an important role not only in skeletal growth and development in young people but also in regulating bone remodeling throughout life [70]. Cell surface receptors for GH have been reported to be present in the temporomandibular joint (TMJ) [71].

Children undergoing GH therapy for short stature or isolated GH deficiency (who usually have normal jaw size) can experience a burst in jaw growth while on the GH therapy [72, 73].

In spite of the potential side effects of GH administration such as inducing body weight gain [74] and upregulation of proto-oncogenes like C-jun in liver [75], kidney, and other vital tissues [76], there has been an attempt to enhance mandibular growth by local injection of recombinant growth hormone (rGH) into the posterior attachment of mandibular condyle of growing rats with or without LIPUS application [77]. The hypothesized mechanism of action of local rGH application is to increase endochondral bone formation in the mandibular condyles without possible side effect of systemic use of rGH. The findings indicated that local rGH injection into mandibular condyles in rats increased mandibular growth compared to the control group. The study concluded that the used rGH dose does not have synergistic effect in combination with LIPUS application in enhancing mandibular bone volume or mandibular surface area while the combined treatment increased mandibular head length compared to either treatment alone (Figures 2(a) and 2(b)). Also, local injection of rGH increased C-jun in the liver



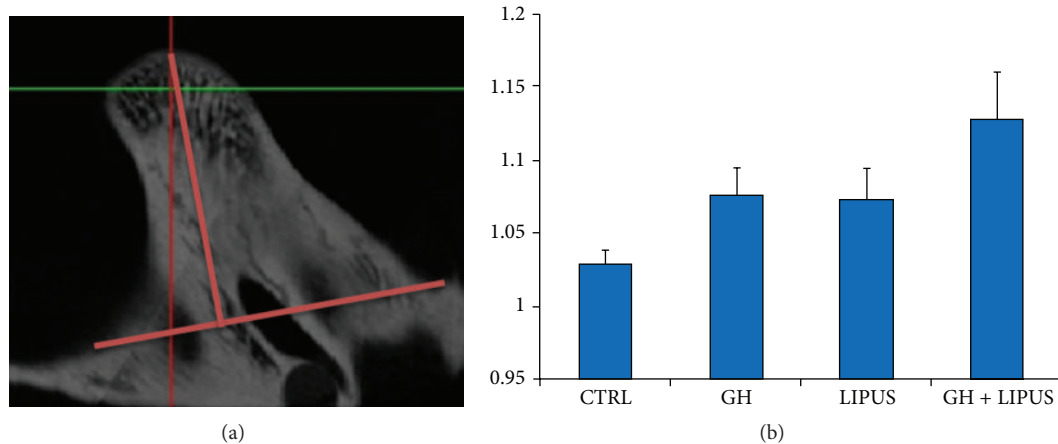


FIGURE 2: Effect of LIPUS and growth hormone on mandibular head length changes. (a) Measurement of mandibular head. (Straight line was drawn in between the two points that are anatomically situated in the lowest position in 2D reconstructed images. Length of mandibular head was measured by drawing a perpendicular line from the highest point of the condylar process towards the former line.) (b) Effect of treatment on the length of the mandibular head (LMH). After measurement length of the left mandibular head was divided by length of the right mandibular head. Ratio was analyzed among four different groups mentioned before. \*  $P < 0.05$ , compared to control.

[77]. Therefore, it seems to be prudent to have an optimized rGH/LIPUS protocol to enhance mandibular growth with minimum potential side effects and to study the effect of rGH in the long term. Future studies are needed to test the hypothesis that local injection of different rGH doses to mandibular condyle can modulate molecular mechanisms of mandibular growth, especially Runx2, VEGF, Sox9, and type-II collagen. Until the optimized rGH dose with or without LIPUS application can stimulate mandibular growth with minimum or no systemic side effect, the possible clinical application of rGH may not be foreseen.

**3.3. Photobiomodulation.** Photobiomodulation has been recently reported to be an effective therapeutic technique by which low-level laser light is used to enhance tissue growth and regeneration. This technique has been shown to minimize pain after orthodontic appliance adjustment [78–80] and minimize inflammation caused by the orthodontic appliances [81]. Low-level laser (LLL) therapy is a form of photobiomodulation that has been shown to enhance bone formation in the midpalatal suture after orthodontic maxillary expansion [82]. Also, the use of LLL has been proposed to accelerate tooth movement by inducing alveolar bone remodeling in the form of bone formation and cell proliferation in the tension side as well as increase the number of osteoclasts in the compression side of the orthodontically moved teeth [83, 84].

Light emitting diode (LED) is a monochromatic red-to-near infrared (NIR) light that has been shown to enhance retinal function in an animal model when used in the range of 630–1000 nm [85]. The wavelength of LED is close to that used in LLL (600–1000 nm) with similar energy [85]. Both the LED and the LLL result in photobiomodulation effects [86–88]. However, the difference between LED and the LLL is that LLL is a LASER with the characteristic of coherency, whereas LED light is not coherent, and therefore it is not expected

to result in any side effects [86–89]. The LED can also be produced at a lower cost compared to the LLL and it can be safely applied to a larger area of the body surface. It has been shown that LED light can alter the cellular metabolism following absorption by a cellular photoacceptor known as cytochrome c-oxidase [85, 89]. Moreover, it has been hypothesized that LED-mediated photobiomodulation may have potential in stimulating mandibular growth. A pilot study on the effect of LLL and LED on mandibular growth stimulation reported that both LED and LLL can stimulate mandibular growth in growing rats [90]. The objective of this pilot study was to compare the possible effect of LLL and LED of similar wavelength (850 nm) and energy output ( $6 \text{ J/cm}^2$ ) with or without the use of functional appliance (FA) on mandibular condylar growth in growing rats. The experimental design of this pilot study was as follows. Twenty-four growing Sprague-Dawley rats (6 weeks old) were divided into six groups of four animals each. Group 1 received LLL, group 2 received LLL + FA, group 3 received LED, group 4 received LED + FA, group 5 received FA and was used as a positive control group, and group 6 received no treatment and was used as negative control group. Animals were treated for ten minutes with the corresponding treatment every day on the right side of the mandibular condyle for four weeks. The results showed that there is a statistically significant increase (60%) in the FL in the treated condyles by the laser group compared to the count control condyles. Also, LED increased both the FL and CL significantly and PL more than the negative control condyles ( $P < 0.05$ ). Although LED and FA significantly increased all condylar layers when compared to the untreated negative control condyles, LED alone was more effective in increasing condylar layers than the combined LED and FA treatment ( $P < 0.05$ ). On the other hand, LED and FA increased the CL more than the LLL and FA group ( $P < 0.05$ ). The findings of this study suggest that LED is better than LLL in stimulating mandibular condyles in growing rats (Figure 3) [90]. However, the exact mechanism by which LED

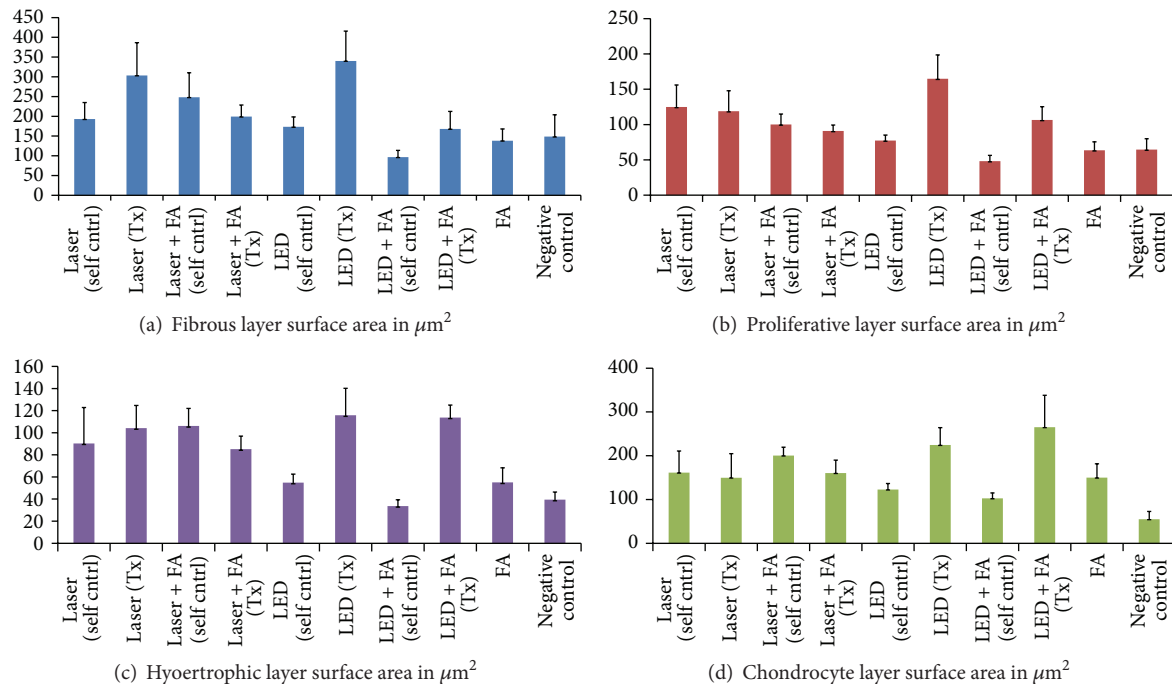


FIGURE 3: Surface area of mandibular condylar layers. (a) Fibrous, (b) proliferative, (c) hypertrophic, and (d) cartilaginous layers in rats treated by LED, laser with or without functional appliance (FA). It can be seen that LED increases surface areas in (a), (b), and (d) compared to control and almost similar to control in (c).

or LLL stimulate mandibular growth is yet to be understood fully so that an optimum technique can be developed using photobiomodulation. Future studies are needed to test the hypothesis that LED treatment to mandibular condyle can modulate molecular mechanisms of mandibular growth, especially Runx2, VEGF, Sox9, and type-II collagen.

Photobiomodulation for stimulation of mandibular condylar growth may be close to application in the clinic because clinical trials using LED in patients undergoing orthodontic treatment have identified enhanced tooth movement and minimal side effects, such as root resorption.

**3.4. Gene Therapy.** Gene therapy involves either physical or chemical transfer of genetic material in the host cell, [82]. Gene therapy involves using plasmid DNA alone (naked DNA) [91, 92] or associated with gene carriers or vectors such as nonviral vectors (liposomes or a polymer matrix) [93]. Liposomes have proven sufficient for gene transfer into chondrocytes, and they have several advantages over adenovirus vectors including ease of preparation, lack of limitations on the size of the DNA, and minimum immunological reaction [94]. However, *in vivo* or clinical application is yet to be proven. Viral vectors carrying vascular endothelial growth factor (rAAV-VEGF) have been shown to stimulate mandibular growth *in vivo* in rats [95]. Yet, more research is needed to optimize the technique and detailed toxicity evaluation of viral and nonviral vectors (both local and systemic), and testing optimized techniques in higher animals before clinical trials can be conducted. The hypothesis underlying local injection of vector-loaded VEGF into mandibular condyles

is that this VEGF can modulate mandibular growth through added VEGF effect that has been shown to be correlated to mandibular growth stimulation [27, 28]. VEGF may stimulate mandibular growth through two mechanisms: (1) through stimulation of endochondral bone growth and (2) through recruitment of new replicating mesenchymal stem cells which is correlated to mandibular growth [32, 33]. It seems that the road towards clinical application of gene therapy to enhance mandibular condylar growth is long compared to other modalities like LIPUS or LED. Many questions remain to be answered regarding the safety, optimization, and mechanism underlying gene therapy, which is also more invasive and currently less accepted than LIPUS or LED.

## 4. Syndromic Mandibular Hypoplasia and Treatment Possibilities

Syndromic mandibular hypoplasia, as in hemifacial microsomia (HFM), is distinct from symmetrical mandibular hypoplasia. HFM is a congenital anomaly that is presented by asymmetric facial structures in which the mandible and overlying structures fail to develop normally. HFM is also known as otomandibular dysostosis, [96] first and second branchial arch syndrome, [97, 98] oculo-auriculovertebral dysplasia, [99] Goldenhar syndrome, [100, 101] lateral facial dysplasia; [102] and craniofacial microsomia [103, 104]. The prevalence of HFM has been previously reported as 1 in 3000 or 1 in 5600 births [105–108]. Males are more affected than females [109], and it has been reported that the right side is affected more than the left side (3 : 2 ratio) [110]. At present, the underlying

cause of HFM remains unknown. It has been hypothesized that HFM results from a developmental abnormality related to hemorrhage and rupture of the stapedia artery (a small blood vessel near the ear), as supported by mouse studies [109–111]. It is to be noted that small animal models of HFM cannot be extrapolated to humans, as there is no published reports that indicate that hypothesized etiology of human HFM is similar to those in lower animal models. Pruzansky classification is the most known HFM classification used by clinicians and researchers [112–114]. Treatment of HFM depends on each case severity and patient's age. Treatment of HFM may include orthodontic hybrid functional appliances in less severe cases and/or surgical intervention utilizing orthognathic surgery or distraction osteogenesis [115]. Since the etiology of HFM is not fully understood, the use of the new proposed techniques may not be fully applicable to syndromic cases like HFM.

## 5. Current Challenges in Available Techniques Used to Enhance Mandibular Growth

As noted above, although LIPUS, LED, GH, or gene therapy may be future techniques that may be used one day for mandibular stimulation in patients with underdeveloped mandibles, the following challenges are foreseen for these techniques. While optimized LIPUS treatment is hypothesized to be dose (treatment-time) dependent, it is a challenge to use LIPUS daily for more than 20 minutes per day to mandibular condyles, especially in growing children. From the preliminary study that showed a proof of principle that local rGH injection can enhance mandibular growth, possible increase in rGH dose might bring a risk of systemic unwanted effect(s). While LED treatment to growing mandibles show promising effect, the underlying mechanisms that are involved in LED-mediated mandibular growth stimulation are not known; hence, possible optimized technique of LED application is not known or cannot be hypothesized. Finally, it seems to be very early for proposing genetherapy for human mandibular growth due to the following challenges. It is not known whether locally injected vector-loaded genes have possible systemic effect or not. Although nonviral vectors have been investigated for possible future use in humans, it is not known the possible side effects of these nonviral vectors. It is also not known the optimum dose of each vector or vector-loaded gene concentration that can enhance mandibular growth without inducing unnecessary overgrowth of the mandibles or inducing neoplastic growth. With these challenges, future research may be directed towards uncovering these mechanisms and studying possible side effects as well as optimized techniques in mandibular growth stimulation.

Although shown to be a clinically acceptable treatment modality, bite-jumping appliances (functional appliances (Fas)) alone may not be fully effective in stimulating mandibular growth to the level that they can substitute surgical repositioning of the mandible in severe mandibular deficiency cases. LIPUS can stimulate mandibular growth in growing animals and in humans; however, an optimized

technique to shorten treatment time requires further investigations in lower and higher animals before any clinical trials may be proposed. An optimized technique that utilizes local rGH administration with or without LIPUS is worth investigation to stimulate mandibular growth with minimum potential side effects. Gene therapy as well as LLL or LED seems to be promising approaches in stimulating mandibular growth. However, detailed toxicity investigations of these techniques are required before potential clinical trials can be performed.

## Acknowledgment

This work was sponsored by King Saud University, Saudi Arabia.

## References

- [1] C. Sunitha and S. A. Kumar, "Obstructive sleep apnea and its management," *Indian Journal of Dental Research*, vol. 21, no. 1, pp. 119–124, 2010.
- [2] E. T. Chang and G. M. Shiao, "Craniofacial abnormalities in Chinese patients with obstructive and positional sleep apnea," *Sleep Medicine*, vol. 9, no. 4, pp. 403–410, 2008.
- [3] S. J. Chang and K. Y. Chae, "Obstructive sleep apnea syndrome in children: epidemiology, pathophysiology, diagnosis and sequelae," *Korean Journal of Pediatrics*, vol. 53, no. 10, pp. 863–871, 2010.
- [4] N. Higurashi, M. Kikuchi, S. Miyazaki, and Y. Itasaka, "Comparison of Ricketts analysis and Downs-Northwestern analysis for the evaluation of obstructive sleep apnea cephalograms," *Psychiatry and Clinical Neurosciences*, vol. 55, no. 3, pp. 259–260, 2001.
- [5] B. B. Vieira, C. E. Itikawa, L. A. de Almeida et al., "Cephalometric evaluation of facial pattern and hyoid bone position in children with obstructive sleep apnea syndrome," *International Journal of Pediatric Otorhinolaryngology*, vol. 75, no. 3, pp. 383–386, 2011.
- [6] P. Lavie, P. Herer, R. Peled et al., "Mortality in sleep apnea patients: a multivariate analysis of risk factors," *Sleep*, vol. 18, no. 3, pp. 149–157, 1995.
- [7] P. Lavie, P. Herer, and L. Lavie, "Mortality risk factors in sleep apnoea: a matched case-control study," *Journal of Sleep Research*, vol. 16, no. 1, pp. 128–134, 2007.
- [8] R. B. Cohen, "Obstructive sleep apnea: a mandibular positioning device for treatment and diagnosis of an obstruction site," *Compendium of Continuing Education in Dentistry*, vol. 16, no. 6, pp. 618–629, 1995.
- [9] M. P. Villa, E. Bernkopf, J. Pagani, V. Broia, M. Montesano, and R. Ronchetti, "Randomized controlled study of an oral jaw-positioning appliance for the treatment of obstructive sleep apnea in children with malocclusion," *American Journal of Respiratory and Critical Care Medicine*, vol. 165, no. 1, pp. 123–127, 2002.
- [10] H. Huo, W. Y. Li, P. Shen, and J. H. Liu, "One night treatment of obstructive sleep apnea and hypopnea syndrome with nasopharyngeal airway," *Zhonghua Er Bi Yan Hou Tou Jing Wai Ke Za Zhi*, vol. 45, no. 5, pp. 382–386, 2010.
- [11] W. Hochban and B. Hoch, "Obstructive sleep apnoea in children: an interdisciplinary approach with special regard to



- craniofacial disorders," *Pneumologie*, vol. 52, no. 3, pp. 147–153, 1998.
- [12] R. M. Corso, E. Piraccini, M. Calli et al., "Obstructive sleep apnea is a risk factor for difficult endotracheal intubation," *Minerva Anestesiologica*, vol. 77, no. 1, pp. 99–100, 2011.
  - [13] G. Freed, M. A. Pearlman, A. S. Brown, and L. R. Barot, "Polysomnographic indications for surgical intervention in Pierre Robin sequence: acute airway management and follow-up studies after repair and take-down of tongue-lip adhesion," *Cleft Palate Journal*, vol. 25, no. 2, pp. 151–155, 1988.
  - [14] K. A. Waters, F. M. Everett, J. W. Bruderer, and C. E. Sullivan, "Obstructive sleep apnea: the use of nasal CPAP in 80 children," *American Journal of Respiratory and Critical Care Medicine*, vol. 152, no. 2, pp. 780–785, 1995.
  - [15] B. Kremer, A. I. Botos-Kremer, H. E. Eckel, and G. Schlöndorff, "Indications, complications, and surgical techniques for pediatric tracheostomies—an update," *Journal of Pediatric Surgery*, vol. 37, no. 11, pp. 1556–1562, 2002.
  - [16] M. Miloro, "Mandibular distraction osteogenesis for pediatric airway management," *Journal of Oral and Maxillofacial Surgery*, vol. 68, no. 7, pp. 1512–1523, 2010.
  - [17] A. Denny and B. Kalantarian, "Mandibular distraction in neonates: a strategy to avoid tracheostomy," *Plastic and Reconstructive Surgery*, vol. 109, no. 3, pp. 896–904, 2002.
  - [18] C. Tison, S. Sébille-Elhage, and J. Ferri, "Mandibular advancement device: a 5-year long experience in obstructive sleep apnea/hypopnea syndrome," *Revue de Stomatologie et de Chirurgie Maxillo-Faciale*, vol. 112, no. 2, pp. 80–86, 2011.
  - [19] B. Lam, K. Sam, J. C. M. Lam, A. Y. K. Lai, C. L. Lam, and M. S. M. Ip, "The efficacy of oral appliances in the treatment of severe obstructive sleep apnea," *Sleep and Breathing*, vol. 15, no. 2, pp. 195–201, 2011.
  - [20] T. Sobue, W. C. Yeh, A. Chhibber et al., "Murine TMJ loading causes increased proliferation and chondrocyte maturation," *Journal of Dental Research*, vol. 90, no. 4, pp. 512–516, 2011.
  - [21] A. B. Rabie and U. Hägg, "Factors regulating mandibular condylar growth," *American Journal of Orthodontics and Dentofacial Orthopedics*, vol. 122, pp. 401–409, 2002.
  - [22] R. Oyonarte, M. Zárate, and F. Rodriguez, "Low-intensity pulsed ultrasound stimulation of condylar growth in rats," *Angle Orthodontist*, vol. 79, no. 5, pp. 964–970, 2009.
  - [23] T. El-Bialy, I. El-Shamy, and T. M. Graber, "Growth modification of the rabbit mandible using therapeutic ultrasound: is it possible to enhance functional appliance results?" *Angle Orthodontist*, vol. 73, no. 6, pp. 631–639, 2003.
  - [24] T. Peltomäki, S. Kylämarkula, H. Vinkka-Puhakka, M. Rintala, T. Kantomaa, and O. Rönning, "Tissue-separating capacity of growth cartilages," *European Journal of Orthodontics*, vol. 19, no. 5, pp. 473–481, 1997.
  - [25] G. Shen and M. A. Darendeliler, "Cephalometric evaluation of condylar and mandibular growth modification: a review," *Orthodontics & Craniofacial Research*, vol. 9, no. 1, pp. 2–9, 2006.
  - [26] G. Shen, A. B. Rabie, U. Hägg, and R. J. Chen, "Neovascularization in condylar cartilage in response to mandibular protrusion," *Chinese Journal of Dental Research*, vol. 6, pp. 28–38, 2003.
  - [27] A. B. M. Rabie, L. Shum, and A. Chayanupatkul, "VEGF and bone formation in the glenoid fossa during forward mandibular positioning," *American Journal of Orthodontics and Dentofacial Orthopedics*, vol. 122, no. 2, pp. 202–209, 2002.
  - [28] A. B. M. Rabie, F. Y. C. Leung, A. Chayanupatkul, and U. Hägg, "The correlation between neovascularization and bone formation in the condyle during forward mandibular positioning," *Angle Orthodontist*, vol. 72, no. 5, pp. 431–438, 2002.
  - [29] A. Sidlauskas, "Clinical effectiveness of the Twin block appliance in the treatment of Class II Division 1 malocclusion," *Stomatologija*, vol. 7, no. 1, pp. 7–10, 2005.
  - [30] X. Du, U. Hägg, and A. B. M. Rabie, "Effects of headgear Herbst and mandibular step-by-step advancement versus conventional Herbst appliance and maximal jumping of the mandible," *European Journal of Orthodontics*, vol. 24, no. 2, pp. 167–174, 2002.
  - [31] M. Bendeus, U. Hägg, and B. Rabie, "Growth and treatment changes in patients treated with a headgear-activator appliance," *American Journal of Orthodontics and Dentofacial Orthopedics*, vol. 121, no. 4, pp. 376–384, 2002.
  - [32] A. B. M. Rabie, L. Wong, and M. Tsai, "Replicating mesenchymal cells in the condyle and the glenoid fossa during mandibular forward positioning," *American Journal of Orthodontics and Dentofacial Orthopedics*, vol. 123, no. 1, pp. 49–57, 2003.
  - [33] A. B. M. Rabie, L. Wong, and U. Hägg, "Correlation of replicating cells and osteogenesis in the glenoid fossa during stepwise advancement," *American Journal of Orthodontics and Dentofacial Orthopedics*, vol. 123, no. 5, pp. 521–526, 2003.
  - [34] G. H. Tang and A. B. M. Rabie, "Runx2 regulates endochondral ossification in condyle during mandibular advancement," *Journal of Dental Research*, vol. 84, no. 2, pp. 166–171, 2005.
  - [35] A. B. M. Rabie, T. T. She, and V. R. Harley, "Forward mandibular positioning up-regulates SOX9 and type II collagen expression in the glenoid fossa," *Journal of Dental Research*, vol. 82, no. 9, pp. 725–730, 2003.
  - [36] J. D. Heckman, J. P. Ryaby, J. McCabe, J. J. Frey, and R. F. Kilcoyne, "Acceleration of tibial fracture-healing by non-invasive, low-intensity pulsed ultrasound," *Journal of Bone and Joint Surgery. American*, vol. 76, no. 1, pp. 26–34, 1994.
  - [37] T. K. Kristiansen, J. P. Ryaby, J. McCabe, J. J. Frey, and L. R. Roe, "Accelerated healing of distal radial fractures with the use of specific, low-intensity ultrasound: a multicenter, prospective, randomized, double-blind, placebo-controlled study," *Journal of Bone and Joint Surgery. American*, vol. 79, no. 7, pp. 961–973, 1997.
  - [38] A. Shimazaki, K. Inui, Y. Azuma, N. Nishimura, and Y. Yamano, "Low-intensity pulsed ultrasound accelerates bone maturation in distraction osteogenesis in rabbits," *Journal of Bone and Joint Surgery. British*, vol. 82, no. 7, pp. 1077–1082, 2000.
  - [39] E. Mayr, A. Laule, G. Suger, A. Rüter, and L. Claes, "Radiographic results of callus distraction aided by pulsed low-intensity ultrasound," *Journal of Orthopaedic Trauma*, vol. 15, no. 6, pp. 407–414, 2001.
  - [40] T. El-Bialy, A. Hassan, T. Albaghdadi, H. A. Fouad, and A. R. Maimani, "Growth modification of the mandible with ultrasound in baboons: a preliminary report," *American Journal of Orthodontics and Dentofacial Orthopedics*, vol. 130, no. 4, pp. e7–e14, 2006.
  - [41] T. El-Bialy, A. Hasan, A. Alyamani, and T. Albaghdadi, "Treatment of hemifacial microsomia by therapeutic ultrasound and hybrid functional appliance. A non-surgical approach," *Open Access Journal of Clinical Trials*, vol. 2, pp. 29–36, 2010.
  - [42] D. Schumann, R. Kujat, J. Zellner et al., "Treatment of human mesenchymal stem cells with pulsed low intensity ultrasound enhances the chondrogenic phenotype in vitro," *Biorheology*, vol. 43, no. 3-4, pp. 431–443, 2006.

- [43] T. El-Bialy, T. J. Royston, R. L. Magin, C. A. Evans, A. E. M. Zaki, and L. A. Frizzell, "The effect of pulsed ultrasound on mandibular distraction," *Annals of Biomedical Engineering*, vol. 30, no. 10, pp. 1251–1261, 2002.
- [44] C. W. Chan, L. Qin, K. M. Lee, W. H. Cheung, J. C. Y. Cheng, and K. S. Leung, "Dose-dependent effect of low-intensity pulsed ultrasound on callus formation during rapid distraction osteogenesis," *Journal of Orthopaedic Research*, vol. 24, no. 11, pp. 2072–2079, 2006.
- [45] S. R. Young and M. Dyson, "The effect of therapeutic ultrasound on angiogenesis," *Ultrasound in Medicine and Biology*, vol. 16, no. 3, pp. 261–269, 1990.
- [46] J. Dai and A. B. M. Rabie, "VEGF: an essential mediator of both angiogenesis and endochondral ossification," *Journal of Dental Research*, vol. 86, no. 10, pp. 937–950, 2007.
- [47] W. T. Ang, C. Scurtescu, W. Hoy, T. El-Bialy, Y. Y. Tsui, and J. Chen, "Design and implementation of therapeutic ultrasound generating circuit for dental tissue formation and tooth-root healing," *IEEE Transactions on Biomedical Circuits and Systems*, vol. 4, no. 1, pp. 49–61, 2010.
- [48] T. A. Aldosary, H. Uludag, M. Doschak, J. Chen, Y. Tsui, and T. EL-Bialy, "Effect of ultrasound on human umbilical cord perivascular-stem cell expansion," in *Proceedings of the International Association for Dental Research (IADR) Meeting*, Toronto, Canada, July 2008, Abstract no. 873.
- [49] S. Marvel, S. Okrasinski, S. H. Bernacki, E. Lobo, and P. A. Dayton, "The development and validation of a lipus system with preliminary observations of ultrasonic effects on human adult stem cells," *IEEE Transactions on Ultrasonics, Ferroelectrics, and Frequency Control*, vol. 57, no. 9, pp. 1977–1984, 2010.
- [50] A. Suzuki, T. Takayama, N. Suzuki, M. Sato, T. Fukuda, and K. Ito, "Daily low-intensity pulsed ultrasound-mediated osteogenic differentiation in rat osteoblasts," *Acta Biochimica et Biophysica Sinica*, vol. 41, no. 2, pp. 108–115, 2009.
- [51] K. Nishizawa, S. Imai, T. Mimura et al., "In-advance trans-medullary stimulation of bone marrow enhances spontaneous repair of full-thickness articular cartilage defects in rabbits," *Cell and Tissue Research*, vol. 341, no. 3, pp. 371–379, 2010.
- [52] T. Jiang, T. Xu, F. Gu, A. Chen, Z. Xiao, and D. Zhang, "Osteogenic effect of low intensity pulsed ultrasound on rat adipose-derived stem cells in vitro," *Journal of Huazhong University of Science and Technology. Medical sciences*, vol. 32, no. 1, pp. 75–81, 2012.
- [53] J. J. Leskinen, H. M. Karjalainen, A. Olkku, K. Hynynen, A. Mahonen, and M. J. Lammi, "Genome-wide microarray analysis of MG-63 osteoblastic cells exposed to ultrasound," *Biorheology*, vol. 45, no. 3–4, pp. 345–354, 2008.
- [54] F. Las Heras, H. K. Gahunia, and K. P. Pritzker, "Articular cartilage development: a molecular perspective," *Orthopedic Clinics of North America*, vol. 43, no. 2, pp. 155–171, 2012.
- [55] N. Z. Mostafa, H. Uludağ, D. N. Dederich, M. R. Doschak, and T. El-Bialy, "Anabolic effects of low-intensity pulsed ultrasound on human gingival fibroblasts," *Archives of Oral Biology*, vol. 54, no. 8, pp. 743–748, 2009.
- [56] T. El-Bialy, H. Uludag, N. Jomha, and S. F. Badylak, "In vivo ultrasound-assisted tissue-engineered mandibular condyle: a pilot study in rabbits," *Tissue Engineering, Part C*, vol. 16, no. 6, pp. 1315–1323, 2010.
- [57] S. Zhou, A. Schmelz, T. Seufferlein, Y. Li, J. Zhao, and M. G. Bachem, "Molecular mechanisms of low intensity pulsed ultrasound in human skin fibroblasts," *Journal of Biological Chemistry*, vol. 279, no. 52, pp. 54463–54469, 2004.
- [58] T. Matsumoto, G. M. Cooper, B. Gharaibeh et al., "Cartilage repair in a rat model of osteoarthritis through intraarticular transplantation of muscle-derived stem cells expressing bone morphogenetic protein 4 and soluble Flt-1," *Arthritis and Rheumatism*, vol. 60, no. 5, pp. 1390–1405, 2009.
- [59] M. Pei, F. He, B. M. Boyce, and V. L. Kish, "Repair of full-thickness femoral condyle cartilage defects using allogeneic synovial cell-engineered tissue constructs," *Osteoarthritis and Cartilage*, vol. 17, no. 6, pp. 714–722, 2009.
- [60] B. Grigolo, G. Lisignoli, G. Desando et al., "Osteoarthritis treated with mesenchymal stem cells on Hyaluronan-based scaffold in rabbit," *Tissue Engineering, Part C*, vol. 15, no. 4, pp. 647–658, 2009.
- [61] F. S. Toghraie, N. Chenari, M. A. Gholipour et al., "Treatment of osteoarthritis with infrapatellar fat pad derived mesenchymal stem cells in Rabbit," *Knee*, vol. 18, no. 2, pp. 71–75, 2011.
- [62] J. M. Murphy, D. J. Fink, E. B. Hunziker, and F. P. Barry, "Stem cell therapy in a caprine model of osteoarthritis," *Arthritis and Rheumatism*, vol. 48, no. 12, pp. 3464–3474, 2003.
- [63] C. Hamou, M. J. Callaghan, H. Thangarajah et al., "Mesenchymal stem cells can participate in ischemic neovascularization," *Plastic and Reconstructive Surgery*, vol. 123, no. 2, supplement, pp. 45S–55S, 2009.
- [64] K. Chen, C. Man, B. Zhang, J. Hu, and S. S. Zhu, "Effect of in vitro chondrogenic differentiation of autologous mesenchymal stem cells on cartilage and subchondral cancellous bone repair in osteoarthritis of temporomandibular joint," *International Journal of Oral and Maxillofacial Surgery*, vol. 42, no. 2, pp. 240–248, 2012.
- [65] C. Ohlsson, B. Å. Bengtsson, O. G. P. Isaksson, T. T. Andreassen, and M. C. Sootweg, "Growth hormone and bone," *Endocrine Reviews*, vol. 19, no. 1, pp. 55–79, 1998.
- [66] A. Giustina, G. Mazziotti, and E. Canalis, "Growth hormone, insulin-like growth factors, and the skeleton," *Endocrine Reviews*, vol. 29, no. 5, pp. 535–559, 2008.
- [67] O. G. P. Isaksson, J. O. Jansson, and I. A. M. Gause, "Growth hormone stimulates longitudinal bone growth directly," *Science*, vol. 216, no. 4551, pp. 1237–1239, 1982.
- [68] E. Hedner, A. Linde, and A. Nilsson, "Systemically and locally administered growth hormone stimulates bone healing in combination with osteopromotive membranes: an experimental study in rats," *Journal of Bone and Mineral Research*, vol. 11, no. 12, pp. 1952–1960, 1996.
- [69] G. Johannsson, T. Rosén, I. Bosaeus, L. Sjöström, and B. Å. Bengtsson, "Two years of growth hormone (GH) treatment increases bone mineral content and density in hypopituitary patients with adult-onset GH deficiency," *Journal of Clinical Endocrinology and Metabolism*, vol. 81, no. 8, pp. 2865–2873, 1996.
- [70] A. M. Parfitt, "Growth hormone and adult bone remodeling," *Clinical Endocrinology*, vol. 35, pp. 467–470, 1991.
- [71] V. Visnapuu, T. Peltomäki, O. Rönning, T. Vahlberg, and H. Helenius, "Growth hormone and insulin-like growth factor I receptors in the temporomandibular joint of the rat," *Journal of Dental Research*, vol. 80, no. 10, pp. 1903–1907, 2001.
- [72] R. van Erum, M. Mulier, C. Cards, G. Verbeke, and F. de Zegher, "Craniofacial growth in short children born small for gestational age: effect of growth hormone treatment," *Journal of Dental Research*, vol. 76, no. 9, pp. 1579–1586, 1997.
- [73] C. M. Forsberg, L. Krekmanova, and G. Dahllöf, "The effect of growth hormone therapy on mandibular and cranial base

- development in children treated with total body irradiation," *European Journal of Orthodontics*, vol. 24, no. 3, pp. 285–292, 2002.
- [74] G. M. Farris, G. K. Miller, G. K. Wollenberg, S. Molon-Noblot, C. Chan, and S. Prahalada, "Recombinant rat and mouse growth hormones: risk assessment of carcinogenic potential in 2-year bioassays in rats and mice," *Toxicological Sciences*, vol. 97, no. 2, pp. 548–561, 2007.
- [75] Y. Murakami, M. Satake, Y. Yamaguchi-Iwai, M. Sakai, M. Muramatsu, and Y. Ito, "The nuclear protooncogenes c-jun and c-fos as regulators of DNA replication," *Proceedings of the National Academy of Sciences of the United States of America*, vol. 88, no. 9, pp. 3947–3951, 1991.
- [76] P. Rotwein, A. M. Granowski, and M. J. Thomas, "Rapid nuclear actions of growth hormone," *Hormone Research*, vol. 42, no. 4-5, pp. 170–175, 1994.
- [77] I. Khan, A. EL-Kadi, and T. El-Bialy, "Effects of growth hormone and ultrasound on mandibular growth in rats: microCT and toxicity analyses," *Archives of Oral Biology*. In press.
- [78] H. M. Lim, K. K. K. Lew, and D. K. L. Tay, "A clinical investigation of the efficacy of low level laser therapy in reducing orthodontic postadjustment pain," *American Journal of Orthodontics and Dentofacial Orthopedics*, vol. 108, no. 6, pp. 614–622, 1995.
- [79] D. Turhani, M. Scheriau, D. Kapral, T. Benesch, E. Jonke, and H. P. Bantleon, "Pain relief by single low-level laser irradiation in orthodontic patients undergoing fixed appliance therapy," *American Journal of Orthodontics and Dentofacial Orthopedics*, vol. 130, no. 3, pp. 371–377, 2006.
- [80] K. Fujiyama, T. Deguchi, T. Murakami, A. Fujii, K. Kushima, and T. Takano-Yamamoto, "Clinical effect of CO<sub>2</sub> laser in reducing pain in orthodontics," *Angle Orthodontist*, vol. 78, no. 2, pp. 299–303, 2008.
- [81] M. T. J. Rodrigues, M. S. Ribeiro, E. B. Grtoth, and D. M. Zzell, "Evaluation of effects of laser therapy on oral ulceration induced by fixed orthodontic appliances," *Lasers in Surgery and Medicine*, vol. 30, supplement 14, p. 15, 2002.
- [82] S. Saito and N. Shimizu, "Stimulatory effects of low-power laser irradiation on bone regeneration in midpalatal suture during expansion in the rat," *American Journal of Orthodontics and Dentofacial Orthopedics*, vol. 111, no. 5, pp. 525–532, 1997.
- [83] K. Kawasaki and N. Shimizu, "Effects of low-energy laser irradiation on bone remodelling during experimental tooth movement in rats," *Lasers in Surgery and Medicine*, vol. 26, pp. 282–291, 2000.
- [84] X. Sun, X. Zhu, C. Xu, N. Ye, and H. Zhu, "Effects of low energy laser on tooth movement and remodeling of alveolar bone in rabbits," *Hua Xi Kou Qiang Yi Xue Za Zhi*, vol. 19, no. 5, pp. 290–293, 2001.
- [85] T. I. Karu, L. V. Pyatibrat, S. F. Kolyakov, and N. I. Afanasyeva, "Absorption measurements of a cell monolayer relevant to phototherapy: reduction of cytochrome c oxidase under near IR radiation," *Journal of Photochemistry and Photobiology B*, vol. 81, no. 2, pp. 98–106, 2005.
- [86] M. Khadra, H. J. Rønold, S. P. Lyngstadaas, J. E. Ellingsen, and H. R. Haanaes, "Low-level laser therapy stimulates bone-implant interaction: an experimental study in rabbits," *Clinical Oral Implants Research*, vol. 15, no. 3, pp. 325–332, 2004.
- [87] J. T. Eells, M. T. T. Wong-Riley, J. VerHoeve et al., "Mitochondrial signal transduction in accelerated wound and retinal healing by near-infrared light therapy," *Mitochondrion*, vol. 4, no. 5-6, pp. 559–567, 2004.
- [88] H. T. Whelan, R. L. Smits Jr., E. V. Buchman et al., "Effect of NASA light-emitting diode irradiation on wound healing," *Journal of Clinical Laser Medicine and Surgery*, vol. 19, no. 6, pp. 305–314, 2001.
- [89] M. T. T. Wong-Riley, H. L. Liang, J. T. Eells et al., "Photobiomodulation directly benefits primary neurons functionally inactivated by toxins: role of cytochrome c oxidase," *Journal of Biological Chemistry*, vol. 280, no. 6, pp. 4761–4771, 2005.
- [90] A. Ebrahim, J. Yeung, A. Habib, T. EL-Bialy, and J. M. AL-Qahtani, "Histomorphometric analysis: effect of laser and LED on mandibular growth," in *Proceedings of the Annual Meeting & Exhibition of the AADR*, Tampa, Fla, USA, March 2012, Poster # 954.
- [91] J. A. Wolff, R. W. Malone, P. Williams et al., "Direct gene transfer into mouse muscle in vivo," *Science*, vol. 247, no. 4949, pp. 1465–1468, 1990.
- [92] H. Herweijer and J. A. Wolff, "Progress and prospects: naked DNA gene transfer and therapy," *Gene Therapy*, vol. 10, no. 6, pp. 453–458, 2003.
- [93] T. Niidome and L. Huang, "Gene therapy progress and prospects: nonviral vectors," *Gene Therapy*, vol. 9, no. 24, pp. 1647–1652, 2002.
- [94] J. Park, J. Ries, K. Gelse et al., "Bone regeneration in critical size defects by cell-mediated BMP-2 gene transfer: a comparison of adenoviral vectors and liposomes," *Gene Therapy*, vol. 10, no. 13, pp. 1089–1098, 2003.
- [95] J. Dai and A. B. M. Rabie, "Gene therapy to enhance condylar growth using rAAV-VEGF," *Angle Orthodontist*, vol. 78, no. 1, pp. 89–94, 2008.
- [96] J. J. Francois and L. Haustrate, "Anomalies colobomateuses du globe oculaire et syndrome du premier arc," *Annales d'Oculistique*, vol. 187, pp. 340–368, 1954.
- [97] R. B. Stark and D. E. Saunders, "The first branchial syndrome. The oral-mandibular-auricular syndrome," *Plastic and Reconstructive Surgery*, vol. 29, pp. 229–239, 1962.
- [98] W. C. Grabb, "The first and second branchial arch syndrome," *Plastic and Reconstructive Surgery*, vol. 36, no. 5, pp. 485–508, 1965.
- [99] R. J. Gorlin, K. L. Jue, U. Jacobsen, and E. Goldschmidt, "Oculoauriculovertebral dysplasia," *The Journal of Pediatrics*, vol. 63, no. 5, pp. 991–999, 1963.
- [100] M. Goldenhar, "Association malformatives de l'oeil et de l'oreille, en particulier le syndrome dermoide epibulbaire-appendices auriculaires-fistula auris congenita et ses relations avec la dysotose mandibulo-faciale," *Journal of Human Genetics*, vol. 1, pp. 243–282, 1952.
- [101] R. J. Gorlin, J. J. Pindborg, and M. M. Cohen Jr., *Syndromes of the Head and Neck*, McGraw-Hill, New York, NY, USA, 2nd edition, 1976.
- [102] R. B. Ross, "Lateral facial dysplasia. (First and second branchial arch syndrome, hemifacial microsomia)," *Birth Defects: Original Article Series*, vol. 11, no. 7, pp. 51–59, 1975.
- [103] J. M. Converse, P. J. Coccardo, M. H. Becker, and D. Wood-Smith, "Clinical aspects of craniofacial microsomia," in *Symposium on Diagnosis and Treatment of Craniofacial Anomalies*, J. M. Converse, J. G. McCarthy, and D. Wood-Smith, Eds., pp. 461–475, CV Mosby, St. Louis, Mo, USA, 1979.
- [104] J. E. Horgan, B. L. Padwa, R. A. LaBrie, and J. B. Mulliken, "OMENS-Plus: analysis of craniofacial and extracraniofacial anomalies in hemifacial microsomia," *The Cleft Palate-Craniofacial Journal*, vol. 32, no. 5, pp. 405–412, 1995.



- [105] M. M. Cohen Jr., "Perspectives on craniofacial asymmetry. I. The biology of asymmetry," *International Journal of Oral and Maxillofacial Surgery*, vol. 24, no. 1, part 1, pp. 2–7, 1995.
- [106] M. M. Cohen Jr., "Perspectives on craniofacial asymmetry. II. Asymmetric embryopathies," *International Journal of Oral and Maxillofacial Surgery*, vol. 24, no. 1, part 1, pp. 8–12, 1995.
- [107] M. M. Cohen Jr., "Perspectives on craniofacial asymmetry. III. Common and/or well-known causes of asymmetry," *International Journal of Oral and Maxillofacial Surgery*, vol. 24, no. 2, pp. 127–133, 1995.
- [108] M. M. Cohen Jr., "Perspectives on craniofacial asymmetry. IV. Hemi-asymmetries," *International Journal of Oral and Maxillofacial Surgery*, vol. 24, no. 2, pp. 134–141, 1995.
- [109] R. R. J. Cousley and D. J. Wilson, "Hemifacial microsomia: developmental consequence of perturbation of the auriculofacial cartilage model?" *American Journal of Medical Genetics*, vol. 42, no. 4, pp. 461–466, 1992.
- [110] R. R. Wang and C. J. Andres, "Hemifacial microsomia and treatment options for auricular replacement: a review of the literature," *The Journal of Prosthetic Dentistry*, vol. 82, no. 2, pp. 197–204, 1999.
- [111] L. K. Robinson, H. E. Hoyme, D. K. Edwards, and K. L. Jones, "Vascular pathogenesis of unilateral craniofacial defects," *Journal of Pediatrics*, vol. 111, no. 2, pp. 236–239, 1987.
- [112] S. Pruzansky, "Not all dwarfed mandibles are alike," *Birth Defects: Original Article Series*, vol. 5, pp. 120–129, 1969.
- [113] L. T. Murray and J. E. Murray, "Asymmetries of the lower part of the face," in *Symposium on Reconstruction of Jaw Deformities*, L. A. Whitaker and P. Randall, Eds., pp. 171–196, CV Mosby, St. Louis, Mo, USA, 1978.
- [114] L. B. Kaban, J. B. Mulliken, and J. E. Murray, "Three-dimensional approach to analysis and treatment of hemifacial microsomia," *Cleft Palate Journal*, vol. 18, no. 2, pp. 90–99, 1981.
- [115] C. Moulin-Romsée, A. Verdonck, J. Schoenaers, and C. Carels, "Treatment of hemifacial microsomia in a growing child: the importance of co-operation between the orthodontist and the maxillofacial surgeon," *Journal of Orthodontics*, vol. 31, no. 3, pp. 190–200, 2004.

## Research Article

# An Immunohistochemistry Study of Sox9, Runx2, and Osterix Expression in the Mandibular Cartilages of Newborn Mouse

Hong Zhang,<sup>1,2</sup> Xiaopeng Zhao,<sup>3</sup> Zhiguang Zhang,<sup>4</sup> Weiwei Chen,<sup>2,5</sup> and Xinli Zhang<sup>2</sup>

<sup>1</sup> Department of Orthodontics, Guanghua School of Stomatology, Sun Yat-Sen University, Guangzhou 510055, China

<sup>2</sup> Dental and Craniofacial Research Institute, School of Dentistry, University of California, Los Angeles, CA, 90095, USA

<sup>3</sup> Department of Oral and Maxillofacial Surgery, Sun Yat-sen Memorial Hospital, Sun Yat-Sen University, Guangzhou 510120, China

<sup>4</sup> Department of Oral and Maxillofacial Surgery, Guanghua School of Stomatology, Sun Yat-Sen University, Guangzhou 510055, China

<sup>5</sup> Institute for Medical Biology, College of Life Sciences, South-Central University for Nationalities, Wuhan 430074, China

Correspondence should be addressed to Zhiguang Zhang; drzhangzg@163.com and Xinli Zhang; xzhang@dentistry.ucla.edu

Received 6 January 2013; Accepted 7 April 2013

Academic Editor: Chad M. Novince

Copyright © 2013 Hong Zhang et al. This is an open access article distributed under the Creative Commons Attribution License, which permits unrestricted use, distribution, and reproduction in any medium, provided the original work is properly cited.

The purpose of this study is to investigate the spacial expression pattern and functional significance of three key transcription factors related to bone and cartilage formation, namely, Sox9, Runx2, and Osterix in cartilages during the late development of mouse mandible. Immunohistochemical examinations of Sox9, Runx2, and Osterix were conducted in the mandibular cartilages of the 15 neonatal C57BL/6N mice. In secondary cartilages, both Sox9 and Runx2 were weakly expressed in the polymorphic cell zone, strongly expressed in the flattened cell zone and throughout the entire hypertrophic cell zone. Similarly, both transcriptional factors were weakly expressed in the uncalcified Meckel's cartilage while strongly expressed in the rostral cartilage. Meanwhile, Osterix was at an extremely low level in cells of the flattened cell zone and the upper hypertrophic cell zone in secondary cartilages. Surprisingly, Osterix was intensely expressed in hypertrophic chondrocytes in the center of the uncalcified Meckel's cartilage while moderately expressed in part of hypertrophic chondrocytes in the rostral process. Consequently, it is suggested that Sox9 is a main and unique positive regulator in the hypertrophic differentiation process of mandibular secondary cartilages, in addition to Runx2. Furthermore, Osterix is likely responsible for phenotypic conversion of Meckel's chondrocytes during its degeneration.

## 1. Introduction

The development of cartilages plays a pivotal role in the development and growth of the mandible. Mandibular cartilages are derived from ectomesenchymal cells of the first pharyngeal arch, but their characteristics differ. Meckel's cartilage is a fetal cartilaginous skeleton in the mandible. Although it is classified as primary cartilage similar to limb bud cartilage, it contains four distinct portions, each having a different fate. The anterior, intermediate, and proximal portions convert to intramandibular symphysis, sphenomandibular ligament, and the inner ear ossicles, respectively. The posterior portion of intramandibular Meckel's cartilage facing the developing molar buds undergoes developmental events similar to endochondral ossification, but the degradation mechanisms of this portion are distinct from those in endochondral ossification [1]. Independent of the chondroskeleton, four secondary

cartilages including the condylar, coronoid, angular, and symphyseal cartilage strongly influence the further development of the mandible. These secondary cartilages differ from the primary cartilage in embryonic origin, morphological and biochemical organization. They are derived from the periosteum of intramembranous bone after (secondary to) bone formation [2, 3]. Furthermore, they display a unique mode of cell proliferation and differentiation. The condylar cartilage, as a principle secondary cartilage, does not form columns of proliferating chondrocytes and grows multidirectionally to adapt to the mandibular fossa of the temporal bone [4].

Recent studies showed that the three master transcription factors of Sox9, Runx2, and Osterix are involved in the formation of Meckel's cartilage and mandibular condylar cartilage [3, 10]. Sox9, Runx2, and Osterix are key transcription factors, which are necessary in skeletal cell fate decision [11]. Sox9 (SRY-box containing gene 9) is an essential

and nonredundant factor of chondrogenesis. Analyses in genetically modified mice revealed that Sox9 promotes the early stage, but suppresses the terminal stage of chondrocyte differentiation in limb bud cartilage [12–14]. On the contrary, the multifunctional transcription factor Runx2, which is expressed in prehypertrophic and hypertrophic chondrocytes, is a main positive regulator of hypertrophic differentiation in late chondrogenesis of the limb buds [5, 15, 16]. New in vitro data demonstrated that Sox9 negatively regulates Runx2 by enhancing Bapx1 expression, which leads to the inhibition of terminal chondrocyte differentiation [17]. Osterix, which acts downstream of Runx2 during bone formation, is expressed in chondrocyte progenitors and prehypertrophic chondrocytes in rib, spine, and limb cartilages, suggesting that Osterix may play a critical role during the primary cartilage maturation in combination with Runx2 and Sox9 [6, 7].

However, the transcriptional control of the later development of mandibular cartilages remains poorly understood. At birth, the rostral process of intramandibular Meckel's cartilage is undergoing endochondral ossification, while the posterior portion of intramandibular Meckel's cartilage is degenerating [18–20]. Meanwhile, four secondary cartilages, especially the condylar cartilage, were not well documented in terms of their developmental characteristics, although they function mainly as a growth cartilage similar to limb bud cartilage. At present, transcription factors are attracting increasing clinical attention because of their roles in the etiology and pathogenesis of malformations and growth disorders, degenerative diseases, and in regenerative and repair processes [21, 22]. The findings that Runx2-deficient mice lack mandibular condylar cartilage and had deformed Meckel's cartilage indicate that Runx2 is essential for the formation of the mandibular cartilages [23]. In many cleidocranial dysplasia (CCD) patients who were linked to Runx2 deficient, however, there are no abnormal findings in the mandible, in spite of cases of condylar malformation, persistent symphysis, or a narrow coronoid process being also known [24, 25]. These investigations provided a hint that Runx2 may be just one of essential biological factors influencing the development and growth of mandibular cartilages. The present study is to examine tissue distribution of Sox9, Runx2, and Osterix in newborn mice mandibular cartilages using immunohistochemistry technique and investigate whether these transcription factors have similar functions to those in limb bud cartilage which will contribute to current understanding of mechanisms of the development of mandible and the possible pathogenesis of some craniofacial anomalies involving mandible.

## 2. Materials and Methods

All animals were housed and handled in accordance with guidelines of the Chancellor's Animal Research Committee of the Office for Protection of Research Subjects at the University of California, Los Angeles, CA, USA.

**2.1. Tissue Preparation.** A total of 15 newborn C57BL/6N mice were collected in 2 hours right after being delivered and

used for this study. The mandibles were then removed and immersed in 4% paraformaldehyde (0.1 M phosphate buffer, pH 7.4) for 1 day at 4°C. The specimens were decalcified with 10% EDTA for 5 days at 4°C and then embedded in paraffin using standard procedures. Sections (5 µm) were cut in the plane parallel to the ascending ramus of the mandible, all the mandibular cartilages being in one section. For general morphology, deparaffinized sections were stained with hematoxylin and eosin. The skeletal staining with Alizarin Red-Alcian Blue was performed for preparation of gross specimen of mandible as reported previously [26].

**2.2. Immunohistochemistry.** Five-micron-thick paraffin sections were dewaxed in xylenes and rehydrated in ethanol baths. Endogenous peroxidases were blocked by incubating sections in 3% hydrogen peroxide for 20 min at room temperature. Sections were incubated with anti-Runx2, anti-Osterix, and anti-Sox9 primary antibodies (Santa Cruz Biotechnology, CA, USA) (dilution 1:100) and biotinylated anti-rabbit or anti-goat IgG secondary antibody (Vector Laboratories, Burlingame, CA) for 1 h at room temperature. Positive immunoreactivity was detected using Vectastain ABC kit (Vector Laboratories, Burlingame, CA, USA) and AEC chromogenic substrate (Dako, Carpinteria, CA, USA) with red positive staining. A negative control was performed by replacing primary antibody solutions with PBS. Sections were counterstained with hematoxylin for 30 sec followed by rinsing 5 min in running water. Photomicrographs were acquired using an Olympus BX51. Image-pro Plus 6.0 software was used to calculate stained area and Integrated Optical Density (IOD). The average optical density (mean density) represented the intensity of protein expression and was counted in 4 random fields (×20 objective) of each cartilage area and trabecular bone area per section. The mean density is equal to (IOD SUM)/area. For exact analysis, three sections were prepared at similar plane for each sample. ANOVA was used for multiple groups' comparison, and Student's *t*-test was used for comparison between any two groups. Statistical significance defined as  $P < 0.05$ .

## 3. Results

**3.1. Histological Analysis of Cartilages in Newborn Mouse Mandible.** Mandibular cartilages in newborn mouse included the portions of Meckel's cartilage, condylar, angular, and symphyseal secondary cartilage, while cartilage was not present in the coronoid process of the newborn mouse (Figure 1(a)). On the basis of the cellular morphological changes, the mandibular condylar and angular cartilages were histologically composed of four different cell zones: a thin fibrous cell zone, a polymorphic cell zone, a wider flattened cell zone, and a broad hypertrophic cell zone occupied the lower half of the organ (Figures 1(b) and 1(c)). Almost all of the intramandibular bar of Meckel's cartilage had ossified completely, but a small amount of Meckel's cartilage remained in a limited portion of the rostral region and at the mylohyoid groove between the condylar and angular processes. At the posterior portion of intramandibular Meckel's cartilage, HE staining pattern of the matrix changed from the intense



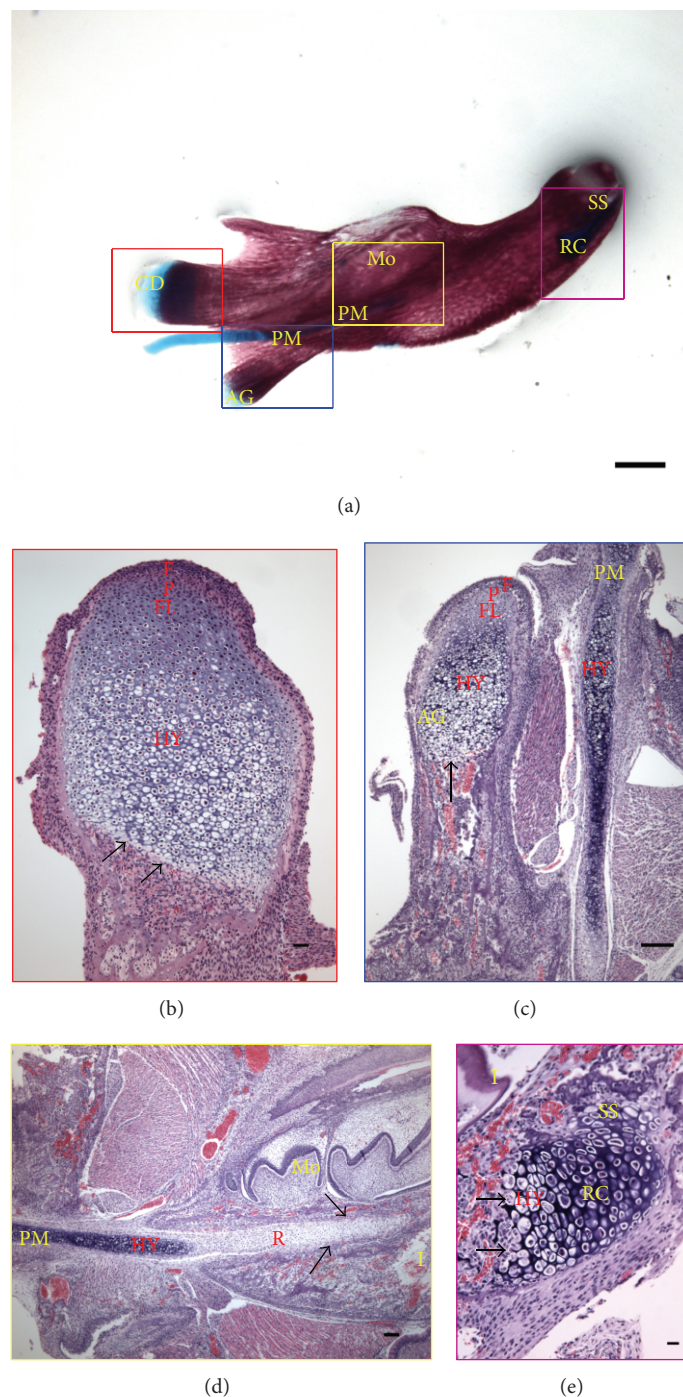


FIGURE 1: Histological analysis of mandibular cartilages of mice at newborn stage. (a) Lingual view of mandible by Alizarin Red and Alcian Blue staining; (b) hematoxylin-eosin sections of condylar cartilage, and (c) hematoxylin-eosin sections of angular cartilage (AG) similarly displaying four different cell zones: a thin fibrous cell zone (F), a polymorphic cell zone (P), a wider flattened cell zone (FL), and a broad hypertrophic cell zone (HY); (d) hematoxylin-eosin staining pattern of the matrix of the posterior portion of intramandibular Meckel's cartilage (PM) changed from the intense hematoxylin to the light eosin in the resorption (R) facing the molar buds (Mo) and incisor (I); (e) hematoxylin-eosin sections of the endochondral ossification rostral process of Meckel's cartilage (RC) and symphyseal secondary cartilage (SS) facing the incisor (I). Scale bar: 100  $\mu\text{m}$  for (a) and (b), 250  $\mu\text{m}$  for (c) and (d), and 50  $\mu\text{m}$  for (e).

hematoxylin to the light eosin in resorption area, which indicated the degradation of Meckel's cartilage matrix during development (Figure 1(d)). Furthermore, the endochondral ossification rostral process of Meckel's cartilage and symphyseal secondary cartilage serve as a chondrogenic mandibular symphysis of newborn mice (Figure 1(e)). The opened chondrocytic lacunae and disconnected cartilaginous matrix (arrows in Figures 1(b), 1(c), and 1(e)) were clearly found in the resorption area of condylar, angular, and symphyseal secondary cartilage, in addition to rostral cartilage, while the appearing perichondrium and the eosinophilic cartilage erode on the lateral sides (arrows in Figure 1(d)) were observed in the posterior portion of intramandibular Meckel's cartilage. These results indicated that the degradation of cartilaginous matrix in the posterior portion of intramandibular Meckel's cartilage is distinct from others among mandibular cartilages.

**3.2. Immunohistochemical Analysis of Sox9, Runx2, and Osterix in Cartilages of the Newborn Mouse Mandible.** Interestingly, transcription factors Sox9 and Runx2 showed similar expression level and tissue distribution patterns throughout all the mandibular cartilages of newborn mice. In secondary cartilages, both Sox9 and Runx2 were weakly expressed by cells in the polymorphic cell zone, strongly in the flattened cell zone and throughout the entire hypertrophic cell zone. To quantitatively measure changes in expression of transcriptional factors critical for chondrogenic differentiation, Sox9 (Figure 2(f)) and Runx2 (Figure 2(h)) immunohistochemistry in hypertrophic zones of mandibular cartilages at newborn stage were quantitated by average optical density of positive staining. The expression levels of both transcriptional factors in the degrading posterior portion of intramandibular Meckel's cartilage (Figures 2(b) and 2(d)) exhibited a significantly decrease, compared with others among mandibular cartilages. Meanwhile, cells in the rostral cartilage (Figures 2(e) and 2(g)) and cells in extramandibular Meckel's cartilage (Figures 2(f) and 2(h)) similarly expressed both transcriptional factors more than in the degrading posterior portion of intramandibular Meckel's cartilage. Unexpectedly, Sox9, as Runx2, was expressed in all the terminal chondrocytes of the mandibular cartilages in newborn mice (Figures 2(a), 2(b), and 2(e)), contrary to the express pattern of Sox9 in limb bud cartilage [8]. This spatial distribution pattern indicated Sox9's requirement in the terminal stage of mandibular chondrocyte differentiation.

Runx2 and Osterix are involved in the formation of Meckel's cartilage and mandibular condylar cartilage [3, 10]. Thus, we correlated the expression patterns of Runx2 (Figures 2(c), 2(d), and 2(g)) and Osterix (Figure 3) in mandibular cartilages at newborn stages. Results showed that Osterix was at an extremely low level in part of cells of the flattened cell zone and the upper hypertrophic cell zone in condylar cartilage and angular cartilage, independent on Runx2. Unlike Sox9, the spatial pattern of Osterix in condylar cartilage and angular cartilage was consistent with that in limb bud cartilage [7, 9]. Notably, Osterix was intensely expressed only in hypertrophic chondrocytes of the center of the uncalcified Meckel's cartilage containing the strong basophilic matrix,

while it was entirely absent in hypertrophic chondrocytes in the resorption area containing the light eosinophilic matrix (Figures 3(b), 1(c), and 1(d)). Additionally, the expression level of Osterix in the hypertrophic chondrocytes of Meckel's cartilage (Figure 3(b)) was significantly higher compared with that in condylar cartilage and angular cartilage which have only few positive cells in the flattened cell zone and the upper hypertrophic cell zone (Figures 3(a), 3(b), and 3(d)). Moreover, Osterix was moderately expressed in part of hypertrophic chondrocytes in the rostral process (Figure 3(c)), while it was absent in extramandibular Meckel's cartilage. At present, the mechanisms of Osterix regulation of chondrocyte differentiation and function are still under investigation, whereas the significantly intense immunohistochemistry of Osterix in hypertrophic chondrocytes of the center of the uncalcified Meckel's cartilage provided evidence of Osterix's role in the degradation of the posterior portion of uncalcified intramandibular Meckel's cartilage.

**3.3. Comparison of Expression Intensity of Runx2 and Osterix in the Chondrocytes with That in the Osteoblasts of the Newborn Mouse Mandible.** Since Runx2 and Osterix are indispensable for osteoblast differentiation and known to be expressed in osteoblasts, we first confirmed the positive staining of osteoblasts using the same sections of cartilages with Runx2 and Osterix positive staining, which also validated our IHC approach to be highly reliable. Then, we compared the expression intensity of the two key transcriptional factors related to bone formation in chondrocytes with that in mandibular osteoblasts to further confirm the significance of both during the development of mandibular cartilages. Similar to the condylar subchondral bone in 56-day-old rats [27], Runx2 protein which was expressed in secondary hypertrophic chondrocytes was not localized in the cells gathering in the erosive front of all the mandibular secondary cartilages (Figure 4(a)), but in some osteoblasts surrounding the trabecular bone and some osteocytes buried in the trabecular bone in the mandible (Figure 4(b)). Thus, we quantitatively analyzed the expression of Runx2 protein in osteoblasts and osteocytes (Figure 4(e)), comparing with that in condylar cartilage and the posterior portion of intramandibular Meckel's cartilage. In the present study, the expression of Runx2 protein in condylar hypertrophic chondrocytes was the most intense (Figures 2(h) and 4(e)), being statistically significant difference from that in osteoblasts, which indicated an important role of Runx2 in secondary chondrocyte maturation, in addition to that in chondrocyte maturation of growth cartilage and osteoblast differentiation. Expectedly, Osterix was localized in some osteoblasts and bone marrow cells in sub-chondral bone area (Figure 4(c)). Furthermore, more positive osteoblasts and osteocytes were visualized in the trabecular bone area (Figure 4(d)). Interestingly, the immunohistochemistry of Osterix in hypertrophic chondrocytes of the center of the uncalcified Meckel's cartilage is still significantly more intense than that in the osteoblasts (Figure 4(f)). This pointed out that Osterix highly likely performed a regulatory effect on the degradation of the posterior portion of uncalcified intramandibular Meckel's cartilage.

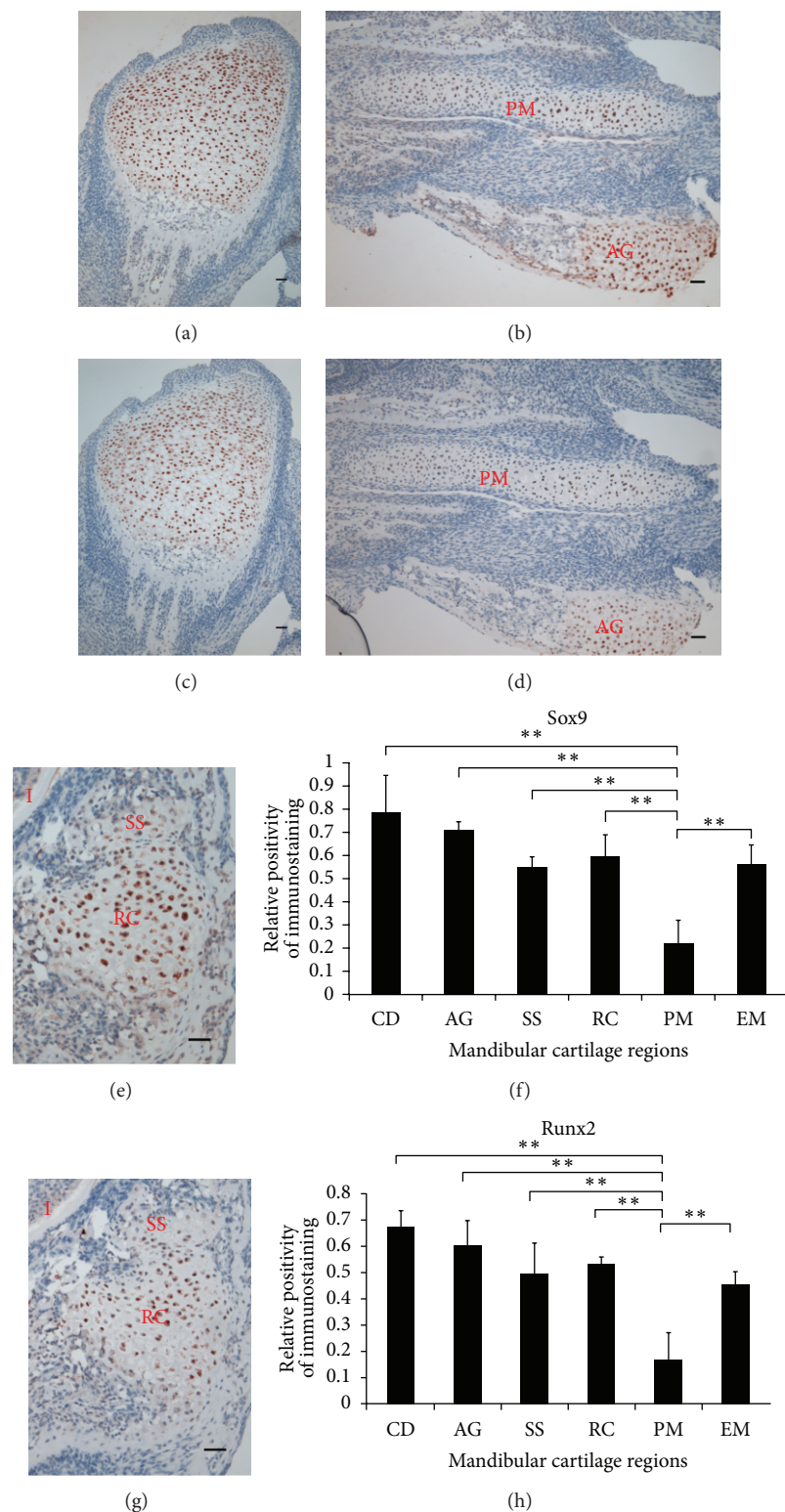


FIGURE 2: Immunohistochemistry of Sox9 and Runx2 in mandibular cartilages of mice at newborn stage. Sox9 (a, b, and e) and Runx2 (c, d, and g) showed similar expression patterns throughout all the mandibular cartilages. In condylar cartilage (a and c), angular cartilage (b and d), and symphyseal secondary cartilage and rostral cartilage (e and g), both Sox9 and Runx2 were strongly expressed by cells entire hypertrophic cell zone. Scale bar: 100  $\mu$ m for (a, b, c, and d) and 50  $\mu$ m for (e and g). Results of Sox9 (f) and Runx2 (h) immunohistochemistry in hypertrophic zones of mandibular cartilages including condylar (CD), angular (AG), and symphyseal secondary cartilage (SS), and rostral process (RC), posterior Meckel's (PM), and extramandibular Meckel's (EM) cartilage were quantitated by average optical density of positive staining per 200 field (\*\* $P < 0.001$ ). The expression levels of both transcriptional factors in the posterior portion of uncalcified intramandibular Meckel's cartilage (b and d) were significantly reduced than in other cartilages.



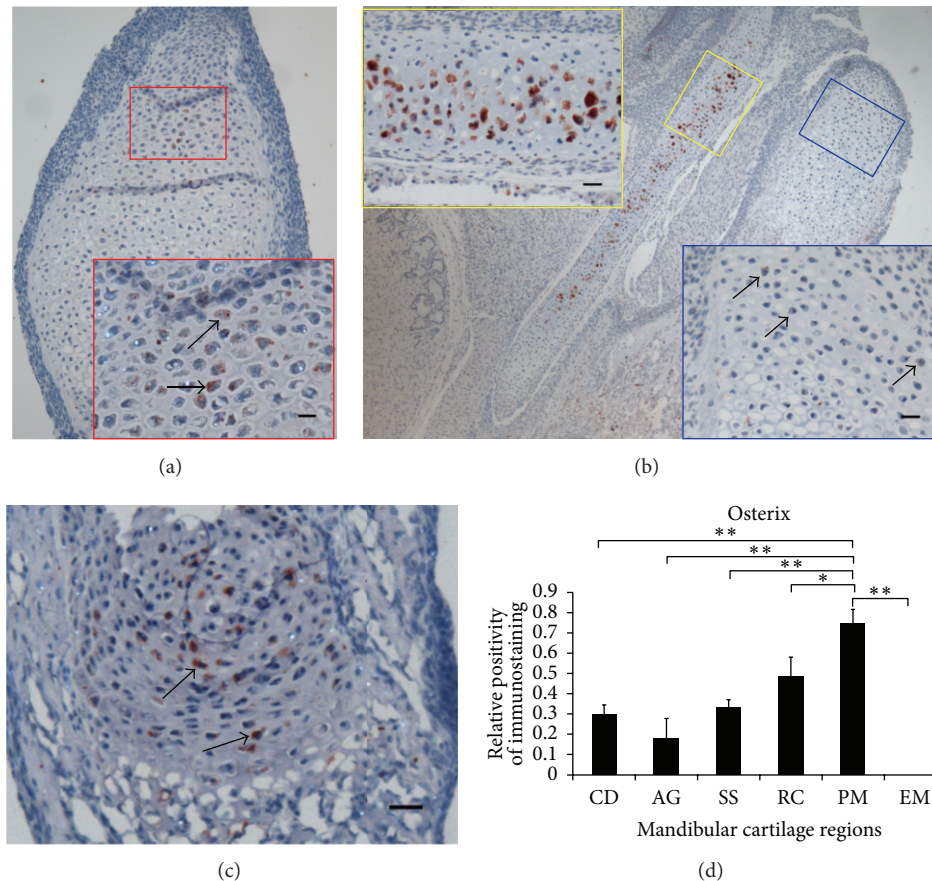


FIGURE 3: Immunohistochemistry of Osterix in mandibular cartilages of mice at newborn stage. Osterix was at a extremely low level in condylar cartilage (in the red box of (a)) and angular cartilage (in the blue box of (b)) while intensely expressed in the center of the Meckel's cartilage containing the strong basophilic matrix (in the yellow box of (b) and Figure 1(c)). Further, Osterix was moderately expressed in the rostral process (c). Scale bar: 25  $\mu$ m for (a', b', and b'') and 50  $\mu$ m for (c). Results of Osterix (d) immunohistochemistry in mandibular cartilages including condylar (CD), angular (AG), and symphyseal secondary cartilage (SS) and rostral process (RC), posterior Meckel's (PM), and extramandibular Meckel's (EM) cartilage were quantitated by average optical density of positive staining per 200 field (\* $P$  < 0.05, \*\* $P$  < 0.001). Immunohistochemistry of Osterix in the posterior portion of intramandibular Meckel's cartilage was significantly stronger and had more positive cells than in other cartilages.

#### 4. Discussion

The majority of *in vivo* studies on cartilage differentiation are carried out using the appendicular skeleton as a model system, with the implicit assumption that chondrogenesis is equivalent throughout the body. However, Eames directly tested that the programs of chick head chondrogenesis are unique by comparing the neural crest-derived pharyngeal arch skeleton to that of the mesoderm-derived limb, due to the fact that each skeleton forms from unique embryonic populations [28]. Meckel's cartilage and mandibular secondary cartilages are markedly distinguished from limb bud cartilage in their embryonic origin. The mechanisms that regulate the diverse developmental programs in Meckel's cartilage and mandibular secondary cartilages remain to be discovered. The present study investigated the expression of the essential transcription factors related to chondrogenesis in these cartilages during the later development of mandibular cartilages.

The accumulated studies confirmed that Sox9 accelerates chondrocyte differentiation in proliferating chondrocytes but inhibits the terminal stages of chondrocyte differentiation in limb bud cartilage [29, 30]. However, few investigations focused on the mechanism of Sox9 in secondary chondrocyte differentiation [31]. Our findings clearly demonstrated that the key transcription factor Sox9 was strongly expressed at the whole hypotrophic cell zone of condylar cartilage and angular cartilage in newborn mice, which was different from the expression pattern of Sox9 in limb bud cartilage (Figure 5(a)) [8]. Moreover, Rabie et al. have demonstrated that Sox9 were expressed at the hypertrophic cell zone of the condylar cartilage in 36-day-old rats and continued to be expressed throughout the examined period until day 52 [32]. Conversely, in limb bud cartilage, both of the Sox9 transcripts and protein were absent or at very diminished levels in hypertrophic chondrocytes [8, 9]. The recent data demonstrated that Sox9 is a major negative regulator of cartilage vascularization, bone marrow formation, and endochondral

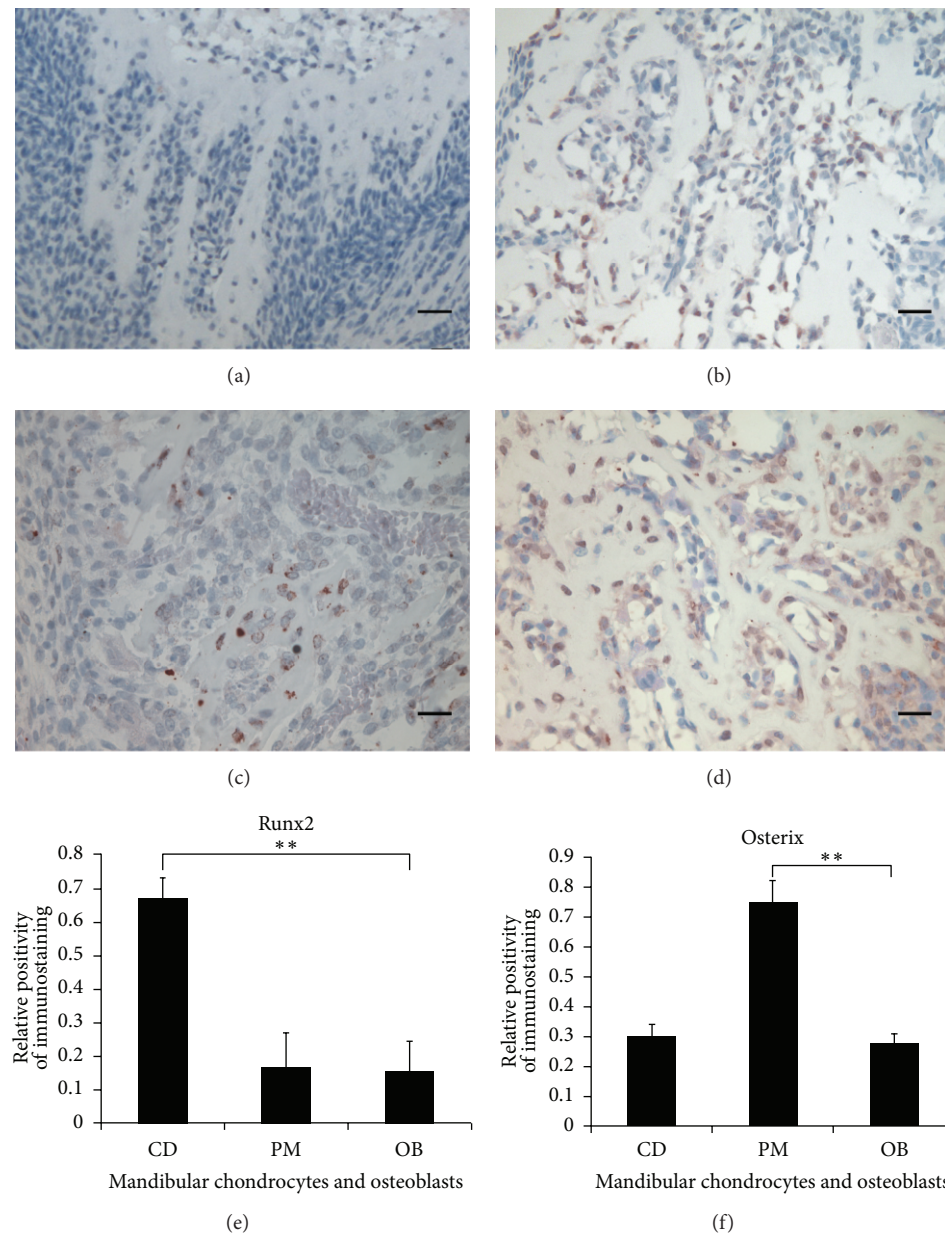


FIGURE 4: Immunohistochemistry of Runx2 and Osterix in mandibular osteoblasts of mice at newborn stage. Runx2 protein which was expressed in secondary hypertrophic chondrocytes was not localized in the cells gathering in the erosive front of mandibular secondary cartilages (a), but in some osteoblasts surrounding the trabecular bone and some osteocytes buried in the trabecular bone in the mandible (b). The expression of Runx2 protein in condylar hypertrophic chondrocytes was significantly stronger than that in osteoblasts (e). Meanwhile, Osterix was localized in some osteoblasts and bone marrow cells in subchondral bone area (c), while more positive osteoblasts and osteocytes were visualized in the trabecular bone area (d). The immunohistochemistry of Osterix in hypertrophic chondrocytes of the center of the uncalcified Meckel's cartilage is still significantly more intense than that in the osteoblasts (f). (\*\* $P < 0.001$ ) CD: condylar cartilage; PM: the posterior portion of intramandibular Meckel's cartilage; and OB: osteoblasts. Scale bar: 25  $\mu\text{m}$  for (a, b, c, and d).

ossification [33]. Despite this observation, our investigations indicate that Sox9 downregulation is not necessary in the terminal stage of secondary cartilage development. We speculated that the transcription factor Sox9 may be a main positive regulator in the secondary cartilage terminal maturation, contrary to its function in later differentiation of limb bud cartilage, based on strong expression of Sox9 in the mandibular secondary hypertrophic cell zone.

In the present study, surprisingly, transcription factors Sox9 and Runx2 were similarly expressed at mandibular secondary cartilages in newborn mice, suggesting that Sox9 and Runx2 may coregulate secondary chondrocyte differentiation. In avian secondary cartilage formation, Buxton reported that Runx2-expressing preosteoblasts exit from the cell cycle and rapidly differentiate into hypertrophic chondrocytes, which is correlated with the up-regulation of Sox9

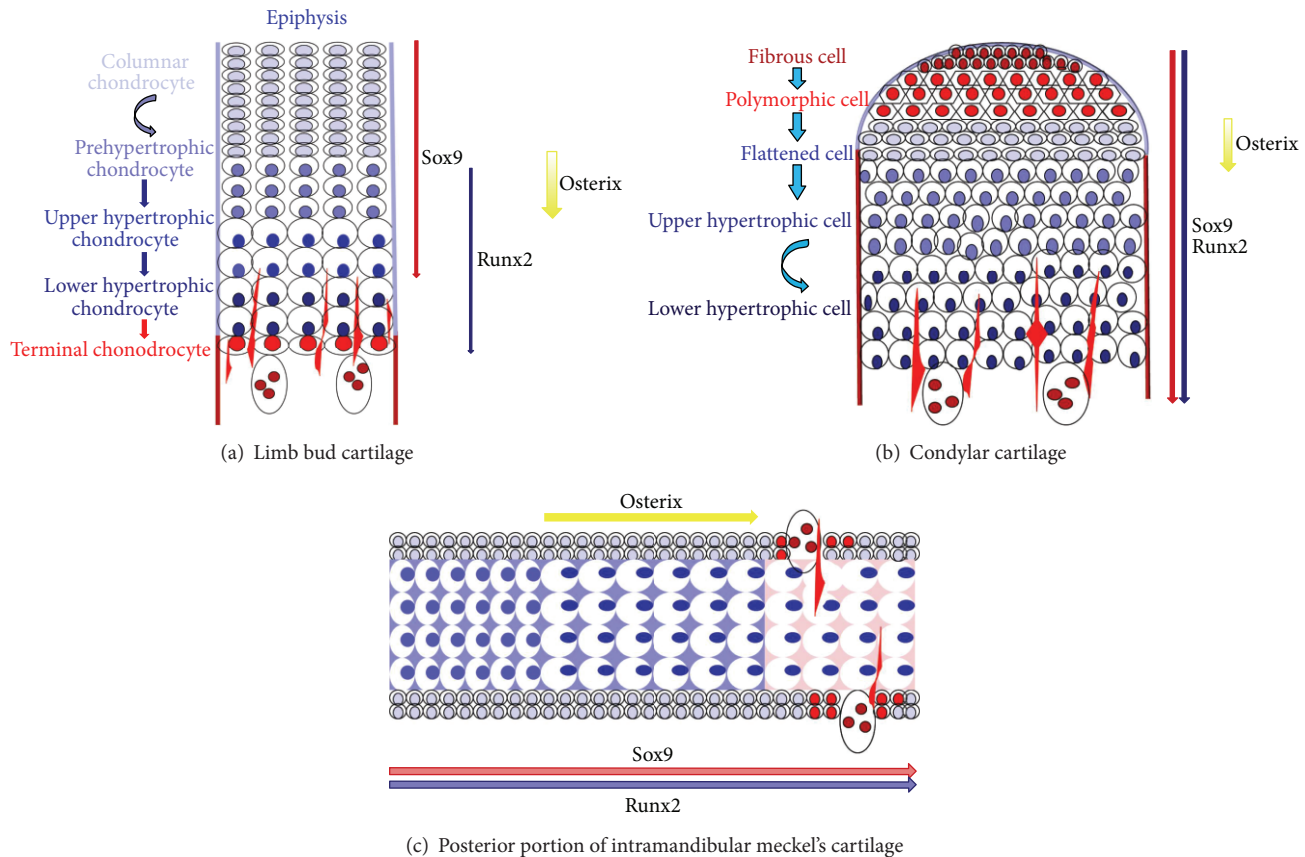


FIGURE 5: Schematic representations of the expression pattern of three key transcription factors in the different types of cartilage during the newborn stage. The expression pattern of Sox9, Runx2, and Osterix in limb bud cartilage is based on previous reports of Kim et al. [5], Kaback et al. [6], Nishimura et al. [7], Ng et al. [8], and Dy et al. [9]. Furthermore, the expression patterns of Sox9 (red), Runx2 (blue), and Osterix (yellow) in condylar cartilage and Meckel's cartilage are based on the present findings. Long arrows indicate the expressing cell zones of transcription factors in cartilage. (a) limb bud cartilage, (b) condylar cartilage, and (c) the posterior portion of intramandibular Meckel's cartilage.

[31]. In addition, Buxton described two routes to chondrocyte hypertrophy and had postulated that precursors expressing Sox9 differentiate into prehypertrophic/hypertrophic chondrocytes mediated by the up-regulation of Runx2 in primary cartilage formation. Whereas, preosteoblasts expressing Runx2 differentiate into prehypertrophic/hypertrophic chondrocytes mediated by the upregulation of Sox9 in secondary cartilage formation [31]. Mammalian mandibular secondary cartilages are a heterogeneous tissue containing cells at various stages of chondrocyte maturation [34]. Moreover, these secondary cartilages manifest a unique zone-like packing of maturing chondrocytes [35]. Shibata and Yokohama-Tamaki recently demonstrated that the mandibular secondary cartilage anlagen are derived from Runx2 mRNA expressing mandibular anlage [10]. Thus, our observations on the overlapping expression of Sox9 and Runx2 at mandibular secondary cartilages in newborn mice support Buxton's proposed concept in principle. The up-regulation of Sox9 from the polymorphic cell zone to the hypertrophic cell zone might act as a trigger for subsequent mammalian secondary chondrocyte differentiation. This can be interpreted as evidence of a unique differentiation pathway: the formation of secondary

hypertrophic chondrocytes from osteoblast precursors, with the help of the positive regulator Sox9.

More unexpectedly, our finding that Sox9 and Runx2 were coexpressed in the hypertrophic cell zone of the rostral region is not in line with the analyses of endochondral ossification in limb bud cartilage. The previous studies revealed that Sox9 inhibits the hypertrophic chondrocyte differentiation through suppression of Runx2 in endochondral ossification of limb bud cartilage [17]. Furthermore, Sox9 protein needs to be degraded to allow chondrocyte terminal maturation in limb bud cartilage [13]. However, Eames et al. had proposed that a unique combination of Sox9 and Runx2 may drive the expression of the major marker of hypertrophic chondrocytes, Col10, based on the analysis of Sox9 and Runx2 functions in primary cartilage differentiation of the avian cranial skeleton [36]. In the present study, the overlapping expression pattern of Sox9 and Runx2 in the hypertrophic cell zone of the rostral region of Meckel's cartilage provides clear evidence that Runx2 can drive the chondrocyte terminal differentiation in the presence of Sox9 protein. Additionally, our data that Sox9 and Runx2 were similarly expressed less in the hypertrophic cell zone of the posterior portion of



intramandibular Meckel's cartilage has reinforced the notion that degeneration of Meckel's cartilage represents a different process from endochondral ossification.

Normally, Osterix is present at an extremely low level in prehypertrophic chondrocytes of limb bud cartilage, compared to osteoblasts [9]. To our knowledge, the present study is the first to demonstrate the expression of Osterix protein in mandibular cartilages. Osterix protein is faintly expressed in prehypertrophic chondrocytes of secondary cartilages, similar to limb bud cartilage, which suggests that Osterix plays similar roles during the two types of cartilage development. By contrast, Osterix protein is intensely expressed in hypertrophic chondrocytes in the central zone of the bars of intramandibular Meckel's cartilage, while Osterix protein is not present in cells around light eosinophilic matrix dynamically changed from the strong basophilic matrix in the front of the degrading Meckel's cartilage. The light eosinophilic matrix in front of the degrading Meckel's cartilage might display the calcified cartilage matrix [37]. A great amount of *in vitro* data demonstrated that the chondrocytes of Meckel's cartilage can transdifferentiate to osteogenic cells as characterized by production of type I collagen [38–40]. Furthermore, the previous *in vivo* investigations revealed that the extracellular matrix of intramandibular portion of the Meckel's cartilage is replaced gradually by type I collagen secreted by chondrocytes during the development of Meckel's cartilage [41]. We speculated that Osterix may be relevant to phenotypic conversion of Meckel's chondrocytes. The enhanced expression of Osterix in mature chondrocytes might be an explanation of type I collagen synthesis by chondrocytes in Meckel's cartilage. Further studies are needed to elucidate the exact role of Osterix during the late development of Meckel's cartilage. On the other hand, the disparity in the expression pattern between Osterix and Runx2 in chondrocytes in the present study, suggested that Osterix might perform its regulation and function in mandibular cartilage development, independent of Runx2. Moreover, with respect to the more remarkable expression of Runx2 in the condylar cartilage and Osterix in intramandibular degrading Meckel's cartilage relative to those in osteoblasts in the present study we speculated that Runx2 or Osterix could need much more intense expression in the chondrocytes than in the osteoblasts, in order to play a functional role during the development of mandibular cartilages.

Cartilage is a complex and developmentally important tissue type. Transcriptional factors are crucial to the development of cartilages. The differential expression of key transcriptional factors in several types of cartilages will dictate the distinct cellular events during the development of the cartilages. The present data provide insights into the similar roles that master transcriptional factors Sox9 and Runx2 play during the later development of mandibular cartilages, which is different from that in limb bud cartilage. It is necessary to investigate in further detail whether the differences in cellular events between ectomesenchymal chondrocytes and mesodermal chondrocytes involve the derivation of the cells. Furthermore, Osterix is likely responsible for phenotypic conversion of Meckel's chondrocytes during its degeneration, based on its intensive expression in hypertrophic

chondrocytes of the degrading Meckel's cartilage of newborn mice. Human mandibular anomaly appears to be a common malformation and appears in multiple congenital birth defect syndromes, ranging from agnathia (agenesis of the jaw) to micrognathia to patterning malformations. These malformations are particularly devastating, as our faces are our identity [42]. The regeneration of complex facial structures requires precision and specificity. A much more thorough understanding of the mechanism of master transcriptional factors in mandibular chondrogenesis lay the important foundation for the application of targeted interventions at the molecular level, endogenous tissue engineering, and cell-based therapies in mandibular anomalies.

## 5. Conclusions

Our study demonstrated similar tissue distribution of Sox9 and Runx2 in newborn mice mandibular cartilages, which is distinguished from that in limb bud cartilage. It is speculated that Sox9 is a main and unique positive regulator in the hypertrophic differentiation process of mandibular secondary cartilages, in addition to Runx2. Moreover, the distinct expression pattern of osterix in degenerating posterior portion of Meckel's cartilage suggests that Osterix may be relevant to phenotypic conversion of Meckel's chondrocytes.

## Conflict of Interests

The authors declare that they have no conflict of interests.

## Acknowledgment

The authors thank the support of the National Natural Science Foundation of China (no. 10972242).

## References

- [1] Y. Sakakura, Y. Hosokawa, E. Tsuruga, K. Irie, M. Nakamura, and T. Yajima, "Contributions of matrix metalloproteinases toward Meckel's cartilage resorption in mice: immunohistochemical studies, including comparisons with developing endochondral bones," *Cell and Tissue Research*, vol. 328, no. 1, pp. 137–151, 2007.
- [2] S. Shibata, K. Fukada, S. Suzuki, and Y. Yamashita, "Immunohistochemistry of collagen types II and X, and enzyme-histochemistry of alkaline phosphatase in the developing condylar cartilage of the fetal mouse mandible," *Journal of Anatomy*, vol. 191, no. 4, pp. 561–570, 1997.
- [3] S. Shibata, N. Suda, S. Suzuki, H. Fukuoka, and Y. Yamashita, "An *in situ* hybridization study of Runx2, Osterix, and Sox9 at the onset of condylar cartilage formation in fetal mouse mandible," *Journal of Anatomy*, vol. 208, no. 2, pp. 169–177, 2006.
- [4] M. S. Kim, S. Y. Jung, J. H. Kang et al., "Effects of bisphosphonate on the endochondral bone formation of the mandibular condyle," *Anatomia, Histologia, Embryologia*, vol. 38, no. 5, pp. 321–326, 2009.
- [5] I. S. Kim, F. Otto, B. Zabel, and S. Mundlos, "Regulation of chondrocyte differentiation by Cbfa1," *Mechanisms of Development*, vol. 80, no. 2, pp. 159–170, 1999.

- [6] L. A. Kaback, D. Y. Soung, A. Naik et al., "Osterix/Sp7 regulates mesenchymal stem cell mediated endochondral ossification," *Journal of Cellular Physiology*, vol. 214, no. 1, pp. 173–182, 2008.
- [7] R. Nishimura, M. Wakabayashi, K. Hata et al., "Osterix regulates calcification and degradation of chondrogenic matrices through matrix metalloproteinase 13 (MMP13) expression in association with transcription factor Runx2 during endochondral ossification," *The Journal of Biological Chemistry*, vol. 287, no. 40, pp. 33179–33190, 2012.
- [8] L. J. Ng, S. Wheatley, G. E. O. Muscat et al., "SOX9 binds DNA, activates transcription, and coexpresses with type II collagen during chondrogenesis in the mouse," *Developmental Biology*, vol. 183, no. 1, pp. 108–121, 1997.
- [9] P. Dy, W. Wang, P. Bhattaram et al., "Sox9 directs hypertrophic maturation and blocks osteoblast differentiation of growth plate chondrocytes," *Developmental Cell*, vol. 22, no. 3, pp. 597–609, 2012.
- [10] S. Shibata and T. Yokohama-Tamaki, "An in situ hybridization study of Runx2, Osterix, and Sox9 in the anlagen of mouse mandibular condylar cartilage in the early stages of embryogenesis," *Journal of Anatomy*, vol. 213, no. 3, pp. 274–283, 2008.
- [11] L. Zou, X. Zou, H. Li et al., "Molecular mechanism of osteochondroprogenitor fate determination during bone formation," *Advances in Experimental Medicine and Biology*, vol. 585, no. 7, pp. 431–441, 2006.
- [12] W. Bi, J. M. Deng, Z. Zhang, R. R. Behringer, and B. de Crombrughe, "Sox9 is required for cartilage formation," *Nature Genetics*, vol. 22, no. 1, pp. 85–89, 1999.
- [13] H. Akiyama, M. C. Chaboissier, J. F. Martin, A. Schedl, and B. de Crombrughe, "The transcription factor Sox9 has essential roles in successive steps of the chondrocyte differentiation pathway and is required for expression of Sox5 and Sox6," *Genes & Development*, vol. 16, no. 21, pp. 2813–2828, 2002.
- [14] H. Akiyama, J. P. Lyons, Y. Mori-Akiyama et al., "Interactions between Sox9 and  $\beta$ -catenin control chondrocyte differentiation," *Genes & Development*, vol. 18, no. 9, pp. 1072–1087, 2004.
- [15] M. Mikasa, S. Rokutanda, H. Komori et al., "Regulation of Tcf7 by Runx2 in chondrocyte maturation and proliferation," *Journal of Bone and Mineral Metabolism*, vol. 29, no. 3, pp. 291–299, 2011.
- [16] M. Ding, Y. Lu, S. Abbassi et al., "Targeting Runx2 expression in hypertrophic chondrocytes impairs endochondral ossification during early skeletal development," *Journal of Cellular Physiology*, vol. 227, no. 10, pp. 3446–3456, 2012.
- [17] S. Yamashita, M. Andoh, H. Ueno-Kudoh, T. Sato, S. Miyaki, and H. Asahara, "Sox9 directly promotes Bapx1 gene expression to repress Runx2 in chondrocytes," *Experimental Cell Research*, vol. 315, no. 13, pp. 2231–2240, 2009.
- [18] H. Sugito, Y. Shibukawa, T. Kinumatsu et al., "Ihh signaling regulates mandibular symphysis development and growth," *Journal of Dental Research*, vol. 90, no. 5, pp. 625–631, 2011.
- [19] F. Tsuzurahara, S. Soeta, T. Kawawa, K. Baba, and M. Nakamura, "The role of macrophages in the disappearance of Meckel's cartilage during mandibular development in mice," *Acta Histochemica*, vol. 113, no. 2, pp. 194–200, 2011.
- [20] Y. Sakakura, Y. Hosokawa, E. Tsuruga, K. Irie, and T. Yajima, "In situ localization of gelatinolytic activity during development and resorption of Meckel's cartilage in mice," *European Journal of Oral Sciences*, vol. 115, no. 3, pp. 212–223, 2007.
- [21] B. Rath-Deschner, N. Daratsianos, S. Dühr et al., "The significance of RUNX2 in postnatal development of the mandibular condyle," *Journal of Orofacial Orthopedics*, vol. 71, no. 1, pp. 17–31, 2010.
- [22] S. Matsushima, N. Isogai, R. Jacquet et al., "The nature and role of periosteum in bone and cartilage regeneration," *Cells Tissues Organs*, vol. 194, no. 2–4, pp. 320–325, 2011.
- [23] S. Shibata, N. Suda, S. Yoda et al., "Runx2-deficient mice lack mandibular condylar cartilage and have deformed Meckel's cartilage," *Anatomy and Embryology*, vol. 208, no. 4, pp. 273–280, 2004.
- [24] K. Ishii, I. L. Nielsen, and K. Vargervik, "Characteristics of jaw growth in cleidocranial dysplasia," *The Cleft Palate-Craniofacial Journal*, vol. 35, no. 2, pp. 161–166, 1998.
- [25] B. L. Jensen, "Cleidocranial dysplasia: craniofacial morphology in adult patients," *Journal of Craniofacial Genetics and Developmental Biology*, vol. 14, no. 3, pp. 163–176, 1994.
- [26] X. L. Zhang, K. Ting, C. M. Bessette et al., "Nell-1, a key functional mediator of Runx2, partially rescues calvarial defects in Runx2+/- mice," *Journal of Bone and Mineral Research*, vol. 26, no. 4, pp. 777–791, 2011.
- [27] A. B. M. Rabie, G. H. Tang, and U. Hägg, "Cbfa1 couples chondrocytes maturation and endochondral ossification in rat mandibular condylar cartilage," *Archives of Oral Biology*, vol. 49, no. 2, pp. 109–118, 2004.
- [28] B. F. Eames and J. A. Helms, "Conserved molecular program regulating cranial and appendicular skeletogenesis," *Developmental Dynamics*, vol. 231, no. 1, pp. 4–13, 2004.
- [29] M. Wuelling and A. Vortkamp, "Transcriptional networks controlling chondrocyte proliferation and differentiation during endochondral ossification," *Pediatric Nephrology*, vol. 25, no. 4, pp. 625–631, 2010.
- [30] V. Lefebvre and P. Smits, "Transcriptional control of chondrocyte fate and differentiation," *Birth Defects Research C*, vol. 75, no. 3, pp. 200–212, 2005.
- [31] P. G. Buxton, B. Hall, C. W. Archer, and P. Francis-West, "Secondary chondrocyte-derived Ihh stimulates proliferation of periosteal cells during chick development," *Development*, vol. 130, no. 19, pp. 4729–4739, 2003.
- [32] A. B. M. Rabie, T. T. She, and U. Hägg, "Functional appliance therapy accelerates and enhances condylar growth," *American Journal of Orthodontics and Dentofacial Orthopedics*, vol. 123, no. 1, pp. 40–48, 2003.
- [33] T. Hattori, C. Müller, S. Gebhard et al., "SOX9 is a major negative regulator of cartilage vascularization, bone marrow formation and endochondral ossification," *Development*, vol. 137, no. 6, pp. 901–911, 2010.
- [34] J. Chen, A. Utreja, Z. Kalajzic, T. Sobue, D. Rowe, and S. Wadhwa, "Isolation and characterization of murine mandibular condylar cartilage cell populations," *Cells, Tissues, Organs*, vol. 195, no. 3, pp. 232–243, 2012.
- [35] G. Shen and M. A. Darendeliler, "The adaptive remodeling of condylar cartilage—a transition from chondrogenesis to osteogenesis," *Journal of Dental Research*, vol. 84, no. 8, pp. 691–699, 2005.
- [36] B. F. Eames, P. T. Sharpe, and J. A. Helms, "Hierarchy revealed in the specification of three skeletal fates by Sox9 and Runx2," *Developmental Biology*, vol. 274, no. 1, pp. 188–200, 2004.
- [37] K. Ishizeki, H. Saito, T. Shinagawa, N. Fujiwara, and T. Nawa, "Histochemical and immunohistochemical analysis of the mechanism of calcification of Meckel's cartilage during mandible development in rodents," *Journal of Anatomy*, vol. 194, no. 2, pp. 265–277, 1999.
- [38] K. Ishizeki, N. Takahashi, and T. Nawa, "Formation of the sphenomandibular ligament by Meckel's cartilage in the mouse:

possible involvement of epidermal growth factor as revealed by studies in vivo and in vitro,” *Cell and Tissue Research*, vol. 304, no. 1, pp. 67–80, 2001.

- [39] K. Ishizeki, T. Kagiya, N. Fujiwara, K. Otsu, and H. Harada, “Expression of osteogenic proteins during the intrasplenic transplantation of Meckel’s chondrocytes: a histochemical and immunohistochemical study,” *Archives of Histology and Cytology*, vol. 72, no. 1, pp. 1–12, 2009.
- [40] K. Ishizeki, “Imaging analysis of osteogenic transformation of Meckel’s chondrocytes from green fluorescent protein-transgenic mice during intrasplenic transplantation,” *Acta Histochemica*, vol. 114, no. 6, pp. 608–619, 2012.
- [41] Y. Harada and K. Ishizeki, “Evidence for transformation of chondrocytes and site-specific resorption during the degradation of Meckel’s cartilage,” *Anatomy and Embryology*, vol. 197, no. 6, pp. 439–450, 1998.
- [42] Y. Chai and R. E. Maxson Jr., “Recent advances in craniofacial morphogenesis,” *Developmental Dynamics*, vol. 235, no. 9, pp. 2353–2375, 2006.



## Research Article

# Craniosynostosis-Associated Fgfr2<sup>C342Y</sup> Mutant Bone Marrow Stromal Cells Exhibit Cell Autonomous Abnormalities in Osteoblast Differentiation and Bone Formation

J. Liu,<sup>1</sup> T.-G. Kwon,<sup>2</sup> H. K. Nam,<sup>1</sup> and N. E. Hatch<sup>1</sup>

<sup>1</sup> Department of Orthodontics and Pediatric Dentistry, School of Dentistry, University of Michigan, Ann Arbor, MI 48109-1078, USA

<sup>2</sup> Department of Oral and Maxillofacial Surgery, School of Dentistry, Kyungpook National University, Jung Gu, Daegu, Republic of Korea

Correspondence should be addressed to N. E. Hatch; [nhatch@umich.edu](mailto:nhatch@umich.edu)

Received 11 January 2013; Revised 18 March 2013; Accepted 29 March 2013

Academic Editor: Zhao Lin

Copyright © 2013 J. Liu et al. This is an open access article distributed under the Creative Commons Attribution License, which permits unrestricted use, distribution, and reproduction in any medium, provided the original work is properly cited.

We recently reported that cranial bones of Fgfr2<sup>C342Y/+</sup> craniosynostotic mice are diminished in density when compared to those of wild type mice, and that cranial bone cells isolated from the mutant mice exhibit inhibited late stage osteoblast differentiation. To provide further support for the idea that craniosynostosis-associated Fgfr mutations lead to cell autonomous defects in osteoblast differentiation and mineralized tissue formation, here we tested bone marrow stromal cells isolated from Fgfr2<sup>C342Y/+</sup> mice for their ability to differentiate into osteoblasts. Additionally, to determine if the low bone mass phenotype of Crouzon syndrome includes the appendicular skeleton, long bones were assessed by micro CT. Fgfr2<sup>C342Y/+</sup> cells showed increased osteoblastic gene expression during early osteoblastic differentiation but decreased expression of alkaline phosphatase mRNA and enzyme activity, and decreased mineralization during later stages of differentiation, when cultured under 2D *in vitro* conditions. Cells isolated from Fgfr2<sup>C342Y/+</sup> mice also formed less bone when allowed to differentiate in a 3D matrix *in vivo*. Cortical bone parameters were diminished in long bones of Fgfr2<sup>C342Y/+</sup> mice. These results demonstrate that marrow stromal cells of Fgfr2<sup>C342Y/+</sup> mice have an autonomous defect in osteoblast differentiation and bone mineralization, and that the Fgfr2<sup>C342Y</sup> mutation influences both the axial and appendicular skeletons.

## 1. Introduction

Craniosynostosis is a debilitating pediatric condition characterized by the premature fusion of cranial bones. This fusion leads to high intracranial pressure and abnormal skull and facial shapes presumably resulting from limited growth at fused craniofacial sutures with compensating overgrowth at nonfused cranial sutures [1–5]. Untreated craniosynostosis can lead to blindness, seizures, and death [6–10]. Current treatment options for craniosynostosis and its associated craniofacial abnormalities are limited to surgery with genetic counseling, orthodontic, medical, and social support [11]. Notably, even with an appropriately early and accurate diagnosis, craniosynostosis can carry high morbidity, with some

patients requiring multiple surgeries throughout infancy and childhood for treatment of recurring craniosynostosis and normalization of skull and facial shapes [12].

It has been known for over a decade that craniosynostosis occurs in association with mutations in the genes for fibroblast growth factor receptors (Fgfr's). Mutations in Fgfr2 cause Apert, Crouzon, Jackson-Weiss, and Pfeiffer craniosynostosis syndromes, while mutations in Fgfr1 cause Pfeiffer syndrome and mutations in Fgfr3 cause Muenke craniosynostosis syndrome and Crouzon syndrome with acanthosis nigricans [13–17]. Numerous prior studies have shown that these craniosynostosis-associated Fgfr mutations lead to a gain of function in terms of Fgfr signaling [18–22]. Yet, despite our extensive knowledge in the genetics

underlying syndromic craniosynostosis, the pathogenesis by which mutations in *Fgfr*'s lead to craniosynostosis has yet to be fully elucidated. Because *Fgf*/*Fgfr* signaling is an important form of intercellular communication, it has been proposed that craniosynostosis-associated mutations in *Fgf* receptors lead to craniosynostosis by causing inappropriate signaling to cranial cells from neighboring tissues such as the dura mater [23–25]. In contrast, it has also been proposed that craniosynostosis-associated mutations in *Fgf* receptors lead to intrinsic defects in the behavior of cranial bone cells and tissues [26–28]. Importantly, while the biologic pathogenesis of craniosynostosis remains unknown, the only treatment for craniosynostosis will remain that of surgical intervention.

To advance our understanding of mechanisms that lead to craniosynostosis, we are investigating the *Fgfr2*<sup>C342Y/+</sup> mouse model of Crouzon syndrome. Common features of Crouzon syndrome in humans include coronal suture synostosis with rare pansynostosis, hypertelorism, severe ocular proptosis, strabismus, hypoplastic maxilla, and relative mandibular prognathism [11, 29]. Notably, high rates of stylohyoid ligament calcification and vertebral fusions, as well as the occasional fusion of limb joints, have also been reported [30–32]. Mice carrying the classic Crouzon syndrome associated *Fgfr2*<sup>C342Y</sup> mutation were initially reported to have characteristics similar to those of Crouzon syndrome patients including a dome-shaped skull, wide set and proptotic eyes, premature fusion of cranial sutures, and a shortened maxilla [32]. Notably, fusions were also evident between the femur and tibia and between cervical vertebral arches in homozygous mutant mice. The homozygous mutant mice also lacked vertebral body ossification. These findings indicate that the Crouzon syndrome phenotype involves both the axial and appendicular skeletons. The findings also suggest that the bony fusions of Crouzon syndrome occur in the context of diminished eutopic bone formation.

We recently reported that the frontal bones of Crouzon *Fgfr2*<sup>C342Y/+</sup> mice are diminished in bone volume and density when compared to those of wild type mice, and that while frontal bone cells isolated from the mutant mice exhibit increased osteoblastic gene during early stages of osteoblast differentiation, the cells are also diminished in their ability to differentiate into mature osteoblasts *in vitro* [5]. To provide further support for the idea that the Crouzon syndrome associated *Fgfr2*<sup>C342Y</sup> mutation leads to intrinsic changes in osteoblast differentiation and bone formation, we isolated cells from Crouzon mice and assayed their ability to differentiate into osteoblasts and form mineralized tissue, as compared to cells isolated from wild type mice. Because cell culture in a three-dimensional matrix supports a more physiologically relevant environment than more traditional two-dimensional cell culture methods [33], we assayed cells in traditional *in vitro* monolayer culture and in a three-dimensional collagenous matrix *in vivo*. Additionally, to determine if the appendicular skeleton is altered in *Fgfr2*<sup>C342Y/+</sup> mice, we used microcomputed tomography to quantify parameters of tibial bone quality and quantity. Here we report that the *Fgfr2*<sup>C342Y</sup> mutation enhances expression of osteoblastic genes during early stages of differentiation

while inhibiting expression of alkaline phosphatase enzyme (AP/*Tnap*/*Alpl*/*Akp2*) and mineralization during later differentiation, in two-dimensional *in vitro* cell culture. Here we also show that the *Fgfr2*<sup>C342Y</sup> mutation inhibits the ability of these cells to express *Tnap* enzyme and form mineralized tissue when allowed to differentiate in a three-dimensional matrix *in vivo*. Additionally, here we report for the first time that the long bones of *Fgfr2*<sup>C342Y/+</sup> mice have significantly diminished cortical bone quality and quantity, when compared to those of wild type mice. Together, these results demonstrate that the Crouzon syndrome associated *Fgfr2*<sup>C342Y</sup> mutation causes cell autonomous abnormalities in osteoblast differentiation that include enhanced early differentiation but inhibited later expression of *Tnap* enzyme and mineralization by bone marrow stromal cells. Results also show that Crouzon syndrome is associated with significantly diminished appendicular bone volume and density.

## 2. Experimental Procedures

**2.1. Animals.** *Fgfr2*<sup>C342Y/+</sup> and wild type mice were genotyped as previously described [29]. Briefly, DNA from tail digests was amplified by polymerase chain reaction using 5'-gagtaccatgctgactgcatgc-3' and 5'-ggagaggcatctctgttcaagacc-3' primers. The reaction product was resolved by gel electrophoresis, yielding a 200 base pair band for wild type *Fgfr2* and a 300 base pair band for *Fgfr2*<sup>C342Y</sup>. *Fgfr2*<sup>C342Y/+</sup> and wild type mice on the Balb/C genetic background were utilized for cell isolations and for micro-CT analyses. NIH III nude mice were obtained from Charles River Laboratories International, Inc. (Wilmington, MA) and utilized as donor mice for subcutaneous implant experiments. All animal procedures were performed according to University of Michigan's University Committee on Use and Care of Animals.

**2.2. Microcomputed Tomography.** Tibias of *Fgfr2*<sup>C342Y/+</sup> (*n* = 14) and wild type (*n* = 14) four-week-old mice were embedded in 1% agarose and scanned at the proximal metaphysis and the mid-diaphysis using a microcomputed tomography imaging system (Scanco  $\mu$ CT100, Scanco Medical, Bassersdorf, Switzerland). Scan settings were voxel size 12  $\mu$ m, 70 kVp, 114  $\mu$ A, 0.5 mm AL filter, and integration time of 500 ms. Density measurements were calibrated to the manufacturer's hydroxyapatite phantom. Analysis was performed using the manufacturer's evaluation software (Scanco  $\mu$ CT100, Scanco Medical, Bassersdorf, Switzerland) using a fixed global threshold of 28% (280 on a grayscale of 0–1000) to segment bone from nonbone. Micro-CT bone data was analyzed and is reported in accordance with the recommendations of Buxsein et al., 2010 [34]. Statistical significance between groups was established by use of the Student's *t*-test.

**2.3. Primary Cell Isolation.** Bone marrow stromal cells were isolated from the long bones of four-week-old Crouzon mice and wild type littermates, as previously described [35]. Briefly, marrow cells were aspirated using a 25-gauge needle and a 5 mL syringe containing media. Marrow was flushed and

cells were then dispersed by aspirating several times through a 22-gauge needle. Cells were cultured in  $\alpha$ MEM supplemented with 20% fetal bovine serum (FBS) and 10,000  $\mu$ g/mL penicillin/streptomycin for several days. Media was changed every three days until all suspension cells were removed and adherent cells were confluent.

**2.4. In Vitro Osteoblast Differentiation.** Cells were induced to differentiate *in vitro* by culture in media containing 50  $\mu$ g/mL ascorbate for the indicated number of days. RNA was isolated using Trizol reagent (Invitrogen) following manufacturer protocols. mRNA levels were assayed by reverse transcription and real-time PCR. Real-time PCR was performed utilizing the murine tissue nonspecific alkaline phosphatase (TNAP) primer/probe set Mm00475834\_m1, the murine bone sialoprotein (BSP) primer/probe set Mm00492555\_m1, the murine osteocalcin (OCN) primer/probe set Mm03413826\_mH, the murine runt related transcription factor 2 (Runx2) primer/probe set Mm00501578\_m1, the murine collagen type I, alpha 1 (colla1) primer/probe set Mm00801666\_g1, the murine hypoxanthine phosphoribosyltransferase-1 (Hprt1) primer/probe set Mm01545399\_m1, and Taqman Universal PCR Master Mix (Applied Biosystems). Real-time PCR was performed on a GeneAmp 7700 thermocycler (Applied Biosystems) and quantified by comparison to a standard curve. mRNA levels are reported after normalization to Hprt1 mRNA levels. Cells were induced to form mineral by addition of 10 mM  $\beta$ -glycerophosphate. Mineralized nodules were stained by Von Kossa. Briefly, cells were rinsed with phosphate-buffered saline, fixed with 100% ethanol and rehydrated in a graded ethanol series. Cells were then incubated in 5% AgNO<sub>3</sub>, rinsed with dH<sub>2</sub>O and exposed to light for 1 hour. For quantification, wells were scanned and densitometry was measured using NIH Image software. Tissue non-specific alkaline phosphatase (AP) enzyme activity was assayed using the colorimetric substrate, NBT/BCIP (Sigma). Cells were fixed in 70% ethanol for 10 minutes at room temperature, air dried, and incubated with substrate for 1 hour at 37°C. Cells were then rinsed with dH<sub>2</sub>O, air dried, and visualized macroscopically for evidence of staining. For quantification, wells were scanned and densitometry was measured using NIH Image software. Statistical significance between genotypes for mRNA levels, quantification of mineralization, and quantification of AP enzyme activity was established by use of the Student's *t*-test.

**2.5. Subcutaneous Implant Preparation and Analysis of Ossicles.** Subcutaneous implants were prepared as previously described [36].  $4 \times 10^7$  bone marrow stromal cells were mixed with 0.01% NaOH in phosphate buffered saline and 1ml of rat tail collagen solution (BD Biosciences, San Jose, CA) on ice. The solution was aliquoted into glass tissue culture wells (Lab-Tek 16 well chamber slide system; Nalge Nunc International, Rochester, NY) and then incubated at 37°C for 1 hour to allow for gel hardening. Midline longitudinal incisions were made along the dorsal surface of each six-week-old NIH III mouse, and subcutaneous pockets were formed laterally, by gentle blunt dissection. A single implant was placed into

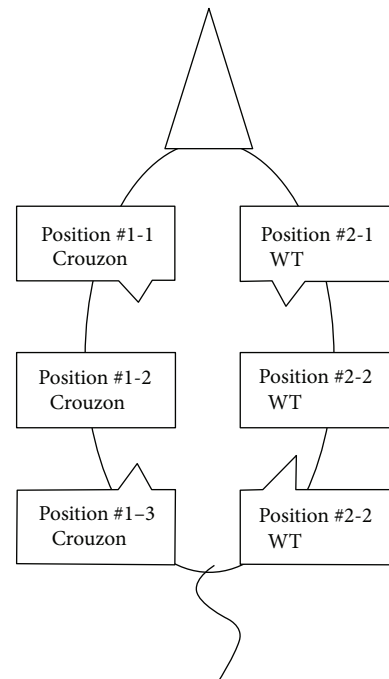


FIGURE 1: Subcutaneous implant placement. This schematic shows the position of six implants that were placed subcutaneously, on the dorsal surface of immunodeficient mice.

each subcutaneous pocket, for a total of six implants per animal (Figure 1). Implants were removed eight weeks after implantation and analyzed for mineralized tissue formation by radiography (Faxitron MX-20, Faxitron Bioptics LLC, Tucson, AZ). All implants were imaged on the same film. Mineralized tissue of twelve implants from each genotype was quantified by densitometry (ImageJ, NIH). Statistical significance between genotypes was established by use of the Student's *t*-test. Implants were then homogenized for alkaline phosphatase measurements or decalcified and embedded in paraffin for histologic analysis by trichrome or hematoxylin and eosin staining. Alkaline phosphatase enzyme activity of implants was measured by homogenizing the implants in a solution containing 1.6 M MgCl<sub>2</sub>, 0.2 M Tris-Cl pH 8.1, and 1% triton X-100 followed by incubation of lysate with 7.5 mM of 4-nitrophenyl-phosphate at room temperature for 1 hour. Absorbance at 405 nm was measured and results were normalized to DNA content. Statistical significance between genotypes was established by use of the Student's *t*-test.

### 3. Results

**3.1. Animals.** The Crouzon *Fgfr2*<sup>C342Y/+</sup> mutant mice show a phenotype similar to that which was previously reported [5, 32, 37]. The mutant mice are slightly smaller in body size than their wild type littermates and exhibit craniofacial abnormalities associated with craniosynostosis including a dome-shaped skull, wide set and proptotic eyes, and severe midface hypoplasia.



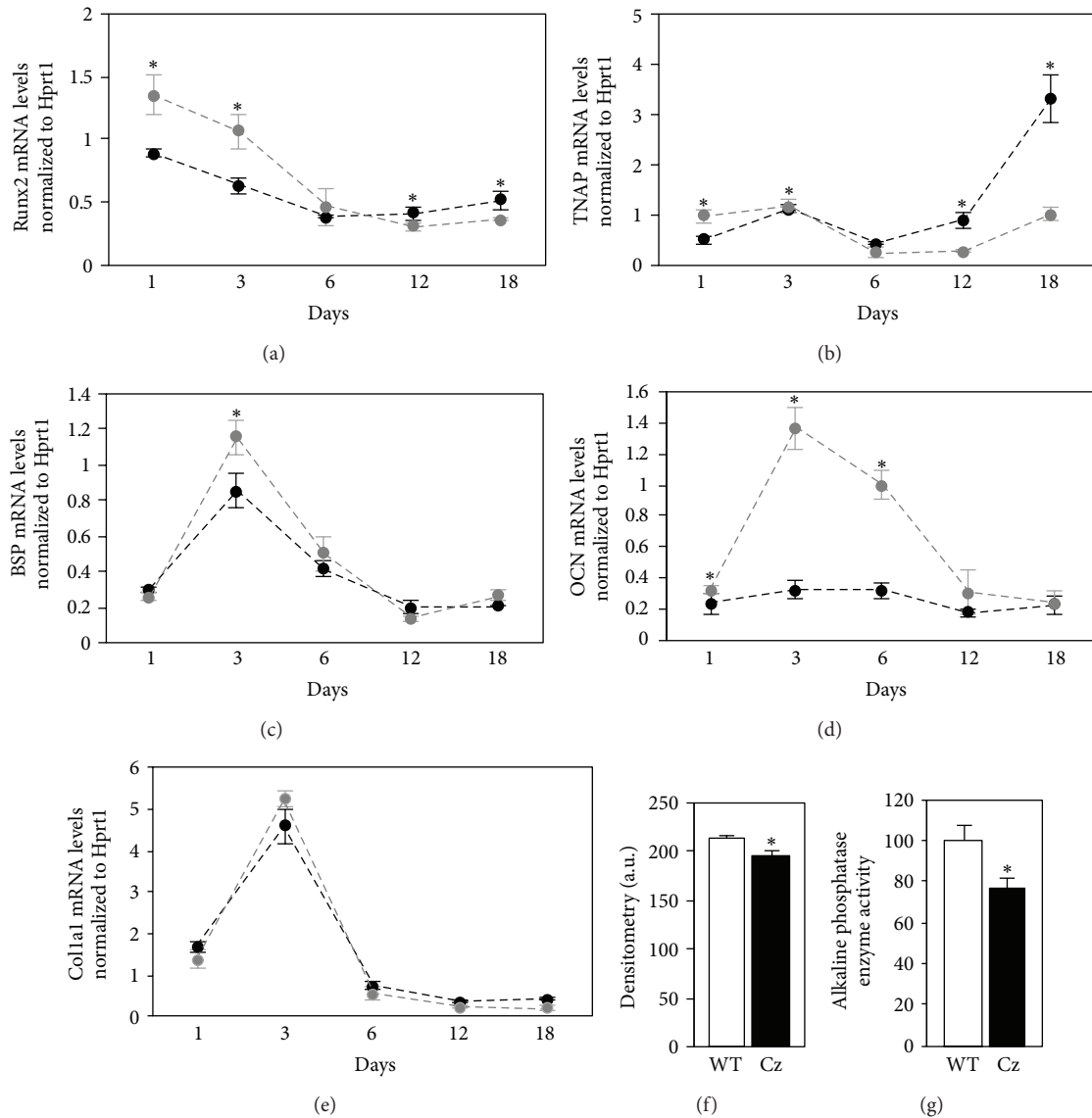


FIGURE 2: The *Fgfr2*<sup>C342Y</sup> mutant bone marrow stromal cells exhibit abnormal osteoblastic gene expression and diminished mineralization *in vitro*. Bone marrow stromal cells were isolated from Crouzon *Fgfr2*<sup>C342Y/+</sup> (Cz) and wild type (WT) littermates and then cultured with ascorbate for the indicated number of days to induce osteoblast differentiation. Runx2, bone sialoprotein (BSP), osteocalcin (OCN), and tissue non-specific alkaline phosphatase (TNAP) and collagen type 1 alpha1 (coll1a1) mRNA levels were measured by real-time PCR. Black lines represent wild type; grey lines represent Crouzon (a, b, c, d, and e). Results are presented as normalized to Hprt1. Cells were cultured with ascorbate and  $\beta$ -glycerolphosphate to induce mineralization for 18 days (f). Mineralized nodules were stained by Von Kossa and quantified by densitometry. Cells were cultured with ascorbate for 18 days, and alkaline phosphatase (Tnap/Alpl/Akp2) enzyme activity was quantified by incubation of cells with a colorimetric substrate. Enzyme activity was quantified by densitometry (g). Results shown are means  $\pm$  standard deviations from triplicate experiments for all data shown. \* $P < .05$  between genotypes.

**3.2. In Vitro Osteoblast Differentiation.** Analysis of mRNA levels demonstrates that bone marrow stromal cells isolated from Crouzon mice express significantly higher levels of Runx2 and tissue non-specific alkaline phosphatase enzyme (AP) at days 1 and 3 of differentiation, significantly higher levels of bone sialoprotein at day 3 of differentiation, and significantly higher levels of osteocalcin at days 1, 3, and 6 of differentiation (Figures 2(a), 2(b), 2(c), and 2(d)). This data indicates that the *Fgfr2*<sup>C342Y</sup> mutation enhances the expression

of osteoblastic genes in bone marrow stromal cells during early stages of osteoblast differentiation. In contrast, Runx2 and tissue non-specific alkaline phosphatase mRNA levels were significantly lower in cells isolated from Crouzon mice at days 12 and 18 of differentiation (Figures 2(a) and 2(b)). Cells isolated from Crouzon mice also exhibited less alkaline phosphatase enzyme activity at day 18 of differentiation and mineralized to a diminished extent than cells isolated from wild type littermates (Figures 2(f) and 2(g)). In combination,

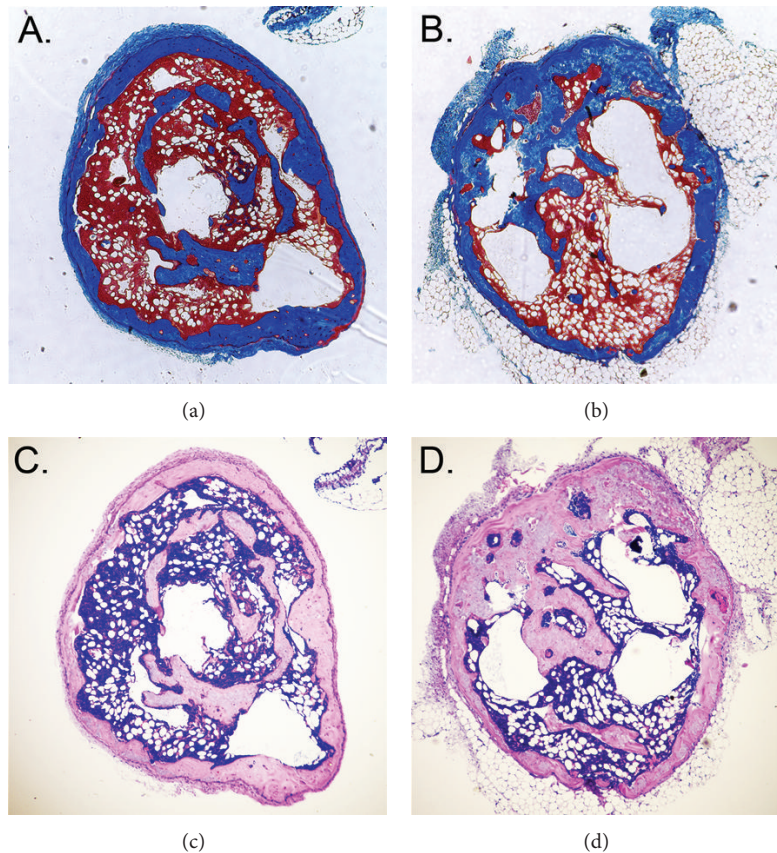


FIGURE 3: Histologic staining of implants. Ossicles formed eight weeks after subcutaneous implantation of cells mixed with a collagenous matrix were stained by trichrome (a and b) or by hematoxylin and eosin (c and d). Note the greater amount of deep blue (a) and light pink (c) staining in ossicles formed by wild type cells, indicative of greater bone formation by these cells. In comparison, note the greater amount of light blue (b) and greyish-pink (d) staining in ossicles formed by Crouzon cells, indicative of greater amounts of original implanted collagen. Also note that ossicles formed by either wild type or mutant cells contain bone marrow.

this data suggests that the  $Fgfr2^{C342Y}$  mutation may inhibit later stages of osteoblast differentiation and inhibit mineralization. Notably, collagen type 1,  $\alpha 1$  mRNA expression levels were not different between Crouzon and wild type cells at any stages of differentiation. This data suggests that the diminished mineralization by Crouzon cells is not likely due to diminished collagen expression. Together, these results indicate that while the  $Fgfr2^{C342Y}$  mutation may enhance early osteoblast differentiation, it also appears to inhibit expression of tissue non-specific alkaline phosphatase and mineralization by more differentiated cells. The findings also indicate that the  $Fgfr2^{C342Y}$  mutation induces autonomous abnormalities in osteoblast differentiation when bone marrow stromal cells are cultured in a conventional two-dimensional monolayer system *in vitro*.

**3.3. In Vivo Mineralized Tissue Formation.** Because a three-dimensional matrix promotes a more physiologically relevant cellular state than conventional *in vitro* monolayer cell culture [33, 38–40], we next assayed the cells when allowed to differentiate in a collagenous matrix *in vivo*. In accordance with the *in vitro* data, bone marrow stromal cells isolated

from Crouzon mice formed significantly less mineralized tissue than cells isolated from wild type mice, when allowed to differentiation in a three-dimensional collagenous matrix *in vivo*. Both trichrome (bone tissue stains deep blue and implanted collagen stains lighter blue) and H&E histologic stains (bone tissue stains pink and implanted collagen stains greyish-pink) indicate that the ossicles formed by Crouzon cells may contain less mineralized tissue than ossicles formed by wild type cells (Figure 3). Notably, the marrow of implants prepared using either Crouzon or wild type cells contains both hematopoietic and adipocytic cells (small empty ovals are adipocyte ghosts). This may indicate that the  $Fgfr2^{C342Y}$  mutation does not influence hematopoietic or adipocytic cell differentiation, although more comprehensive analyses of these cell types in both heterozygous and homozygous mutant mice are required to definitely determine if this is the case. Radiographs of representative implants dissected eight weeks after implantation reveal apparently diminished radiodensity of ossicles prepared using cells isolated from the mutant, as compared to the wild type mice (Figure 4(a)). Quantification of mineralized tissue confirms that the mutant cell implants have significantly less mineralized tissue than the wild type cell implants (Figure 4(b)). Finally, alkaline

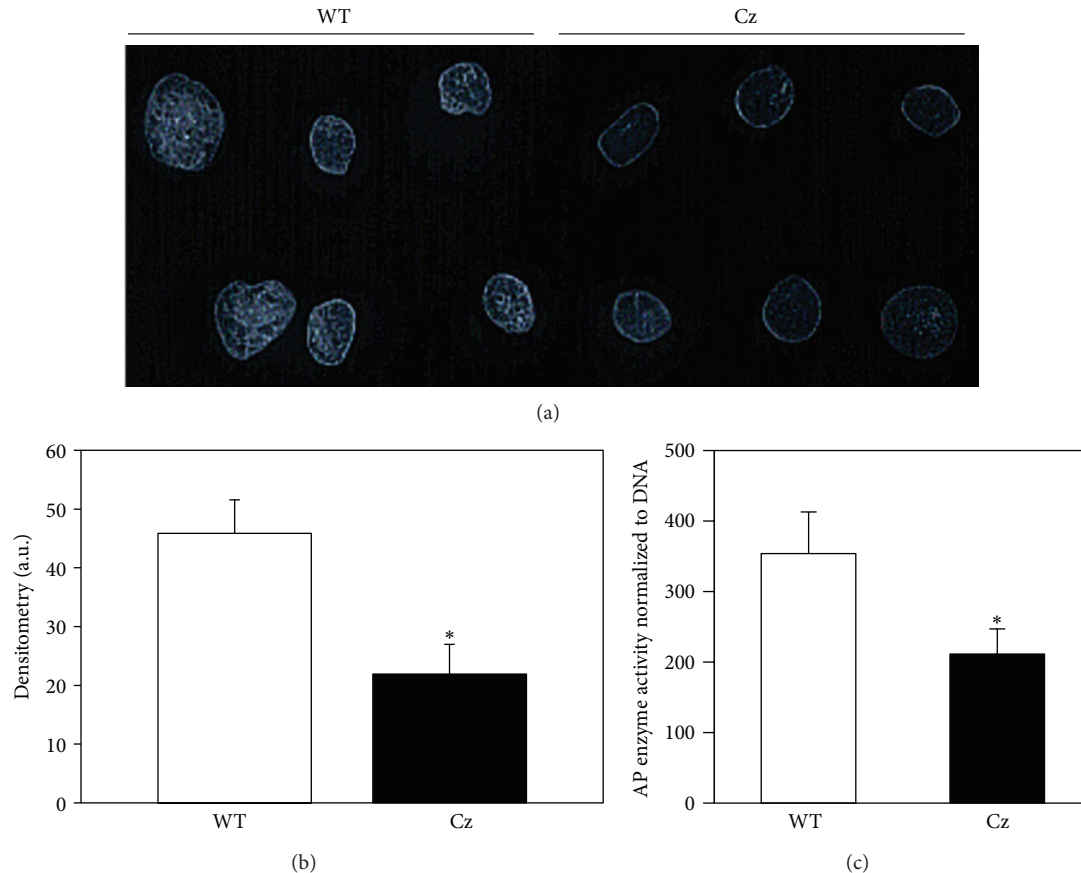


FIGURE 4: The  $Fgfr2^{C342Y}$  mutation inhibits mineralized tissue formation *in vivo*. (a) Radiographic image of representative implants shows increased radiodensity of ossicles formed by wild type (WT), as compared to those formed by Crouzon (Cz) cells. (b) Quantification of radiodense tissue by densitometry confirms that implanted wild type cells formed significantly greater amounts of mineralized tissue compared to mutant cells ( $n = 12$  implants per genotype). \* $P < .05$  versus WT. (c) Homogenized implants formed by wild type cells also have significantly greater levels of alkaline phosphatase enzyme expression than homogenized implants formed by Crouzon cells ( $n = 3$  implants per genotype). \* $P < .05$  versus WT.

phosphatase enzyme expression, which is essential for mineral deposition in collagenous tissues [41] was found to be significantly lower in implants prepared using mutant than wild type cells (Figure 4(c)). Together, these results demonstrate that the  $Fgfr2^{C342Y}$  mutation inhibits alkaline phosphatase enzyme expression and the formation of mineralized tissue by osteoprogenitor cells when allowed to differentiate in a three-dimensional matrix *in vivo*.

**3.4. Microcomputed Tomographic Analysis of Long Bones.** We recently showed that the frontal cranial bones of  $Fgfr2^{C342Y/+}$  mice are diminished in bone volume and density when compared to those of wild type mice [5]. To determine if bones of the appendicular skeleton are similarly affected, we utilized microcomputed tomography to analyze parameters of bone quality and quantity in tibias of four-week-old  $Fgfr2^{C342Y/+}$  and  $Fgfr2^{+/+}$  mice. Results demonstrate that  $Fgfr2^{C342Y/+}$  mice have significantly diminished tibial cortical bone volume/total volume, bone mineral density, and tissue mineral density (Figure 5), when compared to  $FGFR2^{+/+}$  mice.

Trabecular measures of tibial bone volume/total volume, bone mineral density, and tissue mineral density were not different between  $Fgfr2^{C342Y/+}$  and  $Fgfr2^{+/+}$  mice (Figure 6). These results demonstrate that the  $Fgfr2^{C342Y/+}$  mutation is associated with decreased bone volume and density that is not limited to the craniofacial skeleton.

## 4. Discussion

The pathogenesis of craniosynostosis remains unknown and until this knowledge has been realized, the only treatment for craniosynostosis will remain that of surgical intervention. While it is not known if craniosynostosis results primarily from abnormalities in cranial bone cells, cranial suture cells and/or abnormalities in other cell types, mounting evidence does indicate that craniosynostosis occurs in the context of diminished cranial bone quantity and quality.  $Fgfr2^{S250W}$  Apert mice and  $Fgfr3^{P244R}$  Muenke mice were both previously shown to exhibit craniosynostosis in combination with lower levels of bone formation and/or mineralization when



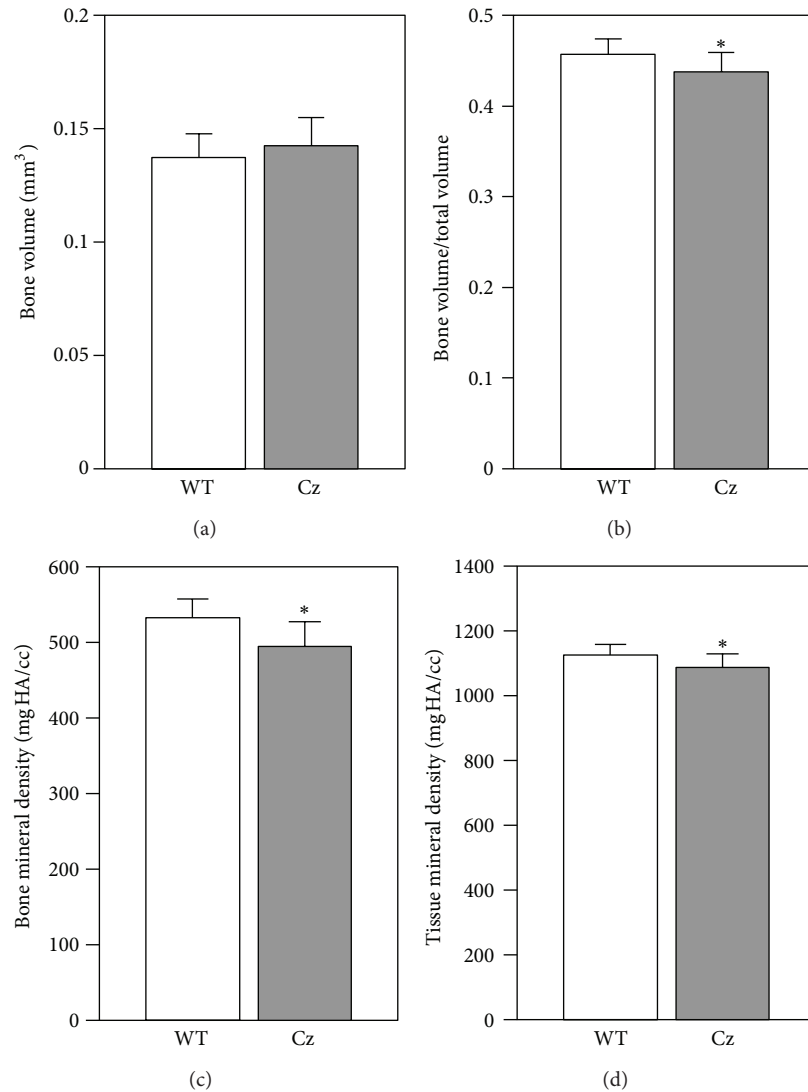


FIGURE 5: Diminished cortical bone volume and density in the long bones of  $Fgfr2^{C342Y/+}$  mice. Micro-CT analyses demonstrate significantly diminished cortical bone volume/total volume, bone mineral density, and tissue mineral density in tibias of  $Fgfr2^{C342Y/+}$  (Cz) mice as compared to wild type (WT) mice. \* $P < .05$  between genotypes.

compared to wild type littermates [42, 43]. As noted previously,  $Fgfr2^{C342Y/C342Y}$  Crouzon mice were originally characterized as having decreased ossification of vertebral bodies [32]. In addition, we recently reported that  $Fgfr2^{C342Y/+}$  mice on a BALB/c genetic background have diminished cranial bone volume and density when compared to wild type mice [5]. Abnormal BMP signaling in neural crest cells was also recently shown to cause diminished cranial bone volume and density in combination with craniosynostosis [44]. Taken together, these results appear to indicate that craniosynostosis is an abnormality involving excessive ectopic mineralization (bone formation at a temporally and spatially inappropriate location, such as the juvenile cranial suture) and not a disorder of excessive eutopic bone formation. In fact, craniosynostosis associated with several distinct genetic mutations (cited earlier) appears to occur in combination with diminished eutopic bone mass. This distinction is critical for

the future development of biologically based therapeutics for the prevention and/or treatment of craniosynostosis.

Here we report that bone marrow stromal cells isolated from Crouzon  $Fgfr2^{C342Y/+}$  mice express significantly higher levels of some osteoblastic genes during early stages of differentiation but significantly lower levels of tissue non-specific alkaline phosphatase mRNA and enzyme activity, as well as diminished mineralization when cells are further differentiated in a 2D *in vitro* cell culture system. These results are in accordance with our previous report which showed that frontal bone cells isolated from  $Fgfr2^{C342Y/+}$  mice exhibited enhanced early osteoblastic differentiation but diminished later stage differentiation and a decreased tendency to form mineralized tissue, when compared to cells isolated from wild type mice *in vitro* [5]. That the  $Fgfr2^{C342Y}$  mutation stimulates early osteoblast differentiation while inhibiting later maturation into fully functional osteoblasts could explain

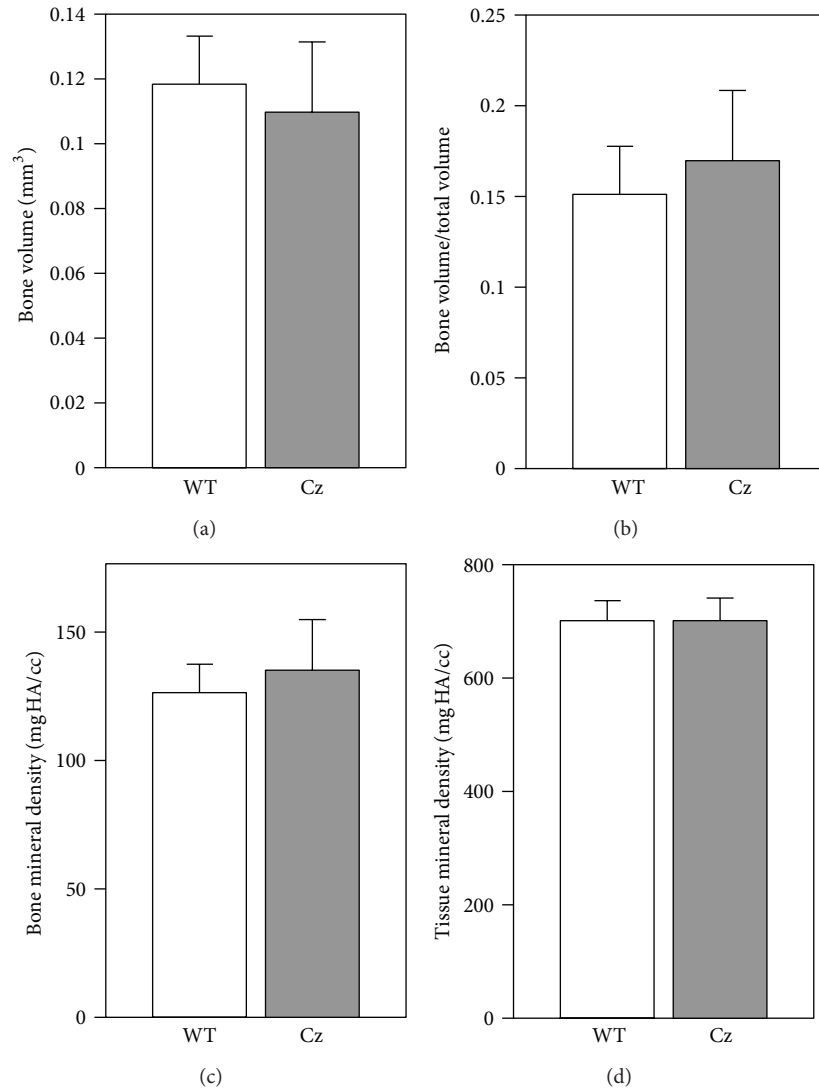


FIGURE 6: Similar trabecular bone volume and density in the long bones of  $\text{Fgfr2}^{\text{C342Y/+}}$  mice. Micro-CT analyses demonstrate no significant differences in bone volume, bone volume/total volume, bone mineral density, and tissue mineral density in tibias of  $\text{Fgfr2}^{\text{C342Y/+}}$  (Cz) mice as compared to wild type (WT) mice.

the apparently discrepant results found in the literature regarding effects of craniosynostosis-associated FGFR mutations on osteoblast differentiation. Our *in vitro* data, showing that Crouzon  $\text{Fgfr2}^{\text{C342Y}}$  marrow stromal cells express higher levels of multiple osteoblastic genes than wild type cells during early stages of differentiation, is in accordance with previous reports which showed increased osteoblastic gene expression in cranial suture tissues. Previous *in vivo* analyses of the  $\text{Fgfr2}^{\text{P253R/+}}$  and  $\text{Fgfr2}^{\text{S252W/+}}$  mouse models of Apert syndrome revealed increased osteoblastic gene expression around the coronal suture [45, 46]. Mice carrying the P250R mutation in  $\text{Fgfr1}$  associated with Pfeiffer syndrome were also previously shown to exhibit enhanced osteoblastic differentiation of cells within the sagittal suture [47]. Finally, newborn  $\text{Fgfr2}^{\text{C342Y/+}}$  mice were also previously shown to have increased Runx2 mRNA levels around the coronal

suture, as compared to wild type littermates [32]. Increased expression of osteoblastic genes in suture tissues is well reconciled with our results showing increased osteoblastic gene expression in  $\text{Fgfr2}^{\text{C342Y/+}}$  bone marrow stromal cells during early stages of differentiation. In contrast, our data showing that  $\text{Fgfr2}^{\text{C342Y}}$  marrow stromal cells express significantly lower levels of Runx2 and tissue non-specific alkaline phosphatase mRNA, as well as significantly diminished alkaline phosphatase enzyme activity and mineralization, is in accordance with previous studies showing that S252W, C342Y, and P253R craniosynostosis-associated mutations in FGFR2 inhibit osteoblast differentiation [48–50]. The data can also potentially explain the diminished eutopic bone mass that is seen in multiple mouse models of craniosynostosis, including the  $\text{Fgfr2}^{\text{C342Y}}$  mouse model of Crouzon syndrome. Taken together, it appears that craniosynostosis

syndrome-associated mutations in Fgfr's enhance or inhibit osteoblast differentiation in a cell type, environment, and differentiation stage dependent manner.

Importantly, two-dimensional cell culture on plastic does not well represent the environmental conditions that cells find in physiologic tissues, and it has been suggested that three-dimensional cell culture helps to "bridge the gap" between cultured cells and the *in vivo* environment [33]. Therefore, to increase confidence in our *in vitro* findings, we also mixed bone marrow stromal cells in a three dimensional collagenous matrix and allowed them to differentiate when implanted into donor mice. Results of these experiments showed that the Crouzon Fgfr2<sup>C342Y</sup> mutation inhibited bone formation and alkaline phosphatase enzyme expression, again supporting the idea that the Fgfr2<sup>C342Y</sup> mutation inhibits later stage osteoblast differentiation and bone formation. While our results also show significantly diminished bone volume and density in the long bones of Fgfr2<sup>C342Y</sup> mice, future studies are required to definitively establish that Crouzon bone marrow stromal cells are deficient in their ability to differentiate into fully functional osteoblasts and form bone *in vivo*. If correct, our results suggest that patients carrying craniosynostosis syndrome associated Fgfr mutations may be at higher risk for osteoporosis and/or slow repair of long bone fractures.

While the diminished cranial bone formation in these Fgfr-associated mouse models of craniosynostosis has not been previously considered as contributing to the development of craniosynostosis, it is interesting to note that craniosynostosis is also known to occur in other disorders of low bone mineralization. Mutations in the phosphate regulating protein Phex cause X-linked hypophosphatemic rickets involving low serum phosphate, defective bone mineralization and also craniosynostosis [51–53]. It is unknown how Phex mutations lead to craniosynostosis, but, similar to studies of human patients with Fgfr2-associated craniosynostosis [30], these patients also commonly have paradoxical heterotopic calcification of normally nonmineralizing tissues, such as tendons and ligaments [53]. Craniosynostosis is also seen in infantile hypophosphatasia due to inactivating mutations in the enzyme, tissue non-specific alkaline phosphatase (TNAP) [54–56]. These patients have severely deficient bone mineralization [57]. TNAP is an enzymatic generator of inorganic phosphate and an established essential promoter of tissue mineralization, but it is again unknown how diminished TNAP activity leads to craniosynostosis [41, 58]. Finally, craniosynostosis was also previously reported to occur secondary to antacid-induced infantile hypophosphatemia [59]. This data indicates that craniosynostosis occurs in multiple disorders involving dysregulated phosphate homeostasis and bone mineralization. Notably, signaling through Fgfr's was also previously shown to regulate expression of enzymes that control the local production of inorganic phosphate [35], and here we show that cells isolated from Crouzon mice express significantly lower levels of tissue non-specific alkaline phosphatase mRNA and significantly diminished alkaline phosphatase enzyme expression. Together, these results make it tempting to hypothesize that craniosynostosis

may be promoted by abnormal tissue levels of phosphate leading to aberrant tissue mineralization.

In conclusion, this study demonstrates that the Crouzon syndrome associated C342Y mutation in Fgfr2 enhances early osteoblast differentiation but inhibits later differentiation of bone marrow stromal cells into fully functional osteoblasts when cultured in a conventional *in vitro* monolayer system and when allowed to differentiate in a three-dimensional matrix *in vivo*. This study also demonstrates that the long bones of Fgfr2<sup>C342Y</sup> mice have significantly diminished bone volume and density when compared to wild type littermates. Taken together, our results indicate that Crouzon cells have an intrinsic or cell autonomous defect in osteoblast differentiation and bone formation that includes cells of the appendicular skeleton. Future studies are required to determine if Crouzon syndrome patients are at increased risk for osteoporosis and/or poor repair of bony fractures due to this abnormal cell behavior.

## Conflict of Interests

The authors have no relationship with the aforementioned companies and so have no conflict of interests to report.

## Acknowledgment

This work was supported by NIDCR Grant R03DE021082.

## References

- [1] D. Renier, E. Lajeunie, E. Arnaud, and D. Marchac, "Management of craniosynostoses," *Child's Nervous System*, vol. 16, no. 10-11, pp. 645–658, 2000.
- [2] M. Seruya, A. Oh, M. J. Boyajian, J. C. Posnick, and R. F. Keating, "Treatment for delayed presentation of sagittal synostosis: challenges pertaining to occult intracranial hypertension—clinical article," *Journal of Neurosurgery*, vol. 8, no. 1, pp. 40–48, 2011.
- [3] G. M. Morriss-Kay and A. O. M. Wilkie, "Growth of the normal skull vault and its alteration in craniosynostosis: insights from human genetics and experimental studies," *Journal of Anatomy*, vol. 207, no. 5, pp. 637–653, 2005.
- [4] S. Kreiborg, "Craniofacial growth in plagiocephaly and Crouzon syndrome," *Scandinavian Journal of Plastic and Reconstructive Surgery*, vol. 15, no. 3, pp. 187–197, 1981.
- [5] J. Liu, H. K. Na, E. Wang, and N. E. Hatch, "Further analysis of the crouzon mouse: effects of the FGFR2<sup>C342Y</sup> mutation are cranial bone dependent," *Calcified Tissue International*, vol. 92, no. 5, pp. 451–466, 2013.
- [6] K. Okajima, L. K. Robinson, M. A. Hart et al., "Ocular anterior chamber dysgenesis in craniosynostosis syndromes with a fibroblast growth factor receptor 2 mutation," *American Journal of Medical Genetics*, vol. 85, no. 2, pp. 160–170, 1999.
- [7] P. Stavrou, S. Sgouros, H. E. Willshaw, J. H. Goldin, A. D. Hockley, and M. J. C. Wake, "Visual failure caused by raised intracranial pressure in craniosynostosis," *Child's Nervous System*, vol. 13, no. 2, pp. 64–67, 1997.
- [8] H. Abe, T. Ikota, M. Akino, K. Kitami, and M. Tsuru, "Functional prognosis of surgical treatment of craniosynostosis," *Child's Nervous System*, vol. 1, no. 1, pp. 53–61, 1985.



- [9] P. S. Shah, K. Siriwardena, G. Taylor et al., "Sudden infant death in a patient with FGFR3 P250R mutation," *American Journal of Medical Genetics A*, vol. 140, no. 24, pp. 2794–2796, 2006.
- [10] M. M. Cohen and S. Kreiborg, "Upper and lower airway compromise in the Apert syndrome," *American Journal of Medical Genetics*, vol. 44, no. 1, pp. 90–93, 1992.
- [11] S. A. Rasmussen, M. M. Yazdy, J. L. Frias, and M. A. Honein, "Priorities for public health research on craniosynostosis: summary and recommendations from a Centers for Disease Control and Prevention-sponsored meeting," *American Journal of Medical Genetics A*, vol. 146, no. 2, pp. 149–158, 2008.
- [12] J. K. Williams, S. R. Cohen, F. D. Burstein, R. Hudgins, W. Boydston, and C. Simms, "A longitudinal, statistical study of reoperation rates in craniosynostosis," *Plastic and Reconstructive Surgery*, vol. 100, no. 2, pp. 305–310, 1997.
- [13] W. Reardon, R. M. Winter, P. Rutland, L. J. Pulleyn, B. M. Jones, and S. Malcolm, "Mutations in the fibroblast growth factor receptor 2 gene cause Crouzon syndrome," *Nature Genetics*, vol. 8, no. 1, pp. 98–103, 1994.
- [14] U. Schell, A. Hehr, G. J. Feldman et al., "Mutations in FGFR1 and FGFR2 cause familial and sporadic Pfeiffer syndrome," *Human Molecular Genetics*, vol. 4, no. 3, pp. 323–328, 1995.
- [15] A. O. M. Wilkie, S. F. Slaney, M. Oldridge et al., "Apert syndrome results from localized mutations of FGFR2 and is allelic with Crouzon syndrome," *Nature Genetics*, vol. 9, no. 2, pp. 165–172, 1995.
- [16] O. A. Ibrahim, F. Zhang, A. V. Eliseenkova, R. J. Linhardt, and M. Mohammadi, "Proline to arginine mutations in FGF receptors 1 and 3 result in Pfeiffer and Muenke craniosynostosis syndromes through enhancement of FGF binding affinity," *Human Molecular Genetics*, vol. 13, no. 1, pp. 69–78, 2004.
- [17] N. E. Hatch, "FGF signaling in craniofacial biological control and pathological craniofacial development," *Critical Reviews in Eukaryotic Gene Expression*, vol. 20, no. 4, pp. 295–311, 2010.
- [18] J. Andersen, H. D. Burns, P. Enriquez-Harris, A. O. M. Wilkie, and J. K. Heath, "Apert syndrome mutations in fibroblast growth factor receptor 2 exhibit increased affinity for FGF ligand," *Human Molecular Genetics*, vol. 7, no. 9, pp. 1475–1483, 1998.
- [19] K. Yu, A. B. Herr, G. Waksman, and D. M. Ornitz, "Loss of fibroblast growth factor receptor 2 ligand-binding specificity in Apert syndrome," *Proceedings of the National Academy of Sciences of the United States of America*, vol. 97, no. 26, pp. 14536–14541, 2000.
- [20] K. M. Neilson and R. E. Friesel, "Constitutive activation of fibroblast growth factor receptor-2 by a point mutation associated with Crouzon syndrome," *Journal of Biological Chemistry*, vol. 270, no. 44, pp. 26037–26040, 1995.
- [21] V. Shukla, X. Coumoul, R. H. Wang, H. S. Kim, and C. X. Deng, "RNA interference and inhibition of MEK-ERK signaling prevent abnormal skeletal phenotypes in a mouse model of craniosynostosis," *Nature Genetics*, vol. 39, no. 9, pp. 1145–1150, 2007.
- [22] V. P. Eswarakumar, F. Özcan, E. D. Lew et al., "Attenuation of signaling pathways stimulated by pathologically activated FGF-receptor 2 mutants prevents craniosynostosis," *Proceedings of the National Academy of Sciences of the United States of America*, vol. 103, no. 49, pp. 18603–18608, 2006.
- [23] G. M. Cooper, E. L. Durham, J. J. Cray, M. I. Siegel, J. E. Losee, and M. P. Mooney, "Tissue interactions between craniosynostotic dura mater and bone," *Journal of Craniofacial Surgery*, vol. 23, no. 3, pp. 919–924, 2012.
- [24] B. U. Ang, R. M. Spivak, H. D. Nah, and R. E. Kirschner, "Dura in the pathogenesis of syndromic craniosynostosis: fibroblast growth factor receptor 2 mutations in dural cells promote osteogenic proliferation and differentiation of osteoblasts," *Journal of Craniofacial Surgery*, vol. 21, no. 2, pp. 462–467, 2010.
- [25] B. J. Slater, M. D. Kwan, D. M. Gupta, R. R. Amasha, D. C. Wan, and M. T. Longaker, "Dissecting the influence of regional dura mater on cranial suture biology," *Plastic and Reconstructive Surgery*, vol. 122, no. 1, pp. 77–84, 2008.
- [26] K. Mangasarian, Y. Li, A. Mansukhani, and C. Basilico, "Mutation associated with Crouzon syndrome causes ligand-independent dimerization and activation of FGF receptor-2," *Journal of Cellular Physiology*, vol. 172, no. 1, pp. 117–125, 1997.
- [27] A. Lomri, J. Lemonnier, M. Hott et al., "Increased calvaria cell differentiation and bone matrix formation induced by fibroblast growth factor receptor 2 mutations in Apert syndrome," *Journal of Clinical Investigation*, vol. 101, no. 6, pp. 1310–1317, 1998.
- [28] G. Holmes, G. Rothschild, U. B. Roy, C. X. Deng, A. Mansukhani, and C. Basilico, "Early onset of craniosynostosis in an Apert mouse model reveals critical features of this pathology," *Developmental Biology*, vol. 328, no. 2, pp. 273–284, 2009.
- [29] Online Mendelian Inheritance in Man and OMIM, MIM Number 123500, Johns Hopkins University, Baltimore, Md, USA, 2011, <http://omim.org/entry/123500>.
- [30] S. Kreiborg, "Crouzon Syndrome. A clinical and roentgen-cephalometric study," *Scandinavian Journal of Plastic and Reconstructive Surgery and Hand Surgery*, vol. 18, pp. 1–198, 1981.
- [31] T. W. Proudman, M. H. Moore, A. H. Abbott, and D. J. David, "Noncraniofacial manifestations of Crouzon's disease," *Journal of Craniofacial Surgery*, vol. 5, no. 4, pp. 218–222, 1994.
- [32] V. P. Eswarakumar, M. C. Horowitz, R. Locklin, G. M. Morriss-Kay, and P. Lonai, "A gain-of-function mutation of Fgfr2c demonstrates the roles of this receptor variant in osteogenesis," *Proceedings of the National Academy of Sciences of the United States of America*, vol. 101, no. 34, pp. 12555–12560, 2004.
- [33] F. Pampaloni, E. G. Reynaud, and E. H. K. Stelzer, "The third dimension bridges the gap between cell culture and live tissue," *Nature Reviews Molecular Cell Biology*, vol. 8, no. 10, pp. 839–845, 2007.
- [34] M. L. Bouxsein, S. K. Boyd, B. A. Christiansen, R. E. Guldberg, K. J. Jepsen, and R. Müller, "Guidelines for assessment of bone microstructure in rodents using micro-computed tomography," *Journal of Bone and Mineral Research*, vol. 25, no. 7, pp. 1468–1486, 2010.
- [35] N. E. Hatch, Y. Li, and R. T. Franceschi, "FGF2 stimulation of the pyrophosphate-generating enzyme, PC-1, in pre-osteoblast cells is mediated by RUNX2," *Journal of Bone and Mineral Research*, vol. 24, no. 4, pp. 652–662, 2009.
- [36] P. H. Krebsbach, K. Gu, R. T. Franceschi, and R. B. Rutherford, "Gene therapy-directed osteogenesis: BMP-7-transduced human fibroblasts form bone *in vivo*," *Human Gene Therapy*, vol. 11, no. 8, pp. 1201–1210, 2000.
- [37] C. A. Perlyn, V. B. DeLeon, C. Babbs et al., "The craniofacial phenotype of the Crouzon mouse: analysis of a model for syndromic craniosynostosis using three-dimensional microCT," *Cleft Palate-Craniofacial Journal*, vol. 43, no. 6, pp. 740–747, 2006.
- [38] A. Birgersdotter, R. Sandberg, and I. Ernberg, "Gene expression perturbation *in vitro*—a growing case for three-dimensional (3D) culture systems," *Seminars in Cancer Biology*, vol. 15, no. 5, pp. 405–412, 2005.

- [39] U. A. Gurkan, V. Kishore, K. W. Condon, T. M. Bellido, and O. Akkus, "A scaffold-free multicellular three-dimensional *in vitro* model of osteogenesis," *Calcified Tissue International*, vol. 88, no. 5, pp. 388–401, 2011.
- [40] P. R. Baraniak and T. C. McDevitt, "Scaffold-free culture of mesenchymal stem cell spheroids in suspension preserves multilineage potential," *Cell and Tissue Research*, vol. 347, no. 3, pp. 701–711, 2012.
- [41] M. Murshed, D. Harmey, J. L. Millán, M. D. McKee, and G. Karsenty, "Unique coexpression in osteoblasts of broadly expressed genes accounts for the spatial restriction of ECM mineralization to bone," *Genes and Development*, vol. 19, no. 9, pp. 1093–1104, 2005.
- [42] L. Chen, D. Li, C. Li, A. Engel, and C. X. Deng, "A Ser250Trp substitution in mouse fibroblast growth factor receptor 2 (Fgfr2) results in craniosynostosis," *Bone*, vol. 33, no. 2, pp. 169–178, 2003.
- [43] S. R. F. Twigg, C. Healy, C. Babbs et al., "Skeletal analysis of the *Fgfr3*<sup>P244R</sup> mouse, a genetic model for the muenke craniosynostosis syndrome," *Developmental Dynamics*, vol. 238, no. 2, pp. 331–342, 2009.
- [44] Y. Komatsu, P. B. Yu, N. Kamiya et al., "Augmentation of Smad-dependent BMP signaling in neural crest cells causes craniosynostosis in mice," *Journal of Bone and Mineral Research*, 2012.
- [45] G. Holmes, G. Rothschild, U. B. Roy, C. X. Deng, A. Mansukhani, and C. Basilico, "Early onset of craniosynostosis in an Apert mouse model reveals critical features of this pathology," *Developmental Biology*, vol. 328, no. 2, pp. 273–284, 2009.
- [46] L. Yin, X. Du, C. Li et al., "A Pro253Arg mutation in fibroblast growth factor receptor 2 (Fgfr2) causes skeleton malformation mimicking human Apert syndrome by affecting both chondrogenesis and osteogenesis," *Bone*, vol. 42, no. 4, pp. 631–643, 2008.
- [47] Y. X. Zhou, X. Xu, L. Chen, C. Li, S. G. Brodie, and C. X. Deng, "A Pro250Arg substitution in mouse Fgfr1 causes increased expression of Cbfa1 and premature fusion of calvarial sutures," *Human Molecular Genetics*, vol. 9, no. 13, pp. 2001–2008, 2000.
- [48] A. Fragale, M. Tartaglia, S. Bernardini et al., "Decreased proliferation and altered differentiation in osteoblasts from genetically and clinically distinct craniosynostotic disorders," *American Journal of Pathology*, vol. 154, no. 5, pp. 1465–1477, 1999.
- [49] A. Mansukhani, P. Bellosta, M. Sahni, and C. Basilico, "Signaling by fibroblast growth factors (FGF) and fibroblast growth factor receptor 2 (FGFR2)-activating mutations blocks mineralization and induces apoptosis in osteoblasts," *Journal of Bone and Mineral Research*, vol. 149, pp. 1297–1308, 2000.
- [50] Online Mendelian Inheritance in Man and OMIM, MIM Number 307800, Johns Hopkins University, Baltimore, Md, USA, 2011, <http://omim.org/entry/307800>.
- [51] W. A. Roy, R. J. Iorio, and G. A. Meyer, "Craniosynostosis in vitamin D-resistant rickets. A mouse model," *Journal of Neurosurgery*, vol. 55, no. 2, pp. 265–271, 1981.
- [52] Y. Sabbagh, A. O. Jones, and H. S. Tenenhouse, "PHEXdb, a locus-specific database for mutations causing X-linked hypophosphatemia," *Human Mutation*, vol. 16, pp. 1–6, 2000.
- [53] G. Liang, L. D. Katz, K. L. Insogna, T. O. Carpenter, and C. M. MacIca, "Survey of the enthesopathy of X-linked hypophosphatemia and its characterization in Hyp mice," *Calcified Tissue International*, vol. 85, no. 3, pp. 235–246, 2009.
- [54] Online Mendelian Inheritance in Man and OMIM, MIM Number 171760, Johns Hopkins University, Baltimore, Md, USA, 2009, <http://omim.org/entry/171760>.
- [55] D. Wenkert, M. Benigno, K. Mack, W. McAlister, S. Mumm, and M. Whyte, "Hypophosphatasia: prevalence of clinical problems in 175 pediatric patients," in *Proceedings of the American Society for Bone and Mineral Research 31st Annual Meeting*, Denver, Colo, USA, 2009, Abstract A09001674.
- [56] M. P. Whyte, "Physiological role of alkaline phosphatase explored in hypophosphatasia," *Annals of the New York Academy of Sciences*, vol. 1192, pp. 190–200, 2010.
- [57] E. Mornet, "Hypophosphatasia," *Orphanet Journal of Rare Diseases*, vol. 2, p. 40, 2007.
- [58] S. Narisawa, N. Fröhlander, and J.L. Millán, "Inactivation of two mouse alkaline phosphatase genes and establishment of a model of infantile hypophosphatasia," *Developmental Dynamics*, vol. 208, pp. 432–446, 1997.
- [59] A. K. Shetty, T. Thomas, J. Rao, and A. Vargas, "Rickets and secondary craniosynostosis associated with long-term antacid use in an infant," *Archives of Pediatrics and Adolescent Medicine*, vol. 152, no. 12, pp. 1243–1245, 1998.

## Research Article

# Platelet-Rich Fibrin Promotes Periodontal Regeneration and Enhances Alveolar Bone Augmentation

Qi Li,<sup>1,2</sup> Shuang Pan,<sup>3</sup> Smit J. Dangaria,<sup>1</sup> Gokul Gopinathan,<sup>1</sup> Antonia Kolokythas,<sup>4</sup> Shunli Chu,<sup>2</sup> Yajun Geng,<sup>5</sup> Yanmin Zhou,<sup>2</sup> and Xianghong Luan<sup>1</sup>

<sup>1</sup> UIC Brodie Laboratory for Craniofacial Genetics, 801 South Paulina, Chicago, IL 60612, USA

<sup>2</sup> Department of Implantology, Stomatological Hospital, Jilin University, Changchun, Jilin 130021, China

<sup>3</sup> Department of Endodontics, School of Dentistry, Harbin Medical University, Harbin, China

<sup>4</sup> Department of Oral and Maxillofacial Surgery, UIC College of Dentistry, Chicago, IL, USA

<sup>5</sup> The First Hospital of Jilin University, Jilin, China

Correspondence should be addressed to Yanmin Zhou; [zhouym62@126.com](mailto:zhouym62@126.com) and Xianghong Luan; [luan@uic.edu](mailto:luan@uic.edu)

Received 12 November 2012; Revised 2 January 2013; Accepted 4 January 2013

Academic Editor: Brian L. Foster

Copyright © 2013 Qi Li et al. This is an open access article distributed under the Creative Commons Attribution License, which permits unrestricted use, distribution, and reproduction in any medium, provided the original work is properly cited.

In the present study we have determined the suitability of platelet-rich fibrin (PRF) as a complex scaffold for periodontal tissue regeneration. Replacing PRF with its major component fibrin increased mineralization in alveolar bone progenitors when compared to periodontal progenitors, suggesting that fibrin played a substantial role in PRF-induced osteogenic lineage differentiation. Moreover, there was a 3.6-fold increase in the early osteoblast transcription factor RUNX2 and a 3.1-fold reduction of the mineralization inhibitor MGP as a result of PRF application in alveolar bone progenitors, a trend not observed in periodontal progenitors. Subcutaneous implantation studies revealed that PRF readily integrated with surrounding tissues and was partially replaced with collagen fibers 2 weeks after implantation. Finally, clinical pilot studies in human patients documented an approximately 5 mm elevation of alveolar bone height in tandem with oral mucosal wound healing. Together, these studies suggest that PRF enhances osteogenic lineage differentiation of alveolar bone progenitors more than of periodontal progenitors by augmenting osteoblast differentiation, RUNX2 expression, and mineralized nodule formation via its principal component fibrin. They also document that PRF functions as a complex regenerative scaffold promoting both tissue-specific alveolar bone augmentation and surrounding periodontal soft tissue regeneration via progenitor-specific mechanisms.

## 1. Introduction

Regenerative oral medicine entails the replacement of tissues lost to disease or injury with physiologically equivalent engineered tissues. Often, tissues in the oral cavity are of complex nature with bordering mineralized and soft tissue components, both of which harbor unique progenitor populations residing within specialized extracellular matrix frameworks [1, 2]. Mimicking such complex environments by using chemically homogenous scaffolds and uniform stem cell populations is often challenging. Instead, recent approaches favor complex natural scaffolds that allow for repopulation with the patient's own cells, thereby producing an autologous tissue-engineered organ [3].

One such complex natural scaffold ideally suited for autologous tissue regeneration is platelet-rich fibrin (PRF),

a second generation platelet concentrate developed as an improvement over the earlier introduced platelet-rich plasma (PRP) as an aid for tissue repair and regeneration [4]. In contrast to PRP, which was prepared by adding bovine thrombin and anticoagulants, PRF is generated from centrifuged blood and is strictly autologous. PRF predominantly consists of a fibrin matrix rich in platelet and leukocyte cytokines such as IL-1 $\beta$ , -4, and -6, and growth factors such as TGF- $\beta$ 1, PDGF-AB, and VEGF [5]. Fibrin gels exploit the final stage of the coagulation cascade in which fibrinogen molecules self-assemble into a highly biocompatible three-dimensional fiber network [6]. The combination of fibrins and cytokines within PRF becomes a powerful bioscaffold with an integrated reservoir of growth factors for tissue regeneration [7]. The suitability of PRF as a biologically active scaffold has been



illustrated in a number of studies revealing proliferation and differentiation of osteoblasts and gingival fibroblasts [8, 9]. Clinical studies have demonstrated that PRF promotes soft tissue and bone regeneration [10, 11], as well as periodontal tissue regeneration [12, 13]. The ability of PRF to augment and regenerate compromised tissues may be enhanced in combination with bone substitutes such as Bio-Oss or autologous bone [14, 15]. Together, these studies have established PRF as a highly biocompatible and inductive scaffold useful for a broad range of tissue engineering applications.

In the present study, we have hypothesized that PRF may provide a scaffold material for periodontal tissue regeneration. Earlier studies have reported the effect of PRF on periodontal cells [16, 17]. Here we have compared the effects of PRF on dental follicle, periodontal ligament, and alveolar bone cells [1] using microscopy as well as biological assays for migration, proliferation, mineralization, and gene expression. We also tested PRF scaffold properties in subcutaneous implants in nude mice. Finally, we report on the use of PRF as a scaffold for peri-implant alveolar bone augmentation in clinical use. Together, these studies for the first time characterize the tissue-specific biological effects of PRF as a bioactive scaffold to promote periodontal soft and hard tissue regeneration.

## 2. Materials and Methods

**2.1. Preparation of PRF.** To prepare PRF, 10 mL of fresh blood from the precaval vein of a pig was collected into 10 mL glass-coated tubes without anticoagulants. All pigs used in this study were female with an average age of 3.1 months (range from 2.9 to 3.5 months). The platelet count of whole pig blood was  $10^5/\mu\text{L}$ . This study was approved by the Ethics Committee of the University of Illinois at Chicago, USA. As described in previous studies [4, 18], samples were immediately centrifuged at 2100 rpm (approximately 400 g) for 12 minutes using a Beckman centrifuge. The PRF clots were concentrated between the red blood cell corpuscles at the bottom of the centrifuge tubes, and acellular plasma called platelet-poor plasma (PPP) at the top of the tubes. PPP was collected by pipetting the supernatant of the centrifuged blood preparation. After PPP removal, PRF clots were mechanically separated from red blood cells and gently compressed using gauze to drain the remaining fluid.

Reproducibility of studies was ensured by maintaining consistent preparation conditions for PRF membranes, including centrifugation force and time, tube size, and platelet count of pig blood, and by completing blood collection procedures within 2 minutes. For *in vitro* studies, all cell culture wells were treated with one whole PRF clot consisting of identical amounts of fibrin, platelets, and white blood cells, and each PRF clot was freshly prepared from blood.

**2.2. Preparation of Conditioned Medium.** To prepare conditioned medium, PRF membranes were soaked in 5 mL fresh DMEM medium without fetal bovine serum in 6-well cell culture plates. The conditioned medium was collected every 48 h, and fresh medium was added into wells after collection.

**2.3. Isolation of Human Dental Progenitor Cells.** To generate human dental progenitor cells, healthy human teeth (patients ranging from 12 to 15 years) were extracted for orthodontic reasons in accordance with the human subjects protocol approved by UIC's Institutional Review Boards and the Office for the Protection Research Subjects. The dental follicle (DF) was dissected from developing tooth organs, and alveolar bone (AB) and periodontal ligament (PDL) were prepared from teeth with tooth roots already formed. Mesenchymal stem cells were isolated from the dental tissues after digestion with collagenase/dispase as described before [2].

**2.4. MTT Cell Proliferation Assay.** PDL, DF, and AB cells ( $10^4$  cells/well) were seeded into 96-well plates and cultured for 8 hours. After cells were attached, each well was washed twice with phosphate-buffered saline solution (PBS), and either PRF-conditioned medium + 10% FBS or DMEM + 10% PPP + 10% FBS was added to the well. DMEM + 10% FBS was used as a control. Prior to the termination of culture, cells were incubated in MTT solution ( $2 \mu\text{g/mL}$  of MTT in DMEM with 2% FBS) for 4 hours. To quantify proliferative activity, the MTT-stained cells were lysed in HCL/isopropanol, and the absorbance was detected at 570 nm with background subtraction at 630 nm. Cell proliferation was detected on a daily basis over the entire 7-day culture period.

**2.5. Chemotaxis Assay.** Cell migration assays were performed using a FluoroBlok-24-multiwell insert system (DB Biosciences, Bedford, MA). PRF-conditioned medium, DMEM + 10% PPP, or DMEM was added into separate wells of the lower chambers of the FluoroBlok system. Serum-starved cells ( $10^5$ ) were seeded into each insert and allowed to migrate to the bottom of the membrane for 12 hours. The nonmigrated cells on the upper surface of the membrane were removed with a cotton swab, and the migratory cells that were attached to the lower surface were stained with DAPI. The numbers of migrated cells per membrane were counted under a Leica DMRX fluorescent microscope.

**2.6. Induction of Osteogenic Differentiation, Alkaline Phosphatase (ALP) Activity Assessment, and Alizarin Red S Staining.** PDL, DF, and AB were seeded into 6-well plates at a concentration of  $10^4$  cells/well and cultured for 8 hours. After cell attachment, PRF membranes were added to individual wells, soaked, and subjected to osteogenic treatment, which included addition of osteogenic medium (OM), DMEM + 10% PPP + 10% FBS, or DMEM to each individual well. The following four groups were employed in this study: (i) PRF in DMEM with 10% FBS, (ii) 10% PPP in DMEM with 10% FBS, (iii) osteogenic medium with 10% FBS, and (iv) DMEM with 10% FBS. To test the effect of fibrin as the major PRF component on periodontal progenitor differentiation and mineralization, fibrin was used to coat otherwise untreated cell culture dishes and compared with vacuum gas plasma-treated and plasma-untreated dishes. To generate fibrin, equal amounts of fibrinogen ( $100 \text{ mg/mL}$ ) and thrombin ( $500 \mu\text{g/mL}$ ) were mixed prior to application. Subsequently, treated cells were cultured for an additional 7,

14, or 21 days. For alkaline phosphatase activity assays, cells were washed and stained with NBT/BCIP (Roche Diagnosis GmbH, Mannheim, Germany) after rinsing with PBS. For quantification of mineralized nodules, cells were fixed with methanol and stained with 10% alizarin red solution. Mineralized nodules were identified as red spots on the culture dish. Alkaline phosphatase activity was determined after one week and alizarin red S staining was performed after three weeks. Wells were scanned and the integrated optical density (average intensity/object density) of the stained area was calculated using the Image Pro Plus 6.0 software (Mediacy, Chicago, IL, USA).

**2.7. RNA Extraction and RT PCR.** Total RNAs were isolated from cultured cells using the TRIZOL LS Reagent (Invitrogen, Carlsbad, CA, USA) according to the manufacturer's instructions. Two micrograms of total extracted RNA was applied toward cDNA generation with the Sprint RT Complete kit (Clontech, Mountain View, CA, USA). PCR primers were designed based on EMBL/GenBank searches, and primer sequences were as follows: *RUNX2*: 5'-TTA CTT ACA CCC CGC CAG TC-3' (sense), 3'-CAC TCT GGC TTT GGG AAG AG-5' (antisense); *MGP*: 5'-CCC TCA GCA GAG ATG GAG AG-3' (sense), 3'-GCTTCCCTATTGAGCTCGTG-5' (antisense),  $\beta$ -*ACTIN*: 5'-GCA TGG GTC AGA AGG ATT CCT-3 (sense), and 3'-TCG TCC CAG TTG GTG ACG AT-5' (antisense). Real-time PCR was performed using sequence-specific SyberGreen primers and the ABI Prism 7000 sequence detection system (Applied Biosystems, Foster City, CA, USA). Reaction conditions were as follows: 2 min at 50°C (one cycle), 10 min at 95°C (one cycle), 15 sec at 95°C, and 1 min at 60°C (40 cycles). Samples were normalized using  $\beta$ -*actin*. The analyses were performed in triplicate for three independent experiments to confirm reproducibility of the results. Relative expression levels were calculated using the  $2^{-\Delta\Delta C_t}$  method [19], and values were graphed as the mean expression level  $\pm$  standard deviation.

**2.8. Protein Extraction and Western Blot Analysis.** For western blot evaluation of the effect of PRF on *RUNX2* in cultured periodontal progenitors, cells were collected, and equal amounts of protein extracts in a lysis buffer containing 100 mM Tris HCl pH 9.0, 200 mM KCl, 25 mM EGTA, 36 mM  $MgCl_2$ , 2% deoxycholic acid, and 10% DTT v/v were subjected to SDS-polyacrylamide gel electrophoresis. The separated proteins were transferred to a PVDF membrane (Immobilon P, Millipore) and the membrane was incubated with anti-*RUNX2* or anti-GAPDH primary antibodies (Abcam, Cambridge, MA, USA). Immune complexes were detected with peroxidase-conjugated secondary antibody (Molecular Probes, Carlsbad, CA, USA) and enhanced by chemiluminescence reagents (Pierce Biotechnology, Rockford, IL, USA). The amounts of protein expression were compared after normalization against GAPDH as an internal calibrator in each lane.

**2.9. Subcutaneous Implant.** Fresh PRF membranes measuring 5 mm<sup>2</sup> in diameter and 1 mm<sup>2</sup> in thickness were

implanted under the cutis of nude mice (male, 6 weeks of age, Charles River). After 7 and 14 days of implantation, nude mice were sacrificed and implants were dissected for histological analyses.

**2.10. Mallory Staining.** Implants were fixed with 10% formalin at 4°C and processed for paraffin sections. Deparaffinized and rehydrated sections were stained in a series of toluidine blue, acid fuchsine, and aniline, for 2 minutes, respectively.

**2.11. Clinical Application.** Two clinical pilot studies were conducted to test the effect of PRF on peri-implant sites in human patients. These studies were approved by the Ethics Committee of the Jilin University Health Science Center, Changchun, China. Informed consent was obtained from patients before surgery. Studies were conducted at Jilin University Stomatological Hospital and were consistent with the principles enunciated in the Declaration of Helsinki on the protection of human subjects. All patients selected for implant placement and PRF treatment were required to demonstrate superior oral hygiene with no or minimal plaque. Two Asian healthy adults, one male aged 28 years and one female aged 22 years, served as volunteers. Both patients demonstrated evidence of residual root tips prior to tooth extraction according to radiographs. For the rehabilitation of the patient, the fractured incisor (patient I) and the decayed molar (patient II) were extracted. Implant dimensions slightly varied between patients (13 mm  $\times$  3.5 mm, patient I, and 12 mm  $\times$  4.8 mm, patient II). Both patients exhibited substantial gaps between implant and alveolar bone socket. To close the gap between implant and extraction socket, PRF was prepared individually from each patient's blood sample, and squeezed PRF membranes were placed between implant and adjacent bone. Subsequently, the surgical site was closed using silk sutures. As a followup, radiographs were taken immediately and three months after surgery. Wound healing and bone levels were examined using intraoral photographs and oral radiographs. To calculate bone levels, implant dimensions served as a reference.

**2.12. Statistical Analysis.** Statistical analysis was performed using the SPSS 13.0 software (Chicago, IL, USA) and Student's *t*-test. Data were expressed as mean  $\pm$  SD. For all tests, statistical significance was assigned when  $P < 0.05$ . Experiments were repeated 3 times to ensure reproducibility.

### 3. Results

**3.1. PRF Clot Prepared from Fresh Blood Contained Fibrin, White Blood Cells, and Leukocytes.** The focus of the present study was to determine the suitability of PRF for biological reengineering of complex periodontal tissues, including soft and mineralized tissues. As a first step, we have analyzed the histological composition of the PRF scaffold used in our studies. For our experiments, PRF was generated by low-speed centrifugation from whole blood. Centrifugation resulted in separation of three distinct fractions: platelet-poor plasma (PPP), platelet-rich fibrin (PRF), and red blood cells

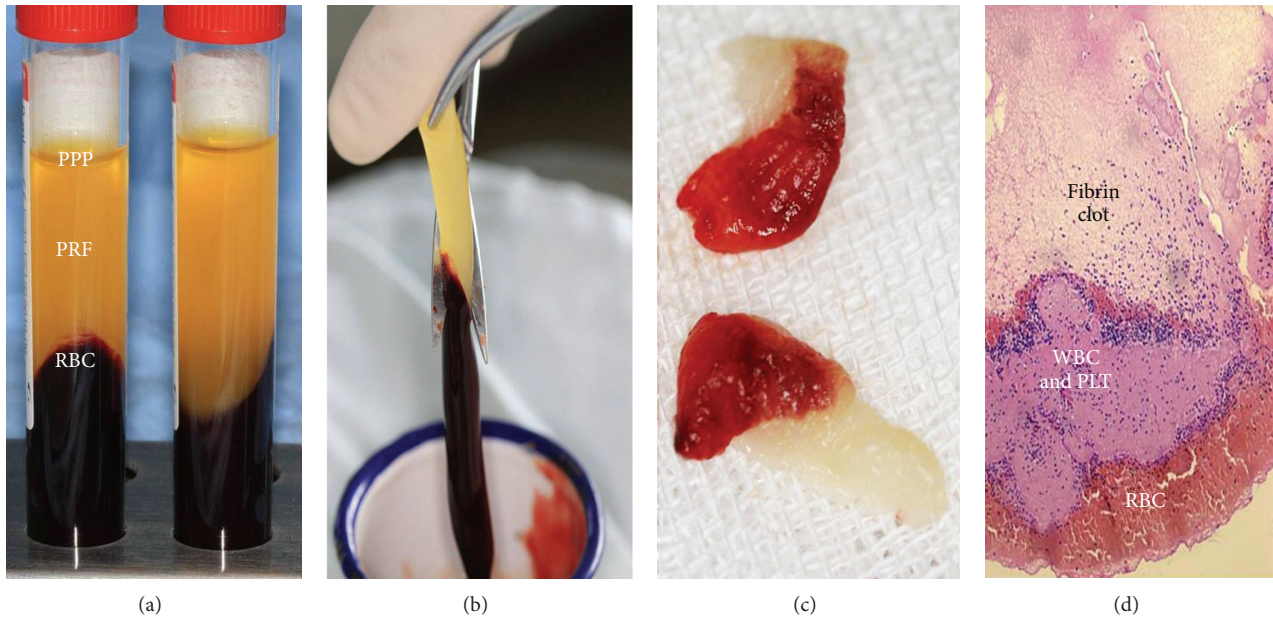


FIGURE 1: Preparation and structure of platelet-rich fibrin (PRF). (a) shows three fractions of whole blood generated by low-speed centrifugation: platelet-poor plasma (PPP), platelet-rich fibrin (PRF), and red blood cells (RBC). At this stage, PRF and RBC have formed a gel, while the PPP fraction remains liquid. (b) Mechanical separation of the RBC fraction from the PRF fraction after decanting the PPP fraction. (c) Generation of solid PRF after liquid removal. (d) 5  $\mu$ m paraffin section through solidified PRF generated in (c). The section contains three portions: (i) the cell-free fibrin clot, (ii) the buffy coat portion containing white blood cells (WBC) and platelets (PLT), and (iii) the red blood cell (RBC) portion. Note that the majority of the white blood cells and platelets are trapped in the buffy coat.

(RBC) (Figure 1(a)). The PRF fraction was further isolated by decanting the soluble PPP fraction and by mechanically removing the RBC fraction (Figure 1(b)). Liquid removal from the PRF fraction through mechanical pressure between gauze layers resulted in a fairly solid, gel-like material (Figure 1(c)). H&E-stained paraffin sections through the PRF clot revealed three portions: (i) the cell-free fibrin clot, (ii) the buffy coat portion containing white blood cells (WBC) and platelets (PLT), and (iii) the red blood cell (RBC) portion (Figure 1(d)). For the experiments described herein, the entire PRF clot was used, including fibrin, white blood cells, and platelets. The red blood cells immediately attached to the PRF clot were not further separated.

**3.2. PRF Significantly Increased Periodontal Progenitor Cell Migration and Proliferation In Vitro When Compared to PPP and DMEM Media.** Effective biocompatible tissue engineering scaffolds provide a template for cells to migrate and proliferate [20]. To determine the ability of PRF-based scaffolds to promote cell proliferation and migration, periodontal progenitors were cultured for up to 7 days using PRF, PPP, or DMEM alone (Figure 2). PRF was compared with PPP to compare the effects of a fibrin-rich (PRF) and a fibrin-poor (PPP) blood centrifugate on periodontal cells. Our cell proliferation assays using PDL fibroblasts, dental follicle progenitors, and alveolar bone osteoblasts demonstrated a gradual increase in cell density over a culture period of 7 days with all three culture conditions (Figures 2(a)–2(c)). PRF resulted in higher proliferation rates than DMEM

medium alone or platelet-poor plasma (PPP) (Figures 2(a)–2(c)). After 7 days of culture, the PRF-induced increase in proliferation significantly surpassed the PPP- and DMEM-induced proliferation rate in all cell cultures examined (30.1% for DF, 34% for PDL, and 22.4% for AB;  $P < 0.05$ ). Migration assays revealed that PRF caused a highly significant ( $P < 0.0001$ ) and higher than 15-fold increase (19.3-fold for DF, 18-fold for PDL, and 17.1-fold for AB) in the number of migrated cells when compared to DMEM medium, while platelet-poor plasma (PPP) only caused a moderate 5–10-fold increase in the number of migrated cells (7.8-fold for DF, 5-fold for PDL, and 7.1-fold for AB).

**3.3. PRF Almost Equaled Osteogenic Medium in Its Effect on Mineralization Behavior of Cultured Periodontal Progenitors and in Comparison to DMEM and PPP.** Previous studies have established the osteogenic potential of periodontal progenitors, including dental follicle and periodontal ligament progenitors [21, 22]. However, periodontal progenitors do not form bone or other mineralized tissues in routine tissue engineering applications without osteoinduction [2]. Moreover, *in vivo* studies have demonstrated the suitability of fibrin-based scaffolds for bone tissue engineering [23]. We therefore asked the question to what extent PRF unleashes the osteogenic potential of periodontal progenitors. In our studies, DF, PDL, and AB cells were subjected to coculture with platelet-rich fibrin (PRF), osteogenic medium (OM), platelet-poor plasma (PPP), or Dulbecco's modified Eagle's medium (DMEM), and alkaline phosphatase and alizarin red staining were used to evaluate osteoblast activity and



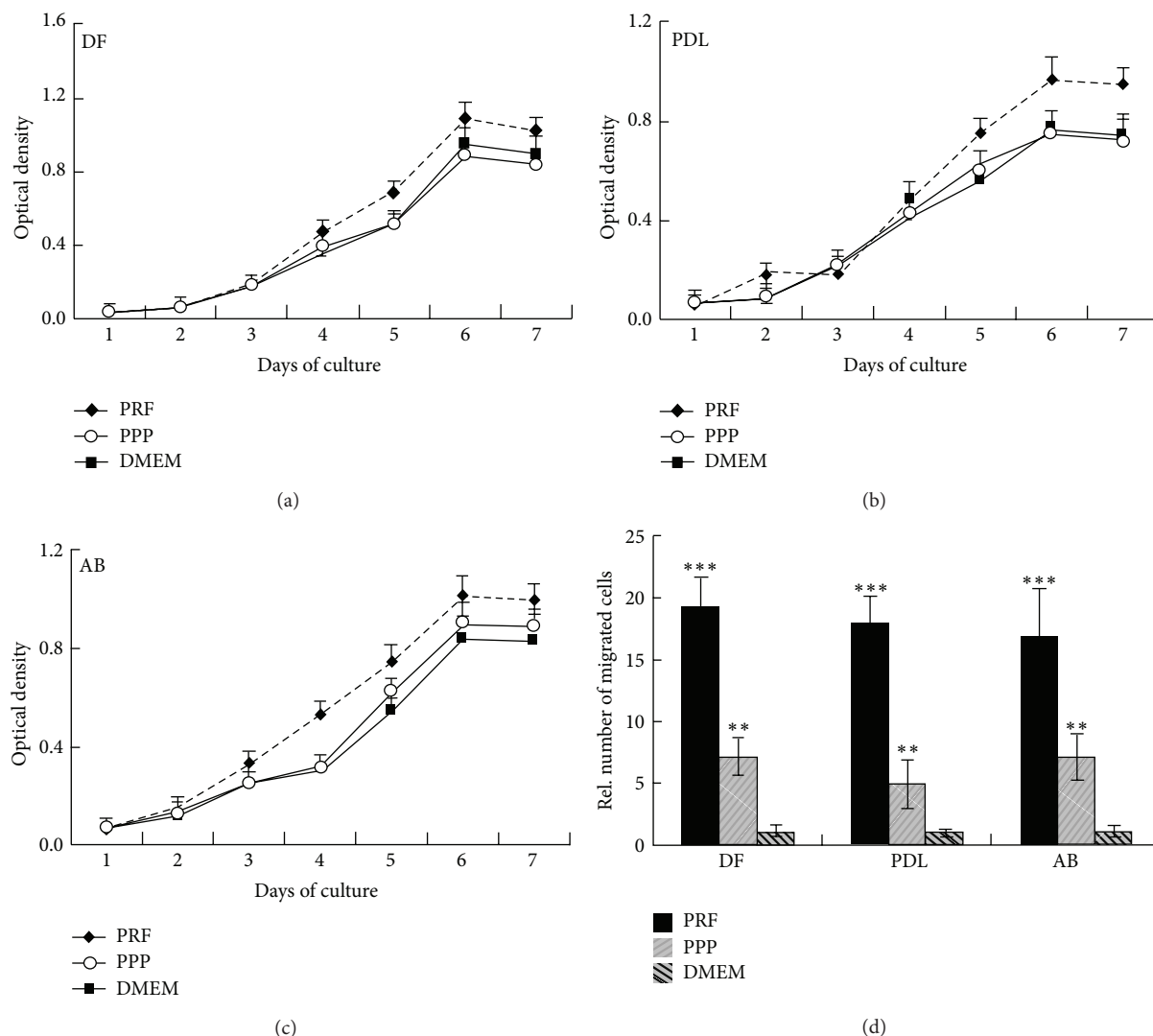


FIGURE 2: Effects of PRF when compared to PPP and medium alone on proliferation and migration of periodontal progenitor populations. Figures 2(a)–2(c) illustrate the results of MTT proliferation assays when dental follicle progenitors (DF, (a)), periodontal ligament progenitors (PDL, (b)), and alveolar bone osteoblast progenitors (AB, (c)) were cultured on PRF-related substrates. The three different substrates used in this proliferation study, PRF, PPP, and DMEM media, are distinguished by line patterns (Figure 2(a)). (d) Difference in chemotaxis behavior between periodontal progenitors when cultured in PRF-conditioned media, PPP, and DMEM medium. Level of significance was calculated in comparison to the DMEM-treated cells within each group. \*\* $P < 0.01$  and \*\*\* $P < 0.001$ .

mineralized nodule formation. After 7 days, alkaline phosphatase levels as a result of PRF coculture increased 4.1-fold (DF), 3.7-fold (PDL), and 12.6-fold (AB), while OM coculture resulted in an 5.1-fold (DF), 5.8-fold (PDL), and 14.8-fold (AB) increase of alkaline phosphatase levels (Figure 3(a)). These effects were highly significant ( $P < 0.01$ ), while there was no significant difference in alkaline phosphatase levels between PPP-treated cells and DMEM-treated cells. After 14 days, alkaline phosphatase levels as a result of PRF coculture increased 7-fold (DF), 10.8-fold (PDL), and 25-fold (AB), while OM coculture resulted in a 10.6-fold (DF), 15.7-fold (PDL), and 35.8-fold (AB) increase of alkaline phosphatase levels (Figure 3(c)). Differences once more were highly significant ( $P < 0.001$  for DF/OM,  $P < 0.01$  for DF/PRF,  $P < 0.001$  for PDL, and  $P < 0.0001$  for AB),

while alkaline phosphate levels of PPP-treated and DMEM-treated cells were at the same level. Alkaline phosphatase levels after 21 days of culture were decreased compared to 14-day levels, but still are higher than those after 7 days. Specifically, alkaline phosphatase levels in the PRF-treated group increased 10.4-fold (DF), 2.9-fold (PDL), and 20.1-fold (AB), while alkaline phosphatase levels in the OM-treated group increased 8.5-fold (DF), 3.3-fold (PDL), and 22.3-fold (AB), once more at statistically highly significant levels ( $P < 0.01$  for DF and PDL, and  $P < 0.001$  for AB) (Figure 3(e)).

In addition to alkaline phosphate levels, alizarin red S staining was performed as a means to assess matrix mineralization. After 7 days, alizarin red S staining as a result of PRF coculture increased 2-fold (DF), 2.3-fold (PDL), and 4.9-fold (AB), while OM coculture resulted in an increase



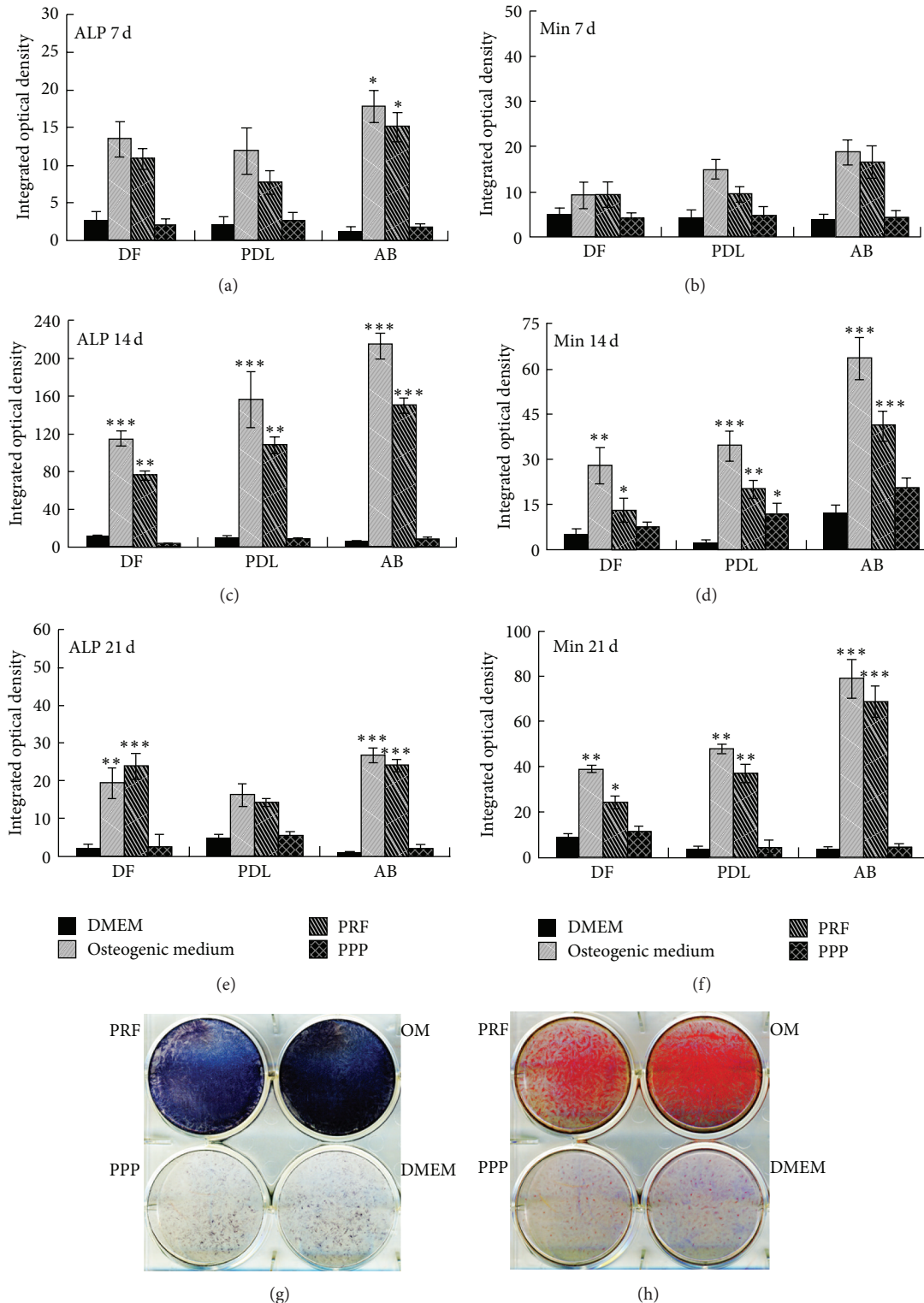


FIGURE 3: Effect of PRF, PPP, and DMEM media on mineralization behavior of periodontal progenitor populations. (a), (c), (e), and (g) are alkaline phosphatase staining assays and (b), (d), (f), and (h) are alizarin red S mineralization assays. In (a)–(f), alkaline phosphatase ((a), (c), and (e)) or alizarin red ((b), (d), and (f)) staining in periodontal progenitor cells cultured for 7, 14, and 21 days were compared. Different coculture conditions (PRF, PPP, OM, and DMEM) are distinguished by different bar patterns which are identified in the bar legend above (b). The three periodontal progenitor populations compared in this study, dental follicle (DF), periodontal ligament (PDL), and alveolar bone (AB) are labeled on the x-axis of the graphs in (a)–(f). (g) and (h) illustrate the differences in mineralization behavior between alveolar bone progenitors cocultured with PRF, OM, PPP, and DMEM for 14 days; (g) is a photograph of the alkaline phosphate-stained 6-well plate and (h) is a photograph of the alizarin red-stained 6-well plate. Level of significance was calculated in comparison to the DMEM-treated cells within each group. \*  $P < 0.05$ , \*\*  $P < 0.01$ , and \*\*\*  $P < 0.001$ .

of alizarin red S staining by 1.9-fold (DF), 3.7-fold (PDL), and 5.5-fold (AB) (Figure 3(b)). These effects were highly significant ( $P < 0.05$  for DF,  $P < 0.01$  for PDL/OM,  $P < 0.05$  for PDL/PRF, and  $P < 0.01$  for AB), while there was no significant difference in alizarin red S staining between PPP-treated cells and DMEM-treated cells. After 14 days, alizarin red S staining as a result of PRF coculture increased 2.6-fold (DF), 9.3-fold (PDL), and 3.3-fold (AB), while OM coculture resulted in an increase of alizarin red S staining by 5.6-fold (DF), 15.9-fold (PDL), and 5.2-fold (AB), when compared to DMEM-treated cells (Figure 3(d)). Differences once more were highly significant ( $P < 0.01$  for DF/OM,  $P < 0.05$  for DF/PRF,  $P < 0.001$  for PDL/OM,  $P < 0.01$  for PDL/PRF,  $P < 0.0001$  for AB/OM, and  $P < 0.001$  for AB/PRF). Alizarin red S staining after 21 days of culture was further enhanced, with staining levels in the PRF-treated group increased to 2.8-fold (DF), 10.8-fold (PDL), and 20.2-fold (AB), while alizarin red S staining in the OM-treated group increased 4.5-fold (DF), 14-fold (PDL), and 23.1-fold (AB), once more at statistically highly significant levels ( $P < 0.01$  for DF,  $P < 0.001$  for PDL, and  $P < 0.0001$  for AB) (Figure 3(f)). Effects of PRF, OM, PPP, and DMEM on alkaline phosphatase levels (Figure 3(g)) and alizarin red S staining (Figure 3(h)) as mineralization indicators after 14 days of alveolar bone progenitor culture were documented.

**3.4. PRF Significantly Enhanced RUNX2 Expression and Reduced MGP Expression in AB Progenitors, While It Affected DF and PDL Cells to a Lesser Degree.** To test whether changes in mineralization behavior of periodontal progenitors as a result of PRF application or treatment with osteogenic medium (OM) corresponded to the changes in gene expression levels, expression levels of two osteogenic modulators, the osteoblastic differentiation transcription factor *RUNX2* [24] and the extracellular matrix mineralization inhibitor [25] matrix GLA protein (*MGP*). After 7 days of culture, neither *RUNX2* nor *MGP* was substantially affected by PRF or OM in any of the three cell types investigated (Figures 4(a) and 4(b)). After 14 days of culture, *RUNX2* expression in all three cell types was significantly increased as a result of PRF, OM, and PPP application (Figure 4(c)). Notably, PRF and OM treatment had a remarkable effect on *RUNX2* levels in AB cells when compared to DF and PDL cells. While *RUNX2* expression in DF and PDL progenitors approximately doubled in response to OM and PRF exposure, *RUNX2* levels increased 3.3-fold after OM application and 3.6-fold after PRF application in AB cells (Figure 4(c),  $P < 0.01$ ). This general trend was retained after 21 days, albeit at slightly reduced levels: OM caused a 1.8-fold increase in *RUNX2* expression in AB cells and PRF resulted in a 2.6-fold increase in *RUNX2* expression in AB cells, while there was little effect in the other two progenitor cell populations (Figure 4(e)). On western blots, PRF resulted in a 10.4-fold increase and OM in a 23.52-fold increase in *RUNX2* levels in AB cells cultured for 2 weeks when compared to the DMEM group (Figures 4(g) and 4(h),  $P < 0.001$ ). As mentioned above, *MGP* was little affected by PRF or OM in any of the cell types after one week of culture (Figure 4(b)). Two or three weeks in the presence of PPP resulted in an approximately 2-fold elevation of *MGP* in

all three cell types (Figures 4(d) and 4(f),  $P < 0.05$ ). Most notable was a 3.1-fold reduction in *MGP* expression as a result of PRF application in AB cells after 2 weeks ( $P < 0.01$ ) and a 2-fold PRF-induced reduction in *MGP* expression in DF cells (Figures 4(d) and 4(f),  $P < 0.05$ ). There was still a 1.2-fold reduction in *MGP* expression in AB progenitors as a result of PRF treatment after 3 weeks of culture, while there were few differences in all other groups and cells after three weeks of culture, with the exception of the *MGP* upregulation caused by PPP (Figure 4(f)).

**3.5. Fibrin-Enhanced Alkaline Phosphatase Activity and Mineralization in AB Progenitors.** Studies so far indicated that PRF affects mineralization of periodontal progenitors, especially AB progenitors. To determine whether fibrin as the major structural component of the PRF scaffold affects mineralization behavior of periodontal progenitors, cells were cultured on fibrin-coated culture dishes, vacuum gas plasma-treated tissue culture dishes, and untreated Petri dishes, for 5 days, and stained for alkaline phosphatase activity (Figure 5(a)) or alizarin red S (Figure 5(b)). Alkaline phosphatase levels of PDL and AB progenitors were significantly elevated on fibrin-coated dishes when compared to vacuum gas plasma-coated dishes (4.57-fold for AB and 3.9-fold for PDL), while there was only a 1.77 elevation of DF cell progenitor alkaline phosphatase levels on fibrin-coated dishes. In contrast, alizarin red S as an indicator of mineralization was significantly increased in the AB progenitor group when compared to the PDL (4.76-fold increase when comparing AB versus PDL) and the DF groups (3.26-fold increase when comparing AB versus DF); AB culture alizarin red S levels were 2.15-fold higher on fibrin-coated dishes than on commercially pretreated dishes.

**3.6. PRF Scaffolds Integrated with Surrounding Tissues and Were Partially Replaced with Collagen Fibers Two Weeks after Subcutaneous Implantation in Nude Mice.** To determine the suitability of PRF as a scaffold for tissue regeneration, PRF membranes were subcutaneously implanted in nude mice. One week after implantation, PRF membranes were completely surrounded by subcutaneous collagen fibers (Figure 6(a)). After 14 days, the thickness of the membrane was reduced to 0.5 mm and the remaining tissue had been replaced by dense collagen fibers (Figures 6(b) and 6(d)). At this time point, pores inside of the PRF membrane contained meshworks of thin collagen fibrils (Figure 6(c)).

**3.7. Soft Tissue Healing and New Bone Formation after PRF Application for Peri-Implant Periodontal Regeneration.** To test the effect of PRF on peri-implant sites in human patients, clinical pilot studies were conducted. In these studies, PRF was placed into peri-implant tissue gaps of both human molars and incisors (Figure 7). Intraoral images illustrate soft tissue healing 5 days after surgery and PRF membrane placement (Figure 7(h)) as well as complete integration three months after surgery (Figures 7(c) and 7(i)). Radiographs demonstrate substantial new alveolar bone formation surrounding both implants (Figures 7(e) and 7(l) versus Figures 7(d) and 7(k)). On the mesial aspect of the incisor implant,

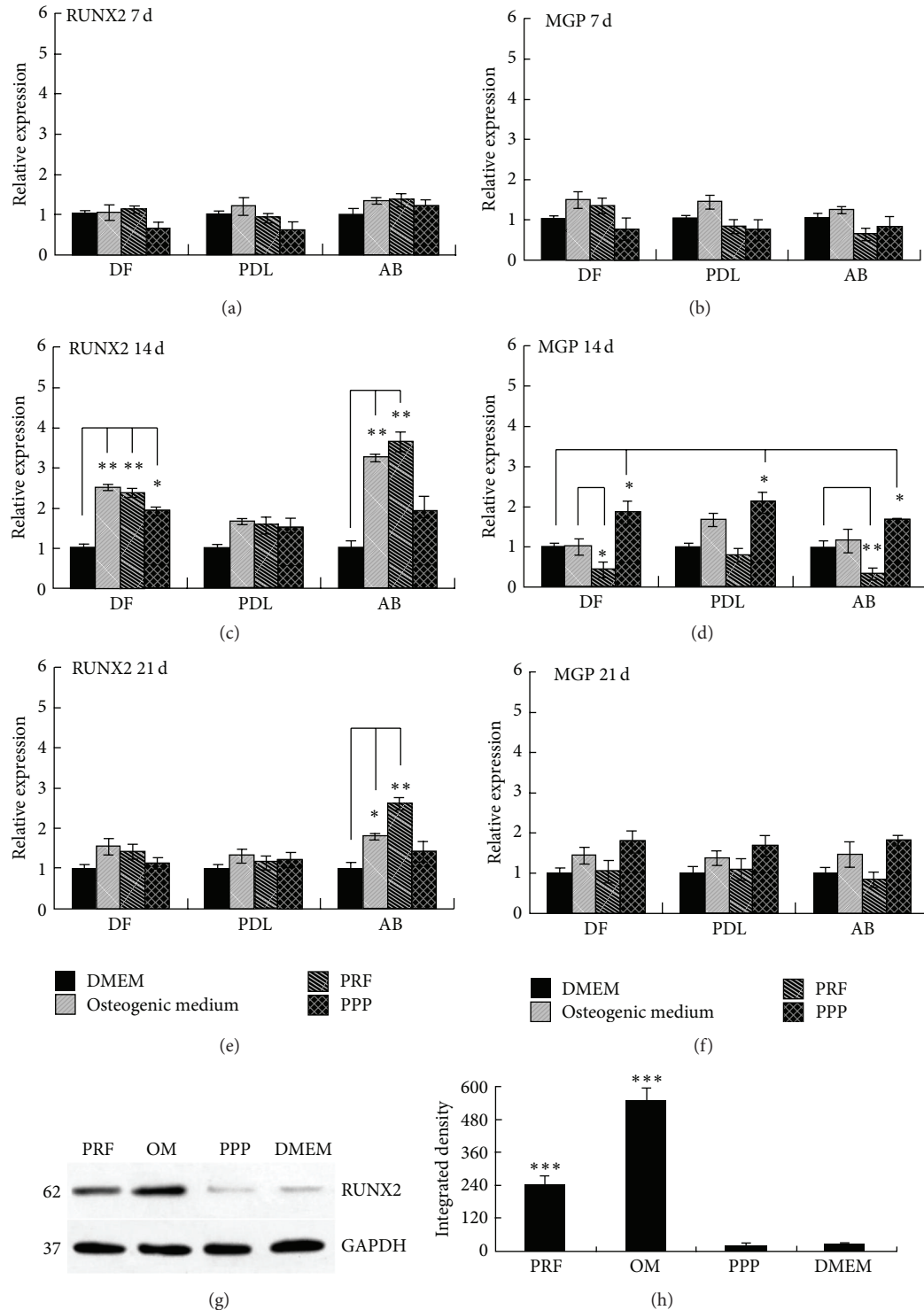


FIGURE 4: Differences in mineralization-associated gene expression patterns in cocultures of periodontal progenitors and centrifuged blood derivatives. (a), (c), and (e) are real-time RT-PCR assays for the osteoblast transcription factor Runx2, and (b), (d), and (f) are real-time RT-PCR assays for the calcification inhibitor Matrix Gla Protein (MGP). Different coculture conditions (PRF, PPP, and DMEM) are distinguished by different bar patterns identified in the upper right corner of the figure. The three periodontal progenitor populations compared in this study, dental follicle (DF), periodontal ligament (PDL), and alveolar bone (AB), are labeled on the x-axis of the graphs in (a)–(f). (g) is a western blot comparing Runx2 protein levels generated by AB cells cocultured either with PRF, OM, PPP, or DMEM. GAPDH served as a control. (h) is the corresponding densitometry evaluation. Level of significance was calculated in comparison to the DMEM-treated cells within each group. \* $P < 0.05$ , \*\* $P < 0.01$ , and \*\*\* $P < 0.001$ .



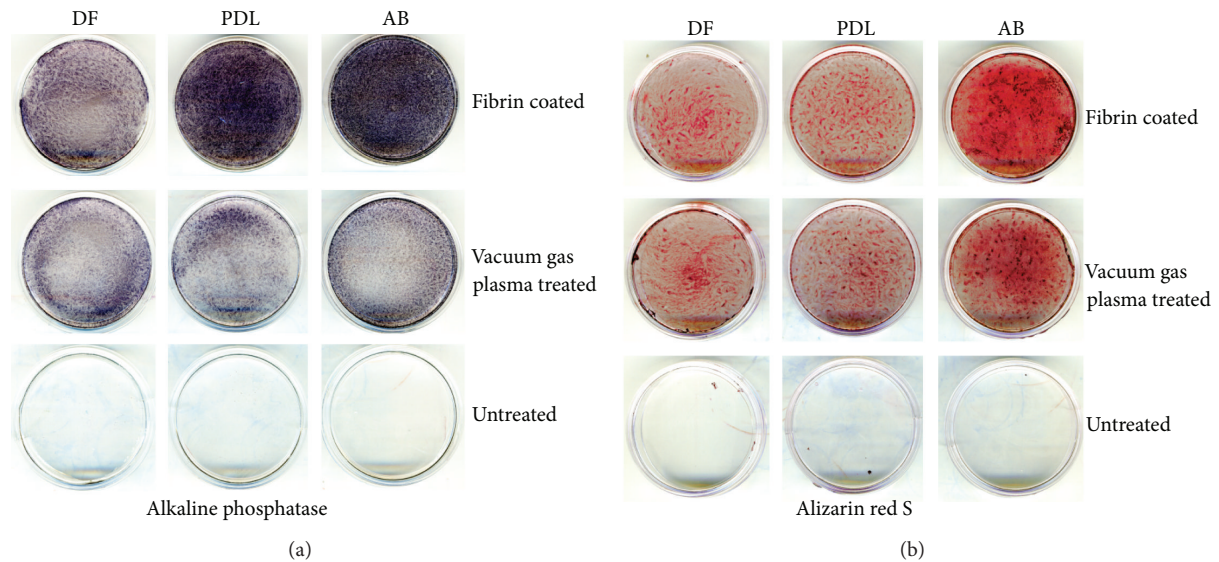


FIGURE 5: Effect of the major PRF component, fibrin, on periodontal progenitor attachment and mineralization. Osteogenic lineage differentiation (a) and mineralized nodule formation (b) of dental follicle cells (DF), periodontal progenitors (PDL), and alveolar bone progenitors (AB) on fibrin-coated dishes, vacuum gas plasma-treated tissue culture dishes, and untreated Petri dishes as revealed by alkaline phosphatase (a) and alizarin red S (b). Alkaline phosphatase activity was determined after one week and alizarin red S staining was performed after three weeks.

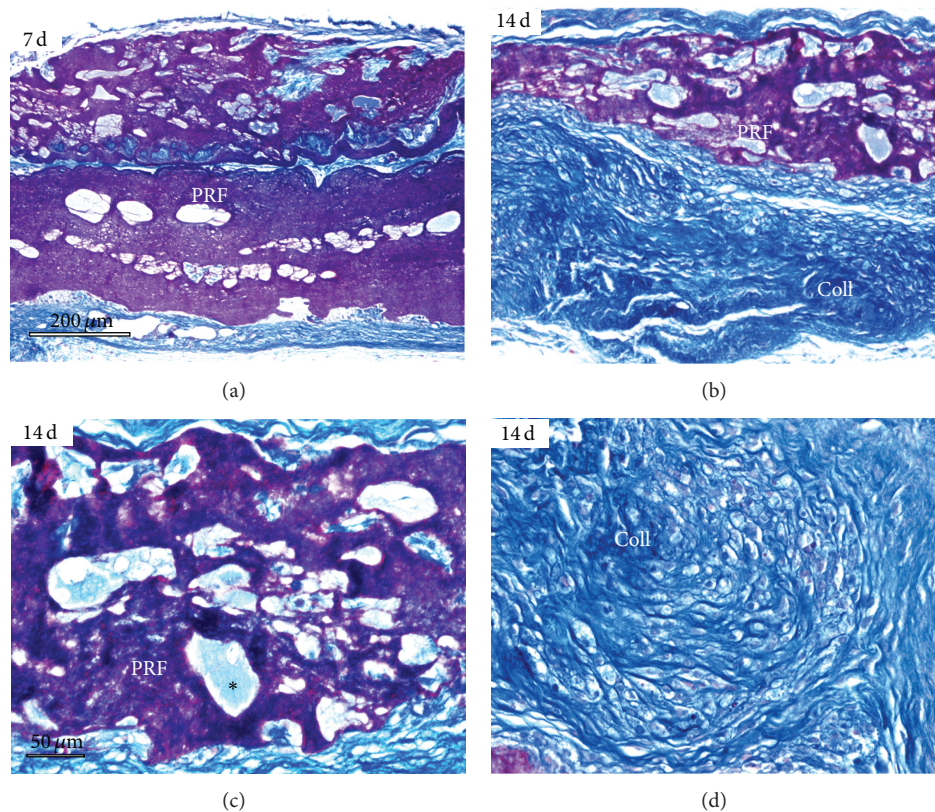


FIGURE 6: Evaluation of PRF as a scaffold in nude mice subcutaneous implants. This figure contains micrographs of paraffin sections through the center of the implant stained using Mallory's connective tissue stain. (a) After 7 days of implantation, the PRF implant remained fairly intact and was only surrounded by collagen fibers in the periphery of the implant. (b) After 14 days of implantation, the size of the PRF scaffold (PRF) was reduced and mostly replaced with collagen fibers (Coll, here stained in blue). (c) and (d) illustrate histology of the 14-day implant at higher magnification. Note small collagen fibers (light blue) present within the pores of the implant (\*, (c)). (d) demonstrates new collagen fiber formation (Coll) replacing the PRF implant. (a) and (b) bar = 200  $\mu$ m; (c) and (d) bar = 50  $\mu$ m.

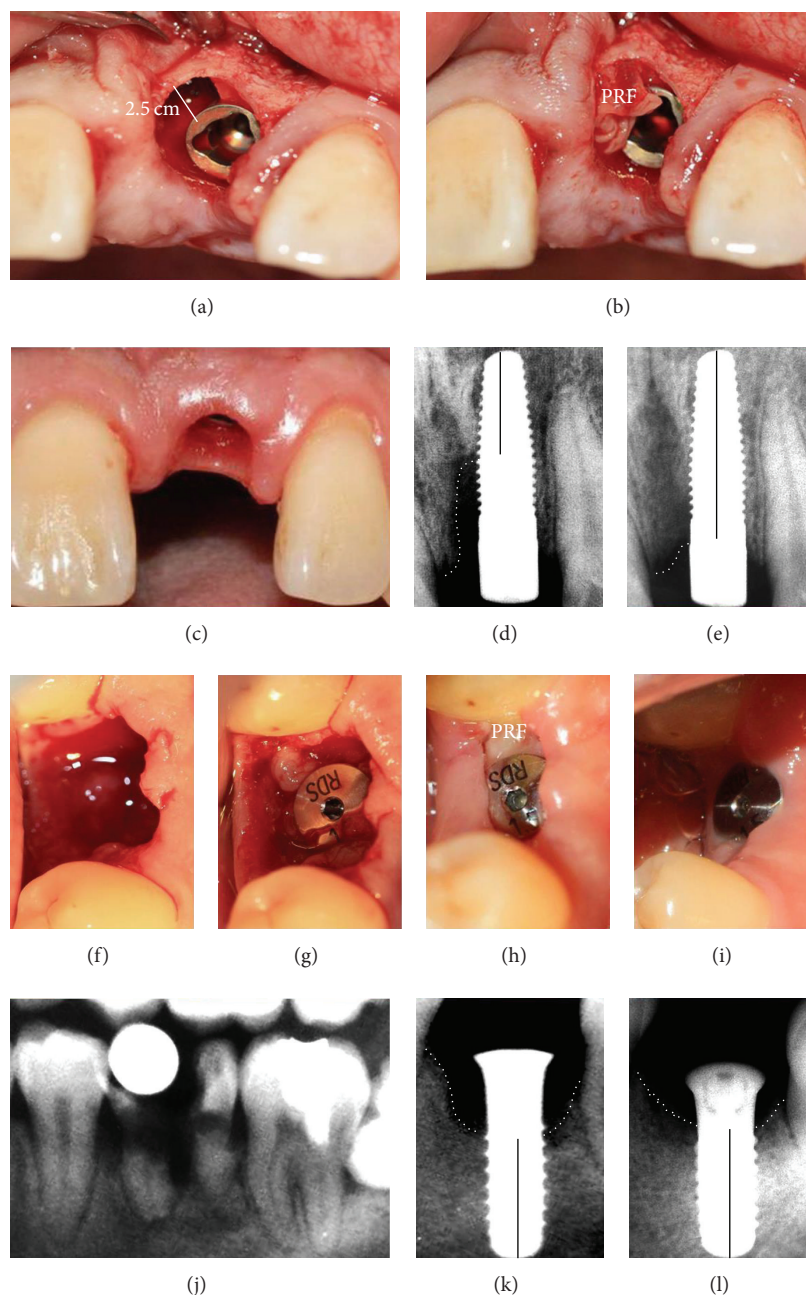


FIGURE 7: PRF application simultaneous with dental implant surgery. (a)–(e) Case I and (f)–(l) Case II, (a)–(c) and (f)–(i) are intraoral micrographs, and (d), (e), and (j)–(l) are X-rays. Case I: (a) reveals a 2.5 mm gap at the mesial aspect of the implant replacing the upper left incisor, (b) illustrates PRF placement in the gap between implant and adjacent alveolar bone, (c) demonstrates healing of the implant site and healthy gingiva three months after implant placement, (d) X-ray documenting gap between implant and alveolar bone immediately after implant placement (Case I), and (e) X-ray demonstrating new alveolar bone formation at the site of PRF application three months after implant placement (Case I). Case II: (f) extraction socket of a lower left molar immediately after tooth extraction, (g) implant placement and filling of bone-deficient peri-implant space with PRF, (h) healing of surgery site and PRF implant five days after surgery, (i) healthy soft tissue surrounding implant three months after implant placement, (j) X-ray of decayed lower left molar treated in Case II prior to extraction, (k) X-ray of implant taken immediately after surgery. (l) X-ray illustrating new alveolar bone formation three months after surgery. Note the disappearance of the bony defect between implant and adjacent sockets. The black bar drawn in the implant center on the radiographs ((d), (e), (k), and (l)) represents the distance from the foramen apical to the cervical-most margin of the surrounding alveolar bone.



there was a 5.4 mm alveolar bone gain (Figure 7(e) versus Figure 7(d)), while there was bone gain on both aspects of the molar implant amounting to approximately 4.9 mm (Figure 7(l) versus Figure 7(k)). Newly formed alveolar bone was radioopaque and contained trabeculae (Figures 7(e) and 7(l)).

#### 4. Discussion

In the present study, a series of experiments was conducted to determine the usefulness of PRF as a bioactive scaffold for periodontal tissue regeneration. In a first set of experiments, the effect of PRF on proliferation and migration of DF, PDL, and AB progenitors was investigated. DF, PDL, and AB progenitors were chosen as metabolically active periodontal progenitor populations [1]. In a second set of studies, the effect of PRF on periodontal progenitor mineralization was determined *in vitro*. In these experiments, classic osteoblast differentiation and mineralization markers such as alkaline phosphatase and alizarin red S as well as *RUNX2* expression were employed to gain detailed insight into the effect of PRF on mineralization behavior of periodontal progenitors. To ask whether the major PRF component fibrin was associated with the effect of PRF on periodontal progenitor mineralization, our alkaline phosphatase and alizarin red S assays were conducted on fibrin-coated dishes. Finally, subcutaneous implantation studies and human pilot studies were performed to determine the applicability of PRF as a scaffold for periodontal tissue regeneration. Together these studies demonstrated that the application of PRF in periodontal regeneration had two major benefits: (i) the promotion of soft tissue healing as explained by the effect of PRF on progenitor proliferation and migration and (ii) the induction of new alveolar bone formation as possibly facilitated by the fibrin-mediated effect of PRF on *RUNX2* expression, osteoblast differentiation, and matrix mineralization, and also by the alkaline phosphatase activity-stimulating effect of fibrin.

The PRF membranes used for the present study contained the entire PRF clot centrifuged from fresh blood, including fibrin, leukocytes, and platelets. By the very nature of this preparation, the PRF membranes used for the current study were three-component scaffolds that were not further biochemically dissected for individual components as the biological and therapeutic effects of the PRF scaffold have been reported to depend on the fresh preparation of an autologous blood fraction [4]. Moreover, the compound PRF membrane contains not only the structural scaffold components fibrin, leukocytes, and platelets, but also a multitude of growth factors such as TGF- $\beta$ 1, VEGF, IGFs, and PDGF-AB, as well as matricellular proteins such as thrombospondin-1 [26]. In the present study, the composition of the PRF membrane was kept as homogeneous as possible by maintaining strict and reproducible preparation conditions. We expect some limited variability among PRF samples due to differences between blood of individual host organisms, including humans. Nevertheless, our studies reported excellent reproducibility between individual PRF preparations from different donor individuals in terms of mineralization, proliferation, and migration effects, indicating that for the purpose of

the present study, our PRF membranes elicited highly repeatable biological effects.

Our data demonstrated that PRF significantly improved periodontal progenitor cell proliferation and migration *in vitro* when compared to PPP and DMEM media. The effect of PRF on cell proliferation is well established and has been described in a wide variety of cell types, including periodontal ligament cells, osteoblasts, gingival fibroblasts, oral epithelial cells, BMSCs, preadipocytes, and prekeratinocytes [9, 27]. PRF's role in the stimulation of cell proliferation may be due to a gradual release of growth factors [8], some of which might be released by platelets and others might have been trapped within the fibrin scaffold and gradually diffused into the culture medium. Even though both PRF and PPP media are blood plasma preparations, PRF had a significantly stronger effect on proliferation than PPP. We attribute this effect to different subsets of cytokines in PRF and PPP and to the controlled release of cytokines trapped in PRF fibrin meshes [28]. Interestingly, there was a stronger effect of PRF on AB and DF cells than on PDL progenitors, and the PRF-induced elevation of proliferation occurred earlier in AB progenitors than in the other two cell types investigated, suggesting that the effects of PRF are tissue specific and favor AB osteoblasts over the other two cell types studied here. While the PRF-induced enhancement of cell proliferation remained in the 30% range over PPP or DMEM controls, the effect of PRF on cell migration was much more pronounced, featuring a 2.5-fold elevation compared to PPP and an approximately 20-fold elevation when compared to DMEM. This dramatic PRF-induced increase in cell migration has not been reported previously and might be explained by chemokines released by leukocytes trapped in PRF [29] or by the effect of soluble fibrin components on cell migration [30].

From a clinical perspective, the reported effects of PRF on bone regeneration [31, 32] are of great interest for orthopedic applications because of the limitations of current strategies to enhance bone regeneration [33]. Moreover, alveolar ridge augmentation is of great benefit to implant dentistry because of the lack of supporting bone for implant placement [34]. Our *in vitro* studies indicated that PRF almost equaled osteogenic medium in its effect on mineralization behavior of cultured periodontal progenitors, surpassing DMEM and PPP by a significant margin. While the effect of PRF on osteoblast alkaline phosphatase levels [8] and on the formation of mineral nodules [35] has already been reported, we have demonstrated here that PRF significantly enhances the expression of the osteoblast differentiation transcription factor *RUNX2* and reduces expression of the mineralization inhibitor *MGP*, preferentially in alveolar bone osteoblast progenitors, and less so in dental follicle cells and periodontal ligament progenitors. We propose that this tissue-specific enhancement of osteoblast mineralization might be due to the enhanced alkaline phosphatase activity induced by the fibrin component of PRF (shown in the present study) and to the greater susceptibility of osteoblast cells to differentiate along osteogenic lineage pathways.

Both our *in vitro* and our clinical studies indicate that the benefit of PRF for bone regenerative procedures lies in its combined competency as a cell proliferation, migration, and

wound-healing agent together with its tissue-specific ability to promote osteoblast differentiation and new bone formation. Our clinical pilot experiments revealed peri-implant bone gain of approximately 5 mm in conjunction with soft tissue healing around the implant site—a highly desirable outcome, in which we attribute the combined biological effects of PRF on gingival fibroblast and periodontal ligament cell migration, as well as alveolar bone osteoblast proliferation and mineralization. Moreover, PRF is a biodegradable scaffold as our studies have demonstrated that PRF subcutaneous implants were readily replaced with dense collagen even after 2 weeks of implant placement in nude mice, suggesting excellent biodegradability. The combinatorial effects of PRF on soft tissue healing and bone regeneration may limit its use in regenerative medicine applications in which calcification is not a desired outcome; however, our studies indicate that PRF contains a number of attributes ideally suited for its use as a scaffold for alveolar ridge augmentation and bone healing.

## Conflict of Interests

The authors declare no conflict of interests.

## Acknowledgment

The authors gratefully acknowledge the Research Open Access Publishing (ROAAP) Fund of the University of Illinois at Chicago for financial support towards the open access publishing fee for this paper.

## References

- [1] S. J. Dangaria, Y. Ito, C. Walker, R. Druzinsky, X. Luan, and T. G. H. Diekwisch, "Extracellular matrix-mediated differentiation of periodontal progenitor cells," *Differentiation*, vol. 78, no. 2-3, pp. 79–90, 2009.
- [2] S. J. Dangaria, Y. Ito, X. Luan, and T. G. Diekwisch, "Successful periodontal ligament regeneration by periodontal progenitor preseeded on natural tooth root surfaces," *Stem Cells*, vol. 20, no. 10, pp. 1659–1668, 2011.
- [3] A. Hollander, P. Macchiarini, B. Gordijn, and M. Birchall, "The first stem cell-based tissue-engineered organ replacement: implications for regenerative medicine and society," *Regenerative Medicine*, vol. 4, no. 2, pp. 147–148, 2009.
- [4] J. Choukroun, F. Adda, C. Schoeffer, and A. Vervelle, "PRF: an opportunity in perio- implantology," *Implantodontie*, vol. 42, pp. 55–62, 2000.
- [5] D. M. Dohan, J. Choukroun, A. Diss et al., "Platelet-rich fibrin (PRF): a second-generation platelet concentrate. Part II: platelet-related biologic features," *Oral Surgery, Oral Medicine, Oral Pathology, Oral Radiology and Endodontology*, vol. 101, no. 3, pp. E45–E50, 2006.
- [6] W. Bensaïd, J. T. Triffitt, C. Blanchat, K. Oudina, L. Sedel, and H. Petite, "A biodegradable fibrin scaffold for mesenchymal stem cell transplantation," *Biomaterials*, vol. 24, no. 14, pp. 2497–2502, 2003.
- [7] Y. H. Kang, S. H. Jeon, J. Y. Park et al., "Platelet-rich fibrin is a bioscaffold and reservoir of growth factors for tissue regeneration," *Tissue Engineering A*, vol. 17, no. 3-4, pp. 349–359, 2011.
- [8] L. He, Y. Lin, X. Hu, Y. Zhang, and H. Wu, "A comparative study of platelet-rich fibrin (PRF) and platelet-rich plasma (PRP) on the effect of proliferation and differentiation of rat osteoblasts *in vitro*," *Oral Surgery, Oral Medicine, Oral Pathology, Oral Radiology and Endodontology*, vol. 108, no. 5, pp. 707–713, 2009.
- [9] D. M. D. Ehrenfest, A. Diss, G. Odin, P. Doglioli, M. P. Hippolyte, and J. B. Charrier, "In vitro effects of Choukroun's PRF (platelet-rich fibrin) on human gingival fibroblasts, dermal prekeratinocytes, preadipocytes, and maxillofacial osteoblasts in primary cultures," *Oral Surgery, Oral Medicine, Oral Pathology, Oral Radiology and Endodontology*, vol. 108, no. 3, pp. 341–352, 2009.
- [10] J. Choukroun, A. Diss, A. Simonpieri et al., "Platelet-rich fibrin (PRF): a second-generation platelet concentrate. Part IV: clinical effects on tissue healing," *Oral Surgery, Oral Medicine, Oral Pathology, Oral Radiology and Endodontology*, vol. 101, no. 3, pp. E56–E60, 2006.
- [11] M. T. Peck, J. Marnewick, and L. Stephen, "Alveolar ridge preservation using leukocyte and platelet-rich fibrin: a report of a case," *Case Reports in Dentistry*, vol. 2011, Article ID 345048, 5 pages, 2011.
- [12] A. Sharma and A. R. Pradeep, "Treatment of 3-wall intrabony defects in patients with chronic periodontitis with autologous platelet-rich fibrin: a randomized controlled clinical trial," *Journal of Periodontology*, vol. 82, no. 12, pp. 1705–1712, 2011.
- [13] M. Thorat, A. R. Pradeep, and B. Pallavi, "Clinical effect of autologous platelet-rich fibrin in the treatment of intrabony defects: a controlled clinical trial," *Journal of Clinical Periodontology*, vol. 38, no. 10, pp. 925–932, 2011.
- [14] F. Inchingolo, M. Tatullo, M. Marrelli et al., "Trial with platelet-rich fibrin and Bio-Oss used as grafting materials in the treatment of the severe maxillary bone atrophy: clinical and radiological evaluations," *European Review for Medical and Pharmacological Sciences*, vol. 14, no. 12, pp. 1075–1084, 2010.
- [15] Y. Zhang, S. Tangl, C. D. Huber, Y. Lin, L. Qiu, and X. Rausch-Fan, "Effects of Choukroun's platelet-rich fibrin on bone regeneration in combination with deproteinized bovine bone mineral in maxillary sinus augmentation: a histological and histomorphometric study," *Journal of Cranio-Maxillofacial Surgery*, vol. 40, no. 4, pp. 321–328, 2011.
- [16] C. H. Tsai, S. Y. Shen, J. H. Zhao, and Y. C. Chang, "Platelet-rich fibrin modulates cell proliferation of human periodontally related cells *in vitro*," *Journal of Dental Sciences*, vol. 4, no. 3, pp. 130–135, 2009.
- [17] Y. C. Chang and J. H. Zhao, "Effects of platelet-rich fibrin on human periodontal ligament fibroblasts and application for periodontal infra-bony defects," *Australian Dental Journal*, vol. 56, no. 4, pp. 365–371, 2011.
- [18] D. M. Dohan, J. Choukroun, A. Diss et al., "Platelet-rich fibrin (PRF): a second-generation platelet concentrate. Part I: technological concepts and evolution," *Oral Surgery, Oral Medicine, Oral Pathology, Oral Radiology and Endodontology*, vol. 101, no. 3, pp. E37–E44, 2006.
- [19] K. J. Livak and T. D. Schmittgen, "Analysis of relative gene expression data using real-time quantitative PCR and the  $2^{-\Delta\Delta C_T}$  method," *Methods*, vol. 25, no. 4, pp. 402–408, 2001.
- [20] E. Sachlos and J. T. Czernuszka, "Making tissue engineering scaffolds work. Review: the application of solid freeform fabrication technology to the production of tissue engineering scaffolds," *European Cells & Materials Journal*, vol. 5, pp. 29–39, 2003.



- [21] X. Luan, Y. Ito, S. Dangaria, and T. G. H. Diekwisch, "Dental follicle progenitor cell heterogeneity in the developing mouse periodontium," *Stem Cells and Development*, vol. 15, no. 4, pp. 595–608, 2006.
- [22] S. Tsuchiya, S. Ohshima, Y. Yamakoshi, J. P. Simmer, and M. J. Honda, "Osteogenic differentiation capacity of porcine dental follicle progenitor cells," *Connective Tissue Research*, vol. 51, no. 3, pp. 197–207, 2010.
- [23] J. M. Karp, F. Sarraf, M. S. Shoichet, and J. E. Davies, "Fibrin-filled scaffolds for bone-tissue engineering: an in vivo study," *Journal of Biomedical Materials Research A*, vol. 71, no. 1, pp. 162–171, 2004.
- [24] R. T. Franceschi and G. Xiao, "Regulation of the osteoblast-specific transcription factor, *Runx2*: responsiveness to multiple signal transduction pathways," *Journal of Cellular Biochemistry*, vol. 88, no. 3, pp. 446–454, 2003.
- [25] B. Newman, L. I. Gigout, L. Sudre, M. E. Grant, and G. A. Wallis, "Coordinated expression of matrix Gla protein is required during endochondral ossification for chondrocyte survival," *Journal of Cell Biology*, vol. 154, no. 3, pp. 659–666, 2001.
- [26] D. M. D. Ehrenfest, G. M. de Peppo, P. Doglioli, and G. Sammartino, "Slow release of growth factors and thrombospondin-1 in Choukroun's platelet-rich fibrin (PRF): a gold standard to achieve for all surgical platelet concentrates technologies," *Growth Factors*, vol. 27, no. 1, pp. 63–69, 2009.
- [27] Q. Li, Y. Geng, L. Lu, T. Yang, M. Zhang, and Y. Zhou, "Platelet-rich fibrin-induced bone marrow mesenchymal stem cell differentiation into osteoblast-like cells and neural cells," *Neural Regeneration Research*, vol. 6, no. 31, pp. 2419–2423, 2011.
- [28] F. Clipet, S. Tricot, N. Alno et al., "In vitro effects of Choukroun's platelet-rich fibrin conditioned medium on 3 different cell lines implicated in dental implantology," *Implant Dentistry*, vol. 21, no. 1, pp. 51–56, 2012.
- [29] D. M. Dohan, J. Choukroun, A. Diss et al., "Platelet-rich fibrin (PRF): a second-generation platelet concentrate. Part III: leucocyte activation: a new feature for platelet concentrates?" *Oral Surgery, Oral Medicine, Oral Pathology, Oral Radiology and Endodontology*, vol. 101, no. 3, pp. E51–E55, 2006.
- [30] R. A. F. Clark, J. M. Lanigan, and P. DellaPelle, "Fibronectin and fibrin provide a provisional matrix for epidermal cell migration during wound reepithelialization," *Journal of Investigative Dermatology*, vol. 79, no. 5, pp. 264–269, 1982.
- [31] J. Choukroun, A. Diss, A. Simonpieri et al., "Platelet-rich fibrin (PRF): a second-generation platelet concentrate. Part V: histologic evaluations of PRF effects on bone allograft maturation in sinus lift," *Oral Surgery, Oral Medicine, Oral Pathology, Oral Radiology and Endodontology*, vol. 101, no. 3, pp. 299–303, 2006.
- [32] A. Simonpieri, J. Choukroun, M. D. Corso, G. Sammartino, and D. M. D. Ehrenfest, "Simultaneous sinus-lift and implantation using microthreaded implants and leukocyte- and platelet-rich fibrin as sole grafting material: a six-year experience," *Implant Dentistry*, vol. 20, no. 1, pp. 2–12, 2011.
- [33] R. Dimitriou, E. Jones, D. McGonagle, and P. V. Giannoudis, "Bone regeneration: current concepts and future directions," *BMC Medicine*, vol. 3, no. 9, p. 66, 2011.
- [34] F. Carinci, A. Farina, U. Zanetti et al., "Alveolar ridge augmentation: a comparative longitudinal study between calvaria and iliac crest bone grafts," *The Journal of oral implantology*, vol. 31, no. 1, pp. 39–45, 2005.
- [35] D. M. D. Ehrenfest, P. Doglioli, G. M. de Peppo, M. Del Corso, and J. B. Charrier, "Choukroun's platelet-rich fibrin (PRF) stimulates *in vitro* proliferation and differentiation of human oral bone mesenchymal stem cell in a dose-dependent way," *Archives of Oral Biology*, vol. 55, no. 3, pp. 185–194, 2010.

## Research Article

# Heparanase Localization during Palatogenesis in Mice

**Azumi Hirata,<sup>1</sup> Kentaro Katayama,<sup>2</sup> Takehito Tsuji,<sup>3</sup> Nagato Natsume,<sup>4</sup> Toshio Sugahara,<sup>4</sup> Yuichi Koga,<sup>5</sup> Kazufumi Takano,<sup>6</sup> Yoshinori Otsuki,<sup>1</sup> and Hiroaki Nakamura<sup>7</sup>**

<sup>1</sup> Department of Anatomy and Cell Biology, Faculty of Medicine, Osaka Medical College, Takatsuki 569-8686, Japan

<sup>2</sup> Laboratory of Veterinary Physiology, Nippon Veterinary and Life Science University, Musashino 180-8602, Japan

<sup>3</sup> Graduate School of Environmental and Life Science, Okayama University, Okayama 700-8530, Japan

<sup>4</sup> Division of Research and Treatment for Oral and Maxillofacial Congenital Anomalies, School of Dentistry, Aichi Gakuin University, Nagoya 464-0821, Japan

<sup>5</sup> Departments of Material and Life Science, Graduate School of Engineering, Osaka University, Suita 565-0871, Japan

<sup>6</sup> Laboratory of Biological Chemistry, Department of Biomolecular Chemistry, Kyoto Prefectural University, Kyoto 606-8522, Japan

<sup>7</sup> Department of Oral Histology, Matsumoto Dental University, Shiojiri 399-0781, Japan

Correspondence should be addressed to Azumi Hirata; [an1026@art.osaka-med.ac.jp](mailto:an1026@art.osaka-med.ac.jp)

Received 14 November 2012; Accepted 1 January 2013

Academic Editor: Erica L. Scheller

Copyright © 2013 Azumi Hirata et al. This is an open access article distributed under the Creative Commons Attribution License, which permits unrestricted use, distribution, and reproduction in any medium, provided the original work is properly cited.

Palatogenesis is directed by epithelial-mesenchymal interactions and results partly from remodeling of the extracellular matrix (ECM) of the palatal shelves. Here, we assessed heparanase distribution in developing mouse palates. No heparanase was observed in the vertically oriented palatal shelves in early stages of palate formation. As palate formation progressed, the palatal shelves were reorganized and arranged horizontally above the tongue, and heparanase localized to the epithelial cells of these shelves. When the palatal bilateral shelves first made contact, the heparanase localized to epithelial cells at the tips of shelves. Later in fusing palatal shelves, the cells of the medial epithelial seam (MES) were labeled with intense heparanase signal. In contrast, the basement membrane heparan sulfate (HS) was scarcely observed in the palatal shelves in contact. Moreover, perlecan labeling was sparse in the basement membrane of the MES, on which laminin and type IV collagen were observed. Moreover, we assessed the distribution of matrix metalloproteinase- (MMP-) 9, MMP-2, and MMP-3 in developing mouse palates and these MMPs were observed in the MES. Our findings indicated that heparanase was important for palate formation because it mediated degradation of the ECM of palatal shelves. Heparanase may, in concert with other proteases, participate in the regression of the MES.

## 1. Introduction

Development of the mammalian secondary palate is a dramatic event that depends on multiple steps and a network of several factors. Palate formation starts with the appearance of two palatal shelves that protrude from the lateral walls of oronasal cavity. Both palatal shelves grow downward vertically along the side of the tongue. Subsequently, the palatal shelves are raised above the tongue, which moves downward as the mandible elongates. The bilateral palatal shelves grow towards each other until they make contact and adhere at the midline along the medial edge epithelium (MEE). Finally, the epithelium disappears from the shelves, thus allowing for complete palatal fusion [1].

The processes of the morphological changes and the accompanying histological changes in the palate are directed by epithelial-mesenchymal interactions [1]. They result partly from remodeling of the extracellular matrix (ECM) of the palatal shelves. Components of the ECM such as hyaluronan and fibronectin are expressed in the mesenchyme of the palatal shelves [2] and may contribute to the elevation of the palatal shelves [3]. After adhesion of the bilateral palatal shelves in the midline, formation and subsequent disappearance of the medial epithelial seam (MES) are essential for complete palatal fusion. Changes in the distribution of ECM components within the basement membrane of the MES (e.g., type IV collagen, laminin, and perlecan) during palate formation have been examined [4, 5]. However, the fate of the cells of the MES is controversial [2, 6].

Moreover, palatogenesis requires proteolytic degradation of the ECM, and some proteases, such as matrix metalloproteinases (MMPs), are responsible for remodeling of the ECM during palatal fusion [7]. MMPs mediate changes in the basement membrane (BM) components of the MES [8]. Heparanase, an endoglucuronidase, cleaves HS chain in perlecan [9–11], and heparanase releases ECM resident, HS-bound polypeptides, and then converts them to bioactive molecules. Heparan sulfate proteoglycan (HSPG) binds many ECM molecules, growth factors, and cell surface receptors via HS chains, and HSPG has multiple developmental and physiological functions [12]. Afterwards, heparanase homolog, termed heparanase 2 (Hpa2), was cloned [13]. It encodes three proteins generated by alternative splicing (Hpa2a, Hpa2b, Hpa2c) and shares an overall identity of ~40% with heparanase. Hpa2 tends to show tissue-specific patterns of expression. Additionally, Hpa2 exhibits no enzymatic activity typical of heparanase and Hpa2c protein inhibits heparanase enzymatic activity [14]. We have previously reported that heparanase, not Hpa2, secreted by the cells of Hertwig's epithelial root sheath may contribute to formation of tooth roots by degrading the dental basement membrane [15]. However, the role of heparanase during formation of the palate has not yet been reported. Mechanisms leading to the disappearance of the cells of the MES are controversial [2, 6]. The aim of the present study was to use immunohistochemistry (IHC) to determine heparanase localization in the developing murine palatal shelves to assess whether heparanase might be involved in palate formation. Moreover, we used IHC to assess the distribution of ECM components and MMPs in fusing palatal shelves to determine whether expression of these proteins correlated with the disappearance of the MES cells during palatogenesis.

## 2. Materials and Methods

All animal experiments were conducted in accordance with the Guidelines for Animal Experiments, Okayama University, Okayama, Japan.

**2.1. Tissue Preparation for Histology.** C57BL/6By mice were used in the present study. Pregnant females ( $n = 9$ ) that had mated with males were euthanized with CO<sub>2</sub> such that six embryos each could be harvested at different developmental stages, that is, embryonic day 13.5 (E13.5), E14.5, and E15.5. Twenty-seven embryos along with three newborn mice (P0) were immersed in 4% paraformaldehyde and 0.1% glutaraldehyde in 0.05 M phosphate buffer (pH 7.4) for heparanase, heparan sulfate, MMP-2, MMP-3, and MMP-9 IHC. The remnants of embryos and three newborn mice were immersed in an acid-alcohol fixative comprising 96% ethanol, 1% acetic acid, and 3% distilled water for perlecan, laminin, and type IV collagen IHC [15]. Heads were dissected, immersed in the same fixative for 20 h at 4°C, and decalcified in 5% EDTA, pH 7.4, for 2 days at 4°C.

For light or immunofluorescent microscopy, specimens were dehydrated in a graded ethanol series and embedded in paraffin. Sections (4 µm thick) were prepared and dewaxed with xylene and graded ethanol.

**2.2. Heparanase, Heparan Sulfate, and MMPs IHC.** Serial sections were transferred to 5 mM periodic acid for 10 min to block endogenous peroxidase and then immersed in PBS containing 10% BSA for 30 min. For heparanase IHC, sections were washed in PBS and then incubated with an antiheparanase polyclonal antibody (3 µg/mL) [15] for 12 h at 4°C. The heparanase rabbit polyclonal antibody was generated using a cysteine-conjugated peptide corresponding to residues 28–45 (DDVVDFYTKRPLRSVS) of mouse heparanase (GenBank accession no. AY077467) [15, 16]. This antibody specifically reacts with an active form of mouse heparanase, not Hpa2 [15]. Sections were then incubated with a secondary antibody (ChemMate ENVISION; Dako Cytomation, Glostrup, Denmark) for 1 h at RT. For heparan sulfate IHC, sections were washed in PBS and then incubated with an anti-heparan sulfate (NAH46 epitope) monoclonal antibody (Seikagaku Biobusiness Co., Ltd.; Tokyo, Japan) diluted 1:1000 for 12 h at 4°C. They were reacted with Histofine MOUSESTAIN KIT (Nichirei Biosciences, Inc.; Tokyo, Japan) for 1 h at RT. For MMPs IHC, sections subsequently incubated with an anti-MMP-2 polyclonal antibody diluted 1:100 (MILLIPORE, Temecula, CA, USA) or an anti-MMP-3 polyclonal antibody diluted 1:100 (MILLIPORE) or an anti-MMP-9 polyclonal antibody diluted 1:100 (MILLIPORE) for 12 h at 4°C. Sections were then incubated with ChemMate ENVISION (Dako Cytomation) for 1 h at RT. Control sections were incubated with rabbit IgG preimmune serum, then incubated with a secondary antibody (ChemMate ENVISION or HISTOFINE) for 12 h at 4°C. Immunoreactivity was visualized using diaminobenzidine (DAB) (DAKO, Carpinteria, CA, USA). Sections were then counterstained with hematoxylin and examined under an All-in-one Type Fluorescence Microscope (BZ-9000; Keyence, Osaka, Japan) using BZ Analyzer software (BZ-9000; Keyence). These immunohistochemical staining procedures were performed in 120 serial sections from each mouse.

**2.3. Localization of Perlecan, Laminin, and Type IV Collagen.** Serial sections were transferred to 5 mM periodic acid for 10 min at room temperature (RT) to block endogenous peroxidase and were then immersed in PBS containing 10% BSA for 30 min. For double staining of perlecan and laminin, sections were treated with 15,000 U/mL of hyaluronidase (Sigma, St. Louis, MO, USA) in PBS for 30 min at 37°C. Sections were washed with PBS and then incubated with an anti-perlecan (clone A7L6) monoclonal antibody (MILLIPORE) diluted 1:200 and an anti-laminin polyclonal antibody (Sigma) diluted 1:100 for 12 h at 4°C. Clone A7L6 recognizes domain IV of the core protein of perlecan. Anti-laminin antibody was developed in rabbit using laminin purified from the basement membrane of Englebreth Holm-Swarm (EHS) mouse sarcoma as the immunogen. For double staining of perlecan and type IV collagen, sections were treated with 15,000 U/mL of hyaluronidase (Sigma) in PBS for 30 min at 37°C and 0.1% pepsin in 0.01 N HCl for 15 min at RT. Sections were washed in PBS and then incubated with an anti-perlecan monoclonal antibody diluted 1:200 (MILLIPORE) and an anti-type IV collagen polyclonal antibody (PROGEN



Biotechnik; Heidelberg, Germany) diluted 1:100 for 12 h at 4°C. For immunofluorescence, sections were incubated with Alexa Fluor-488 goat anti-rat IgG (Molecular Probes, Eugene, OR) diluted 1:200 and Alexa Fluor-594 goat anti-rabbit IgG (Molecular Probes) diluted 1:200 for 1 h at RT. Sections were then observed under a microscope (Keyence). These immunohistochemical staining procedures were performed in 60 serial sections from each mouse.

### 3. Results

**3.1. Localization of Heparanase and Heparan Sulfate.** At E13.5, the palatal shelves were positioned bilaterally along the sides of the tongue and elongated vertically and perpendicular to the tongue (Figure 1(a)). Heparanase signal was not observed in the palatal shelves at E13.5. Some epithelial cells and underlying mesenchymal cells facing the palatal shelves at the bottom of the tongue showed weak labeling (Figure 1(b)). By E14.5, the shelves had reoriented such that they had elongated horizontally above and parallel with the surface of the tongue. Intense heparanase immunoreactivity was evident in the cytoplasm of epithelial cells of the palatal shelves. Heparanase was also expressed at the mesenchyme (as shown by arrows) (Figures 1(c) and 1(d)). At E15.5, the bilateral palatal shelves had connected, and the MES was observed at the midline (Figure 1(e)). Cells of the epithelial triangle, the MES, and epithelial island had strong heparanase labeling (Figure 1(f)). As palatogenesis was complete, heparanase localization was evident in the basal cells of oral and nasal epithelium of the palate at P0 (Figures 1(g) and 1(h)). Osteoblasts on the palatal and maxillary bone surface also had heparanase reactivity (Figures 1(g) and 1(h)). Additionally, some epithelial cells located near the tip of the shelves that had made contact above the tongue had heparanase immunoreactivity (Figures 2(a) and 2(b)). In contrast, HS-labeling was faint in the basement membrane located nearby the tip of shelves (Figure 2(c)).

No specific immunoreactivity was observed in control sections (see Figure S1 in Supplementary Material available online at <http://dx.doi.org/10.1155/2013/760236>).

**3.2. Distribution of Perlecan, Laminin, and Type IV Collagen in the MES.** The MES was first observed at the midline of the connected palate at E15.5 (Figure 3(a)). ECM components were evident in the palate. Perlecan was diffusely distributed in stroma; moreover, perlecan, laminin, and type IV collagen were evident in the basement membrane of blood vessels (Figures 3(a), 3(b), 3(d), and 3(e)). Furthermore, perlecan labeling was largely absent on the basement membrane of the MES, which was labeled with laminin signal (Figures 3(a)–3(c)), or perlecan labeling on the basement membrane of the MES was partially absent, although type IV collagen labeling was visible (Figures 3(d)–3(f)).

No specific immunoreactivity was detected in the control sections (data not shown).

**3.3. Localization of MMP-9, MMP-2, and MMP-3 in the MES.** Immunolocalizations of MMP-9, MMP-2, and MMP-3 in the MES at E15.5 are shown in Figure 4. MMP-9, MMP-2, and

MMP-3 were evident in the MES. Intense MMP-9 signal was observed around the cells of the MES that corresponded to the basement membrane; moderate MMP-2 signal and strong MMP-3 signal were evident in the cells of the MES. MMP-2 and MMP-3 signal were evident in the mesenchyme of the palate.

No specific immunoreactivity was observed in the control sections incubated without any primary antibody (Supplemental data).

### 4. Discussion

Here, we assessed the distribution of heparanase during palate formation in mice. In the initial stage of palate formation, heparanase signal was not evident in the palatal shelves. As palate formation progressed to elevation, heparanase signal was evident in the epithelial cells of palatal shelves. Heparanase signal was evident in some nasal epithelium cells of palate as these shelves made contact. At this same stage, the basement membrane HS was faint and largely absent from the epithelial cells near the tip of shelves. After bilateral palatal shelves connected, heparanase signal in cells of the MES was very strong. These results suggest that epithelial cells of the palatal shelves mediated the degradation of basement membrane by secreting heparanase during palate formation. These data also suggest that heparanase activity and the disappearance of basement membrane may have been spatially and temporally coordinated. Heparanase secreted by the palatal epithelial cells may participate in the formation of the palate, particularly in the fusion of palatal shelves via the degradation of palate basement membrane. Heparanase might also be required for the cleavage of HS on the epithelial plasma membrane during palate connection.

Moreover, heparanase labeling was evident in osteoblasts that faced the surface of the palatal bone and the maxillary bone. Increases in HS signal were evident in the bone matrix as palate formation progressed (data not shown). The presence of HS in bone and its association with skeletal physiologic and pathologic processes are well established [17–19]; osteoblasts and osteoclast lineage cells synthesize HSPG and this HSPG localized on their plasma membrane is involved in the binding of cell-cell interaction between osteoblasts and osteoclast lineage cells. Moreover, HSPG in bone matrix is involved in cell-matrix attachment and is also a reservoir of bioactive molecules and concerned with bone metabolism [20, 21]. Additionally, heparanase expression in osteoblasts and its biological function in osteogenesis have been documented [22–24]. Our data also provided evidence that heparanase localized in osteoblasts. Perlecan expression is associated with increased lacunocanalicular space in cortical bone [25]. This data is consistent with an inhibitory role for perlecan heparan sulfate chains in biomineralization and with the current study which shows that heparanase signal is associated with increased osteogenesis [25]. Heparanase may have an important role during the process of bone formation in palatogenesis.

Furthermore, heparanase expression is not restricted to pathological conditions and the activity has been found in hair follicle [26, 27] and in the skin [28]. Heparanase was

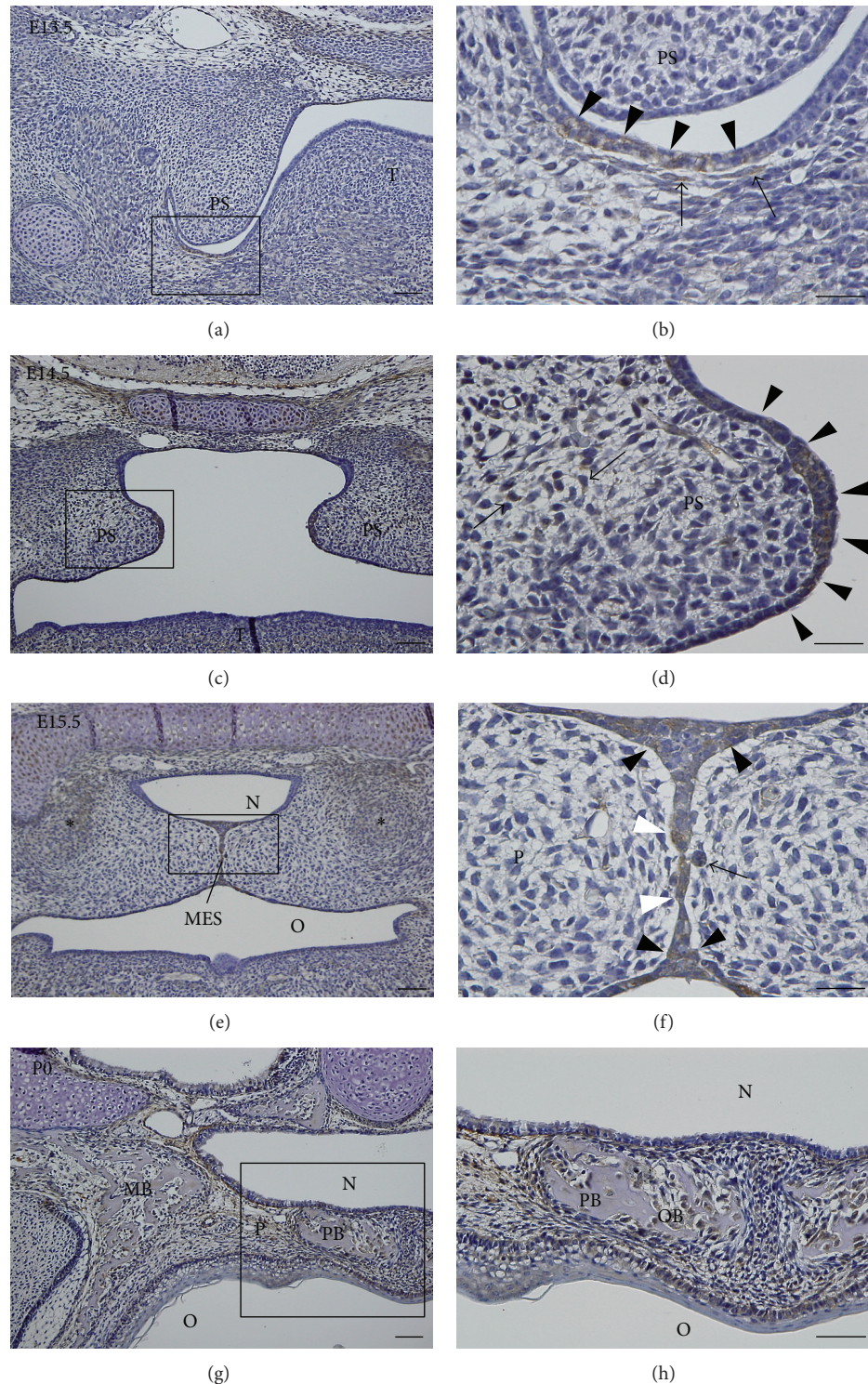
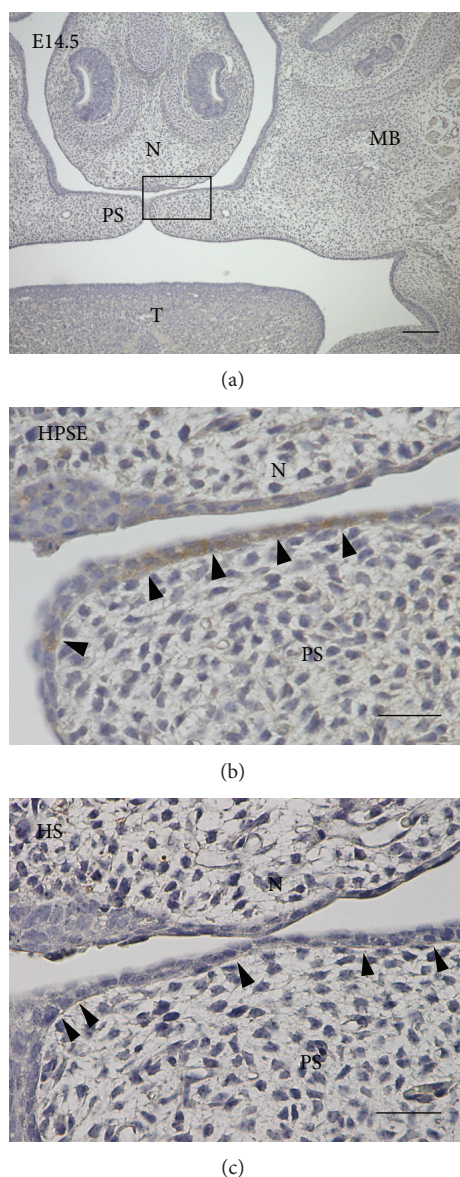


FIGURE 1: Light micrographs showing the localization of heparanase during palate formation. (a) Palatal shelf of a mouse embryo at E13.5. Heparanase signal was not evident in the palatal shelf. (b) Higher magnification of square marked in (a). Some epithelial cells and mesenchymal cells facing the palatal shelf at the bottom of the tongue had weak heparanase labeling (arrows and arrowheads). (c) Palatal shelves of a mouse at E14.5. The epithelial cells of palatal shelves had heparanase labeling. (d) Higher magnification of the square marked in (c). Intense reactivity was evident in the cytoplasm of the epithelial cells (arrowheads). Some stromal cells also had heparanase reactivity (arrows). (e) Palate of a mouse embryo at E15.5. The MES was observed in the middle of palate. Epithelial cells of palate and mesenchymal cells located at the ossification center (\*) had heparanase reactivity. (f) Higher magnification of the square marked in (e). The cells of the MES (white arrowheads), epithelial triangle (arrowheads), and epithelial island (arrow) show heparanase reactivity. (g) Palate of a mouse at P0. The palatal and maxillary bone was observed. (h) Higher magnification of the square marked in (g). Heparanase localization was evident in osteoblasts on the palatal bone surface. Strong reactivity of heparanase was evident in the basal cells of oral and nasal epithelium of the palate. Some stromal cells also had heparanase reactivity. PS, palatal shelf; P, palate; T, tongue; MES, medial epithelial seam; PB, palatal bone; MB, maxillary bone; OB, osteoblasts; O, oropharynx; N, nasopharynx. Bars: (a, c, e, g, and h), 50  $\mu$ m; (b, d, f), 25  $\mu$ m.





**FIGURE 2:** Light micrographs showing the localization of heparanase and heparan sulfate in palatal shelves of a mouse embryo at E14.5. (a) The palatal shelves were horizontal in apposition. (b) A higher magnification of the square marked in (a). Some epithelial cells at the tip of palatal shelves had heparanase labeling (arrowheads). Adjacent section to the section shown in (c). (c) HS labeling was diffuse and weak in the basement membrane at the tip of palate epithelium (arrowheads). Adjacent section to the section shown in (b). PS, palatal shelf; T, tongue; MB, maxillary bone; N, nasal septum. Bars: a, 100  $\mu\text{m}$ ; b, c, 25  $\mu\text{m}$ .

detected in the outer root sheath of murine hair follicle [26], while it mainly expressed in the inner root sheath of human hair follicle [27], suggesting, despite of differential expression between the species, that heparanase may be a key factor in differentiation of a follicular stem cell and hair homeostasis. In human epidermis, heparanase expression has been reported to be closely related to keratinocyte differentiation and was mainly found in the stratum granulosum

[28]. As HSPG was supposed to modulate proliferation and differentiation by its ability to affect growth factor signaling and binding, heparanase could play an important role in keratinocyte differentiation by acting on heparan sulfate. The inner root sheath of hair follicle is also keratinized and its keratinocytes terminal differentiation process could share some traits with epidermal terminal differentiation process [26–28]. In our study, heparanase localization was observed in the basal cells of the oral and nasal epithelium at P0; these findings indicated that heparanase could have contributed to regeneration of and cell renewal in the epithelium. In addition, some epithelial cells and underlying mesenchymal cells facing the palatal shelves at the bottom of tongue at E13.5 and the palatal mesenchyme at E14.5 showed heparanase reactivity, suggesting that heparanase could be involved in the generation of these cells, similar to in the hair cycle and in epidermal physiology. One might speculate that heparanase activity might play important role in the migration and remodeling of the palatal mesenchyme during palate formation.

The appearance of heparanase labeling in the cytoplasm seemed to coincide with lysosomal localization of the enzyme. Our results are also consistent with previous findings that heparanase localized to lysosomes in fibroblasts, osteoblasts, osteo (chondro) clasts, and tumor cells [22, 23, 29, 30]. Specific localization of the latent and active heparanase forms has been detected to perinuclear vesicles, suggesting that heparanase processing and activation occurs in lysosomes [29, 30]. In other cases, heparanase appeared less localized and more diffusely distributed in the cytoplasm, suggesting that under different biological situations, heparanase may be localized in different cellular compartments and hence may exert diverse functions [29]. The determination of its exact role requires further investigation, including electron microscopy studies to examine its exact location.

Heparanase, an endo- $\beta$ -D-glucuronidase expressed in a variety of tissues and cells during normal development and in pathological conditions, can selectively cleave perlecan and syndecan, and this enzyme releases complexes of HS fragments that are bound to the core protein [31]. These released HS complexes, such as growth factors, promote cell growth and migration [32]. Moreover, recent studies indicate that HSPG-growth factor complexes become available in bioactive form for binding to the cognate receptors to promote growth factor-mediated signaling [33–35]. Therefore, it is possible that heparanase-labeled cells contribute to degradation of HS chains present in the palate basement membrane and that release of growth factors might accelerate the proliferation and differentiation of mesenchymal cells of the palatal shelves. In addition to heparanase localization, cells of the MES had MMP-9, MMP-2, and MMP-3 reactivity. However, there were some differences in the distributions of these proteins. For example, MMP-9 was apparently co-localized with the basement membrane, and moderate MMP-2 and intense MMP-3 labeling were seen in the MES cells. Additionally, these MMPs were evident in mesenchyme around the MES. MMPs are involved in the degradation of ECM during normal physiological processes, such as embryonic development, reproduction, and tissue remodeling; MMPs



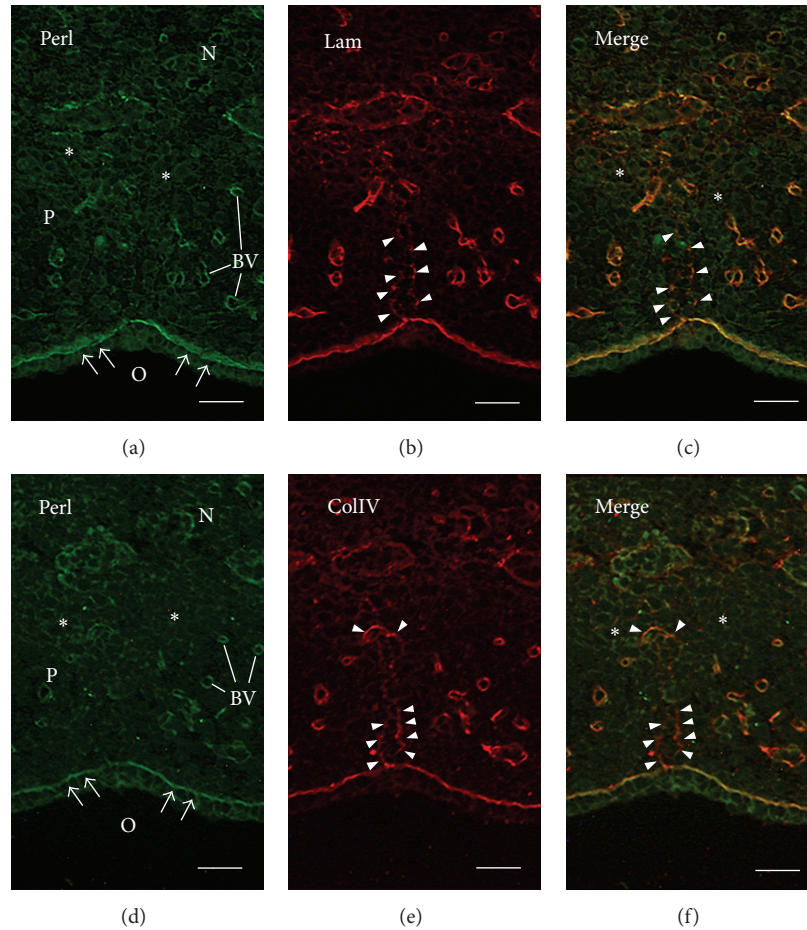


FIGURE 3: Micrographs of double-immunofluorescence staining reveal the localization of perlecan and laminin ((a)–(c)) or type IV collagen ((d)–(f)) in palate of a mouse embryo at E15.5. ((a), (d)) Perlecan reactivity was evident in the basement membrane of oral palate epithelium (arrows), blood vessels, and some stroma (\*) in palate. ((b), (e)) Weak or discontinuous laminin (b) or type IV collagen (e) immunoreactivity was evident in the basement membrane of the MES (arrowheads). ((c), (f)) Colocalization of perlecan and laminin (c) or type IV collagen (f) was observed in the basement membrane of oral epithelium and blood vessels. Some parts of the basement membrane of the MES had only laminin (c) or type IV collagen (f) reactivity (arrowheads). Adjacent sections. P, palate; O, oropharynx; N, nasal septum; BV, blood vessels; MES, medial epithelial seam. Bars: 25  $\mu$ m.

also degrade the ECM during disease processes [36]. The localization of heparanase and MMPs in this study suggests that they have the ability to participate in ECM remodeling during palate growth and formation. MMP-9, MMP-2, and MMP-3 may be involved in the degradation of basement membrane proteins, including type IV collagen, laminin, and perlecan. In our perlecan double-labeling experiments, the basement membrane of the MES had faint perlecan labeling even though laminin was present. In addition, the basement membrane of the MES contained type IV collagen though perlecan was absent; however, we were unable to detect any differences between heparan sulfate and perlecan localization in the basement membrane of the MES. Based on these results, it is conceivable that the degradation of components of the palatal basement membrane may occur in a regulated sequence. Thus, given the localization of heparanase, we propose that the degradation of the MES basement membrane results from the coordinated activity

of several proteolytic enzymes. This is supported by a previous study demonstrating that heparanase knockout mice developed normally, were fertile, and exhibit no apparent anatomical or functional abnormalities despite the complete lack of heparanase gene expression and enzymatic activity [37]. Heparanase deficiency was compensated by a tissue-specific marked elevation of MMP family members such as MMP-2, MMP-9, and MMP-14 [37]. These findings provided the evidence for cooperation between heparanase and MMPs in spite of their different enzymatic substrate and suggested that a combined interdependent control mechanism between heparanase and MMPs regulates the ECM degrading enzyme in cells and tissues.

Three processes—programmed cell death [38, 39], cell migration to the oral and nasal side of the palate [40], and epithelial-mesenchymal transdifferentiation (EMT) [41]—have been proposed as the mechanisms involved in the disappearance of the MES. Here, nucleus condensation, a change

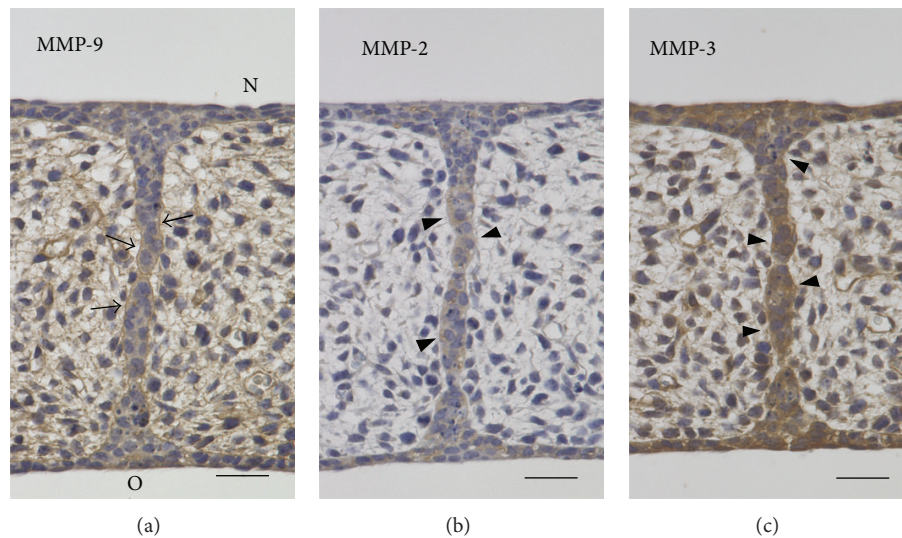


FIGURE 4: Light micrographs showing the localization of MMP-9 (a), MMP-2 (b), and MMP-3 (c) in the MES of palate of a mouse embryo at E15.5. (a) MMP-9 reactivity was observed throughout the basement membrane of the MES (arrows). Stroma cells had diffuse MMP-9 labeling. (b) Moderate MMP-2 reactivity was seen in cells of the MES (arrowheads). Stroma cells had weak labeling. (c) Strong labeling of MMP-3 was seen in cells of the MES (arrowheads) and stroma cells. P, palate; O, oropharynx; N, nasopharynx. Bars: 25  $\mu$ m.

characteristic of programmed cell death, was evident during histological examination in some MES cells. Additionally, MMP-3, which is known to induce EMT in mammary epithelial cells [42], localized in the MES cells, confirming the possibility that EMT occurred in the MES cells [42]. However, based on our data, we could not determine whether the MES cells underwent, separately or concurrently, any of these three processes. Further studies are required to understand the precise mechanism by which the MES cells vanish from palate.

## 5. Conclusions

In conclusion, we provided evidence that heparanase localized in the palate epithelial cells, the MES cells, and osteoblasts during palate formation, whereas signal from the components of the basement membrane was faint and weak in the palatal shelves. We also observed MMP-9, MMP-2, and MMP-3 signals in the MES, while perlecan, laminin, and collagen type IV signals disappeared from the basement membrane of the MES. Hence, the distribution heparanase and MMPs were consistent with the hypothesis that these proteins had a role in palate ECM remodeling; additionally, these findings suggest that heparanase, in cooperation with other proteases, contributed to palate development. Our results also indicated that further analysis of heparanase might shed light on the fate of the MES in palatogenesis.

## Acknowledgments

This work was supported in part by Grants-in-Aid for Scientific Research (nos. 21592571, 22592269, 24592996) from the Japan Society for the Promotion of Science. The authors would like to thank Professor Takaaki Ueno, Department of

Oral Surgery, Osaka Medical College; Dr. Tomohiro Yamada, Department of Oral and Maxillofacial Surgery, Kochi Medical School, Kochi University; Dr. Katsuaki Mishima, Department of Oral and Maxillofacial Surgery, Graduate School of Medicine, Yamaguchi University; and Dr. Hideto Imura, Division of Research and Treatment for Oral and Maxillofacial Congenital Anomalies, School of Dentistry, Aichi Gakuin University; for their valuable advice. The authors would like to send special thanks to Professor Norikazu Ohno, Department of Oral Anatomy, School of Dentistry, Aichi Gakuin University, for his kind support.

## References

- [1] M. W. Ferguson, "Palate development," *Development*, vol. 103, supplement, pp. 41S–60S, 1988.
- [2] L. Meng, Z. Bian, R. Torensma, and J. W. Von Den Hoff, "Biological mechanisms in palatogenesis and cleft palate," *Journal of Dental Research*, vol. 88, no. 1, pp. 22–33, 2009.
- [3] J. Morris-Wiman and L. Brinkley, "Rapid changes in the extracellular matrix accompany in vitro palatal shelf remodelling," *Anatomy and Embryology*, vol. 188, no. 1, pp. 75–85, 1993.
- [4] J. Morris-Wiman and L. Brinkley, "An extracellular matrix infrastructure provides support for murine secondary palatal shelf remodelling," *Anatomical Record*, vol. 234, no. 4, pp. 575–586, 1992.
- [5] A. Iamaroon and V. M. Diewert, "Distribution of basement membrane components in the mouse primary palate," *Journal of Craniofacial Genetics and Developmental Biology*, vol. 16, no. 1, pp. 48–51, 1996.
- [6] M. Dudas, W. Y. Li, J. Kim, A. Yang, and V. Kaartinen, "Palatal fusion—where do the midline cells go?. A review on cleft palate, a major human birth defect," *Acta Histochemica*, vol. 109, no. 1, pp. 1–14, 2007.

- [7] L. Blavier, A. Lazaryev, J. Groffen, N. Heisterkamp, Y. A. DeClerck, and V. Kaartinen, "TGF- $\beta$ 3-induced palatogenesis requires matrix metalloproteinases," *Molecular Biology of the Cell*, vol. 12, no. 5, pp. 1457–1466, 2001.
- [8] N. L. Brown, S. J. Yarram, J. P. Mansell, and J. R. Sandy, "Matrix metalloproteinases have a role in palatogenesis," *Journal of Dental Research*, vol. 81, no. 12, pp. 826–830, 2002.
- [9] M. D. Hulett, C. Freeman, B. J. Hamdorf, R. T. Baker, M. J. Harris, and C. R. Parish, "Cloning of mammalian heparanase, an important enzyme in tumor invasion and metastasis," *Nature Medicine*, vol. 5, no. 7, pp. 803–809, 1999.
- [10] M. Toyoshima and M. Nakajima, "Human heparanase. Purification, characterization, cloning, and expression," *The Journal of Biological Chemistry*, vol. 274, no. 34, pp. 24153–24160, 1999.
- [11] I. Vlodavsky, Y. Friedmann, M. Elkin et al., "Mammalian heparanase: gene cloning, expression and function in tumor progression and metastasis," *Nature Medicine*, vol. 5, no. 7, pp. 793–802, 1999.
- [12] J. Kruegel and N. Miosge, "Basement membrane components are key players in specialized extracellular matrices," *Cellular and Molecular Life Sciences*, vol. 67, no. 17, pp. 2879–2895, 2010.
- [13] E. McKenzie, K. Tyson, A. Stamps et al., "Cloning and expression profiling of Hpa2, a novel mammalian heparanase family member," *Biochemical and Biophysical Research Communications*, vol. 276, no. 3, pp. 1170–1177, 2000.
- [14] F. Levy-Adam, S. Feld, V. Cohen-Kaplan et al., "Heparanase 2 interacts with heparan sulfate with high affinity and inhibits heparanase activity," *The Journal of Biological Chemistry*, vol. 285, no. 36, pp. 28010–28019, 2010.
- [15] A. Hirata and H. Nakamura, "Localization of perlecan and heparanase in Hertwig's epithelial root sheath during root formation in mouse molars," *Journal of Histochemistry and Cytochemistry*, vol. 54, no. 10, pp. 1105–1113, 2006.
- [16] H. Q. Miao, E. Navarro, S. Patel et al., "Cloning, expression, and purification of mouse heparanase," *Protein Expression and Purification*, vol. 26, no. 3, pp. 425–431, 2002.
- [17] H. Nakamura and H. Ozawa, "Immunohistochemical localization of heparan sulfate proteoglycan in rat tibiae," *Journal of Bone and Mineral Research*, vol. 9, no. 8, pp. 1289–1299, 1994.
- [18] W. J. Grzesik, C. R. Frazier, J. R. Shapiro, P. D. Sponseller, P. Gehron Robey, and N. S. Fedarko, "Age-related changes in human bone proteoglycan structure: impact of osteogenesis imperfecta," *The Journal of Biological Chemistry*, vol. 277, no. 46, pp. 43638–43647, 2002.
- [19] P. Newman, F. Bonello, A. S. Wierzbicki, P. Lumb, G. F. Savidge, and M. J. Shearer, "The uptake of lipoprotein-borne phyloquinone (vitamin K1) by osteoblasts and osteoblast-like cells: role of heparan sulfate proteoglycans and apolipoprotein E," *Journal of Bone and Mineral Research*, vol. 17, no. 3, pp. 426–433, 2002.
- [20] S. M. Cool and V. Nurcombe, "The osteoblast-heparan sulfate axis: control of the bone cell lineage," *International Journal of Biochemistry and Cell Biology*, vol. 37, no. 9, pp. 1739–1745, 2005.
- [21] S. A. Khan, M. S. Nelson, C. Pan, P. M. Gaffney, and P. Gupta, "Endogenous heparan sulfate and heparin modulate bone morphogenetic protein-4 signaling and activity," *American Journal of Physiology*, vol. 294, no. 6, pp. C1387–C1397, 2008.
- [22] M. Saijo, R. Kitazawa, M. Nakajima, M. Kurosaka, S. Maeda, and S. Kitazawa, "Heparanase mRNA expression during fracture repair in mice," *Histochemistry and Cell Biology*, vol. 120, no. 6, pp. 493–503, 2003.
- [23] V. Kram, E. Zcharia, O. Yacoby-Zeevi et al., "Heparanase is expressed in osteoblastic cells and stimulates bone formation and bone mass," *Journal of Cellular Physiology*, vol. 207, no. 3, pp. 784–792, 2006.
- [24] P. N. Smith, C. Freeman, D. Yu et al., "Heparanase in primary human osteoblasts," *Journal of Orthopaedic Research*, vol. 28, no. 10, pp. 1315–1322, 2010.
- [25] W. R. Thompson, S. Modla, B. J. Grindel et al., "Perlecan/Hspg2 deficiency alters the pericellular space of the lacunocanalicular system surrounding osteocytic processes in cortical bone," *Journal of Bone and Mineral Research*, vol. 26, no. 3, pp. 618–629, 2011.
- [26] E. Zcharia, D. Philp, E. Edovitsky et al., "Heparanase regulates murine hair growth," *American Journal of Pathology*, vol. 166, no. 4, pp. 999–1008, 2005.
- [27] S. Malignous, M. Donovan, S. Thibaut, and B. A. Bernard, "Heparanase 1: a key participant of inner root sheath differentiation program and hair follicle homeostasis," *Experimental Dermatology*, vol. 17, no. 12, pp. 1017–1023, 2008.
- [28] D. Bernard, B. Méhul, C. Delattre, L. Simonetti, A. Thomas-Collignon, and R. Schmidt, "Purification and characterization of the endoglycosidase heparanase 1 from human plantar stratum corneum: a key enzyme in epidermal physiology?" *Journal of Investigative Dermatology*, vol. 117, no. 5, pp. 1266–1273, 2001.
- [29] O. Goldshmidt, L. Nadav, H. Aingorn et al., "Human heparanase is localized within lysosomes in a stable form," *Experimental Cell Research*, vol. 281, no. 1, pp. 50–62, 2002.
- [30] A. Zetser, F. Levy-Adam, V. Kaplan et al., "Processing and activation of latent heparanase occurs in lysosomes," *Journal of Cell Science*, vol. 117, no. 11, pp. 2249–2258, 2004.
- [31] N. J. Nasser, "Heparanase involvement in physiology and disease," *Cellular and Molecular Life Sciences*, vol. 65, no. 11, pp. 1706–1715, 2008.
- [32] C. R. Parish, "The role of heparan sulphate in inflammation," *Nature Reviews Immunology*, vol. 6, no. 9, pp. 633–643, 2006.
- [33] C. Kirn-Safran, M. C. Farach-Carson, and D. D. Carson, "Multifunctionality of extracellular and cell surface heparan sulfate proteoglycans," *Cellular and Molecular Life Sciences*, vol. 66, no. 21, pp. 3421–3434, 2009.
- [34] A. D. Theocharis, S. S. Skandalis, G. N. Tzanakakis, and N. K. Karamanos, "Proteoglycans in health and disease: novel roles for proteoglycans in malignancy and their pharmacological targeting," *The FEBS Journal*, vol. 277, no. 19, pp. 3904–3923, 2010.
- [35] S. H. Kim, J. Turnbull, and S. Guimond, "Extracellular matrix and cell signalling: the dynamic cooperation of integrin, proteoglycan and growth factor receptor," *Journal of Endocrinology*, vol. 209, no. 2, pp. 139–151, 2011.
- [36] H. J. Ra and W. C. Parks, "Control of matrix metalloproteinase catalytic activity," *Matrix Biology*, vol. 26, no. 8, pp. 587–596, 2007.
- [37] E. Zcharia, J. Jia, X. Zhang et al., "Newly generated heparanase knock-out mice unravel co-regulation of heparanase and matrix metalloproteinases," *PLoS ONE*, vol. 4, no. 4, Article ID e5181, 2009.
- [38] C. Martínez-Álvarez, C. Tudela, J. Pérez-Miguelsanz, S. O'Kane, J. Puerta, and M. W. J. Ferguson, "Medial edge epithelial cell fate during palatal fusion," *Developmental Biology*, vol. 220, no. 2, pp. 343–357, 2000.



- [39] R. Cuervo and L. Covarrubias, "Death is the major fate of medial edge epithelial cells and the cause of basal lamina degradation during palatogenesis," *Development*, vol. 131, no. 1, pp. 15–24, 2004.
- [40] J. Z. Jin and J. Ding, "Analysis of cell migration, transdifferentiation and apoptosis during mouse secondary palate fusion," *Development*, vol. 133, no. 17, pp. 3341–3347, 2006.
- [41] F. V. Sani, K. Hallberg, B. D. Harfe, A. P. McMahon, A. Linde, and A. Gritli-Linde, "Fate-mapping of the epithelial seam during palatal fusion rules out epithelial-mesenchymal transformation," *Developmental Biology*, vol. 285, no. 2, pp. 490–495, 2005.
- [42] A. Lochter, S. Galosy, J. Muschler, N. Freedman, Z. Werb, and M. J. Bissell, "Matrix metalloproteinase stromelysin-1 triggers a cascade of molecular alterations that leads to stable epithelial-to-mesenchymal conversion and a premalignant phenotype in mammary epithelial cells," *Journal of Cell Biology*, vol. 139, no. 7, pp. 1861–1872, 1997.

## Research Article

# A DSPP Mutation Causing Dentinogenesis Imperfecta and Characterization of the Mutational Effect

Sook-Kyung Lee,<sup>1</sup> Kyung-Eun Lee,<sup>1</sup> Su Jeong Song,<sup>1</sup> Hong-Keun Hyun,<sup>1</sup>  
Sang-Hoon Lee,<sup>1</sup> and Jung-Wook Kim<sup>1,2</sup>

<sup>1</sup> Department of Pediatric Dentistry and Dental Research Institute, School of Dentistry, Seoul National University, 275-1 Yongon-dong, Chongno-gu, Seoul 110-768, Republic of Korea

<sup>2</sup> Department of Molecular Genetics and Dental Research Institute, School of Dentistry, Seoul National University, 275-1 Yongon-dong, Chongno-gu, Seoul 110-768, Republic of Korea

Correspondence should be addressed to Jung-Wook Kim; pedoman@snu.ac.kr

Received 14 September 2012; Revised 28 September 2012; Accepted 12 October 2012

Academic Editor: Brian L. Foster

Copyright © 2013 Sook-Kyung Lee et al. This is an open access article distributed under the Creative Commons Attribution License, which permits unrestricted use, distribution, and reproduction in any medium, provided the original work is properly cited.

Mutations in the *DSPP* gene have been identified in nonsyndromic hereditary dentin defects, but the genotype-phenotype correlations are not fully understood. Recently, it has been demonstrated that the mutations of *DSPP* affecting the IPV leader sequence result in mutant DSPP retention in rough endoplasmic reticulum (ER). In this study, we identified a Korean family with dentinogenesis imperfecta type III. To identify the disease causing mutation in this family, we performed mutational analysis based on candidate gene sequencing. Exons and exon-intron boundaries of *DSPP* gene were sequenced, and the effects of the identified mutation on the pre-mRNA splicing and protein secretion were investigated. Candidate gene sequencing revealed a mutation (c.50C > T, p.P17L) in exon 2 of the *DSPP* gene. The splicing assay showed that the mutation did not influence pre-mRNA splicing. However, the mutation interfered with protein secretion and resulted in the mutant protein remaining largely in the ER. These results suggest that the mutation affects ER-to-Golgi apparatus export and results in the reduction of secreted DSPP and ER overload. This may induce cell stress and damage processing and/or transport of dentin matrix proteins or other critical proteins.

## 1. Introduction

Hereditary dentin defects are categorized into three types of dentinogenesis imperfecta (DGI) and two types of dentin dysplasia (DD) [1]. DGI type I (MIM 166240) is a syndromic dental phenotype of osteogenesis imperfecta. The phenotype is similar to DGI type II but the penetrance is incomplete and the expressivity is also variable [1]. DGI type II (MIM 125490) is characterized by opalescent discolored dentition, pulpal calcification, and bulbous crown shape. DGI type III (MIM 125500), originally thought to be specific to the Brandywine isolate, is a severe form of DGI type II with multiple pulp exposures and shell-like teeth [2]. DD type II (MIM 125420) is similar to DGI type II in the deciduous dentition but tooth discoloration is minimal, and pulp chambers are thistle-tube shaped with pulp stones in the permanent dentition. In DD type I (MIM 125400), teeth are

normal in shape, form, and consistency in the deciduous and permanent dentition. In some cases, color of the teeth may display a slight amber discoloration. However, the roots are short and the pulp obliteration results in a crescent-shaped pulpal remnant in the permanent dentition and a total pulpal obliteration in the deciduous dentition [1].

The dentin sialophosphoprotein (*DSPP*) gene is located on chromosome 4q21 and encodes the major non-collagenous protein in the dentin matrix [2]. *DSPP* is rapidly cleaved by proteases into three major proteins: dentin sialoprotein (DSP), dentin glycoprotein (DGP), and dentin phosphoprotein (DPP) [3, 4]. Mutations in the *DSPP* gene have been identified to cause DGI type II, III, and DD type II [5–25]. Therefore, these diseases are not separate, but are allelic with differing severity [2]. Even though there are several other candidate genes for nonsyndromic hereditary dentin defects

[26], only mutations in the *DSPP* gene have been identified to date.

Reduction of DSPP and/or improper mineralization induced by the mutant *DSPP* gene could result in defective dentin mineralization. Alternatively, accumulation of the mutant DSPP in the odontoblast would result in cellular damage and influence protein processing and/or transporting system during rapid dentin matrix formation, particularly for dentin matrix proteins including DSPP [21].

A functional domain at the N-terminus of DSPP and its possible role in the signal peptide cleavage have been suggested due to its proximity to the signal peptide cleavage site [21]. Secreted DSPP has a highly conserved N-terminal sequence beginning with Ile Pro Val (IPV) after cleavage of the 15 amino acid signal peptide. Mutations affecting the IPV domain would result in errors in signal peptide cleavage processing and subsequently affect protein secretion.

In this study, we identified a mutation in the *DSPP* gene that causes DGI type III and investigated the effect of the mutation on pre-mRNA splicing and protein secretion in order to better understand the molecular genetic pathogenesis underlying the aberrant dentin biomineralization.

## 2. Materials and Methods

**2.1. Enrollment of Human Subjects.** The protocols and subject consents for this study were reviewed and approved by the Institutional Review Board at Seoul National University Dental Hospital. We identified a Korean family with dentinogenesis imperfecta type III, and seven family members were recruited for this study. Clinical and radiologic examinations were performed, and blood samples were collected with the understanding and written consent of each subject according to the Declaration of Helsinki.

**2.2. Primers, Polymerase Chain Reaction (PCR), and DNA Sequencing.** Genomic DNA was extracted from peripheral whole blood using the QuickGene DNA whole blood kit S with QuickGene-Mini80 equipment (Fujifilm, Tokyo, Japan) according to the manufacturer's instructions. Primers and conditions for PCR and DNA sequencing were previously described [10]. PCR reactions were performed using HiPi DNA polymerase premix (ElpisBio, Daejeon, Korea), and the PCR products were purified with a PCR Purification Kit (ElpisBio). DNA sequencing was performed at the DNA sequencing center (Macrogen, Seoul, Korea). All nucleotide numbering began from the A of the ATG translational initiation codon of the human *DSPP* reference sequence (NM-014208.3).

**2.3. Cloning of Genomic DNA and Mutagenesis.** A wildtype human *DSPP* gene fragment including exons two, three, and four was cloned into the pSPL3 splicing vector as previously described [13]. Mutation was introduced by PCR mutagenesis (forward: 5'-GTA GCA TGG GCC ATT CTA GTA AGT ATG CCT TTC-3', reverse: 5'-GAA AGG CAT ACT TAC TAG AAT GGC CCA TGC TAC-3'), and the sequence was confirmed by direct sequencing.

**2.4. In Silico Splicing Assay.** The mutational effect on pre-mRNA splicing was analyzed by two computer programs: SplicePort (<http://spliceport.cbcb.umd.edu/>) and NNSPLICE version 0.9 ([http://www.fruitfly.org/seq\\_tools/splice.html](http://www.fruitfly.org/seq_tools/splice.html)).

**2.5. In Vitro Splicing Assay.** COS-7 cells were transfected with wildtype and mutant pSPL3 vectors, and total RNA was isolated after 48 hours using TRIzol reagent (Invitrogen, Carlsbad, CA, USA). cDNA was generated from 4 µg RNA using RT-PCR premix (ElpisBio). RT-PCR amplification (wild type amplicon size: 666 bp; forward: 5'-TAG AGT CGA CCC AGC ACC AT-3', reverse: 5'-CCT CGT TTC TAC AGG AAT TCT CA-3') was performed using HiPi PCR premix (ElpisBio). Amplification products were resolved on a 1% agarose gel and characterized by DNA sequencing.

**2.6. DSP Secretion Analysis.** The coding region of the entire human DSP protein (from aa 1 to aa 382) was amplified by an RT-PCR reaction using PCR primers (forward: 5'-GGA AGC TTG AAA ATG AAG ATA ATT ACA TA-3', reverse: 5'-GGG GAT CCC CGC TGG GAC CCT TGA TTT CTA-3') and cloned into a pEGFP-N1 vector after double digestion with *Hind*III and *Bam*HI restriction endonucleases. PCR mutagenesis was performed to replace C with T (c.50C > T) using primers (forward: 5'-GCA GTA GCA TGG GCC ATT CTA GTT CCT CAA AGC-3', reverse: 5'-GCT TTG AGG AAC TAG AAT GGC CCA TGC TAC TGC-3'). Sequences of normal and mutant pEGFP-N1 vectors were confirmed by direct plasmid sequencing. Normal and mutant DSP pEGFP-N1 vectors were transiently transfected into HEK293T cells using Lipofectamine 2000 reagent (Invitrogen, Carlsbad, CA, USA). Cell lysate and culture media (Dulbecco's Modified Eagle's Media) without serum were harvested after 48 hours. Cell lysate (40 µg) and culture media (20 µL) were run on a 10% SDS-polyacrylamide gel and subjected to Western blot using anti-DSP (Santa Cruz Biotechnology, Santa Cruz, CA, USA) and anti-GAPDH (ABM, Richmond, ON, Canada) antibodies. Silver staining was performed to normalize the amount of the culture media. Band intensity was measured using ImageJ (NIH). Experiments were duplicated, and statistical analysis (independent *t*-test) was performed to compare the amount of wildtype and mutant DSP in the media and cell lysate.

**2.7. Fluorescent Immunocytochemistry.** Normal and mutant DSP pEGFP-N1 vectors were transiently transfected into HEK293T cells using lipofectamine 2000 reagent (Invitrogen). The transfected cells were seeded on the cover glass coated with poly-L-lysine (Sigma-Aldrich, St. Louis, MO, USA). After 24 hours, cells were washed with PBS and fixed with 4% paraformaldehyde for 20 min. Permeabilized cells were treated with 0.1% Triton X-100 for 15 min and subsequently blocked with 10% goat serum (Vector Lab, Burlingame, CA, USA) for 1 hr. For ER staining, slides were incubated with mouse monoclonal anti-Calnexin (CANX)



antibody (Millipore, Milford, MA, USA) for 2 hr followed by incubation with Texas Red conjugated goat anti-mouse secondary antibody (Santa Cruz Biotechnology) for 1 hr. For Golgi apparatus staining, the slides were incubated with rabbit monoclonal anti-Golgi matrix protein (GM130) antibody (Epitomics, Burlingame, CA, USA) for 2 hr followed by incubation with Texas Red conjugated goat anti-rabbit secondary antibody (Vector Lab) for 1 hr. Nuclei were stained with 20  $\mu$ M H33342 (Sigma-Aldrich) for 10 min. Slides were coverslipped with fluorescence mounting medium (Dako, Carpinteria, CA, USA) and the fluorescent images were captured using an Olympus FV300 laser-scanning confocal microscope.

### 3. Results and Discussion

**3.1. Clinical Findings.** The proband (IV:2) first visited the Pediatric Dental Clinic of the Seoul National University Dental Hospital at 2.5 years of age (Figure 1(a)). Her deciduous dentition displayed severe attrition and marked discoloration. Periapical inflammations were observed in several teeth in which the pulp tissue was exposed by attrition (Figure 1(d)). Her father (III:2) was 29 years old, but had lost many teeth and had full-coverage prosthodontics on his remaining permanent teeth (Figure 1(e)). There was no history of bone fragility or symptoms of hearing loss in the family.

**3.2. Mutation Results.** Sequencing analysis revealed a C to T transition in exon 2 (c.50C > T) of the *DSPP* gene. This sequence variation correlated perfectly with the presence of the disease (Figure 1). This sequence variation was not present in 100 unaffected control individuals from the Korean population (data not shown). This suggests that the mutation is not a common variant of the *DSPP* gene. The same mutation has been recently identified in a Chinese family [25]. This mutation changes the proline residue at the +2-position (P2') from the signal peptide cleavage site to the leucine residue (p.P17L). The Pro17 residue is conserved in human, mouse, rat, pig, and cow.

**3.3. Splicing Assay.** *In silico* analyses of the mutational effect on pre-mRNA splicing were inconsistent. One program yielded a change in the prediction value suggesting a defective splicing event (0.90  $\rightarrow$  0.78 as a donor site), while the other program did not (0.98  $\rightarrow$  0.98).

RT-PCR showed a single amplified product in both the wildtype and the mutant pSPL3 vectors (Figure 2). The forward primer binds at the boundary of the donor site of the pSPL3 vector and at the beginning of exon 2 of the *DSPP* gene, while the reverse primer binds at the middle of exon 4 of the *DSPP* gene. If intron 2 was not properly excised, the size of the amplicon would be 1811 bp. Sequencing analysis of the amplicons exhibited normally spliced sequences, indicating that this mutation in the second position from the end of exon

2 (c.50C > T) did not influence normal pre-mRNA splicing and resulted in pure missense mutations (p.P17L) (Figure 2).

**3.4. DSP Secretion Analysis.** Wildtype DSP was efficiently secreted to the culture media, while only a small amount of the mutant DSP was detected in the culture media. The secreted amount of wildtype DSP was more than 7-fold greater compared to the P17L mutant DSP ( $P < 0.01$ ) (Figure 3). Cellular retention of the mutant DSP was detected in the cell lysate. Western blot of the cell lysate showed that intracellular retention of the P17L mutant DSP was much higher (12.1-fold) than the wildtype DSP ( $P < 0.01$ ).

**3.5. Fluorescent Immunocytochemistry.** Wildtype DSP was localized exclusively in the Golgi apparatus (Figure 4). In contrast, the P17L mutant DSP showed widespread expression in the cytoplasm. The mutant DSP largely remained in the ER, even though a portion was localized in the Golgi apparatus.

**3.6. Discussion.** The proband showed multiple pulp exposures and severe attrition. The father of the proband was 29 years old, but had lost many teeth. Interestingly, the disease causing the mutation of the Brandywine isolate was c.49C > T (p.P17S) [14]. The same mutation (c.49C > T, p.P17S) was also found in a Chinese family [15]. The clinical phenotype was also severe according to the clinical photos and panoramic radiograph. Pro17 is a well-conserved amino acid, and it is one of the mutational hot spots in the *DSPP* gene [25]. This data confirms that DGI type III is not confined to a specific (Brandywine isolate) population and is a severe form of DGI type II. Another mutation changing Pro17 (c.49C > A, p.P17T) was reported in a Chinese family [6]. Clinical severity was not reported in detail, but the affected individuals also presented with progressive sensorineural high-frequency hearing loss. However, hearing loss is not common in DGI families, so further studies are needed to characterize the functional role of *DSPP* mutations in the pathogenesis of hearing loss.

The identified mutation was located in the second nucleotide position from the end of exon 2. Despite its close proximity to the exon-intron boundary, the mutation did not influence normal pre-mRNA splicing. Therefore, the mutation resulted in a pure missense mutation and changed the highly conserved amino acid from Pro17 to Leu17.

The mutation could affect normal signal peptide cleavage based on its proximity to the cleavage site and the nature of the changed amino acid. Pro17 is located at the P2' position from the signal peptide cleavage site (between Ala15 and Ile16). Proline is a nonpolar neutral amino acid with a hydropathy index of -1.6, while leucine is a non-polar neutral amino acid with a hydropathy index of 3.8. *In silico* analyses predicted reduced efficiency in the signal peptide cleavage. Changing Pro17 to Leu17 decreased the signal peptide probability (0.995  $\rightarrow$  0.964) and the maximum cleavage site probability score (0.947  $\rightarrow$  0.694) by SignalP 3.0

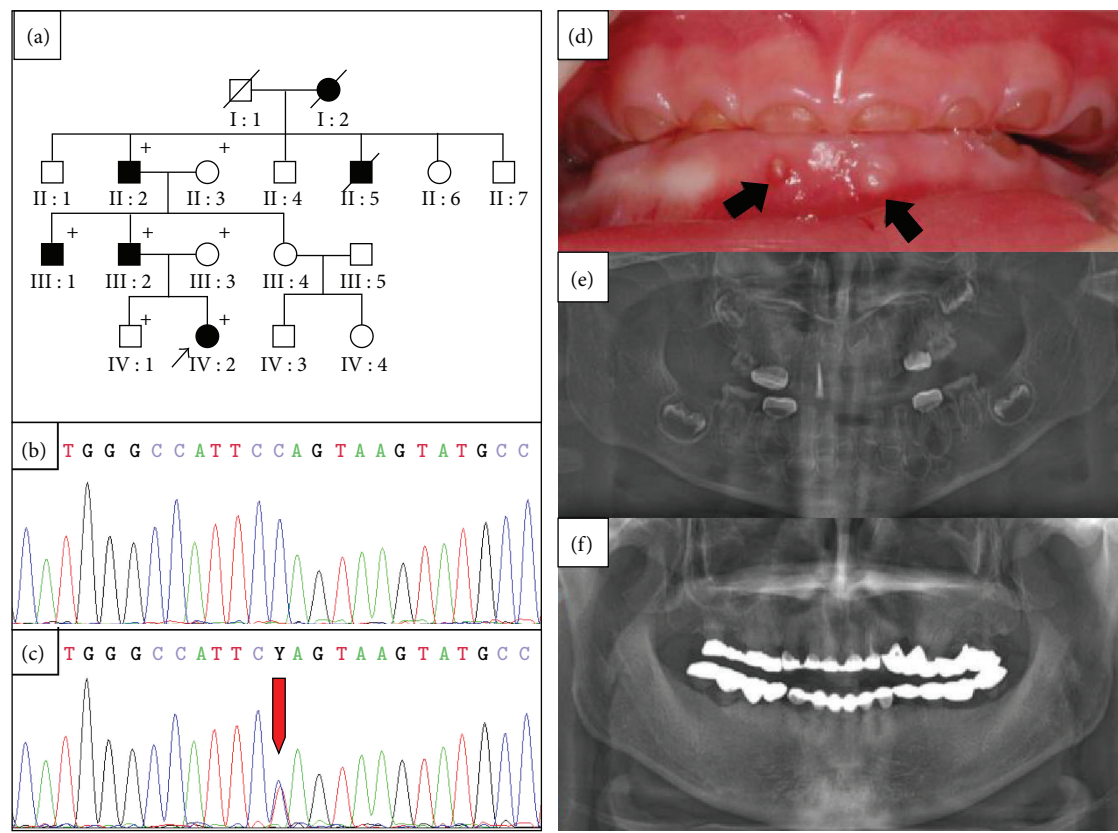


FIGURE 1: Pedigree, mutational analysis, and clinical photos. (a) Pedigree of the proband's family. The "plus" symbol indicates members recruited for this study. (b) and (c) DNA sequencing chromatogram of a normal control and an affected individual. The red arrow indicates the mutated nucleotide (c.50C > T). (d) Frontal clinical photo of the proband. The deciduous dentition exhibits severe attrition and marked discoloration. Periapical abscesses are indicated by black arrows. (e) Panoramic radiogram of the proband during treatment at 2.8 yrs of age. The mandibular primary central incisors were extracted, and all primary first molars were treated with stainless steel crowns. Pulp treatment was performed for the maxillary primary lateral incisor, and wide pulp chambers can be identified in the remaining anterior teeth. (f) panoramic radiogram of an affected individual at 29.7 yrs of age (III : 2).

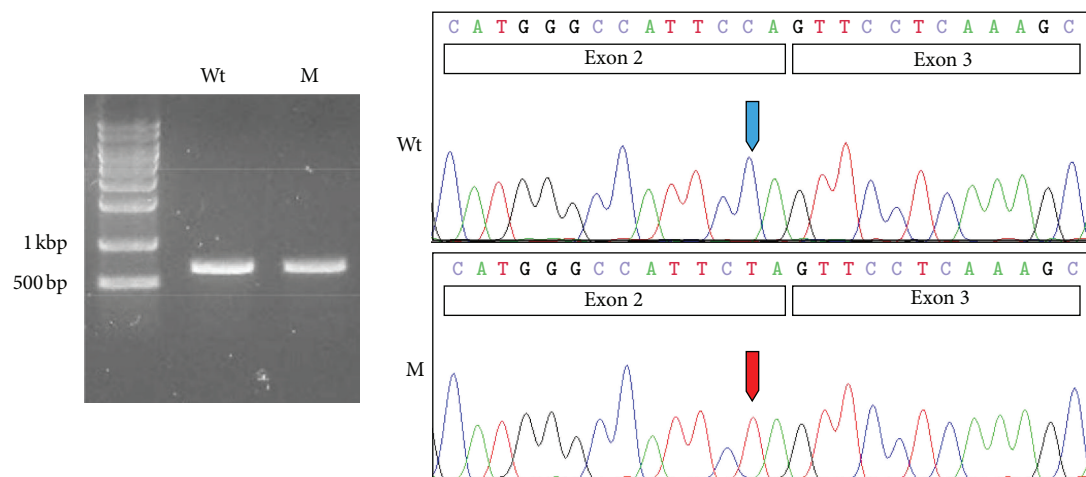


FIGURE 2: *In vitro* splicing assay. RT-PCR analyses of the wildtype (Wt) and mutated (M) pSPL3 vector. Both showed one normally spliced product that was confirmed by sequencing. The sizes of the marker band are shown in the gel image. Exons are shown in the box in the sequencing chromatogram. Wildtype and mutated nucleotide are indicated by blue and red arrows, respectively.

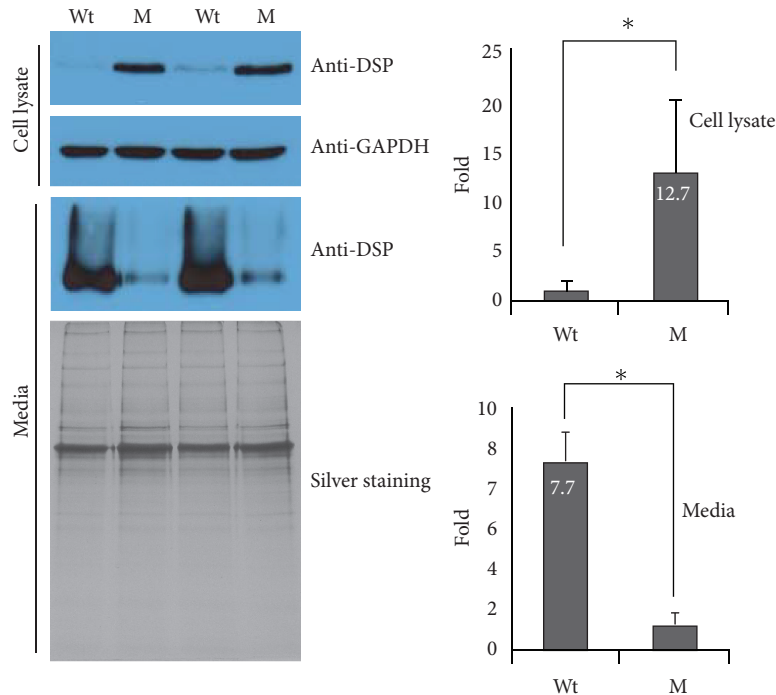


FIGURE 3: Protein expression analysis. Western blot analysis was performed to detect wildtype (Wt) and mutant (M) DSP in the cell lysate and culture media. The cell lysate was normalized with GAPDH. The secreted amount of wildtype DSP was more than 7-fold greater compared to the P17L mutant DSP ( $P < 0.01$ ). Cellular retention of the mutant DSP was detected in the cell lysate. Western blot of the cell lysate showed that intracellular retention of the P17L mutant DSP was much higher (12.1 folds) than the wildtype DSP ( $P < 0.01$ ). The asterisk indicates a statistically significant difference ( $P < 0.01$ ). Fold increase values are shown in the bar.

(<http://www.cbs.dtu.dk/services/SignalP/>). A decreased cleavage score (9.2  $\rightarrow$  7.0) was also obtained by SIG-Pred ([http://bmbpcu36.leeds.ac.uk/cgi-bin/sig\\_pred/Signal.cgi](http://bmbpcu36.leeds.ac.uk/cgi-bin/sig_pred/Signal.cgi)).

DSP expression and secretion were greatly affected by the introduction of the mutation. The amount of mutant DSP in the culture media was extremely small compared to the amount of wildtype DSP. In contrast to the culture media, mutant DSP was detected in the cell lysate, while wildtype DSP was faintly detected. These results indicate that the secretion of mutant DSP protein was severely affected and some mutant DSP protein was retained in the cell. This result is in accordance with the recent study on the rough ER trafficking errors caused by mutant DSPP [27].

Fluorescent immunocytochemical data showed that the wildtype DSP was efficiently transported to the Golgi apparatus for further export to the secretory pathway. However, the mutant DSP was largely retained in the ER, even though a portion was transported to the Golgi apparatus. Reduced efficiency in signal peptide cleavage could result in ER retention. However, this retention could also be resulted from disruption of the ER export signal by the Proline at the P2' position [28].

A mutation (c.16T  $\rightarrow$  G, p.Y6D) in the signal peptide resulted in DD type II, which is considered as a mild form of DGI type II. This mutation was shown to result in an absence of DSPP protein production from the mutated allele due to the defective signal peptide [8]. The amount of DSPP protein resulting from the mutated allele was nearly as absent

as the mutation in this study. Therefore, the phenotypic difference cannot be explained only by the reduction in the amount of wildtype DSPP. The P17L mutant DSPP protein can be translocated into the ER with an intact signal peptide, but is expected to have a dominant-negative effect on cell function and/or on dentin matrix mineralization due to incomplete signal peptide cleavage [21], loss of the ER export signal, or protein misfolding. In addition to the defect in secretory pathway itself, some secreted mutant DSPP may cause defective mineralization. Further study is required to determine the exact cause of the pathogenesis of the DSPP-associated dentin defect.

#### 4. Conclusion

In summary, we have identified a mutation in exon 2 of the *DSPP* gene that caused DGI type III. The mutation did not influence pre-mRNA splicing but caused ER retention and defective protein secretion. It is possible that the severe phenotype observed in the affected family is caused by a dominant negative effect. Future molecular studies on the effect of individual mutation and function of DSPP may provide better insight into the normal and pathological basis of dentin biomineralization.

#### Acknowledgments

This work was supported by a Grant from the Bio & Medical Technology Development Program (2012-0006173) and a



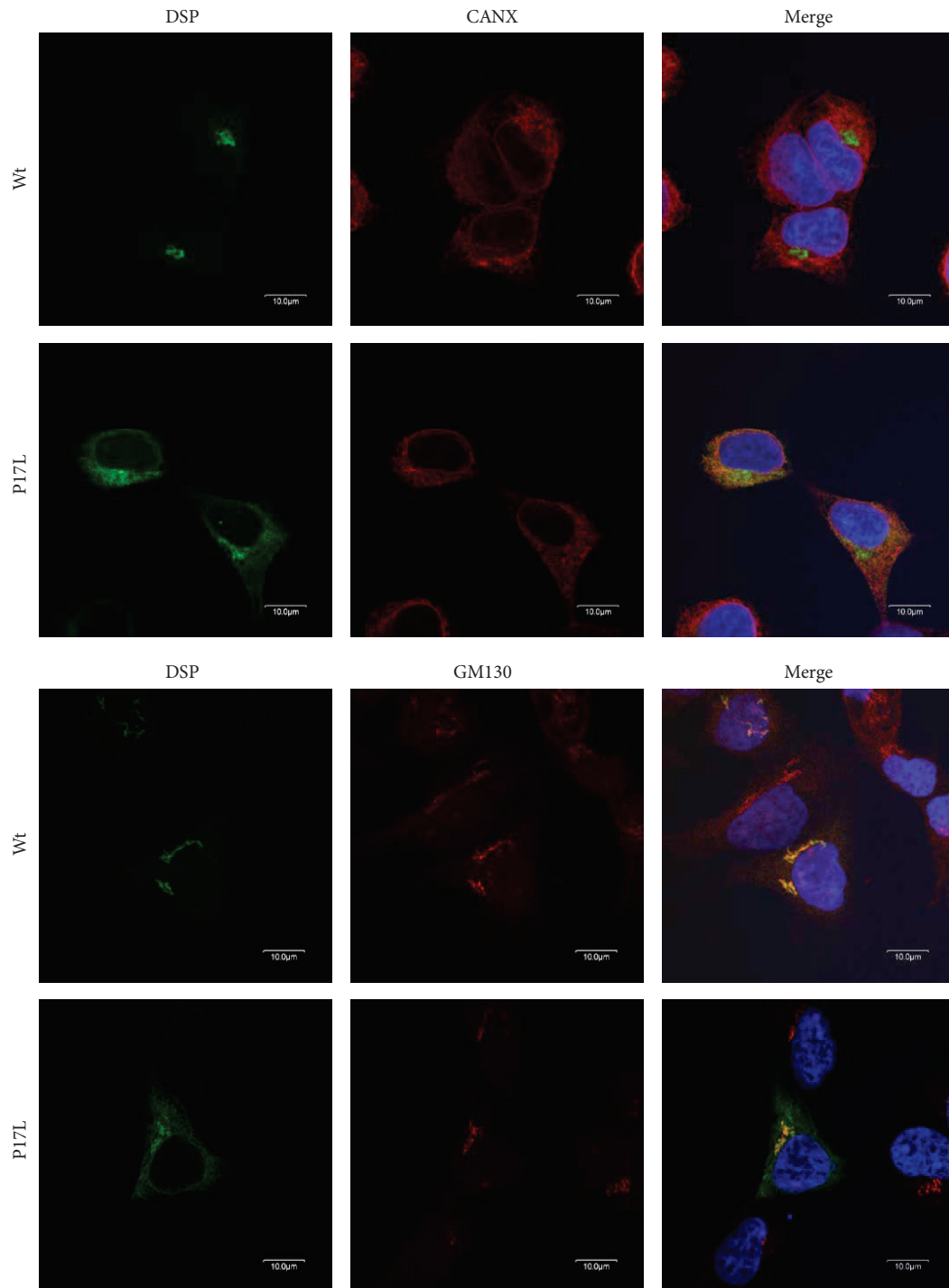


FIGURE 4: Fluorescent immunocytochemistry. Confocal laser-scanning images were captured to detect localization of the GFP-tagged wildtype (Wt) and mutant (P17L) DSP in HEK293T cells. Anti-Calnexin (CANX) antibody was used for ER staining, and anti-Golgi matrix protein (GM130) antibody was used for Golgi apparatus staining. Nuclei were stained with H33342. Wildtype DSP was localized exclusively in the Golgi apparatus. The mutant DSP largely remained in the ER, although a portion was localized in the Golgi apparatus.

Science Research Center Grant to the Bone Metabolism Research Center (2012-0000487) of the National Research Foundation (NRF) funded by the Korean Government (MEST).

## References

- [1] E. D. Shields, D. Bixler, and A. M. El-Kafrawy, "A proposed classification for heritable human dentine defects with a description of a new entity," *Archives of Oral Biology*, vol. 18, no. 4, pp. 543–553, 1973.
- [2] J. W. Kim and J. P. Simmer, "Hereditary dentin defects," *Journal of Dental Research*, vol. 86, no. 5, pp. 392–399, 2007.
- [3] Z. von Marschall and L. W. Fisher, "Dentin sialophosphoprotein (DSPP) is cleaved into its two natural dentin matrix products by three isoforms of bone morphogenetic protein-1 (BMP1)," *Matrix Biology*, vol. 29, no. 4, pp. 295–303, 2010.
- [4] Y. Yamakoshi, J. C. C. Hu, T. Iwata, K. Kobayashi, M. Fukae, and J. P. Simmer, "Dentin sialophosphoprotein is processed by MMP-2 and MMP-20 in vitro and in vivo," *Journal of Biological Chemistry*, vol. 281, no. 50, pp. 38235–38243, 2006.
- [5] J. Zhang, J. Wang, Y. Ma et al., "A novel splicing mutation alters DSPP transcription and leads to dentinogenesis imperfecta type II," *PLoS One*, vol. 6, no. 11, article e27982, 2011.
- [6] S. Xiao, C. Yu, X. Chou et al., "Dentinogenesis imperfecta 1 with or without progressive hearing loss is associated with distinct mutations in DSPP," *Nature Genetics*, vol. 27, no. 2, pp. 201–204, 2001.
- [7] X. Zhang, J. Zhao, C. Li et al., "DSPP mutation in dentinogenesis imperfecta shields type II," *Nature Genetics*, vol. 27, no. 2, pp. 151–152, 2001.
- [8] M. H. Rajpar, M. J. Koch, R. M. Davies, K. T. Mellody, C. M. Kiely, and M. J. Dixon, "Mutation of the signal peptide region of the bicistronic gene DSPP affects translocation to the endoplasmic reticulum and results in defective dentine biomineralization," *Human Molecular Genetics*, vol. 11, no. 21, pp. 2559–2565, 2002.
- [9] B. Malmgren, S. Lindskog, A. Elgadi, and S. Norgren, "Clinical, histopathologic, and genetic investigation in two large families with dentinogenesis imperfecta type II," *Human Genetics*, vol. 114, no. 5, pp. 491–498, 2004.
- [10] J. W. Kim, S. H. Nam, K. T. Jang et al., "A novel splice acceptor mutation in the DSPP gene causing dentinogenesis imperfecta type II," *Human Genetics*, vol. 115, no. 3, pp. 248–254, 2004.
- [11] J. W. Kim, J. C. C. Hu, J. I. Lee et al., "Mutational hot spot in the DSPP gene causing dentinogenesis imperfecta type II," *Human Genetics*, vol. 116, no. 3, pp. 186–191, 2005.
- [12] S. K. Lee, K. E. Lee, D. Jeon et al., "A novel mutation in the DSPP gene associated with dentinogenesis imperfecta type II," *Journal of Dental Research*, vol. 88, no. 1, pp. 51–55, 2009.
- [13] S. K. Lee, J. C. C. Hu, K. E. Lee, J. P. Simmer, and J. W. Kim, "A Dentin Sialophosphoprotein Mutation That Partially Disrupts a Splice Acceptor Site Causes Type II Dentin Dysplasia," *Journal of Endodontics*, vol. 34, no. 12, pp. 1470–1473, 2008.
- [14] P. S. Hart and T. C. Hart, "Disorders of human dentin," *Cells Tissues Organs*, vol. 186, no. 1, pp. 70–77, 2007.
- [15] X. Zhang, L. Chen, J. Liu et al., "A novel DSPP mutation is associated with type II dentinogenesis Imperfecta in a chinese family," *BMC Medical Genetics*, vol. 8, article 52, 2007.
- [16] H. Holappa, P. Nieminen, L. Tolva, P. L. Lukinmaa, and S. Alaluusua, "Splicing site mutations in dentin sialophosphoprotein causing dentinogenesis imperfecta type II," *European Journal of Oral Sciences*, vol. 114, no. 5, pp. 381–384, 2006.
- [17] H. Wang, Y. Hou, Y. Cui et al., "A novel splice site mutation in the dentin sialophosphoprotein gene in a Chinese family with dentinogenesis imperfecta type II," *Mutation Research*, vol. 662, no. 1–2, pp. 22–27, 2009.
- [18] Y. Song, C. Wang, B. Peng et al., "Phenotypes and genotypes in 2 DGI families with different DSPP mutations," *Oral Surgery, Oral Medicine, Oral Pathology, Oral Radiology and Endodontology*, vol. 102, no. 3, pp. 360–374, 2006.
- [19] Y. L. Song, C. N. Wang, M. W. Fan, B. Su, and Z. Bian, "Dentin phosphoprotein frameshift mutations in hereditary dentin disorders and their variation patterns in normal human population," *Journal of Medical Genetics*, vol. 45, no. 7, pp. 457–464, 2008.
- [20] M. Kida, T. Tsutsumi, M. Shindoh, H. Ikeda, and T. Ariga, "De novo mutation in the DSPP gene associated with dentinogenesis imperfecta type II in a Japanese family," *European Journal of Oral Sciences*, vol. 117, no. 6, pp. 691–694, 2009.
- [21] D. A. McKnight, P. S. Hart, T. C. Hart et al., "A comprehensive analysis of normal variation and disease-causing mutations in the human DSPP gene," *Human Mutation*, vol. 29, no. 12, pp. 1392–1404, 2008.
- [22] D. A. McKnight, J. P. Simmer, P. S. Hart, T. C. Hart, and L. W. Fisher, "Overlapping DSPP mutations cause dentin dysplasia and dentinogenesis imperfecta," *Journal of Dental Research*, vol. 87, no. 12, pp. 1108–1111, 2008.
- [23] H. Bai, H. Agula, Q. Wu et al., "A novel DSPP mutation causes dentinogenesis imperfecta type II in a large Mongolian family," *BMC Medical Genetics*, vol. 11, no. 1, article 23, 2010.
- [24] P. Nieminen, L. Papagiannoulis-Lascarides, J. Waltimo-Siren et al., "Frameshift mutations in dentin phosphoprotein and dependence of dentin disease phenotype on mutation location," *Journal of Bone and Mineral Research*, vol. 26, no. 4, pp. 873–880, 2011.
- [25] D. Li, X. Du, R. Zhang et al., "Mutation identification of the DSPP in a Chinese family with DGI-II and an up-to-date bioinformatic analysis," *Genomics*, vol. 99, no. 4, pp. 220–226, 2012.
- [26] L. Ye, M. MacDougall, S. Zhang et al., "Deletion of Dentin Matrix Protein-1 Leads to a Partial Failure of Maturation of Predentin into Dentin, Hypomineralization, and Expanded Cavities of Pulp and Root Canal during Postnatal Tooth Development," *Journal of Biological Chemistry*, vol. 279, no. 18, pp. 19141–19148, 2004.
- [27] Z. von Marschall, S. Mok, M. D. Phillips, D. A. McKnight, and L. W. Fisher, "Rough endoplasmic reticulum trafficking errors by different classes of mutant dentin sialophosphoprotein (DSPP) cause dominant negative effects in both dentinogenesis imperfecta and dentin dysplasia by entrapping normal DSPP," *Journal of Bone and Mineral Research*, vol. 27, no. 6, pp. 1309–1321, 2012.
- [28] Y. Tsukumo, S. Tsukahara, S. Saito, T. Tsuruo, and A. Tomida, "A novel endoplasmic reticulum export signal: proline at the +2-position from the signal peptide cleavage site," *Journal of Biological Chemistry*, vol. 284, no. 40, pp. 27500–27510, 2009.

## Research Article

# Bodyweight Assessment of Enamelin Null Mice

Albert H.-L. Chan,<sup>1</sup> Rangsiyakorn Lertlam,<sup>2</sup> James P. Simmer,<sup>2</sup>  
Chia-Ning Wang,<sup>3</sup> and Jan C. C. Hu<sup>2</sup>

<sup>1</sup> Department of Periodontics and Oral Medicine, University of Michigan School of Dentistry, 1011 North University Avenue, Ann Arbor, MI 48109-1078, USA

<sup>2</sup> Department of Biologic and Materials Sciences, University of Michigan School of Dentistry, 1210 Eisenhower Place, Ann Arbor, MI 48108, USA

<sup>3</sup> Department of Biostatistics, University of Michigan School of Public Health, 109 Observatory Street, 1700 SPH I, Ann Arbor, MI 48109-2029, USA

Correspondence should be addressed to Jan C. C. Hu; [janhu@umich.edu](mailto:janhu@umich.edu)

Received 21 August 2012; Revised 17 October 2012; Accepted 22 October 2012

Academic Editor: L. Brian Foster

Copyright © 2013 Albert H.-L. Chan et al. This is an open access article distributed under the Creative Commons Attribution License, which permits unrestricted use, distribution, and reproduction in any medium, provided the original work is properly cited.

The *Enam* null mice appear to be smaller than wild-type mice, which prompted the hypothesis that enamel defects negatively influence nutritional intake and bodyweight gain (BWG). We compared the BWG of *Enam*<sup>-/-</sup> and wild-type mice from birth (D0) to Day 42 (D42). Wild-type (WT) and *Enam*<sup>-/-</sup> (N) mice were given either hard chow (HC) or soft chow (SC). Four experimental groups were studied: WTHC, WTSC, NHC, and NSC. The mother's bodyweight (DBW) and the average litter bodyweight (ALBW) were obtained from D0 to D21. After D21, the pups were separated from the mother and provided the same type of food. Litter bodyweights were measured until D42. ALBW was compared at 7-day intervals using one-way ANOVA, while the influence of DBW on ALBW was analyzed by mixed-model analyses. The ALBW of *Enam*<sup>-/-</sup> mice maintained on hard chow (NHC) was significantly lower than the two WT groups at D21 and the differences persisted into young adulthood. The ALBW of *Enam*<sup>-/-</sup> mice maintained on soft chow (NSC) trended lower, but was not significantly different than that of the WT groups. We conclude that genotype, which affects enamel integrity, and food hardness influence bodyweight gain in postnatal and young adult mice.

## 1. Introduction

Enamelin is the largest (~200 kDa) but the least abundant (3–5%) of the three major secretory stage enamel matrix proteins. Twelve mutations in the enamel gene (*ENAM*, 4q13.2) have been published associated with autosomal dominant amelogenesis imperfecta (ADAI) [1–16]. Clinical features of affected teeth showed thin enamel, with either severe or localized hypoplasia. The enamel phenotype is dose-dependent and ranges from small, well-circumscribed enamel pits to enamel agenesis (when both *ENAM* alleles are mutated) [7]. None of these *ENAM* mutation studies reported a phenotype outside the dentition. In mice, mutations in the *Enam* gene have been induced with the mutagen N-ethyl-N-nitrosourea (ENU), and four separate point mutations

have been identified: p.Ser55Ile, p.Glu57Gly, a splice donor site in exon 4, and a premature stop codon in exon 8 (p.Gln176\*) [17, 18]. Heterozygous mice exhibited rough and pitted enamel while the null mice showed enamel agenesis. Enamelin null mice were generated by replacing the *Enam* coding sequence from the translation initiation site through exon 7 with a *lacZ* reporter gene [19]. The enamel defects were dose-dependent. The enamel layer was completely absent in *Enam* null mice compared to the mild enamel phenotype in the heterozygotes (*Enam*<sup>+/-</sup>). A thin, highly irregular, easily abraded mineralized crust over the dentin was observed in the *Enam* null mice. The affected teeth showed significant wear and were generally chalky-white. The histologic, morphometric, and protein/mineral analyses demonstrated that enamel is essential for proper



enamel matrix organization and mineralization. Serum calcium, phosphate, alkaline phosphatase, and glucose levels overlapped normal ranges.

There is considerable evidence that enamelin is an enamel-specific protein. The *lacZ* knock-in in the *Enam*<sup>-/-</sup> only detected enamelin expression in ameloblasts. Although not all ages and organs were surveyed, *Enam* tooth-specific expression is consistent with the human and mouse expressed sequence tag EST profiles. The human (Hs.667018) lists only three *ENAM* transcripts per million for healthy (nondental) tissues. The mouse (Mm.8014) lists four *Enam* transcripts per million in embryonic tissue (which has developing teeth), 1414 per million in molars, and zero in all other tissues. Humans with *ENAM* defects only show an enamel phenotype. Among the reports of 16 kindreds with 12 different amelogenesis imperfecta (AI) causing *ENAM* mutations, none revealed a history of systemic problems associated with the genetic condition. Finally, *Enam* is consistently found to be pseudogenized in vertebrates that have lost the ability to make teeth during evolution [20–23]. These findings support the conclusion that *Enam* defects are unlikely to directly cause a significant reduction in animal bodyweight (BW). Perhaps absence of enamel covering the dentin surface causes pain that discourages eating, especially if the food is hard and requires mastication.

The relationship between poor oral health and lower bodyweight has been observed in human studies. Acs et al. showed that three-year-old children with dental caries and with at least one pulp-involved tooth weighed 1 kg less than the counterparts [24]. A follow-up study reported that there was significant “catch-up” in growth following complete dental rehabilitation of the children who suffered severe dental caries with pulpal involvement. There are several plausible mechanisms for which dental caries may contribute to underweight and poor growth in young children and one of them is pain and discomfort from dental caries reducing nutritional intake because eating is painful [25]. Severe forms of amelogenesis imperfecta are definitely associated with increased dental pain and can lead to behavioral compensations. When both *ENAM* alleles are defective, the chief complaint typically includes dental pain, particularly thermal sensitivity [7, 12]. Anterior open-bites, which are often associated with tongue-thrust and thumb sucking behaviors, are observed with increased frequency in AI patients, regardless of the genetic etiology, including AI caused by *ENAM* [6], *KLK4* [26], *MMP20* [27], *FAM83H* [28], or *AMELX* [29] mutations.

Enamelin null mice have virtually no enamel [19]. Given that genetic (AI) or environmental (caries and pulp involvement) factors can cause pain upon chewing in humans, it is reasonable to deduce that mice with severe enamel defects might experience eating difficulties that reduce BW gain, especially following the transition from milk to chow. If true, soft chow may prove more tolerable than hard chow, given the lack of enamel. The primary aim of this study was to compare the patterns of BW gain in *Enam* null and wild-type mice during the first 6 weeks of postnatal life, when maintained separately on hard or soft chow. As the mothers of the *Enam* null mice also had no enamel covering the crown of their teeth (which could affect their nutrition and the quantity

of their milk), a secondary aim was to evaluate whether maternal bodyweight (DBW) correlated with ALBW among the four experimental groups in the preweaning period.

## 2. Materials and Methods

**2.1. Animal Protocol.** All procedures involving animals were reviewed and approved by the UCUC Committee at the University of Michigan.

**2.2. Animal Breeding and Bodyweight Measurement.** Wild-type (strain C57BL/6) and *Enam* null (strain C57BL/6) females at the age of 4 to 6 months were mated to males with the same *Enam* genotype and genetic background. The *Enam* null and wild-type mice were maintained separately on soft or hard chow throughout the experiment. The chow was LabDiet 5001 (Purina Mills, St. Louis, MO, USA). Four experimental groups were generated: wild-type hard chow (WTHC), wild-type soft chow (WTSC), null hard chow (NHC), and null soft chow (NSC). The soft chow was water-moistened hard chow, and therefore both contained the same nutritional value. Signs of pregnancy were checked once a day following breeding and each pregnant mouse was transferred to a new cage with minimal disturbance. The mother mice were checked twice a day to determine the accurate birth time (D0) for each litter. Each litter's bodyweight was measured daily as a group at the same time of day using a digital analytical balance (Denver Instrument, Denver, CO, USA) from D0 to D42. The measured value for the weight of the litter divided by the number of pups in the litter gave the average litter bodyweight (ALBW). Each litter was housed with the mother from D0 to D21, after which the litter was weaned and separated by gender. From D22 to D42, the mean litter weight of males and females in the same litter was measured separately on a daily basis. When a mouse died, the average bodyweight (BW) of the remaining litter was used. Dam bodyweight (DBW) was measured daily from D0 to D21. The young adult male mice (at the age of 4–5 months) that were not sacrificed for morphologic examination were weighed, and the mean BW was compared among the four groups.

**2.3. Morphologic Examination.** After the BW analyses, mice at the age of 8 weeks were sacrificed by inhalation anesthesia using isoflurane (Sigma, St. Louis, MO, USA) and perfused with ice-cold 4% paraformaldehyde. Mandibles were dissected from the skull, fixed in 4% paraformaldehyde for 24 h, rinsed with phosphate buffered saline, and stored in 70% ethanol-diethyl pyrocarbonate. Mandibles were separated into halves by incision in the symphysis using a no. 11 scalpel blade. The right hemimandibles were photographed at 3x magnification (SMZ1000, Nikon) for morphologic evaluation under a stereomicroscope.

**2.4. Statistic Analysis.** Descriptive analysis of BW (in grams) was presented as the mean  $\pm$  SD. ALBW on D0 and on subsequent days at an interval of 7 days until D42 was compared among the four experimental groups by one-way ANOVA

and the Tukey test for pairwise group comparisons. DBW was compared on D0, D7, D14, and D21 as well as the mean BW of young adult males using the same method. Subsequently, the mixed model (SPSS 16.0) was implemented to assess the association of ALBW with DBM. Other independent variables include day, group (WHC, WSC, NHC, and NSC), litter size, and combinations. "Day" was treated as a categorical factor. All statistical analyses were conducted by consulting the Center for Statistical Consultation and Research, University of Michigan Ann Arbor, MI, USA.

### 3. Results

Four litters in the wild-type hard chow (WTHC) and wild-type soft chow (WTSC) groups, six litters in the null hard chow (NHC) group and five litters in the null soft chow (NSC) group were available for data analyses. One mother in the WTSC group died for an unknown reason on D17. A foster mother of the same genotype nursed her litter until D21, and the data from this litter was included in the analysis. The foster mother was not also nursing her own pups at that time.

Plots of the average pup weights (litter weight/pups per litter)  $\pm 2$  standard errors for each group at specific time points are shown in Figures 1 and 2 and the ANOVA analysis in Table 1. The average bodyweight (BW) of pups from all four groups was not significantly different until D21, when the NHC group was significantly lighter than both of the wild-type groups (Figure 1 and Table 1). In the postweaning period (after D21) when male and female pups were weighed separately, the mean male average litter bodyweight (ALBW) in the NHC group was significantly lower than the other three groups at D35 and D42 (Figure 2(a) and Table 1). The same pattern was observed for female mean ALBW at D28 and D35 (Figure 2(b) and Table 1). These data are consistent with the interpretation that null pups, especially null pups fed hard chow, were gaining weight more slowly because they were eating less due to the lack of enamel on their teeth.

Table 2 shows the mothers' average bodyweights (DBW) of the four groups starting at the birth of their pups (day 0) and again at days 7, 14, and 21. The mothers of the two wild-type groups were significantly heavier than the NSC group on days 0 and 7. On day 14, the mothers of the two null mice groups weighed significantly less than the mothers of the wild-type groups. However, on day 21, no statistically significant differences in maternal bodyweight (DBW) among the four groups were observed, although the null mothers' bodyweights trended lower. Perhaps a larger sample size would have demonstrated significance at day 21 or other variables besides genetic background affected the analysis. The mixed model analyses (Table 3) demonstrated that ALBW was significantly related to the group ( $P = 0.01$ ), litter size ( $P < 0.00$ ), day ( $P < 0.00$ ) but not DBW ( $P = 0.72$ ). We suspect that nursing mothers may exhibit adaptation behaviors in managing dietary intake.

One-way ANOVA analysis of adult male mouse bodyweight and *post hoc* comparison of four experimental groups revealed that the mean bodyweight in the NHC group was still significantly lower than the other three groups (Table 4).

Although the average bodyweight of NSC group was 7.8% lower than the average weight of the WTSC, there was no statistical difference between the two groups, which suggests that maintaining *Enam* null mice with tooth defects on soft chow may allow them to obtain adequate nutrition for proper weight gain.

Morphologic evaluation of the hemimandibles (Figure 3) showed that the appearance of molars was identical to what was described in previous work [19]. The color of molars was chalky-white and the surface was rough in the null mice. There was no apparent enamel layer, occlusal wear was apparent, and periodontal defects associated food and debris impaction was observed between molars with open interproximal contacts. All findings suggested that the enamel layer of null mice was defective and chewing function may have been compromised.

### 4. Discussion

The ANOVA analyses showed the BW of NHC was significantly different from the two wild-type groups after day 21. In contrast, the BW of NSC was not significantly different from the wild-type groups throughout the 6-week experimental period, even though it was consistently lower than that of wild-type. This result indicated that the food hardness is important for null mice as a factor in determining BW. As soon as the eyes of young mice open, they start to consume solid food [30]. The timing of opening their eyes, around day 14, approximates the timing of BW deviation that we observed. It is plausible that when the young null mice tried to eat solid food as a supplement, they had difficulties because of their defective enamel. Furthermore, they had more trouble gaining weight when they were given only hard chow. The impeded ability to eat hard chow effectively among the null mice resulted in lower bodyweight gain.

The mean BW of pups decreased by 0.3 gm with each additional pup in the litter on day 21 (the results of the mixed model analyses). The negative relationship between litter size and average litter BW is in accordance with previous studies. The study evaluated the effect of litter size on average pup weight in rats using regression analysis showed that the relation was negative and increased in magnitude from birth to weaning (3 wk) [31]. The effect persisted into the postweaning period; although a compensatory growth spurt seemed to occur during wk 3 to 5. It was noted that when litter size was not adjusted in the mixed model, there was only marginal difference in bodyweight ( $P = 0.08$ ) among groups. The average litter size (average of D0 to D21) in the null groups was about 1 to 2 less than wild-type groups. There were an average of 6.2 pups per litter in null groups, regardless of food type; 7 in WTSC and 8 in WTHC mice. Although no statistic analysis was performed to compare litter size among groups, the fact that the litter size was smaller in null mice suggested that the attrition of pups might have occurred. It may be due to the mother selectively nurse healthier pups and/or smaller/weaker pups in the same litter were outcompeted. Both indicated that the nutrition from

TABLE 1: One-way ANOVA analyses of ALBW at days 0, 7, 14, 21, 28, 35, and 42. The average litter bodyweights (g) with standard deviations in parentheses are presented. Each litter weight was divided by the number of pups in the litter. Statistically significant ( $P < 0.05$ ) differences between groups within each time point are noted.

Day	Gender	WTHC	WTSC	NHC	NSC
0	M + F	1.4 (0.1)	1.4 (0.1)	1.3 (0.1)	1.3 (0.1)
7	M + F	4.1 (0.5)	3.9 (0.4)	3.4 (0.3)	3.8 (0.2)
14	M + F	6.8 (0.6)	6.8 (1.0)	5.7 (0.8)	6.4 (0.6)
21	M + F	9.0* (0.8)	8.6* (1.2)	6.4** (1.2)	7.9 (0.4)
28	M	14.1* (1.1)	13.4* (1.3)	9.1** (1.8)	11.6 (1.6)
	F	12.5* (0.7)	12.2* (1.3)	7.8*** (2.1)	11.2 <sup>‡</sup> (1.1)
35	M	18.6* (1.4)	18.2* (1.1)	11.5*** (3.8)	16.5 <sup>‡</sup> (1.7)
	F	15.8* (0.7)	15.6* (1.6)	10.4*** (2.7)	14.3 <sup>‡</sup> (1.0)
42	M	20.3* (1.1)	20.1* (0.5)	14.6*** (3.7)	18.9 <sup>‡</sup> (0.9)
	F	17.0 (0.5)	17.2 (1.2)	13.8 (2.3)	15.4 (1.2)

Statistically significant differences (SSDs) between NHC and WTHC (\*); NHC and WTSC (\*); NHC and NSC (<sup>‡</sup>). Until day 21, the males and females of each litter were weighed together. There were no statistically significant differences among the groups until day 21, suggesting that bodyweight differences might be associated with the transition to eating chow.

TABLE 2: One-way ANOVA analyses of dam bodyweights on litter days 0, 7, 14, and 21. The average bodyweights (g) of the mothers with standard deviations in parentheses are presented. Statistically significant ( $P < 0.05$ ) differences between groups within each time point are noted.

Group	WTHC	WTSC	NHC	NSC
N	4	4	6	5
D0	31.94 <sup>†*</sup> (0.84)	30.27 <sup>‡</sup> (1.74)	27.92* (1.37)	26.48 <sup>‡‡</sup> (1.59)
D7	35.33 <sup>†*</sup> (1.70)	33.77 <sup>‡</sup> (1.53)	30.74* (1.80)	29.61 <sup>‡‡</sup> (2.33)
D14	36.56 <sup>†*</sup> (3.54)	36.68 <sup>‡‡</sup> (2.59)	31.73** (2.18)	30.89 <sup>‡‡</sup> (1.99)
D21	34.00 (4.77)	34.23 (4.71)	31.38 (2.52)	31.12 (2.15)

Statistically significant differences (SSD) between NHC and WTHC (\*); NHC and WTSC (\*); NSC and WTHC (<sup>†</sup>); NSC and WTSC (<sup>‡</sup>); N: number of litters. This data shows that the null mothers fed hard chow did not show significant differences in bodyweight with null mothers fed soft chow. The null mothers' bodyweights were smaller than those of the wild-type mothers.

TABLE 3: Mixed-model analyses of independent variables and ALBW. The potential for independent variables to influence the average litter bodyweight was assessed. The intercept is the ALBW at D21. A  $P$  value  $< 0.05$  was accepted as significant.

Source	Numerator df	Denominator df	F	P
Intercept	1	87.32	405.12	$< 0.00$
Day	21	108.72	14.67	$< 0.00$
Group	3	16.04	5.45	0.01
Litter size	1	74.81	22.00	$< 0.00$
DBW	1	225.85	0.13	0.72
Day-group	63	103.78	1.70	0.01
Day-litter size	21	109.79	3.51	$< 0.00$
Day-DBW	21	110.17	0.85	0.66

df: degrees of freedom. The table shows that factors such as litter size could influence the average litter bodyweight, while the mother's bodyweight (DBW) did not.

TABLE 4: One-way ANOVA analyses comparing adult male mouse bodyweights. Statistically significant ( $P < 0.05$ ) differences between groups at time point of 4-5 months are noted.

Group	WTHC	WTSC	NHC	NSC
N	9	13	10	11
Mean BW (g)	25.64* (1.55)	28.03* (1.08)	21.94*** (4.54)	25.85 <sup>‡</sup> (2.09)

Statistically significant differences (SSD) between NHC and WTHC (\*); NHC and WTSC (\*); NHC and NSC (<sup>‡</sup>). The bodyweight of NHC adult male mice was significantly lower than that of the other three groups.



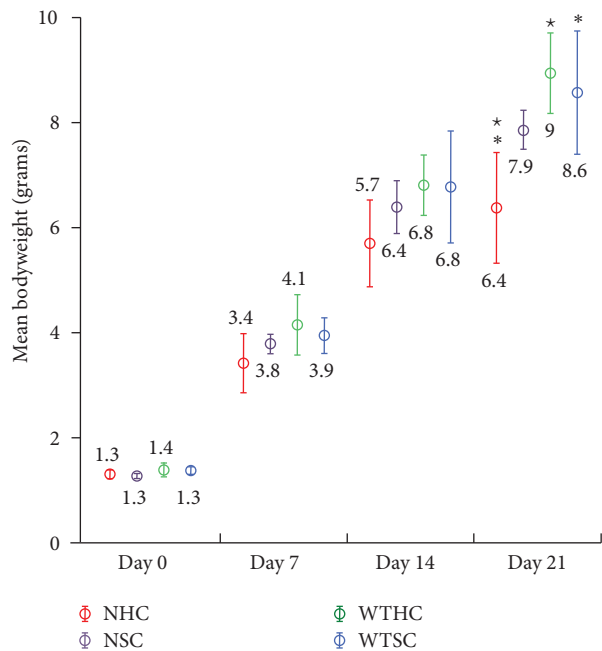


FIGURE 1: Mean bodyweights of pups at days 0, 7, 14, and 21 (prior to weaning). Four groups of mice were measured and compared wild-type hard chow (WTHC), null hard chow (NHC), wild-type soft chow (WTSC), and null soft chow (NSC). At birth, the mean bodyweight of mice in all groups was similar and showed little variance. Over time, the mean bodyweights showed increasing variance within and between groups. The only statistically significant differences were found at 21 days where the mean bodyweight of null mice provided with hard chow was lower than wild-type mice. Statistically significant differences (SSD) between NHC and WTSC (\*) or WTHC (\*).

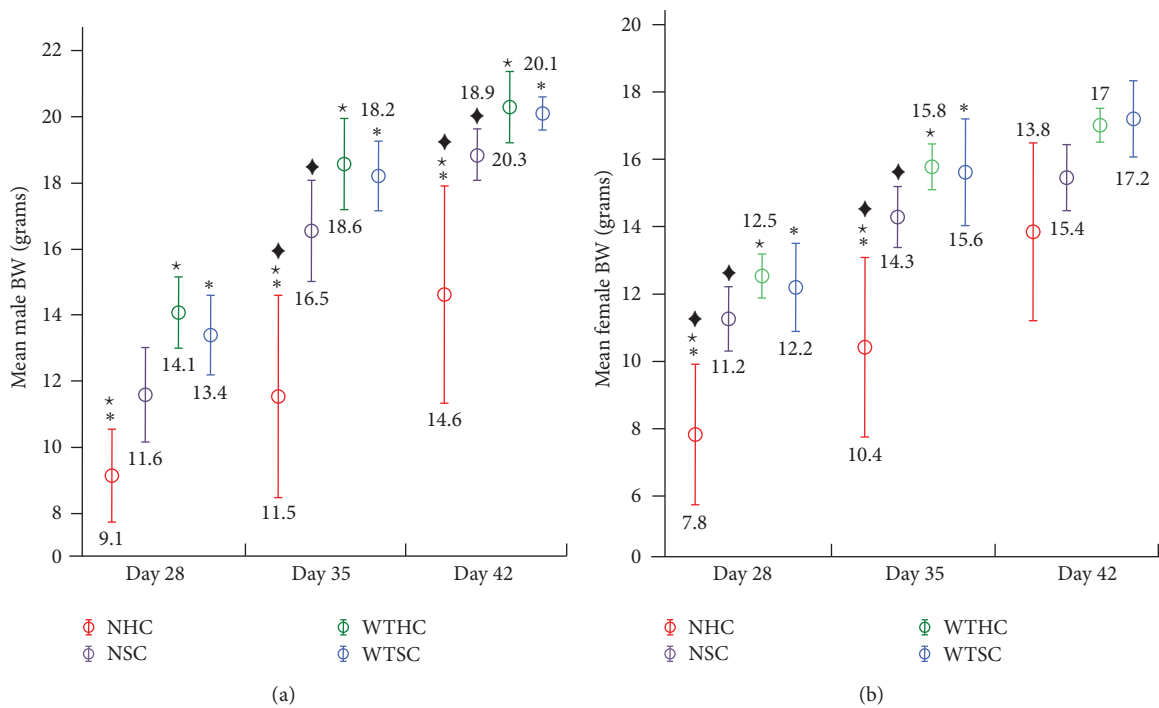


FIGURE 2: Mean bodyweights of male (a) and female (b) pups after weaning (days 28, 35, and 42). Statistically significant differences (SSD) between NHC and WTSC (\*), WTHC (\*), or NSC (◆). The null mice on hard chow had a lower mean bodyweight than null mice on soft chow and wild-type mice on hard or soft chow. Although the mean bodyweight of null mice on soft chow tended to have a lower average bodyweight than wild-type mice, the differences were small and not statistically significant. The mean bodyweight of null mice on hard chow varied more than mice in other groups, suggesting differences in how individual mice adapted to eating with defective dentitions.

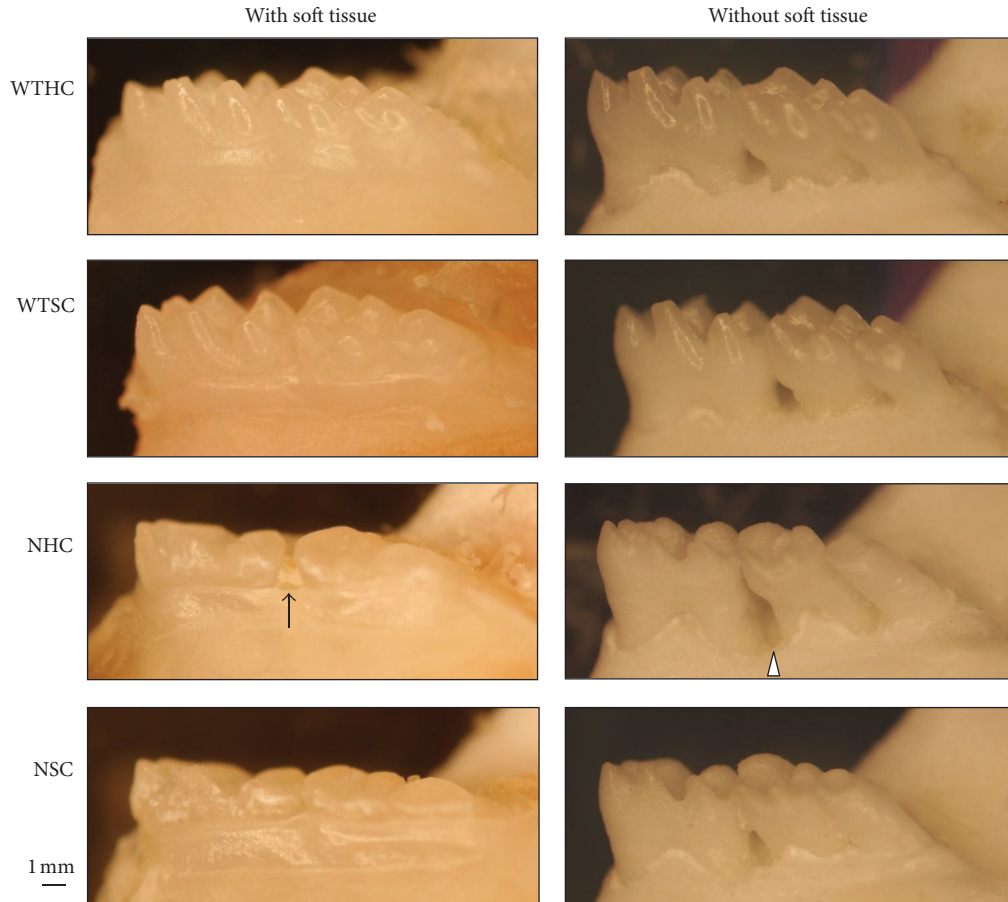


FIGURE 3: Morphology of mandibular molars at 8 weeks. Normal cuspal morphology, coronal crown contour, and supporting bone structure can be observed among wild-type mice maintained on hard chow (WTHC) or soft chow (WTSC). Flattened cusps and smaller occlusal table are consistent features of null mouse molars (NHC and NSC). Food impaction (arrow) between molars was often observed in the null mice and was associated with bony defects (arrowhead).

null mother mice might not be sufficient compared to the wild-type groups with the same litter size.

It was surprising that there was no correlation between DBW and ALBW. The BW of the null mother mice was consistently lower than that of the wild-type mothers; however, the pattern of litter weight gain did not correspond to that of maternal BW. The ALBW was generally similar among groups until the end of preweaning period. After that time point wild-type pups showed higher BW gain than null pups with soft chow, which in time was heavier than null pups with hard chow. Although not statistically significant, the parallel correlation of DBW and ALBW did not exclude the possibility that the nutritional status of null dams was a factor influencing the observed lower BW of their litters. During the experiment, we found that the values of DBW fluctuated frequently and the magnitude can be as high as 5 grams between two consecutive days. The high BW variation of the individual dam may have contributed toward the finding of no significant difference on ALBW among the experimental groups. One study evaluated the genetic and maternal effects of mice using the cross-fostering technique [32]. Two females littering within a 12-hour period were paired and a random half of pups of each sex were then reciprocally switched

within the pair. The BW was taken every 3 days from birth to 6 weeks and weekly weight thereafter until 84 days. The variance due to nurse dams peaked at 12 days, accounting for about 70% of the phenotype variance in D12 weights.

The growth and development of mice in various developmental stages and how they were bred has been studied extensively [30]. In standard husbandry of mice, pups are kept with their mother for the first three weeks after birth, during which their nutrition primarily comes from mother's milk. Young mice start to consume solid food as soon as their eyes open roughly around day 14. They are weaned on day 21, signaling the end of their dependence on their mother. At the age of 6 weeks, they are considered young adult and can be active in reproduction. In a study assessing the impact of inherited enamel defects on bodyweight gain of amelogenin (*Amelx*) null mice [33], it was reported that the average BW of the null mice was less than that of the wild-type mice on each day of the 3-week preweaning period. It is possible that the result is due partially to decreased nutritional intake starting from the affected mother mice. It would be interesting to determine if the BW difference would be even more significant after the young mice start to eat with their defective teeth independently from their mother.

Recently, a phenotyping screening of two enamelin-mutant mouse lines originating from an ENU mutagenesis project for dominant mutations on a C3HeB/FeJ genetic background observed dominant effects of heterozygous enamelin mutations on bone and energy metabolism, as well as on clinical chemistry and hematological parameters, suggesting that enamelin plays a critical role in other organs besides developing teeth [34]. The first mouse, with the p.Gln176\* mutation, had previously been characterized without noting systemic effects [18]. The second mouse *Enam* mutation (c.A382T; p.Lys128\*) was dominant so that mice heterozygous and homozygous for the mutation both showed the same level of defective “whitish” enamel. They concluded that the heterozygous enamelin truncations likely resulted in defective energy metabolism possibly from subtle changes in liver and/or pancreas function. This conclusion is hard to reconcile with the fact that not a single enamelin transcript is listed among the 111,391 (mouse) or 205,232 (human) ESTs for liver and 106,259 (mouse) or 213,410 (human) ESTs for pancreas. Enamelin is a member of the secretory calcium-binding phosphoproteins (SCPPs) encoded by a family of genes clustered on chromosome 4q13 in humans and chromosome 5 in mice [35, 36] that are critical for many processes, such as bone and tooth biomineralization, saliva, and lactation. Perhaps, there are undetected mutations affecting these linked genes that account for their findings. The results of this study cast doubt upon the claim that their mice with severe enamel defects ate as much hard chow as wild-type mice. If there are no differences in food intake by mice with and without enamel, what is the selective pressure that maintains the enamel layer during evolution?

In this study, we first tested the hypothesis that *Enam* null mice have lower bodyweights than wild-type mice. Our results showed that *Enam* null mice have significantly lower bodyweights than wild-type mice starting at day 21, when the mice are weaning. We also showed that weaned null mice fed on hard chow tend to have lower bodyweights than null mice fed on soft chow, revealing that at least part of the lower bodyweight can be explained by eating difficulties secondary to the lack of enamel on the dentition. Our results, in conjunction with evidence that enamelin is expressed specifically by ameloblasts and there is an absence of selection pressure to maintain *Enam* in vertebrates that have lost the ability to make enamel during evolution, support the conclusion that enamelin does not perform necessary functions outside of dental enamel formation.

## Acknowledgments

The authors thank Dr. Yuanyuan Hu for her technical consultations on mouse breeding and Mr. Joe Kazemi at the Center for Statistical Consultation and Research, University of Michigan, for providing statistical consultations. The study was supported by NIDCR Grant DE011301.

## References

- [1] M. H. Rajpar, K. Harley, C. Laing, R. M. Davies, and M. J. Dixon, “Mutation of the gene encoding the enamel-specific protein, enamelin, causes autosomal-dominant amelogenesis imperfecta,” *Human Molecular Genetics*, vol. 10, no. 16, pp. 1673–1677, 2001.
- [2] C. K. Mårdh, B. Bäckman, G. Holmgren, J. C. C. Hu, J. P. Simmer, and K. Forsman-Semb, “A nonsense mutation in the enamelin gene causes local hypoplastic autosomal dominant amelogenesis imperfecta (AIH2),” *Human Molecular Genetics*, vol. 11, no. 9, pp. 1069–1074, 2002.
- [3] M. Kida, T. Ariga, T. Shirakawa, H. Oguchi, and Y. Sakiyama, “Autosomal-dominant hypoplastic form of amelogenesis imperfecta caused by an enamelin gene mutation at the exon-intron boundary,” *Journal of Dental Research*, vol. 81, no. 11, pp. 738–742, 2002.
- [4] P. S. Hart, M. D. Michalec, W. K. Seow, T. C. Hart, and J. T. Wright, “Identification of the enamelin (g.8344delG) mutation in a new kindred and presentation of a standardized ENAM nomenclature,” *Archives of Oral Biology*, vol. 48, no. 8, pp. 589–596, 2003.
- [5] T. C. Hart, P. S. Hart, M. C. Gorry et al., “Novel ENAM mutation responsible for autosomal recessive amelogenesis imperfecta and localised enamel defects,” *Journal of Medical Genetics*, vol. 40, no. 12, pp. 900–906, 2003.
- [6] J. W. Kim, F. Seymen, B. P. J. Lin et al., “ENAM mutations in autosomal-dominant amelogenesis imperfecta,” *Journal of Dental Research*, vol. 84, no. 3, pp. 278–282, 2005.
- [7] D. Ozdemir, P. S. Hart, E. Firatli, G. Aren, O. H. Ryu, and T. C. Hart, “Phenotype of ENAM mutations is dosage-dependent,” *Journal of Dental Research*, vol. 84, no. 11, pp. 1036–1041, 2005.
- [8] J. W. Kim, J. P. Simmer, B. P. L. Lin, F. Seymen, J. D. Bartlett, and J. C. C. Hu, “Mutational analysis of candidate genes in 24 amelogenesis imperfecta families,” *European Journal of Oral Sciences*, vol. 114, supplement 1, pp. 3–12, 2006.
- [9] S. J. Gutierrez, M. Chaves, D. M. Torres, and I. Briceño, “Identification of a novel mutation in the enamelin gene in a family with autosomal-dominant amelogenesis imperfecta,” *Archives of Oral Biology*, vol. 52, no. 5, pp. 503–506, 2007.
- [10] A. Pavlič, M. Petelin, and T. Battelino, “Phenotype and enamel ultrastructure characteristics in patients with ENAM gene mutations g.13185-13186insAG and 8344delG,” *Archives of Oral Biology*, vol. 52, no. 3, pp. 209–217, 2007.
- [11] H. Y. Kang, F. Seymen, S. K. Lee et al., “Candidate gene strategy reveals ENAM mutations,” *Journal of Dental Research*, vol. 88, no. 3, pp. 266–269, 2009.
- [12] H. C. Chan, L. Mai, A. Oikonomopoulou et al., “Altered enamelin phosphorylation site causes amelogenesis imperfecta,” *Journal of Dental Research*, vol. 89, no. 7, pp. 695–699, 2010.
- [13] R. G. Lindemeyer, C. W. Gibson, and T. J. Wright, “Amelogenesis imperfecta due to a mutation of the enamelin gene: clinical case with genotype-phenotype correlations,” *Pediatric Dentistry*, vol. 32, no. 1, pp. 56–60, 2010.
- [14] J. T. Wright, M. Torain, K. Long et al., “Amelogenesis imperfecta: genotype-phenotype studies in 71 families,” *Cells Tissues Organs*, vol. 194, pp. 279–283, 2011.
- [15] Y. L. Song, C. N. Wang, C. Z. Zhang, K. Yang, and Z. Bian, “Molecular characterization of amelogenesis imperfecta in Chinese patients,” *Cells Tissues Organs*, vol. 13, article 13, 2012.
- [16] S. Simmer, N. Estrella, R. Milkovich, and J. Hu, “Autosomal dominant amelogenesis imperfecta associated with ENAM frameshift mutation p.Asn361Ilefs56,” *Clinical Genetics*. In press.
- [17] H. Masuya, K. Shimizu, H. Sezutsu et al., “Enamelin (Enam) is essential for amelogenesis: ENU-induced mouse mutants as



- models for different clinical subtypes of human amelogenesis imperfecta (AI)," *Human Molecular Genetics*, vol. 14, no. 5, pp. 575–583, 2005.
- [18] H. Seedorf, M. Klafken, F. Eke, H. Fuchs, U. Seedorf, and M. Hrabe De Angelis, "A mutation in the enamel gene in a mouse model," *Journal of Dental Research*, vol. 86, no. 8, pp. 764–768, 2007.
- [19] J. C. C. Hu, Y. Hu, C. E. Smith et al., "Enamel defects and ameloblast-specific expression in Enam knock-out/lacZ knock-in mice," *Journal of Biological Chemistry*, vol. 283, no. 16, pp. 10858–10871, 2008.
- [20] T. A. Deméré, M. R. McGowen, A. Berta, and J. Gatesy, "Morphological and molecular evidence for a stepwise evolutionary transition from teeth to baleen in mysticete whales," *Systematic Biology*, vol. 57, no. 1, pp. 15–37, 2008.
- [21] R. W. Meredith, J. Gatesy, W. J. Murphy, O. A. Ryder, and M. S. Springer, "Molecular decay of the tooth gene enamel (ENAM) mirrors the loss of enamel in the fossil record of placental mammals," *PLoS Genetics*, vol. 5, no. 9, Article ID e1000634, 2009.
- [22] N. Al-Hashimi, A. G. Lafont, S. Delgado, K. Kawasaki, and J. Y. Sire, "The enamel genes in lizard, crocodile, and frog and the pseudogene in the chicken provide new insights on enamel evolution in tetrapods," *Molecular Biology and Evolution*, vol. 27, no. 9, pp. 2078–2094, 2010.
- [23] R. W. Meredith, J. Gatesy, J. Cheng, and M. S. Springer, "Pseudogenization of the tooth gene enamelysin (MMP20) in the common ancestor of extant baleen whales," *Proceedings of Biological Sciences*, vol. 278, no. 1708, pp. 993–1002, 2011.
- [24] G. Acs, G. Lodolini, S. Kaminsky, and G. J. Cisneros, "Effect of nursing caries on body weight in a pediatric population," *Pediatric Dentistry*, vol. 14, no. 5, pp. 302–305, 1992.
- [25] A. Sheiham, "Dental caries affects body weight, growth and quality of life in pre-school children," *British Dental Journal*, vol. 201, no. 10, pp. 625–626, 2006.
- [26] P. S. Hart, T. C. Hart, M. D. Michalec et al., "Mutation in kallikrein 4 causes autosomal recessive hypomaturation amelogenesis imperfecta," *Journal of Medical Genetics*, vol. 41, no. 7, pp. 545–549, 2004.
- [27] J. W. Kim, J. P. Simmer, T. C. Hart et al., "MMP-20 mutation in autosomal recessive pigmented hypomaturation amelogenesis imperfecta," *Journal of Medical Genetics*, vol. 42, no. 3, pp. 271–275, 2005.
- [28] P. S. Hart, S. Becerik, D. Cogulu et al., "Novel FAM83H mutations in Turkish families with autosomal dominant hypocalcified amelogenesis imperfecta," *Clinical Genetics*, vol. 75, no. 4, pp. 401–404, 2009.
- [29] J. W. Kim, J. P. Simmer, Y. Y. Hu et al., "Amelogenin p.M1T and p.W4S mutations underlying hypoplastic X-linked amelogenesis imperfecta," *Journal of Dental Research*, vol. 83, no. 5, pp. 378–383, 2004.
- [30] H. A. el-Oksh, T. M. Sutherland, and J. S. Williams, "Prenatal and postnatal maternal influence on growth in mice," *Genetics*, vol. 57, no. 1, pp. 79–94, 1967.
- [31] S. M. Azzam, M. K. Nielsen, and G. E. Dickerson, "Postnatal litter size effects on growth and reproduction in rats," *Journal of Animal Science*, vol. 58, no. 6, pp. 1337–1342, 1984.
- [32] J. J. Rutledge, O. W. Robison, E. J. Eisen, and J. E. Legates, "Dynamics of genetic and maternal effects in mice," *Journal of Animal Science*, vol. 35, no. 5, pp. 911–918, 1972.
- [33] Y. Li, Z. A. Yuan, M. A. Aragon, A. B. Kulkarni, and C. W. Gibson, "Comparison of body weight and gene expression in amelogenin null and wild-type mice," *European Journal of Oral Sciences*, vol. 114, supplement 1, pp. 190–193, 2006.
- [34] H. Fuchs, S. Sabrautzki, H. Seedorf et al., "Does enamel have pleiotropic effects on organs other than the teeth? Lessons from a phenotyping screen of two enamel-mutant mouse lines," *European Journal of Oral Sciences*, vol. 120, pp. 269–277, 2012.
- [35] K. Kawasaki and K. M. Weiss, "Mineralized tissue and vertebrate evolution: the secretory calcium-binding phosphoprotein gene cluster," *Proceedings of the National Academy of Sciences of the United States of America*, vol. 100, no. 7, pp. 4060–4065, 2003.
- [36] K. Kawasaki, A. V. Buchanan, and K. M. Weiss, "Gene duplication and the evolution of vertebrate skeletal mineralization," *Cells Tissues Organs*, vol. 186, no. 1, pp. 7–24, 2007.